

AN INVESTIGATION INTO THE ANTIDIABETIC AND
CATALYTIC PROPERTIES OF OXOVANADIUM(IV)
COMPLEXES

A thesis submitted in fulfilment of the requirements

for the degree of

DOCTOR OF PHILOSOPHY

at

Rhodes University



by

Ryan Steven Walmsley

December 2011

Abstract

In part 1 of this thesis, the antidiabetic activity of a series of novel oxovanadium(IV) complexes was investigated. A range of bidentate N,O-donor ligands, which partially mimic naturally occurring bioligands, were prepared and reacted with the vanadyl ion to form the corresponding *bis*-coordinated complexes. Initially, 2-(2'-hydroxyphenyl)-1*R*-imidazoline (where R = H, ethyl and ethanol) ligands were prepared. The aqueous pH-metric chemical speciation was investigated using glass electrode potentiometry which allowed for the determination of protonation and stability constants of the ligands and complexes, respectively. The species distribution diagrams generated from this information gave an indication of how the complexes might behave across the broad pH range experienced in the digestive and circulatory systems. This information was used to create an improved 2nd generation of ligands that were constructed by combining the imidazole and carboxylic acid functionalities. These corresponding *bis*[(imidazolyl)carboxylato]-oxovanadium(IV) complexes displayed a broader pH-metric stability. Both sets of complexes improved glucose uptake and reduced coagulation *in vitro*.

In part 2 of this thesis, a range of homogeneous and heterogeneous oxovanadium(IV) catalysts were prepared. Firstly, Merrifield beads were functionalized with ligands from Part 1 and then reacted with vanadyl sulfate to afford the corresponding heterogeneous catalysts. These displayed promising catalytic activity for the peroxide facilitated oxidation of thioanisole, styrene and ethylbenzene as well as the oxidative bromination of phenol red. Smaller imidazole-containing beads with higher surface areas than the Merrifield beads were prepared by suspension polymerization. These beads similarly demonstrated excellent catalytic activity for the oxidation of thioanisole and were highly recyclable. In attempt to increase the exposed catalytic surface area, while retaining the ease of separation achieved in the before mentioned systems, micron to nano sized electrospun fibers containing coordinating ligands were fabricated. The corresponding oxovanadium(IV) functionalized fibers were applied to the oxidation of thioanisole using a continuous flow system. The flexible and porous nature of the fiber mats was well suited to this approach. After optimization of the reactant flow rate and catalyst amount, near quantitative (> 99%) oxidation was achieved for an extended period. In addition, leaching of vanadium was mitigated by modification of the attached ligand or polymer material.

Acknowledgements

Firstly, I would like to thank Dr Zenixole Tshentu. His understanding and guidance during times of stress was invaluable. He has shown me unbelievable support throughout my studies, assisting far beyond what is required of a supervisor. I am also very grateful to him for allowing me to use his office while I was lecturing and writing my thesis.

Prof. Nelson Torto so kindly allowed me to freely use his laboratory and electrospinning equipment. I also thank Prof. Tebello Nyokong, Dr Christian Litwinski, Dr Wadzanai Chidawanyika and Dr Edith Antunes from the DST/Mintek National Innovation Centre (Rhodes University) for access to, and assistance with several of the instruments used in this study.

I thank the technical staff, in particular Mr Francis Chindeka who is seemingly capable of fixing anything electronic and does so with a constant smile, as well as Mr Andre Adriaan and his team who also helped hugely. I thank the very capable Mrs Benita Tarr and the office staff, who were very supportive and helpful with all things administrative. I must also thank all my colleagues in the Inorganic Chemistry group for the support and fun times, in particular Ogunlaja Niyi for his assistance with my thesis submission. The happy work environment you all created made my experience at Rhodes a memorable one indeed.

I am extremely grateful to the following individuals from outside Rhodes University:

- Prof. Carminita Frost and Dr Nandipha Mnonopi (NMMU) for the assistance with the biological studies.
- Mr Percy Hlangothi (NMMU) for assistance with thermal gravimetric analysis.
- Dr Manuel Fernandes (WITS) for help with the crystallography.

I would like to thank my mom, Patricia Walmsley, who sacrificed much to get me through University. Her support and belief in me always challenged me to do better and work harder. I would also like to thank the rest of my family for support given. My granny, who has lived with insulin dependent diabetes for over 70 years, has defied all the statistics and convinced me that a good attitude and ability to laugh at oneself can be more beneficial than even the best man-made medicines. I thank my incredible wife, Tara, who was forced to listen to many of my complaints

and frustrations from the lab, all the while making beautiful meals every night, scratching my head and completing her own PhD in microbiology. I am also very grateful to her for proof reading my thesis.

Finally, I would like to thank Sasol for their financial support during my studies. In particular, I would like to thank Drs Reinier Nel, David Phaho and Pieter van Heerden for their inputs into this study. I am also grateful to the South African NRF and Rhodes University for funding.

Table of Contents

Abstract	i
Acknowledgements	ii
List of Figures	x
List of Schemes	xvi
List of Tables	xviii

Part 1

The antidiabetic properties of oxovanadium(IV) complexes

Chapter 1. Introduction	2
1.1 Diabetes mellitus – an overview	2
1.2 Forms of diabetes	3
1.3 Current therapy	4
1.4 Diabetes associated conditions	7
1.4.1 A brief introduction to the coagulation pathways	8
1.5 Medicinal inorganic chemistry.....	11
1.5.1 Metals in the treatment of diabetes	11
1.5.2 Mechanism of action of vanadium complexes	12
1.5.3 Antidiabetic vanadium complexes.....	15
1.6 Vanadium chemistry.....	18
1.6.1 Atomic structure and bonding of oxovanadium.....	19
1.6.2 Infrared spectroscopy of oxovanadium complexes.....	22
1.6.3 Redox chemistry	23
1.6.4 Solution chemistry of vanadium	24
1.7 Vanadium in biology.....	26
1.8 Aims and objectives of this study.....	28
1.9 References.....	30
Chapter 2. Experimental materials and methods	36
2.1 General reagents	36
2.2 Techniques and instrumentation.....	36

2.2.1	General instrumentation	36
2.2.2	Cyclic voltammetry	37
2.2.3	Potentiometric studies	37
2.2.4	X-ray crystal structure resolution and refinement	38
2.2.5	Biological studies	38
2.3	References	41
Chapter 3. Oxovanadium(IV) complexes with 2-(2'-hydroxyphenyl)-1<i>R</i>-imidazoline ligands		43
3.1	Introduction	43
3.2	Preparative work	46
3.2.1	2-(2'-hydroxyphenyl)-1 <i>H</i> -imidazoline (piminH)	46
3.2.2	2-(2'-hydroxyphenyl)-1-ethylimidazoline (EtpiminH)	46
3.2.3	2-(2'-hydroxyphenyl)-1-ethanolimidazoline (EtOHpiminH)	46
3.2.4	[VO(pimin) ₂]	47
3.2.5	[VO ₂ (pimin)(piminH')]	47
3.2.6	[VO(Etpimin) ₂]	47
3.2.7	[VO(EtOHpimin) ₂]	47
3.3	Results and discussion	48
3.3.1	Synthesis and general considerations	48
3.3.2	pH-Metric chemical speciation	56
3.3.3	In vitro glucose uptake studies	61
3.3.4	Anticoagulation studies	64
3.4	Conclusions	66
3.5	References	67
Chapter 4. Oxovanadium(IV) complexes with imidazole-carboxylic acid ligands		71
4.1	Introduction	71
4.2	Preparative work	74
4.2.1	Imidazole-4-carboxylic acid (Im4COOH)	74
4.2.2	1-Methylimidazole-2-carboxaldehyde (Melm2CHO)	74
4.2.3	Imidazole-2-carboxylic acid.H ₂ O (Im2COOH)	74
4.2.4	1-Methylimidazole-2-carboxylic acid.H ₂ O (Melm2COOH)	75
4.2.5	[VO(Im4COO) ₂]	75
4.2.6	[VO(Im2COO) ₂]	75
4.2.7	[VO(Melm2COO) ₂]	76
4.3	Results and discussion	77
4.3.1	Synthesis and general considerations	77
4.3.2	Spectroscopic characterization	81

4.3.3	pH-Metric chemical speciation	83
4.3.4	In vitro glucose uptake studies.....	91
4.3.5	Anticoagulation studies	94
4.4	Conclusions.....	95
4.5	References.....	96
Chapter 5. Conclusions and future work		99
5.1	Conclusions.....	99
5.2	Future work	99

Part 2

Catalytic properties of heterogeneous oxovanadium(IV) complexes

Chapter 1. Introduction	103
1.1 Catalysis.....	103
1.2 Vanadium in catalysis	104
1.2.1 Naturally occurring vanadium-dependent haloperoxidases.....	106
1.2.2 Catalytic mechanism of oxovanadium(IV) oxidations	108
1.3 Support materials for immobilization of homogeneous catalysts.....	109
1.3.1 The basics of polymerization.....	109
1.3.2 Soluble polymer supports.....	111
1.3.3 Techniques for producing polymer beads.....	111
1.3.4 Techniques for producing polymer fibers.....	116
1.4 Functionalization of polymer supports	122
1.4.1 Monomerization.....	122
1.5 Aims and objectives	129
1.6 References.....	131
Chapter 2. Experimental materials and methods	136
2.1 General reagents	136
2.2 Techniques and instrumentation.....	137
2.2.1 General instrumentation.....	137
2.3.2 Scanning electron microscopy	137
2.3.3 Atomic force microscopy	137

2.3.4	X-ray photoelectron spectroscopy.....	137
2.3.5	Inductively coupled plasma – Optical emission spectroscopy.....	138
2.3.6	Brunauer, Emmett, Teller (BET) surface area analysis.....	139
2.3.7	Gas chromatography.....	140
2.3.8	Thermogravimetric analysis.....	140
	References.....	141
	Chapter 3. Merrifield resin-based oxovanadium(IV) catalysts for oxidation reactions.....	143
3.1	Introduction.....	143
3.2	Preparative work.....	146
3.2.1	Synthesis of the ligands.....	146
3.2.2	PS-pimin.....	146
3.2.3	PS-Im4COO.....	146
3.2.4	PS-MelmCOO.....	146
3.2.5	PS-[VO(pimin) _x].....	147
3.2.3	PS-[VO(Im4COO) _x].....	147
3.2.6	PS-[VO(MelmCOO) _x].....	147
3.3	Catalytic activity studies.....	148
3.3.1	Oxidation of styrene, ethylbenzene and thioanisole.....	148
3.3.2	Oxidative bromination.....	148
3.4	Results and discussion.....	149
3.4.1	Synthesis.....	149
3.4.2	Characterization.....	151
3.4.3	Catalytic activity.....	157
3.5	Conclusions.....	178
3.6	References.....	179
	Chapter 4. Polymer-supported oxovanadium(IV) catalysts prepared by suspension polymerization.....	183
4.1	Introduction.....	183
4.2	Preparative work.....	185
4.2.1	p(VIM-co-EGDMA) beads.....	185
4.2.2	p(VIM-co-EGDMA)-VO beads.....	185
4.2.3	Attempted synthesis imidazole-2-carboxylic acid containing beads.....	185
4.2.4	Attempted synthesis 2-(2'-hydroxyphenyl)imidazol(in)e containing beads.....	186
4.3	Catalytic activity studies.....	187
4.4	Results and discussion.....	188
4.4.1	Synthesis.....	188

4.4.2	Attempted syntheses.....	190
4.4.3	Characterization	192
4.4.4	Catalytic activity.....	197
4.5	Conclusions.....	203
4.6	References and notes	204
Chapter 5. Electrospun fibers as support materials for oxovanadium(IV) catalysts.....		208
5.1	Introduction	208
5.2	Preparation of ligands and oxovanadium(IV) complexes	211
5.2.1	2-(2'-Hydroxy-5'-bromophenyl)imidazole (pimBr)	211
5.2.2	N-Benzoyl-2-(2'-benzoxy-5'-bromophenyl)imidazole (dibenzoylpimBr).....	211
5.2.3	N-Benzoyl-2-(2'-benzoxy-5'-ethenylphenyl)imidazole (dibenzoylpim).....	212
5.2.4	2-(2'-Hydroxy-5'-ethenylphenyl)imidazole (vpim).....	212
5.2.5	2-(4,5-Diphenyl-1 <i>H</i> -imidazol-2-yl)phenol (dpimH)	212
5.2.6	4-Methoxy-2-(4,5-diphenyl-1 <i>H</i> -imidazol-2-yl)phenol (dpimMeO).....	213
5.2.7	4-Bromo-2-(4,5-diphenyl-1 <i>H</i> -imidazol-2-yl)phenol (dpimBr).....	213
5.2.8	4-Nitro-2-(4,5-diphenyl-1 <i>H</i> -imidazol-2-yl)phenol (dpimNO ₂).....	214
5.2.9	[VO(dpimH) ₂].....	214
5.2.10	[VO(dpimMeO) ₂].....	214
5.2.11	[VO(dpimBr) ₂].....	215
5.2.12	[VO(dpimNO ₂) ₂].....	215
5.3	Preparation of polymers and fabrication of fibers	216
5.3.1	PS-25 fibers.....	216
5.3.2	PS-25-[VO(dpimMeO) ₂] fibers.....	216
5.3.3	PS-15-[VO(dpimMeO) ₂] fibers.....	217
5.3.4	PS-25-[VO(dpimNO ₂) ₂] fibers.....	217
5.3.5	PS-15-[VO(dpimNO ₂) ₂] fibers.....	217
5.3.6	p(St-co-VIM) copolymer	217
5.3.7	p(ST-co-VIM) fibers.....	217
5.3.8	p(ST-co-VIM)-VO fibers	218
5.3.9	p(ST-co-VPIM) copolymer.....	218
5.3.10	p(ST-co-VPIM) fibers	218
5.3.11	p(ST-co-VPIM)-VO fibers	219
5.3.12	p(benzimidazole) fibers (PBI _f)	219
5.3.13	p(benzimidazole)-VO fibers (PBI _f -VO)	219
5.3.14	Attempted synthesis of p(St-co-VIMCOOH)	220
5.4	Catalytic activity studies	221
5.4.1	Homogeneous batch catalysis using [VO(dpimR) ₂] complexes.....	221

5.4.2	Continuous flow using PS-[VO(dpimR) ₂] fibers.....	221
5.4.3	Continuous flow using p(ST-co-VIM)-VO fibers	222
5.4.4	Continuous flow using p(ST-co-VPIM)-VO fibers.....	222
5.4.5	Batch catalysis using PBI _r -VO fibers	222
5.4.6	Continuous flow using PBI _r -VO fibers	223
5.5	Results and discussion	224
5.5.1	General synthesis and characterization.....	224
5.5.2	Synthesis of polymers, fabrication and characterization of electrospun fibers	229
5.5.3	Catalytic activity.....	249
5.6	Conclusions.....	264
5.7	References and notes	265
Chapter 6.	Conclusions and future work	269
6.1	Conclusions.....	269
6.2	Future work	270

List of Figures

Part 1

The antidiabetic properties of oxovanadium(IV) complexes

Figure 1.1	Population distribution map of people suffering from diabetes created using MapWindow GIS v4.8	2
Figure 1.2	Chemical structures of commonly prescribed sulfonylureas, glybenclamide and tolbutamide	5
Figure 1.3	Chemical structures of the biguanides, phenformin and metformin.....	6
Figure 1.4	Chemical structures of two thiazolidinediones, rosiglitazone and pioglitazone	6
Figure 1.5	Chemical structures of two meglitinides, repaglinide and nateglinide.....	7
Figure 1.6	Mechanism of stimulation of glucose uptake by insulin or vanadate	14
Figure 1.7	Crystal structure of PTP1B (C215S mutant) soaked with an oxovanadium(IV) complex	14
Figure 1.8	Chemical structures of BMOV and BEOV.....	16
Figure 1.9	Chemical structure of [VO(dhp) ₂].....	17
Figure 1.10	Chemical structure of <i>bis</i> (picolinato)oxovanadium(IV) [VO(pic) ₂].....	17
Figure 1.11	The colour of vanadium in biologically relevant oxidation states. From left to right, V ⁵⁺ , V ⁴⁺ , V ³⁺	18
Figure 1.12	Molecular orbital scheme for the VO ²⁺ species as outlined by Ballhausen	21
Figure 1.13	Clustered energy level scheme of OSM for vanadyl(IV) complexes.....	21
Figure 1.14	Some typical geometries of vanadium compounds.....	22
Figure 1.15	Speciation diagram for aqueous vanadate (VO ₂ ⁺). Concentration of [VO ₂ ⁺] = 1.0 mM.....	25
Figure 1.16	Speciation diagram for aqueous vanadyl (VO ²⁺). Concentration of [VO ²⁺] = 10 mM.....	26
Figure 3.1	The proposed coordination environment of the vanadyl-transferrin binary complex.....	44
Figure 3.2	¹ H NMR spectrum of 2-(2'-hydroxyphenyl)-1-ethylimidazoline (δ ppm). This insert shows an expanded view of the aromatic region	49
Figure 3.3	¹³ C NMR spectrum of 2-(2'-hydroxyphenyl)-1-ethylimidazoline (δ ppm). Solvent peak (CDCl ₃) has been omitted.....	49
Figure 3.4	Cyclic voltammograms of complexes [VO(pimin) ₂], [VO(Etpimin) ₂] and [VO(EtOHpimin) ₂] in DMSO.....	51
Figure 3.5	Stacked IR spectra of [VO(pimin) ₂], [VO(Etpimin) ₂] and [VO(EtOHpimin) ₂], in the range 4000 – 650 cm ⁻¹ . 52	
Figure 3.6	Electronic spectrum of [VO(pimin) ₂], in DMSO. Insert shows an expanded view of the region between 450-700 nm.....	52
Figure 3.7	ORTEP diagram of [VO(pimin) ₂], showing 50% thermal probability ellipsoids	54
Figure 3.8	ORTEP diagram of [VO(pimin)(piminH ⁺)], showing 50% thermal probability ellipsoids.....	54
Figure 3.9	Species distribution as a function of pH for 2-(2'-hydroxyphenyl)-1-ethylimidazoline	58
Figure 3.10	Species distribution as a function of pH for 2-(2'-hydroxyphenyl)-1-ethanolimidazoline	58

Figure 3.11	Species distribution diagram for the complexation of VO(IV) with EtpiminH (LH), $c_{VO} = 0.002 \text{ mol.L}^{-1}$ and $c_{ligand} = 0.004 \text{ mol.L}^{-1}$	59
Figure 3.12	Species distribution diagram for the complexation of VO(IV) with EtOHpiminH (LH), $c_{VO} = 0.002 \text{ mol.L}^{-1}$ and $c_{ligand} = 0.004 \text{ mol.L}^{-1}$	60
Figure 3.13	The effects of metformin (Met), vanadyl sulfate ($VOSO_4$), $[VO(pimin)_2]$, $[VO(Etpimin)_2]$ and $[VO(EtOHpimin)_2]$ (at $1 \mu\text{M}$ concentration) on Chang, C2C12 and 3T3-L1 glucose uptake. The basal glucose uptake, is represented as 100% (Control). Error bars indicate SEM (n=3), ($p < 0.05$) and ** ($p < 0.01$) relative to the (Con).....	62
Figure 3.14	The effect of $[VO(pimin)_2]$ ($10 \mu\text{M}$) on APTT (A) and PT (B) clotting times, on fibrin formation (C) and D-Dimer formation. The control represents untreated sample while the positive control represents the anticoagulant heparin (0.1 U.ml^{-1}) (n = 3).....	65
Figure 4.1	Structure of neutral imidazole (a), and the anionic form (b).....	71
Figure 4.2	^1H NMR spectrum of Melm2CHO (δ ppm). The solvent ($CDCl_3$) is responsible for the inflated integration at 7.3 ppm.....	78
Figure 4.3	^1H NMR spectrum of Melm2COOH (δ ppm). The solvent (D_2O) is left un-integrated.....	79
Figure 4.4	Comparison of the ^{13}C NMR spectra of Melm2CHO (top) (in $CDCl_3$ residual solvent peak at ~ 77 ppm) and Melm2COOH (bottom) (in D_2O).....	79
Figure 4.5	Cyclic voltammograms of complexes $[VO(Melm2COO)_2]$ and $[VO(Im4COO)_2]$ in H_2O	81
Figure 4.6	Infrared spectra of (A) $[VO(Im2COO)_2]$ and (B) Im2COOH.....	82
Figure 4.7	Solution electronic spectrum of $[VO(Im4COO)_2]$ in water. Insert shows an expanded view of the region between 400-900 nm.....	82
Figure 4.8	Solid state electronic spectrum of $[VO(Melm2COO)_2]$	83
Figure 4.9	Species distribution as a function of pH for imidazole-2-carboxylic acid.....	85
Figure 4.10	Species distribution as a function of pH for N-methylimidazole-2-carboxylic acid.....	86
Figure 4.11	Species distribution diagram for the complexation of VO(IV) with Im2COOH (LH), $c_{VO} = 0.002 \text{ mol.L}^{-1}$ and $c_{ligand} = 0.004 \text{ mol.L}^{-1}$	87
Figure 4.12	Species distribution diagram for the complexation of VO(IV) with Melm2COOH (LH), $c_{VO} = 0.002 \text{ mol.L}^{-1}$ and $c_{ligand} = 0.004 \text{ mol.L}^{-1}$	87
Figure 4.13	Species distribution diagram for the complexation of VO(IV) with Im4COOH (LH) and citric acid (Cit), $c_{VO} = 0.002 \text{ mol.L}^{-1}$, VO:A:B (1:2:2).....	90
Figure 4.14	Species distribution diagram for the complexation of VO(IV) with Im2COOH (LH) and citric acid (Cit), $c_{VO} = 0.002 \text{ mol.L}^{-1}$, VO:A:B (1:2:2).....	90
Figure 4.15	Species distribution diagram for the complexation of VO(IV) with Melm2COOH (LH) and citric acid (Cit), $c_{VO} = 0.002 \text{ mol.L}^{-1}$, VO:A:B (1:2:2).....	91
Figure 4.16	The effects of metformin (Met), vanadyl sulfate ($VOSO_4$), $[VO(Im4COO)_2]$, $[VO(Im2COO)_2]$ and $[VO(Melm2COO)_2]$ (at $1 \mu\text{M}$ concentration) on Chang, C2C12 and 3T3-L1 glucose uptake. The basal glucose uptake, is represented as 100% (Control). Error bars indicate SEM (n=3), ($p < 0.05$) relative to the (Con).....	92
Figure 4.17	The effect of $[VO(Im4COO)_2]$, $[VO(Im2COO)_2]$ and $[VO(Melm2COO)_2]$ ($10 \mu\text{M}$) on APTT (A) and PT (B) clotting times, on fibrin formation (C) and D-Dimer formation (D). The control represents untreated sample while the positive control represents the anticoagulant heparin (0.1 U.mL^{-1}) (n = 3).....	94

Part 2
Catalytic properties of heterogeneous oxovanadium(IV) complexes

Figure 1.1	Bromoperoxidases are found in <i>A. nodusum</i> (A), <i>Cor. officinalis</i> (B) and <i>X. parietina</i> (C)	107
Figure 1.2	The active site of the bromoperoxidase from <i>Ascophyllum nodusum</i> showing vanadium coordinated to the imidazole group of a histidine residue (HIS 486) and the close proximity of two other histidine residues (HIS 418 and HIS 411). PDB ID: 1QI9, illustrated using UCSF Chimera.....	107
Figure 1.3	Illustration of the process of emulsion polymerization.....	113
Figure 1.4	A schematic of a typical suspension polymerization procedure	114
Figure 1.5	Typical particle sizes obtained using different polymerization techniques	115
Figure 1.6	The electrospinning equipment used for the fabrication of polymer fibers in this thesis.....	118
Figure 1.7	Drawing of the first recorded electrospinning apparatus as described by Cooley in 1902	119
Figure 1.8	Scifinder Scholar® publication frequency analysis for the search term “electrospinning” or “electrospun” between 1994 and 2010.....	119
Figure 3.1	Structures of some imidazole-based ligands that have been anchored to PS-Cl ⁵⁻⁹	145
Figure 3.2	¹ H NMR spectrum of 2-(2'-benzyloxyphenyl)-1 <i>H</i> -imidazoline (δ ppm). The N-H proton signal appears at 10.1 ppm.....	150
Figure 3.3	Stacked IR spectra of PS-Cl, PS-pimin and PS-[VO(pimin) _x] in the range 4000 – 650 cm ⁻¹	152
Figure 3.4	Stacked IR spectra of PS-Cl, PS-MelmCOO and PS-[VO(MelmCOO) _x] in the range 2200 – 650 cm ⁻¹	153
Figure 3.5	Wide scan XPS spectra of PS-[VO(pimin) _x], PS-[VO(Im4COO) _x] and PS-[VO(Melm2COO) _x]. Insert shows an expanded view of the high resolution N 1s signals of PS-[VO(Im4COO) _x]	154
Figure 3.5	TG and DTG curves of PS-Cl, PS-pimin and PS-[VO(pimin) _x] at a heating rate of 10 °C.min ⁻¹ under N ₂ . 155	155
Figure 3.6	SEM images of a single bead and digital (right corner of bead) images of (A) PS-Cl, (B) PS-Im4COO and (C) PS-[VO(Im4COO) _x] (average diameter Ø = 612 µm)	155
Figure 3.7	AFM images of (A) PS-Cl, (B) PS-pimin and (C) PS-[VO(pimin) _x] (scale = 10x10 µm).....	156
Figure 3.8	Nitrogen adsorption-desorption isotherms for (A) PS-Cl and (B) PS-[VO(pimin) _x].....	157
Figure 3.9	The effect of catalyst amount on thioanisole oxidation. Reaction conditions: PS-[VO(pimin) _x], thioanisole (10 mmol), H ₂ O ₂ (20 mmol), acetonitrile (20 mL) and 25 °C.....	159
Figure 3.10	(A) Overall oxidation of thioanisole and (B) product selectivity for the catalysts PS-[VO(pimin) ₂], PS-[VO(Im4COO) ₂] and PS-[VO(Melm2COO) ₂] (0.025 g, ~0.2 mol% of V, wrt thioanisole), thioanisole (10 mmol), H ₂ O ₂ (20 mmol), acetonitrile (20 mL) and 25 °C.....	160
Figure 3.11	The product selectivity over time. Reaction conditions: PS-[VO(pimin) _x] (0.035 g), thioanisole (10 mmol), H ₂ O ₂ (20 mmol), acetonitrile (20 mL) and 25 °C	161
Figure 3.12	Catalyst recyclability for the oxidation of thioanisole. Reaction conditions: (A) PS-[VO(Im4COO) _x] (0.025 g), (B) PS-[VO(pimin) _x], thioanisole (10 mmol), H ₂ O ₂ (20 mmol), acetonitrile (20 mL) and 25 °C	163
Figure 3.13	Oxidation of thioanisole by VOSO ₄ , [VO(pimin) ₂], [VO(Im4COO) ₂] and [VO(Melm2COO) ₂]. Reaction conditions: Catalyst (0.2 mol% wrt. thioanisole), thioanisole (10 mmol), H ₂ O ₂ (20 mmol), acetonitrile (20 mL) and 25 °C.....	164
Figure 3.14	Oxidation of styrene by PS-[VO(pimin) _x], PS-[VO(Im4COO) _x] and PS-[VO(Melm2COO) ₂]. Reaction conditions: Catalyst (0.025 g), styrene (10 mmol), H ₂ O ₂ (20 mmol), acetonitrile (20 mL) and 80 °C.....	166
Figure 3.15	Product selectivity for the oxidation of styrene by PS-[VO(pimin) _x]. Reaction conditions: Catalyst (0.025 g), styrene (10 mmol), H ₂ O ₂ (40 mmol), acetonitrile (20 mL) and 80 °C	167

Figure 3.16	The effect of catalyst amount on the oxidation of styrene by PS-[VO(pimin) _x]. Reaction conditions: Styrene (10 mmol), H ₂ O ₂ (20 mmol), acetonitrile (20 mL) and 80 °C.....	167
Figure 3.17	The effect of peroxide amount on the oxidation of styrene by PS-[VO(Im4COO) _x]. Reaction conditions: Catalyst (0.025 g), styrene (10 mmol), acetonitrile (20 mL) and 80 °C.....	168
Figure 3.18	The effect of the amount of oxidant for the homogeneous oxidation of styrene by [VO(pimin) ₂]. Reaction conditions: Catalyst (0.2 mol%, equiv to 0.025 g of heterogeneous), styrene (10 mmol), acetonitrile (20 mL) and 80 °C.....	169
Figure 3.19	An AFM image (A) and digital image (B) of the surface of a PS-[VO(pimin) _x] bead after a catalytic reaction using styrene as the substrate, at 80 °C and with four-equivalents of H ₂ O ₂ , along with the AFM (C) and digital (D) image of the same beads before a catalytic reaction	169
Figure 3.20	Selectivity for the oxidation of ethylbenzene using PS-[VO(pimin) _x]. Reaction conditions: Catalyst (0.025 g), ethylbenzene (10 mmol), H ₂ O ₂ (40 mmol), acetonitrile (20 mL) and 80 °C.....	171
Figure 3.21	The effect of temperature and catalyst on the oxidation of ethylbenzene using PS-[VO(Melm2COO) _x] and PS-[VO(Im4COO) _x] at 60 and 80 °C. Reaction conditions: Catalyst (0.025 g and 0.035 g), ethylbenzene (10 mmol), H ₂ O ₂ (20 mmol), acetonitrile (20 mL)	172
Figure 3.22	Spectrophotometric titration of [VO(pimin) ₂] (1x10 ⁻⁴ mM, DMSO) with one-drop portions of H ₂ O ₂ (5x10 ⁻² mM) in water. The insert shows two of the d-d transitions which disappear upon addition of H ₂ O ₂	174
Figure 3.23	Spectrophotometric titration of [VO(Im4COO) ₂] (1x10 ⁻⁴ mM, H ₂ O) with one-drop portions of H ₂ O ₂ (5x10 ⁻² mM) in water. The insert shows two of the d-d transitions which disappear upon addition of H ₂ O ₂	175
Figure 3.24	The reaction scheme for (top) and the change in the absorbance spectrum of phenol red due to the formation of bromophenol blue (below). Reaction conditions: PS-[VO(Melm2COO) ₂] (0.010 g), 25 mL of pH 5.5 phosphate buffer (50 mM), H ₂ O ₂ (10 mM), KBr (1 M), phenol red (20 μM)	176
Figure 3.25	Plot of absorbance at 590 nm corresponding to the formation of bromophenol blue vs. time for heterogeneous catalysts. Reaction conditions: Catalyst (0.010 g), 25 mL of pH 5.5 phosphate buffer (50 mM), H ₂ O ₂ (10 mM), KBr (1 M), phenol red (20 μM)	177
Figure 3.26	Plot of absorbance at 590 nm corresponding to the formation of bromophenol blue vs. time for the homogeneous catalysts. Reaction conditions: [VO(Im4COO) ₂] (1.05 mg), [VO(Melm2COO) ₂] (1.15 mg) or [VO(pimin) ₂] (1.33 mg) (equivalent to 0.010 g of corresponding heterogeneous catalyst), 25 mL of pH 5.5 phosphate buffer (50 mM), H ₂ O ₂ (10 mM), KBr (1 M), phenol red (20 μM).....	177
Figure 4.1	Images of two attempts at producing polyvinylimidazole-co-ethyleneglycol dimethacrylate beads using toluene (A) and (B) cyclohexanol as the only solvent (porogen)	189
Figure 4.2	Poly(vinylimidazole-co-ethyleneglycol dimethacrylate) before (A) and after functionalization with vanadium (B).....	189
Figure 4.3	Images of poly[(vinylimidazole-2-carboxyaldehyde)-co-divinylbenzene] beads (A) before and (B) after reaction with hydrogen peroxide.....	191
Figure 4.4	Infrared spectra of poly[(vinylimidazole-2-carboxyaldehyde)-co-divinylbenzene] beads (A) before and (B) after reaction with hydrogen peroxide. Highlighted region confirms no shift of the ν(C=O).....	191
Figure 4.5	Overlaid infrared spectra of p(VIM-co-EGDMA) and p(VIM-co-EGDMA)-VO in the range 3000-650 cm ⁻¹	192
Figure 4.6	Wide scan XPS spectra of p(VIM-co-EGDMA) and p(VIM-co-EGDMA)-VO. The insert shows the expanded V 2p _{3/2} and V 2p _{1/2} signals.....	194
Figure 4.7	TG and DTG curves of p(VIM-co-EGDMA) (left) and p(VIM-co-EGDMA)-VO (right) at a heating rate of 10 °C.min ⁻¹ under N ₂	194
Figure 4.8	SEM images of (A) p(VIM-co-EGDMA) and (B) the oxovanadium(IV) functionalized derivative p(VIM-co-EGDMA)-VO. The insert shows an expanded view of a single bead.....	195
Figure 4.9	Selected 2D and 3D (1x1 μm sections) of (A) p(VIM-co-EGDMA) and (B) p(VIM-co-EGDMA)-VO	196
Figure 4.10	Nitrogen adsorption-desorption isotherms for (A) p(VIM-co-EGDMA) and (B) p(VIM-co-EGDMA)-VO....	197
Figure 4.11	The effect of catalyst amount on thioanisole oxidation. Reaction conditions: H ₂ O ₂ (20 mmol), thioanisole (10 mmol), acetonitrile (20 mL) and 25 °C	198

Figure 4.12	The effect of temperature on thioanisole oxidation. Conditions: p(VIM-co-EGDMA)-VO (0.20 g), H ₂ O ₂ (20 mmol), thioanisole (10 mmol), acetonitrile (20 mL).....	199
Figure 4.13	The effect of temperature on product selectivity. Conditions: p(VIM-co-EGDMA)-VO (0.20 g), H ₂ O ₂ (20 mmol), thioanisole (10 mmol), acetonitrile (20 mL).....	199
Figure 4.14	Recyclability of p(VIM-co-EGDMA)-VO beads at optimal conditions, and the effect of using methanol instead of acetonitrile as the solvent. Conditions: p(VIM-co-EGDMA)-VO (0.20 g), H ₂ O ₂ (20 mmol), thioanisole (10 mmol), acetonitrile/methanol (20 mL) and 25 °C.....	200
Figure 4.15	AFM images of (A) p(VIM-co-EGDMA)-VO and (B) p(VIM-co-EGDMA)-VO after one catalytic cycle.....	200
Figure 4.16	Overlaid infrared spectra of (A) p(VIM-co-EGDMA)-VO and (B) p(VIM-co-EGDMA)-VO recovered mid-reaction.....	202
Figure 5.1	Characteristics of nanofibers and nanofibrous membranes	209
Figure 5.2	Different electrospinning configurations. Shown in (A) is the simple vertical electrospinning using a stationary grounded collector, while (B) shows the same setup except using a rotating drum collector with an oppositely charged electrode underneath to direct fiber collection	216
Figure 5.3	Continuous flow set-up, when using either PS-[VO(dpimR) ₂] or p(ST-co-VIM)-VO fibers.....	221
Figure 5.4	Continuous flow set-up when using p(ST-co-VPIM)-VO fibers.....	222
Figure 5.5	Continuous flow set-up, when using PBI _r -VO fibers. The insert shows an exploded view of the catalyst bed	223
Figure 5.6	¹ H NMR spectrum of dpimH in DMSO (δ ppm). (Peaks at ~3.5 and 2.5 are due to the solvent).....	224
Figure 5.7	¹³ C NMR spectrum of dpimH in DMSO (δ ppm). The solvent peak appears upfield from the range shown here at ~40 ppm.....	225
Figure 5.8	IR spectra of the ligand dpimBr and oxovanadium(IV) complex, [VO(dpimBr) ₂]. The ν(C=N), ν(C-O) and ν(V=O) have been highlighted.....	226
Figure 5.9	UV/Vis spectra of the [VO(dpimR) ₂] complexes in DMSO.....	227
Figure 5.10	IR spectra showing the changes at various stages of synthesis of vpim	228
Figure 5.11	SEM images and digital pictures of the electrospun fibers, from left to right; (A) PS-25, (B) PS-15-[VO(dpimMeO) ₂] and (C) PS-15-[VO(dpimNO ₂) ₂]	229
Figure 5.12	Infrared spectra of unmodified polystyrene (PS-25) fibers, the neat complex [VO(dpimMeO) ₂], and the corresponding fibers, PS-15-[VO(dpimMeO) ₂]. The highlighted areas show peaks found in both [VO(dpimMeO) ₂] and PS-15-[VO(dpimMeO) ₂] fibers.....	230
Figure 5.13	Wide scan XPS spectrum of PS-15-[VO(dpimMeO) ₂]. Insert shows an expanded view of the high resolution (A) V 2p signal and (B) the N 1s signals.....	231
Figure 5.14	TG (A) and DTG (B) curve of PS-15-[VO(dpimNO ₂) ₂]	232
Figure 5.15	SEM images of p(ST-co-VIM) and p(ST-co-VIM)-VO with digital image showing colour changes	234
Figure 5.16	Nitrogen adsorption/desorption isotherms, for (A) p(ST-co-VIM) and (B) p(ST-co-VIM)-VO fibers	235
Figure 5.17	IR spectrum of p(ST-co-VIM) and p(ST-co-VIM)-VO	236
Figure 5.18	Wide scan XPS spectra of p(ST-co-VIM) and p(ST-co-VIM)-VO. Insert shows an expanded view of the V 2p signals of p(ST-co-VIM)-VO	237
Figure 5.19	TG curves for (A) p(ST-co-VIM) and (C) p(ST-co-VIM)-VO and DTG curves for (B) p(ST-co-VIM) and (D) p(ST-co-VIM)-VO; at a heating rate of 10 °C.min ⁻¹ under N ₂ . Insert shows an expanded view of the region between 30 - 200 °C	238
Figure 5.20	SEM images of fibers produced by electrospinning p(ST-co-VPIM) at concentrations (wt/v%) of (A) 20% (Ø = 3.8 µm), (B) 15% (Ø = 2.3 µm), (C) 10% (Ø = 1.0 µm) and (D) 8% (Ø = 0.6 µm) at the same magnification. Ø Indicates average diameter.....	239

Figure 5.21	IR spectra of (A) vpim (B) polystyrene (C) p(ST-co-VPIM) (D) p(ST-co-VPIM)-VO. Highlighted regions illustrate bands common to (A), (C) and (D).	240
Figure 5.22	Digital images of p(ST-co-VPIM) (left) and p(ST-co-VPIM)-VO fibers (right) showing the significant colour change upon functionalization	241
Figure 5.23	Wide scan XPS spectra of p(ST-co-VPIM) and p(ST-co-VPIM)-VO. Insert shows an expanded view of the V 2p signals of p(ST-co-VPIM)-VO	242
Figure 5.24	TG curves for p(ST-co-VPIM) and p(ST-co-VPIM)-VO at a heating rate of 10 °C.min ⁻¹ under N ₂	243
Figure 5.25	Chemical structure of polybenzimidazole	244
Figure 5.26	SEM images and photographs (insert) of (A) PBI _f and (B) PBI _f -VO fibers	246
Figure 5.27	IR spectrum of PBI _f , VOSO ₄ and PBI _f -VO fibers	247
Figure 5.28	Wide scan XPS spectra of PBI _f and PBI _f -VO fibers. Insert shows an expanded view of the V 2p signals of PBI _f -VO	248
Figure 5.29	High resolution XPS spectra of (A) N1s signal for PBI _f and (B) N1s signal for PBI _f -VO	248
Figure 5.30	TG curves for PBI _f and PBI _f -VO at a heating rate of 10 °C.min ⁻¹ under N ₂	249
Figure 5.31	Ligand substituent effects on catalytic activity. Conditions: Catalyst (0.25 mol% wrt thioanisole), thioanisole (10 mmol), H ₂ O ₂ (20 mmol), CH ₃ CN (20 mL), and at 25 °C	250
Figure 5.32	Oxidation of thioanisole under batch conditions using PS-15-[VO(dpimMeO) ₂] and PS-15-[VO(dpimNO ₂) ₂]. Conditions: Catalyst (0.01 g), thioanisole (1 mmol), H ₂ O ₂ (2 mmol), CH ₃ CN (20 mL), and at 25 °C	251
Figure 5.33	Oxidation of thioanisole under continuous flow conditions. Conditions: thioanisole (50 mM), H ₂ O ₂ (100 mM), PS-15-[VO(dpimNO ₂) ₂] (0.01 g) and PS-15-[VO(dpimMeO) ₂] (0.01 g) of catalyst in 1:1 CH ₃ CN/H ₂ O; flow rate (1 mL.h ⁻¹) and at 25 °C	252
Figure 5.34	SEM image of electrospun polystyrene fibers after being placed in acetonitrile	254
Figure 5.35	The effect of the amount of catalyst on overall conversion. Conditions: p(ST-co-VIM)-VO, H ₂ O ₂ (2 mmol), thioanisole (1 mmol), methanol (10 mL), flow rate (1 mL.h ⁻¹) and at 25 °C	255
Figure 5.36	The effect of flow rate on overall conversion. Conditions: 0.025 g of p(ST-co-VIM)-VO, H ₂ O ₂ (2 mmol), thioanisole (1 mmol), methanol (10 mL) and at 25 °C	256
Figure 5.37	Vanadium leaching behaviour of p(ST-co-VIM)-VO. Conditions: p(ST-co-VIM)-VO (0.025g), thioanisole (1 mmol), H ₂ O ₂ (2 mmol), methanol (10 mL), flow rate (2 mL.h ⁻¹) (n = 3)	257
Figure 5.38	The modified column used in the continuous flow reactions, containing the p(ST-co-VPIM)-VO fibers (0.1 g)	258
Figure 5.39	Continuous flow oxidation of thioanisole using p(ST-co-VPIM)-VO. Conditions: p(ST-co-VPIM)-VO (0.1 g), thioanisole (1 mmol), H ₂ O ₂ (2 mmol), methanol (10 mL), flow rate (1 mL.h ⁻¹) and at 25 °C	259
Figure 5.40	Continuous flow oxidation of thioanisole using p(ST-co-VPIM)-VO. Conditions: p(ST-co-VPIM)-VO (0.06 g), thioanisole (1 mmol), H ₂ O ₂ (2 mmol), methanol (10 mL), flow rate (1 mL.h ⁻¹) and at 25 °C	259
Figure 5.41	Effect of catalyst amount for the batch oxidation of thioanisole using PBI _f -VO. Conditions: PBI _f -VO, thioanisole (1 mmol), H ₂ O ₂ (2 mmol), acetonitrile (20 mL), and at 25 °C	261
Figure 5.42	Recyclability for the batch oxidation of thioanisole using PBI _f -VO. Conditions: PBI _f -VO (0.05 g), thioanisole (1 mmol), H ₂ O ₂ (2 mmol), acetonitrile (20 mL), and at 25 °C	261
Figure 5.43	Continuous flow oxidation of thioanisole using PBI _f -VO. Conditions: PBI _f -VO (0.05 g), thioanisole (50 mM), H ₂ O ₂ (100 mM) in acetonitrile, flow rate (1 mL.h ⁻¹) and 25 °C	262

List of Schemes

Part 1

The antidiabetic properties of oxovanadium(IV) complexes

Scheme 1.1	The blood coagulation cascade.....	9
Scheme 3.1	Preparation of $[\text{VO}(\text{pimin})_2]$ and $[\text{VO}_2(\text{pimin})(\text{piminH}^*)]$. The other oxovanadium(IV) complexes were prepared in a similar fashion	50
Scheme 3.2	Deprotonation steps for the 2-(2'-hydroxyphenyl)-1 <i>R</i> -imidazoline ligands. H^+ have been omitted from the equilibria	59
Scheme 3.3	The stepwise formation of oxovanadium(IV) complexes. LH and L^- are omitted in the complexation equilibria as are the hydrolysis equilibria	60
Scheme 4.1	Synthesis of 1-methylimidazole-2-carboxylic acid from the starting material 1-methylimidazole.....	77
Scheme 4.2	Preparation of oxovanadium(IV) imidazole-carboxylic acid complexes	80
Scheme 4.3	Deprotonation steps of the Im_2COOH and Melm_2COOH (A) as well as Im_4COOH (B) systems. H^+ have been omitted from the equilibria	84
Scheme 4.4	The stepwise formation of oxovanadium(IV) complexes with Im_4COOH and Melm_2COOH ($\text{R} = \text{Me}$) or Im_2COOH ($\text{R} = \text{H}$). LH and L^- are omitted in the complexation equilibria as are the hydrolysis equilibria..	86

Part 2

Catalytic properties of heterogeneous oxovanadium(IV) complexes

Scheme 1.1	Simplified catalytic mechanism for the vanadium-peroxide oxidation of alkenes, alkanes and sulfides. Here L may refer to an adjacent donor atom or a solvent molecule.....	108
Scheme 1.2	Radical initiation (a), propagation (b-c) and termination (d).....	110
Scheme 1.3	Introduction of a polymerizable group by alkylation reaction	123
Scheme 1.4	Synthesis of polymerizable diethylenetriamine	124
Scheme 1.5	Synthesis of monosubstituted <i>N</i> -allylethylenediamine	125
Scheme 1.6	Preparation of allyl functionalized monomer by alkylation and Claisen rearrangement	125
Scheme 1.7	Chain transfer in solvent radical polymerization.....	126
Scheme 1.8	Degradative chain transfer in the polymerization of allyl alcohol	126
Scheme 1.9	A schematic showing some of the different approaches used for obtaining ligand-functionalized polymer-supports	129
Scheme 3.1	A simplified reaction scheme for the immobilization of homogeneous catalysts onto Merrifield resin.....	143
Scheme 3.2	Functionalization of Merrifield-type resins.....	144

Scheme 3.3	Immobilization of oxovanadium(IV) onto imidazoline and imidazole functionalized PS-Cl. Only PS-[VO(Im ₄ COO) _x] has been shown as a representative example. R represents a solvent molecule or a nearby ligand	151
Scheme 3.4	Oxidation of methyl phenyl sulfide (thioanisole) gives primarily methyl phenyl sulfoxide and methyl phenyl sulfone ([O] represents an oxidizing agent)	158
Scheme 3.5	The main products of the oxidation of styrene include styrene oxide, benzaldehyde, benzoic acid and phenylethane-1,2-diol ([O] represents an oxidizing agent)	166
Scheme 3.6	The main products of the oxidation of ethylbenzene include acetophenone, benzaldehyde and benzoic acid ([O] represents some oxidizing agent)	170
Scheme 4.1	Synthesis scheme for the preparation of p(VIM-co-EGDMA) microspheres. R represents a solvent molecule or a nearby ligand	190
Scheme 4.2	The proposed catalytic mechanism for the oxidation of thioanisole by vanadium including photographs of beads before and during a reaction	201
Scheme 5.1	Preparation of the <i>bis</i> -coordinated oxovanadium(IV) complexes with 4-R-2-(4,5-diphenyl-1 <i>H</i> -imidazol-2-yl)phenol ligands (R = NO ₂ , Br, H, MeO)	225
Scheme 5.2	Synthetic route for the preparation of the polymerizable ligand, vpim	228
Scheme 5.3	Synthesis of p(ST-co-VIM) copolymer	233
Scheme 5.4	Synthesis of p(ST-co-VPIM) copolymer	238

List of Tables

Part 1

The antidiabetic properties of oxovanadium(IV) complexes

Table 1.1	Chronic and acute complications of diabetes.....	8
Table 3.1	Selected bond lengths (Å) and angles (°) for [VO(pimin) ₂] and [VO ₂ (pimin)(piminH')].....	55
Table 3.2	Selected crystallographic data for [VO(pimin) ₂] and [VO ₂ (pimin)(piminH')].....	56
Table 3.3	Protonation (log <i>K</i>) and complex formation constants (log β) for VO(IV)-ligand systems at 25±0.1 °C and <i>I</i> = 0.10 M (TMACl).....	59
Table 3.4	The effects of metformin (Met), VOSO ₄ , [VO(pimin) ₂], [VO(Etpimin) ₂] and [VO(EtOHpimin) ₂] on 3T3-L1, Chang and C2C12 cells at 0.5, 1.0 and 10 μM concentrations. Basal glucose uptake is represented as 100%.....	63
Table 4.1	Calculated net charges on the nitrogen atoms of imidazole and pyridine.....	72
Table 4.2	Protonation (log <i>K</i>) and complex formation constants (log β) for VO(IV)-ligand systems at 25±0.1 °C and <i>I</i> = 0.10 M (TMACl).....	84
Table 4.3	Proton (log <i>K</i>) and VO ²⁺ stability constants (logβ) for the complexes of citric acid (B) at 25.0±0.1 °C and <i>I</i> = 0.2 M (KCl).....	89
Table 4.4	Stability constants of mixed ligand VO ²⁺ complexes of Im ₂ COOH, Im ₄ COOH and Melm ₂ COOH with citric acid at 25±0.1 °C. P,q,r represents ligand A, ligand B and protons/hydroxides, respectively.....	91
Table 4.5	The effects of metformin (Met), VOSO ₄ , [VO(Im ₄ COO) ₂], [VO(Im ₂ COO) ₂] and [VO(Melm ₂ COO) ₂] on 3T3-L1, Chang and C2C12 cells at 0.5, 1.0 and 10 μM concentrations. Basal glucose uptake is represented as 100%.....	92

Part 2

Catalytic properties of heterogeneous oxovanadium(IV) complexes

Table 1.1	Comparison of homogeneous and heterogeneous catalysts.....	103
Table 1.2	Overview of a few reactions catalyzed by supported vanadium catalysts.....	105
Table 1.3	Some common thermal free radical initiators for polymerization of vinyl monomers.....	110
Table 1.4	Structures and names of some common crosslinking agents.....	112
Table 1.5	Advantages and disadvantages of various fiber processing techniques.....	117
Table 1.6	Names and structures of some common polymerizable groups used to make polymerizable ligands.....	123
Table 1.7	Examples of reaction used for the introduction of the vinyl group.....	128
Table 2.1	ICP-OES method and operating parameters.....	139
Table 2.2	GC temperature programs used identification of the oxidation products of styrene, ethylbenzene and thioanisole.....	140

Table 3.1	Elemental binding energies as determined by XPS	154
Table 3.2	Percentage conversion, turnover frequency (TOF) and product selectivity for the oxidation of thioanisole	165
Table 3.3	Percentage conversion, turnover frequency (TOF) and product selectivity (for the two major products) for the oxidation of styrene (Benzal = benzaldehyde, Phen-1,2-diol = phenylethane-1,2-diol).....	170
Table 3.4	Percentage conversion, turnover frequency (TOF) and product selectivity (for the two major products) for the oxidation of ethylbenzene (Benzal = benzaldehyde, Acetophen = acetophenone).....	173
Table 4.1	Elemental binding energies as determined by XPS	193
Table 4.2	Percentage conversion, turnover frequency (TOF) and product selectivity for the oxidation of thioanisole with hydrogen peroxide (20 mmol) using p(VIM-co-EGDMA)-VO as a catalyst.....	201
Table 5.1	Elemental binding energies as determined by XPS for PS-15-[VO(dpimMeO) ₂] and PS-15-[VO(dpimNO ₂) ₂]	230
Table 5.2	Elemental binding energies as determined by XPS p(ST-co-VIM) and p(ST-co-VIM)-VO	236
Table 5.3	Elemental binding energies as determined by XPS for p(ST-co-VPIM) and p(ST-co-VPIM)-VO	241
Table 5.4	Tensile strength of PBI fibers after immersion in inorganic acids and bases	244
Table 5.5	Tensile strength of PBI fibers after immersion in organic chemicals	244
Table 5.6	Elemental binding energies as determined by XPS for PBI _r and PBI _r -VO.....	247
Table 5.7	Selected overall conversion and product selectivity data for the oxidation of thioanisole using homogeneous oxovanadium(IV) complexes (0.25 mol% wrt thioanisole) with 4- <i>R</i> -2-(4,5-diphenyl-1 <i>H</i> -imidazol-2-yl)phenol ligands as well as the heterogeneous catalytic fibers PS-15-[VO(dpimNO ₂) ₂] and PS-15-[VO(dpimMeO) ₂] (0.1 g of fibers).....	253
Table 5.8	Summary of reaction conversions and selectivities for p(ST-co-VIM)-VO catalyzed reactions under continuous flow set-up.....	257
Table 5.9	Summary of reaction conversions and selectivities for p(ST-co-VPIM)-VO catalyzed reactions under continuous flow conditions	260
Table 5.10	Summary of reaction conversions and selectivities for PBI _r -VO catalyzed reactions under batch and continuous flow conditions	264

Part 1

The antidiabetic properties of oxovanadium(IV) complexes

Chapter 1

Introduction

1.1 Diabetes mellitus – an overview

Diabetes mellitus is a group of metabolic disorders characterized by elevated plasma glucose levels. According to the World Health Organization (WHO), more than 180 million people worldwide are currently living with this disorder, with these numbers looking set to double by the year 2030.¹ In 2005, an estimated 1.1 million people died from diabetes with a projected rise in deaths of 50% over the next 10 years. It is estimated that at least 1 in 20 deaths, globally and across all ages, are attributable to diabetes.² About 80% of all diabetes deaths occur in the low and middle income segments, with the greatest increases expected in Africa and Asia.^{3,4} The increase in incidence of diabetes in developing countries follows the trend of urbanisation and lifestyle changes, perhaps most importantly a “Western-style” diet. The widespread prevalence and distribution of this disease is well illustrated in **figure 1.1**.²

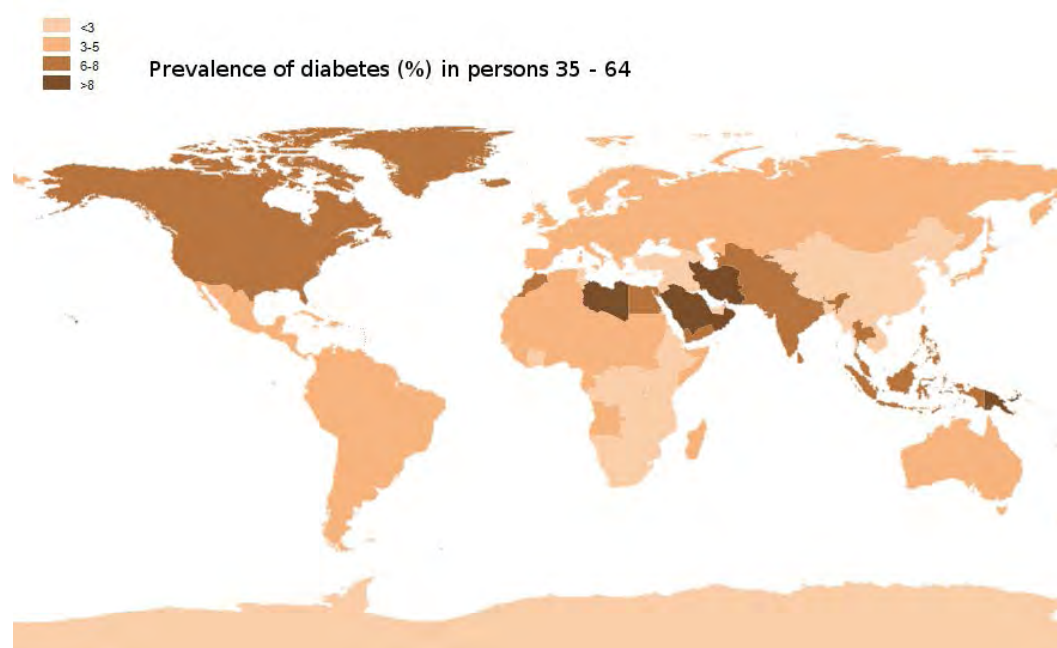


Figure 1.1 Population distribution map of people suffering from diabetes created using MapWindow GIS v4.8

1.2 Forms of diabetes

Diabetes occurs in two main forms; type I (insulin deficiency) and type II (insulin resistance). Type I requires insulin injections, whereas type II diabetes can often be controlled using oral drugs alone.

(a) Type 1 diabetes

Type 1 diabetes was previously termed insulin-dependent diabetes mellitus (IDDM) or juvenile-onset diabetes. It develops when the body's immune system destroys pancreatic β -cells, the only cells in the body that produce the hormone insulin to regulate blood glucose. This form of diabetes usually strikes children and young adults, although disease onset can occur at any age. In adults, type 1 diabetes accounts for 5% to 10% of all diagnosed cases of diabetes. Risk factors for type 1 diabetes may be autoimmune, genetic, or environmental.⁵

The principal treatment of type 1 diabetes mellitus, even in its earliest stages, is the delivery of artificial insulin *via* injection combined with careful monitoring of blood glucose levels using blood testing monitors. Without insulin, diabetic ketoacidosis often develops which may result in coma or death. Treatment emphasis is now also placed on lifestyle adjustments such as diet and exercise which can impede the progress of the disease, but not reverse it. Apart from the common subcutaneous injections, it is also possible to deliver the insulin by a pump, which allows continuous infusion of insulin 24 hours a day at preset levels and the ability to program doses of insulin as needed at meal times. An inhaled form of insulin was approved by the FDA in January 2006, although it was discontinued for business reasons in October 2007.⁶ Non-insulin treatments, such as monoclonal antibodies and stem-cell based therapies, are effective in animal models but have not yet completed clinical trials in humans.⁶

(b) Type 2 diabetes

This type of diabetes was formerly called non-insulin-dependent diabetes mellitus (NIDDM) or adult-onset diabetes mellitus.⁶ It results from the body's ineffective use of insulin. Type 2 diabetes mellitus is mainly due to insulin resistance or reduced insulin sensitivity, combined with relatively reduced insulin secretion which in some cases becomes obsolete.⁶ The defective responsiveness of the body tissues to insulin almost certainly involves the insulin receptor in the cell membranes.

However, the specific defects are not known but the low receptor density is due to destruction by ketonic bodies.⁶ In the early stages of type 2 diabetes, the predominant abnormality is reduced insulin sensitivity, characterized by elevated levels of insulin in the blood. At this stage hyperglycaemia can be reversed by a variety of measures and medication that improve insulin sensitivity or reduce glucose production by the liver.⁶ As the disease progresses, the impairment of insulin secretion worsens and therapeutic replacement of insulin often becomes necessary. Type 2 diabetes mellitus comprises 90% of people with diabetes around the world, and is largely as a result of excess body weight and physical inactivity.⁶

1.3 Current therapy

In 1921 Banting and Best isolated insulin and demonstrated its ability to lower blood glucose levels.⁶ However, with obesity frequently being the resulting cause of diabetes, the first approach in treatment should include a healthy diet and exercise plan that will lead to weight reduction.⁷ A diet alone is often not always sufficient for glycaemic control until it is coupled with antidiabetic drugs and occasionally painful insulin injections.⁸

(a) Insulin

Proinsulin is produced in the β -cells of the islets of Langerhans and then converted to insulin in the same cells. Proinsulin consists of a single chain containing intramolecular disulfide bridges. The center portion, or C-chain, is removed enzymatically resulting in two strands joined by intermolecular disulfide bonds, giving active insulin.⁶ Insulin is utterly necessary for controlling type I diabetes and it is usually derived from pork or bovine sources. Insulin is often administered as a complex with protamine and zinc. This slows down its action, providing longer glucose control.⁶

(b) Sulfonylureas

The discovery of sulfonylureas was by chance. It was observed that certain sulphonamides (antibacterials) often resulted in hypoglycaemia and hence non-antibacterial sulfonylureas which also reduced blood glucose levels were developed.⁶ These drugs function by stimulating the

release of endogenous reserves of insulin from the pancreas and therefore are only effective in patients who are still able to synthesise and secrete insulin. Unfortunately, sulfonylureas do not always succeed in controlling diabetes. Common side effects include; hypoglycaemia, increased appetite and weight gain, as well as an increased cardiovascular risk.⁹ Glybenclamide and tolbutamide (**figure 1.2**) are two examples of commonly used sulfonylureas.

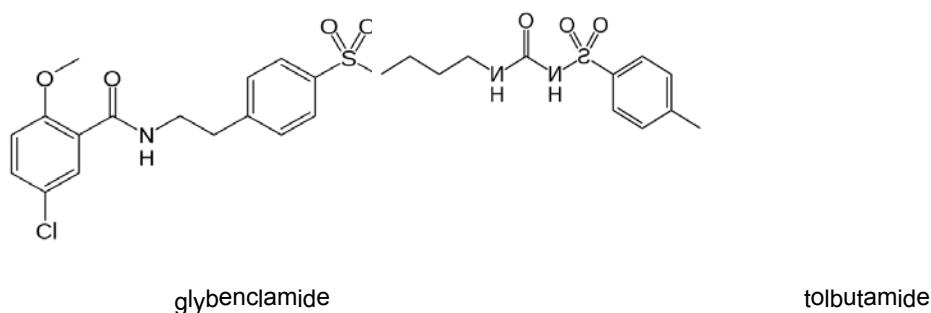


Figure 1.2 Chemical structures of commonly prescribed sulfonylureas, glybenclamide and tolbutamide

(c) Biguanides

Similarly to sulfonylureas, the discovery of the biguanides was also serendipitous. It was found that a guanidine derivative lowered blood glucose levels in rabbits. This led to the development of phenformin (**figure 1.3**). Unlike sulfonylureas, biguanides lower blood glucose levels without stimulating the release of insulin from the pancreas. There are three proposed modes of action:

1. Inhibition of intestinal transport and absorption of sugars
2. Inhibition of gluconeogenesis at the liver
3. Affect metabolism in peripheral tissues by enhancing the uptake of glucose

Metformin and phenformin (**figure 1.3**) were introduced for the treatment of diabetes in the 1950s.⁶ Phenformin, however, was withdrawn from clinical use shortly after introduction, leaving metformin as the only 'surviving' example in this class.

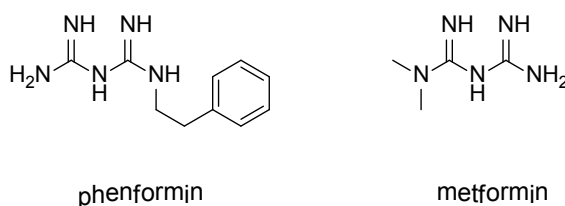


Figure 1.3 Chemical structures of the biguanides, phenformin and metformin

Metformin showed the added benefit of reducing weight gain, and even caused weight loss in certain patients. While the side-effect profile of metformin is mostly favourable, there are certain negatives. Gastrointestinal side effects such as a metallic taste, nausea, abdominal pain and diarrhoea occur in varying severity in up to 30% of patients.⁹

(d) Thiazolidinediones

Thiazolidinediones (TZDs), also known as glitazones, bind to a nuclear receptor known as peroxisome-proliferator-activated receptor gamma. This has several downstream effects including promoting insulin-stimulated glucose uptake by skeletal muscle cells. Thus, these compounds decrease insulin resistance. Furthermore, TZDs also slightly reduce blood pressure, enhance fibrinolysis and improve endothelial function.¹⁰⁻¹² Some adverse effects of TZDs include; weight gain, edema, and an emia.¹³ This class of drugs is currently represented by rosiglitazone and pioglitazone (**figure 1.4**).

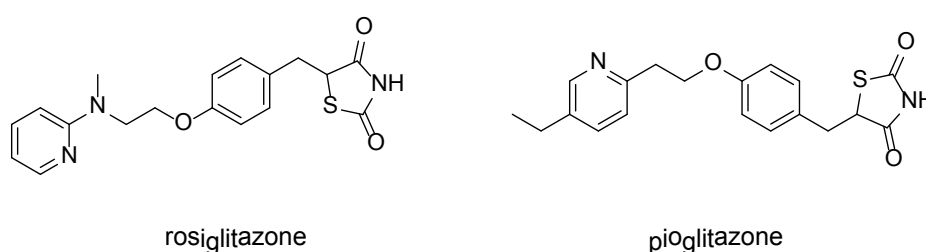


Figure 1.4 Chemical structures of two thiazolidinediones, rosiglitazone and pioglitazone

(e) Meglitinides

The meglitinides, repaglinide and nateglinide (**figure 1.5**), are secretagogues that stimulate rapid insulin production by the pancreas. They achieve this by closing adenosine triphosphate (ATP)-

dependent potassium channels in the membrane of the β -cells. This depolarizes the β -cells, opening the cells' calcium channels, and the resulting calcium influx induces insulin secretion. The glinides have a faster onset and shorter duration of action than the sulphonylureas and as such mimic a more physiological pattern of insulin release. They are associated with a reduced risk of hypoglycaemia, cause less weight gain, and are metabolized and excreted by the liver, and so can be used in patients with impaired renal function.⁹ The most common adverse effects include hypoglycaemia, weight gain and peripheral edema.¹⁴

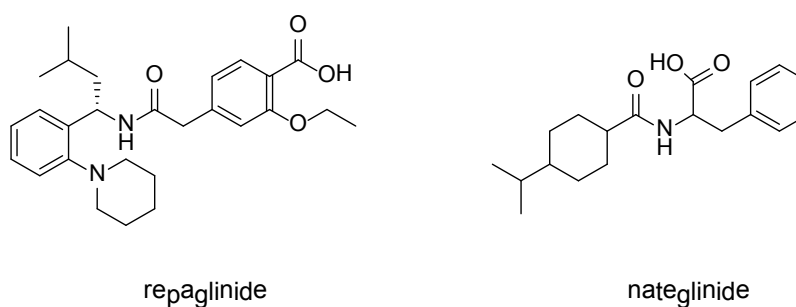


Figure 1.5 Chemical structures of two meglitinides, repaglinide and nateglinide

1.4 Diabetes associated conditions

Together with inadequate blood sugar control, there are several other complications associated with diabetes, some of which have been listed in **table 1.1**.¹⁵ Approximately 80% of diabetic patients pass away due to a thrombotic complication, with 75% of these deaths due to cardiovascular complications and the remainder due to cerebrovascular events and peripheral vascular complications.¹⁶ In diabetic patients, the vascular endothelium, the body's primary defence against thrombosis, is abnormal which together with elevated levels of coagulation activation markers eg. prothrombin activation fragment 1 and 2, thrombin-antithrombin complexes, as well as increased levels of several clotting factors (eg. fibrinogen) puts diabetic patients in a hypercoagulable state. In addition to these factors, anticoagulant protein C levels are decreased and the fibronolytic system (responsible for removing clots) is less effective due to the abnormal clot structures in diabetic patients.^{16,17}

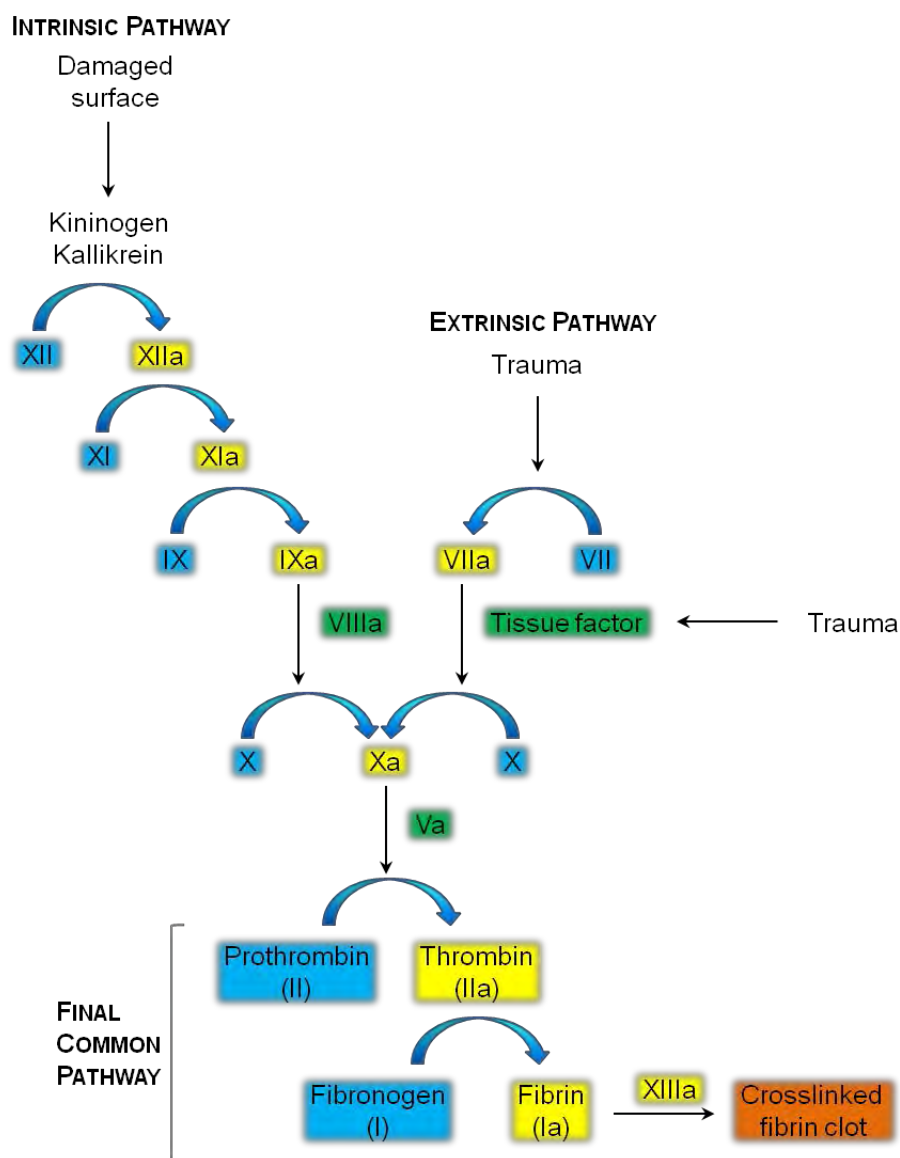
Table 1.1 Chronic and acute complications of diabetes¹⁵

<i>Macrovascular</i>
Retinopathy
- Impaired vision, blindness
Nephropathy
- Proteinuria, chronic kidney disease, dialysis
Neuropathy
- Peripheral: sensory (pain, numbness, paresthesias) and motor neuropathy
- Autonomic: gastroparesis, postural hypotension, impotence
<i>Macrovascular</i>
Coronary artery disease
- Myocardial infarction
Peripheral vascular disease
- Claudication, ulcers, amputation
Cerebrovascular disease
- Stroke
<i>Perioral</i>
Gingivitis
Periodontitis
Xerostomia
Candidiasis
Oral lichen planus
Leucoplakia (pre malignancy)
Oral cancer
<i>Acute complications of diabetes</i>
Hyperosmolar hyperglycemia
Diabetic ketoacidosis
Acute infections

1.4.1 A brief introduction to the coagulation pathways

The formation of clots is an extremely important hemostatic process. Once an injury to the blood vessels has been incurred, platelets aggregate to form a 'plug' (primary hemostasis) which is subsequently strengthened by fibrin strands (secondary hemostasis). The coagulation cascade for

the latter can be divided into two principal pathways namely the intrinsic and the extrinsic pathways which join to form a final common pathway (**scheme 1.1**).^{18,19}



Scheme 1.1 The blood coagulation cascade

(a) The intrinsic pathway

This pathway begins with Factor XII cleaving and activating its substrates, prekallikrein and Factor XI (**scheme 1.1**). These proteins are anchored to the sub-endothelium by high molecular weight kininogen. Prekallikrein is converted to kallikrein which serves to activate Factor XII to Factor XIIa.

After a series of activation steps, Factor IX is activated and forms a complex with activated Factor VIII and calcium which binds to the phospholipid rich surface of platelets where activation of Factor X occurs. This event marks the end of the intrinsic pathway and the start of the common pathway of the coagulation cascade.^{18,20}

(b) The extrinsic pathway

The description of the extrinsic pathway was first reported by Marowitz in 1905.¹⁵ Damage to the endothelium exposes the sub-endothelium, which expresses tissue factor on its cells surface.¹⁵ Once tissue factor is exposed to the blood, circulating Factor VII binds to it to form a TF-Factor VII complex which promotes the auto-activation of Factor VII to Factor VIIa (**scheme 1.1**). In the presence of calcium and membrane phospholipids, the TF-Factor VIIa complex proceeds to activate Factor X which marks the initiation of the first step of the common pathway.¹⁸

(c) Common pathway

The activation of Factor X marks the point where the intrinsic and extrinsic pathways converge. Factor X is activated on the phospholipid rich surface of activated platelets. Activated Factor Xa forms a complex with its activated cofactor, Factor Va, in the presence of calcium which converts prothrombin to thrombin. Thrombin is the master regulator of the coagulation cascade. Thrombin cleaves activation peptides from fibrinogen to form soluble fibrin monomers which subsequently polymerize to form an insoluble loose fibrin clot at the site of injury. Thrombin also activates circulating Factor XIII which catalyzes the formation of covalent intermolecular crosslinks between fibrin molecules combining the necessary structure for a stable fibrin clot. Thrombin also serves to activate surrounding platelets that in conjunction with the clot seal the breach in the vessel wall. Finally, thrombin activates Factor V and Factor VIII in a positive feedback loop to further amplify the activation of the coagulation cascade.^{18,20}

Other than treating the elevated blood sugar levels associated with diabetic patients, it is important to consider adding an anticoagulatory therapy. Aspirin, for example, has been shown to be a highly beneficial treatment and is prescribed for those who are at high risk for cardiovascular complications.²¹ It would be beneficial to create antidiabetic drugs which simultaneously improve glucose metabolism as well as reducing the hypercoagulable state of diabetic patients.

1.5 Medicinal inorganic chemistry

Inorganic compounds have been used in medicine for centuries, but with little understanding of their mechanism of action.²² Regarding design, it is now known that certain events including; hydrolysis, protein binding, membrane transport and molecular targeting should be considered.²² The discovery of cisplatin and its role as a chemotherapeutic agent in the late 1960's stimulated interests in medicinal inorganic chemistry and the development of new metal complexes to treat diseases such as cancer^{23,24} and diabetes,^{4,25} to name a few. The unique chemical and physical properties of metals also make them ideal for applications in the fields of *in vivo* imaging^{26,27} and radiopharmaceuticals.^{28,29}

The investigation of the biochemistry of vanadium has only recently begun to catch up to that of its transition metal neighbours in the first row. The interest in vanadium chemistry was initiated by the discovery of vanadate as a potent inhibitor of Na⁺, K⁺ and ATPase.³⁰

1.5.1 Metals in the treatment of diabetes

In 1979 Tolman *et al.*,³¹ and a bit later in 1981 Degani *et al.*,³² showed that vanadium was capable of affecting glucose metabolism on a cellular level. However, it was not until John McNeill's work in 1985, which focused on the effects of vanadate on elevated blood glucose levels of streptozotocin (STZ)-induced diabetic rats,³³ that the academic world began to take serious notice.³⁴ STZ-induced diabetes is considered to be a model for type 1 diabetes. It is however, essential to note that not all the insulin producing pancreatic β -cells are destroyed, and thus some insulin is still produced. This is especially important considering that vanadium compounds do not substitute for a complete lack of insulin, as is the case in type 1 diabetes, but may alleviate dependence on exogenous insulin or possibly substitute for other oral drugs currently used in the treatment of type 2 diabetes.³⁵

Although the simple inorganic salts of vanadium used in these early studies showed great potential, the undesirable toxicity and poor intestinal absorption of vanadate and vanadyl shifted focus towards designing new organovanadium compounds.^{36,37} Smart ligand design may help to mitigate the latter problem in particular.³⁵ On this note, it is interesting to find that despite the huge

toxicity and carcinogenic concerns, chromium(III) supplements have found their way into the pharmacy.³⁸ Initially, the activity of these compounds was thought to be via binding of Cr^{3+} (the 'safer' species) to chromodulin, which enhances interactions of insulin with its cellular receptors. It has been shown to be quite likely however, that Cr^{3+} undergoes intra or extracellular oxidations to form the genotoxic and carcinogenic Cr^{6+} and Cr^{5+} , which are possibly the real insulin-enhancing species.³⁹ Besides chromium and vanadium, the antidiabetic activities of molybdenum and tungsten have also been investigated.⁴⁰ All of these metals (V, Cr, Mo, W) operate on the same basic principle which involves the formation of an oxo anion (for example VO_4^{3-}) which subsequently acts as a protein tyrosine phosphatase (PTP) inhibitor.⁴⁰ Other than these metals, zinc, magnesium, arsenic and cobalt have also been proposed as possible adjuncts in the treatment of diabetes.⁴¹

Vanadium has been implicated in performing many of the functions related to insulin such as inhibition of lipolysis and gluconeogenesis, as well stimulating lipogenesis and cellular glucose uptake,⁴² hence its compounds are loosely termed insulin-mimetics.^{43,44} Since these compounds do still require insulin to control glucose levels, a slightly preferred term is 'insulin-enhancers'.

1.5.2 Mechanism of action of vanadium complexes

The true form of the necessary vanadium species under physiological conditions is a subject of much debate but a focal mechanism of action which seems to enjoy a broad consensus is its involvement in the inhibition of phosphate-metabolizing enzymes. The action of vanadium at an intracellular level is due to the structural similarity between phosphate and vanadate.⁴⁵⁻⁴⁷ Once the vanadium compounds are in the blood they may decompose partially or completely, losing the coordinated ligands in the process. In this form the metal ion may undergo a series of complex redox processes. Vanadium(V) for example, can be reduced by biological molecules such as ascorbic acid, cysteine and glutathione, while non-bound vanadium(IV) is easily oxidised at intracellular pH. However, blood-circulating method electron paramagnetic resonance (BCM-EPR) studies revealed that almost independently of the initial oxidation state of the vanadium compound administered, the metal ion is transported in the +4 oxidation state in the blood. There are therefore two possible routes for vanadium to enter the cell. Vanadyl may bind to transferrin (Tf)

and subsequently enter the cell via the Tf-receptors following the iron pathway, or it may be oxidised to vanadate (H_2VO_4^-) and enter the cell via the phosphate or sulfate pathways.⁴⁸ Nevertheless, once in the cell it is thought that vanadate may bind to and inhibit PTP.⁴⁹ The proposed mechanism is shown in **figure 1.6**. The processes occurring in this figure are discussed below:

Scenario 1: This is the situation before insulin has bound to its receptor. For simplicity, the cell contains only a phosphate (PO_4^{3-} Ch) channel, an insulin receptor with α and β subunits, a protein tyrosine phosphate (PTP), insulin receptor substrates (IRS) and the glucose transporter – Glut 4.

Scenario 2: Insulin binds to the insulin receptor (α subunit) on the cell membrane. This leads to phosphorylation of a tyrosine residue on the β subunit of the receptor, which in turn initiates the phosphorylation of the insulin receptor substrates (IRS) leading to a signal transduction cascade that inevitably results in the translocation of the glucose transporter Glut 4 to the membrane. At this point glucose may be internalized and metabolized.

Scenario 3: In the absence of insulin as in type 1 diabetes, or lack of an efficient insulin response as is the case with type 2 diabetes, PTP counteracts the autophosphorylation of the β subunit which subsequently halts phosphorylation of IRS and the associated signal transduction.

Scenario 4: Vanadium enters the cell by either diffusion, endocytosis or via ion channels such as phosphate channels, the latter being the likely path for vanadate. Vanadate, a known phosphatase inhibitor, then binds to PTP, thereby re-initiating and prolonging signal transduction. This mechanism of action involving formation of vanadate and binding of this to PTP is supported by crystal structure evidence. Crystals suitable for single crystal X-ray diffraction were obtained after soaking a *bis*-coordinated oxovanadium(IV) complex with a PTP.⁴⁶ This work suggested that the coordination complex was oxidized to vanadate along with an associated loss of ligands. Vanadate subsequently binds to a serine residue as shown in **figure 1.7**, thereby giving evidence for the likely mode for the inhibition of the enzyme.

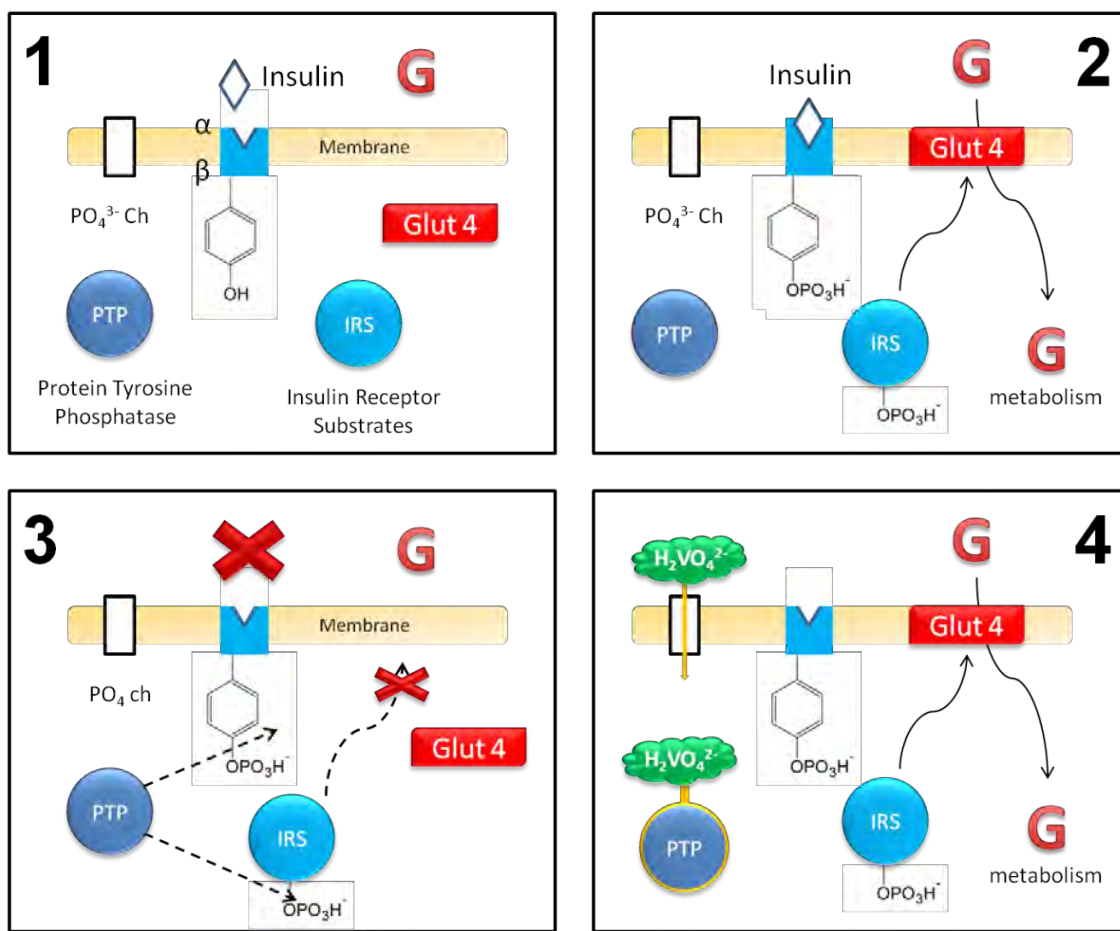


Figure 1.6 Mechanism of stimulation of glucose uptake by insulin or vanadate⁴³

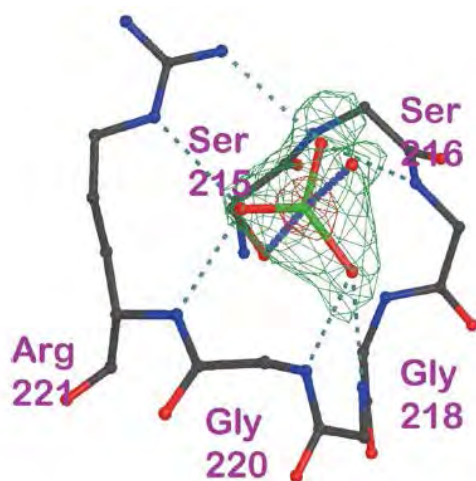


Figure 1.7 Crystal structure of PTP1B (C215S mutant) soaked with an oxovanadium(IV) complex⁴⁶

1.5.3 Antidiabetic vanadium complexes

As mentioned earlier, McNeill et al., (1985) demonstrated that vanadate was capable of affecting glucose metabolism in STZ-induced diabetic rats.²⁵ However, it was nearly a century earlier, that the antidiabetic effects of vanadate were first noticed. Forty-four test subjects with various ailments including diabetes, were treated orally over 24 hours, three times per week, with 4-5 mg of sodium metavanadate which had been dissolved in water. All of the patients showed an increase in appetite, slight weight gain and a general improvement in their physical status. More relevant however, was that of the diabetic patients, two out of three experienced a slight decrease in blood sugar levels.^{25,43} Other than the +5 oxidation state of vanadium, vanadyl sulfate, the +4 oxidation state salt, had also been shown to produce 'insulin-like' effects in diabetic rats.⁵⁰⁻⁵² This was promising considering the lower toxicity of vanadyl compared to vanadate. The facile formation of insoluble vanadyl hydroxides at intestinal pH's, unfortunately results in poor absorption (< 1%). Research in this field declined until the 1990's when both Orvig's group⁵³ and slightly later Sakurai's group⁵⁴ developed chelated oxovanadium(IV) compounds. The idea behind this was that the organic ligands would stabilize vanadyl under physiological conditions as well as improve membrane permeability. Indeed these compounds proved successful and since then, the drive has been to develop suitable ligands which are capable of stabilizing vanadyl under physiological pH.

The literature is saturated with references to *bis(maltolato)oxovanadium(IV)* (BMOV) and *bis(ethylmaltolato)oxovanadium(IV)* (BEOV) (**figure 1.8**) for good reason.^{4,45,55,56} First tested in 1992, these highly popular compounds have proven exemplary as insulin-enhancing agents. Metal complexes of maltol and its derivatives not only show low toxicity and reasonable intrinsic bioactivity,⁵⁵ but also display the desired properties including water solubility, balanced lipophilicity/hydrophilicity, a neutral charge and thermodynamic stability.⁵⁷ Furthermore, both maltol and ethylmaltol are approved food additives in many countries. Considering the pharmacokinetic challenges associated with compounds containing both organic and metal segments (as is the case in coordination complexes), each of which can form a range of by-products in the body, it was a huge advantage that the ligand had at least already undergone extensive pharmacological and pharmacokinetic studies.

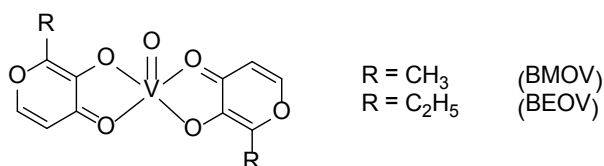


Figure 1.8 Chemical structures of BMOV and BEOV

BMOV not only lowers glucose and lipid levels, but also delays or possibly prevents long term diabetes induced pathology and limits hyperlipidemia and hyperinsulinemia in diabetic rats.⁵⁵ The vanadium uptake in bone, liver and the kidney tissue was approximately 2-3 times greater for BMOV than VOSO₄, while the residence time of BMOV was also significantly longer than that of VOSO₄. BEOV was chosen for clinical studies due to its slightly better hydrolytic stability and lipophilicity. Phase I clinical trials of this compound were successfully completed in early 2000. The outcomes of this were positive; no volunteers experienced any adverse side effects, gastrointestinal, kidney and liver functions as well as blood parameters remained within normal levels.⁵⁸ Phase IIa clinical trials were first disclosed in Lisbon (Vanadium 6 Symposium, Lisbon, Portugal, 18 July, 2008), the objectives being to assess the safety and efficacy of the compound in type 2 diabetic individuals over a 28-day period. Not only was BEOV well-tolerated in this study, but most subjects experienced significant reductions in blood glucose levels compared to those subjects taking a placebo.³⁵

The structurally similar pyridinone derivatives have also been studied. Sakurai *et al.* found that the oxovanadium(IV) complex containing the pyridinone ligand, bis(1,2-dimethyl-3-hydroxy-4-pyridinonate)oxovanadium(IV) ([VO(dmpp)₂] (**figure 1.9**), was effective in suppressing the release of free fatty acids (FFAs) from rat adipocytes and also had significantly better insulin-enhancing behaviour than VOSO₄.^{59,60} These results were confirmed later in a study by Passadouro and co-workers.⁶¹ After incubation of adipocytes with non-toxic concentrations of [VO(dmpp)₂], glucose uptake increased by 5-fold compared to the basal level. Furthermore, the compound showed a significant inhibitory effect on lipolysis (78%). The pyridinone ligand itself also goes by the names of deferiprone and ferriprox and is often used to treat iron-overload and as such has been extensively studied.^{62,63}

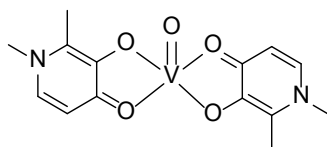


Figure 1.9 Chemical structure of [VO(dhp)₂]

Several oxovanadium(IV) complexes with a VO(N₂O₂) coordination mode have been proposed as insulin-enhancers, one of the most successful of these being *bis*(picolinato)oxovanadium(IV). Although synthesized several years ago,⁵⁵ this compound was only fully characterized and tested biologically a while later.^{54,64} The insulin-enhancing effects of picolinato chelates of oxovanadium(IV) have been clearly shown to be dependent on dose as well as delivery method. When [VO(pic)₂] (**figure 1.10**) was administered orally to STZ-induced diabetic rats (0.2 mmol.kg⁻¹ for 2 days followed by 0.1 mmol.kg⁻¹ for 11 days), plasma glucose levels normalised while plasma insulin levels increased.⁶⁵ However, when administered as a solution (2.4 mM), as a substitute for drinking water, only glucose-lowering tendencies and not insulin-elevation was observed. The latter method was also accompanied with signs of gastrointestinal irritation.⁶⁵ On the other hand, comparing [VO(pic)₂] with BMOV, the picolinate complex had lower solubility and more gastrointestinal irritation for an equivalent dose, suggesting that there is room for further structural improvement in order to increase bioavailability and lessen side effects.

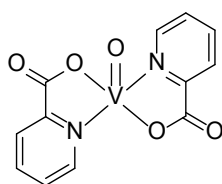


Figure 1.10 Chemical structure of *bis*(picolinato)oxovanadium(IV) [VO(pic)₂]

Only the most successful oxovanadium(IV) compounds or those most related to this study have been discussed, there are several other oxovanadium(IV) complexes that have demonstrated antidiabetic activity and there are numerous reviews dealing with these,^{55,65,66} nevertheless it is evident from the above examples that these complexes show excellent promise. There does

however remain room for improving the stability and biocompatibility of these complexes by appropriate modification of the ligands.

1.6 Vanadium chemistry

Vanadium was named after Vanadis, the Scandinavian goddess of beauty. It is element number 23, has an atomic weight of 50.94, and an electronic configuration of $3d^34s^2$ in the ground state.⁶⁷ The element was initially thought to have been discovered in 1801 by A.M del Rio in a sample of Mexican lead ore. He later withdrew his claim when it was suggested, albeit incorrectly, that the sample he found was in fact lead chromate. In 1830, N.G Sefström rediscovered it in Swedish iron ore.⁶⁷ This transition metal is found in about 65 minerals and makes up about 0.014% of the Earth's crust.⁶⁸ In the marine environment, vanadium is the second most abundant transition element (30 nM) only outmatched by molybdenum (100 nM). Vanadium can be found in a variety of oxidation states including +5 (yellow), +4 (blue), +3 (green), +2 (lavender) all the way to down to -3 (skipping only ox. state of -2) (**figure 1.11**). V^{2+} is not stable in aqueous media, rapidly oxidizing to V^{3+} , thus only the +5, +4 and +3 oxidation states are biologically relevant. The beautiful colours of vanadium were no doubt one of the driving factors for it being named after Vanadis.



Figure 1.11 The colour of vanadium in biologically relevant oxidation states. From left to right, V^{5+} , V^{4+} , V^{3+}

It has been accepted that VO^{2+} can be assigned the name oxovanadium(IV), VO^{3+} oxovanadium(V) and VO_2^+ dioxovanadium(V), this removes ambiguity associated with the term vanadyl. However, this term is still used to describe 'simple' compounds for example vanadyl sulfate (VOSO_4), whilst anionic complexes are commonly referred to as vanadates. Lately there has been a trend to follow the IUPAC principles and call the VO^{2+} core oxidovanadium(IV). Vanadium chemistry has been recorded as far back as 1801, with reviews dating back to the early 1900's.^{69,70}

The highly stable VO^{2+} ($[\text{Ar}]3d^1$) ion forms anionic, cationic and neutral complexes which may exist as solids, liquids or as vapour and the single electron system provides an ideal model for theorists.⁷⁰ High oxidation state metal ions that occur at the beginning of the transition series have been known to frequently form stable oxycations.⁷¹ The VO^{2+} ion occurs coordinated to other groups in both solid and solution state, elevating the coordination number of vanadium to five or six. Oxovanadium complexes have been studied using a wide variety of techniques including, but not limited to; potentiometry, polarography, magnetic susceptibility, X-ray diffraction, UV/VIS spectroscopy, infrared and Raman spectroscopy, and electron paramagnetic resonance.

1.6.1 Atomic structure and bonding of oxovanadium

Ballhausen and Gray,⁷¹ considered VO^{2+} in an aqueous solution as the $\text{VO}(\text{H}_2\text{O})_5^{2+}$ molecule ion to elucidate the molecular orbital description of the vanadyl ion. They proposed that the vanadium 3d, 4s, and 4p orbitals, along with the 2s, $2p_\sigma$ ($2p_z$) and $2p_\pi$ ($2p_x$, $2p_y$) oxide oxygen orbitals, and the sp_σ hybrid oxygen (from water) orbitals were involved in bonding. The possibility of π -bonding of water oxygens was regarded as unlikely. The bonding strengths were arranged in the order (V – O) > (four square planar waters) > (axial water). With this in consideration, one can predict the following (symmetry in parenthesis):

1. A strong σ bond between the sp_σ oxygen hybrid orbital and the ($4s + 3d_{z^2}$) vanadium hybrid orbitals (a_1)
2. Two π -bonds between the oxygen $2p_x$ and $2p_y$ orbitals and the vanadium $3d_{xz}$ and $3d_{yz}$ (e)

3. Four σ bonds between sp_σ orbitals of the water oxygens and the vanadium ($4s-3d_{z^2}$) (a_1), $4p_x$ and $4p_y$ (e), and $3d_{x^2-y^2}$ (b_1) orbitals.
4. The axial water oxygen is bonded to the remaining $4p_z$ (a_1) orbital
5. The vanadium $3d_{xy}$ (b_2) is non-bonding

From this information, the energy level scheme was predicted and is shown in **figure 1.12**. This model allowed for the prediction and interpretation of magnetic, electron spin resonance (ESR) and optical properties. McGlynn proposed, using a ligand field approach, that the π -bonding of the equatorial ligands should not be neglected.⁷²

This consideration only affects the order of the b_1^* and e_π^* , however these energy levels are so close together that the inversion might occur between different complexes.⁷⁰ This model predicts three transitions for the C_{4v} symmetrical VO^{2+} molecular ion:

$$b_2 \rightarrow e_\pi^* ({}^2B_2 \rightarrow {}^2E)$$

$$b_2 \rightarrow b_1^* ({}^2B_2 \rightarrow {}^2B_1)$$

$$b_2 \rightarrow a_1^* ({}^2B_2 \rightarrow {}^2A_1)$$

Bands appearing at a lower wavelength than 200 nm are assumed to be due to charge transfer. The lowering of symmetry to C_{2v} has little or no effect on the observed spectra, since the splitting of the e_π^* level is too small to be observed experimentally most of the time.⁷¹

The Ortolano, Selbin and McGlynn (OSM) scheme predicts three visible transitions from the ground state, b_2 (d_{xy}). These include; $d_{xy} \rightarrow (d_{xz}, d_{yz})$; $d_{xz} \rightarrow (d_{x^2-y^2})$ and $d_{xz} \rightarrow (d_{z^2})$. The first two transitions may invert depending on the σ -donor strength of the ligands. The third transition may overlap or be completely occluded by charge transfer bands. Insertion of a fifth or sixth (polar) ligand would not be expected to lead to any noticeable effects (**figure 1.13**).⁷³

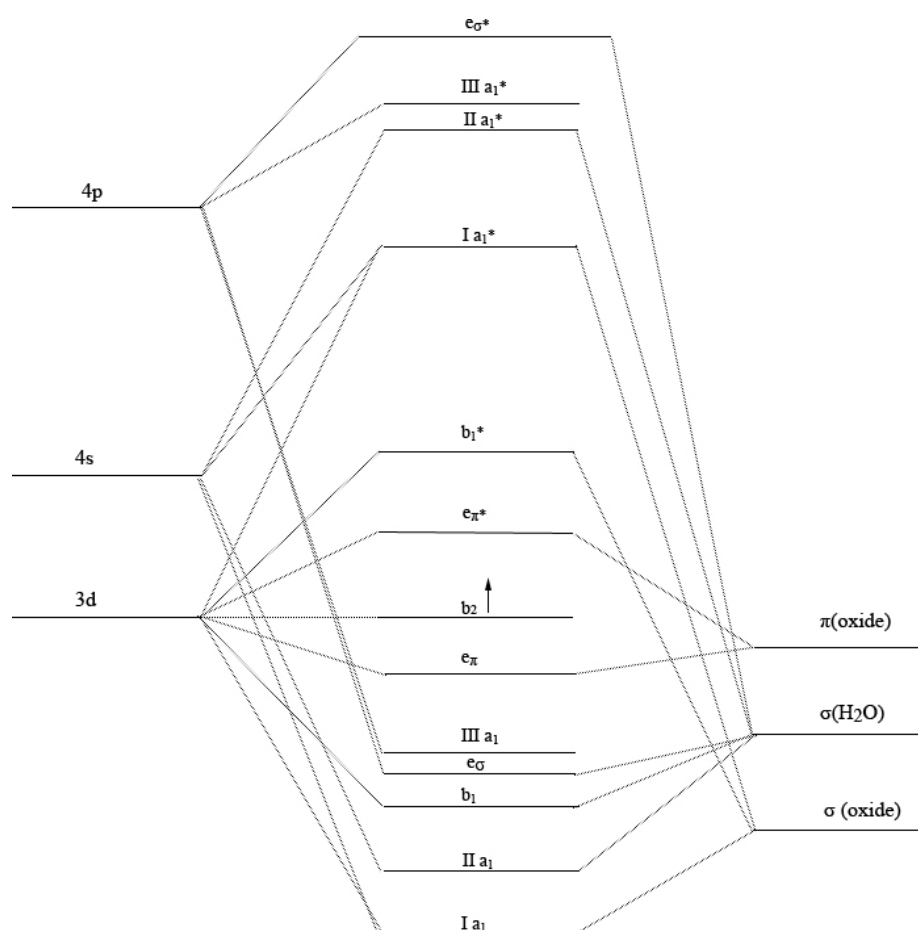


Figure 1.12 Molecular orbital scheme for the VO^{2+} species as outlined by Ballhausen⁷¹

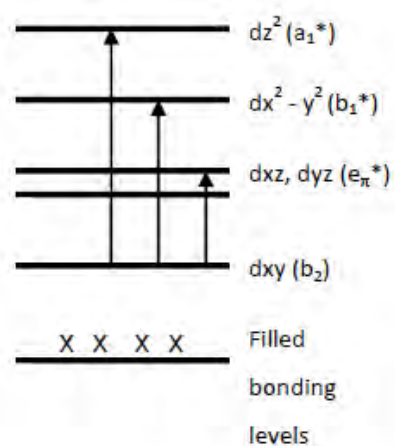


Figure 1.13 Clustered energy level scheme of OSM for vanadyl(IV) complexes⁷³

Vanadium exhibits a multitude of stereochemical arrangements (**figure 1.14**), with V(V) complexes being found in tetrahedral, octahedral, trigonal and pentagonal bipyramidal and square pyramidal geometries while V(IV) exhibits fewer geometries. Mainly square pyramidal, or distorted octahedral (if a sixth position is occupied) are found.⁷⁴

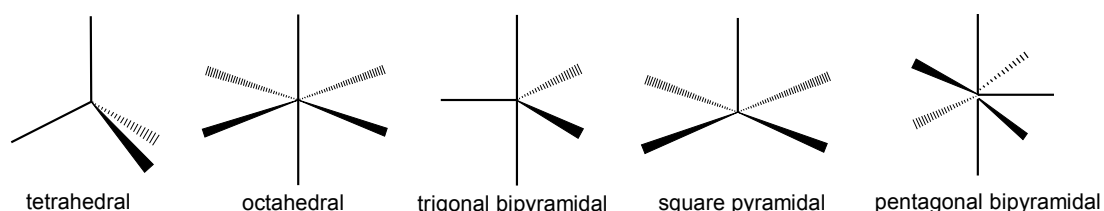


Figure 1.14 Some typical geometries of vanadium compounds

1.6.2 Infrared spectroscopy of oxovanadium complexes

Evidence of the oxovanadium species can be readily detected using infrared. In fact, so characteristic is the $\nu(\text{V}=\text{O})$ mode that attempts have been made to use this stretch to establish a certain ligand series, similar to the spectrochemical series. For example, a complex of type $[\text{VO}(\text{a})_5]^{n\pm}$ can be arranged as follows; $\text{H}_2\text{O} > \text{NCS}^- > \text{CN}^- > \text{DMSO} \sim \text{F}^-$, where H_2O gives the highest VO stretching frequency and F^- the lowest. Similarly for $[\text{VO}(\text{AA})_2\text{a}]$ and $[\text{VO}(\text{AA})_2]$ the series order is; $\text{ophen} > \text{malan}^{2-} \sim \text{ox}^{2-} > \text{dipy}$ and $\text{DBM} > \text{acac}^- > \text{ophen} > \text{dipy}$, respectively.⁷⁵ Although similar, this ligand series is not identical, as seen with CN^- being displaced from its usual extreme spectrochemical position.⁷⁰ This deviation can be attributed to the fact that metal-ligand π -bonding plays a significant role within the spectrochemical series meanwhile infrared vibrations are dependant primarily on σ -bonding and only secondarily on metal-ligand π -bonding.⁷⁰ The frequency of the VO stretch can be broken into three components:

- 1. σ -Bonding:** The V–O bond is a multiple-covalent bond. This consists of electron donation from p_π (oxygen) \rightarrow d_π (vanadium), superimposed on the σ -bond. The stretching frequency of this bond will therefore be affected by the donating ability of the oxygen to the metal and the capacity of the metal to accept electron density. The latter is

largely dependent on the coordinated ligands. Ligands that are strong Lewis bases increase the electron density within the d-orbitals of the metal, thereby lowering the V – O stretching frequency.

2. π_{\perp} -Bonding: This is the same as for σ -bonding, except that overlaps constitute a smaller factor.

3. π_{\parallel} - Bonding: Contribution of charge from the ligand to the original b_2 atomic orbital.

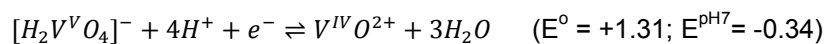
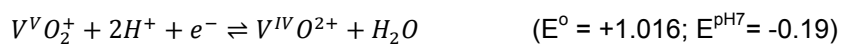
This change in frequency can be written as the sum of these factors, shown below.

$$\Delta\nu = -\sigma(L \rightarrow M) - \pi_{\perp}(L \rightarrow M) - \pi_{\parallel}(L \rightarrow M)$$

A wide number of oxovanadium compounds have been characterised in this way, and in general the $\nu(V=O)$ frequency stretch was summarised by $985 \pm 50 \text{ cm}^{-1}$.⁷⁰ Oxo-bridged oxovanadium species, which have been noted to form readily in the presence of air, can be identified using infrared. The $\nu(V=O)$ stretch appears at comparatively lower wavenumbers of $\sim 920 \text{ cm}^{-1}$, than the non-bridged five coordinate species. An additional lower energy band appearing at approximately 780 cm^{-1} , corresponds to the $\nu(V-O-V)$ mode.⁷⁵ Vanadium can retain its oxidation state of +4 and form polymeric rather than bridged structures, the $\nu(V=O)$ in such complexes appears shifted to lower wavenumbers compared to the monomeric five coordinate species. For example in a *bis*-coordinated polymeric 2-(2'-hydroxyphenyl)benzoxazole oxovanadium(IV) complex prepared by Back *et al.*, this band appeared at 894 cm^{-1} .⁷⁶

1.6.3 Redox chemistry

As already mentioned, the three biologically relevant oxidation states of vanadium are +5, +4 and +3. The one electron redox couples for the above mentioned oxidation states are presented in the equations below, with standard potentials (E°) and potentials at pH 7 (relative to normal hydrogen electrode) shown in parenthesis.⁴³



From the above potentials, one can conclude that under aerobic conditions, V^{5+} is the most stable form. However, in oxygen free environments such as the cytoplasm, biological reducing agents such as ascorbate, glutathione and NADH may reduce $V^V O_2^+$ to $V^{IV} O^{2+}$ provided that the species is not complexed to ligands of any kind (including biological ligands). As can be seen in the above redox potentials, vanadate is reduced with greater difficulty, while reduction of $V^{IV} O^{2+}$ to V^{III} is unlikely under typical physiological conditions.⁴³

1.6.4 Solution chemistry of vanadium

Orally administered metallo-pharmaceuticals need to survive the acidic pH of the stomach and the slightly more alkaline pH of the intestine.⁷⁷ Vanadyl sulfate, while stable under acidic conditions, readily hydrolyzes forming insoluble hydroxides in the slightly more basic pH's experienced in the intestine. The consequence of this is that much less vanadium can be absorbed and thus higher doses are required.⁷⁷

The aqueous chemistry of vanadate and vanadyl is quite complex due to the formation of polyoxometallates and mono/divanadylhydroxy products respectively. This complexity is well displayed in the speciation diagrams for V(V) and V(IV) which are shown in **figure 1.15** and **figure 1.16**, respectively. The stability constants used for each of these species distribution plots were obtained from publications by Pettersson,⁷⁸ Henry⁶⁸ and Komura.^{79,80} Vanadate dissolved in acidic solution turns a yellow colour due to the formation of decavanadate $(H_n V_{10} O_{28})^{6-n}$ (where $n = 0-3$). At pH less than 2, a colourless tetrahydrated VO_2^+ monocation forms.

Considering vanadyl, one can see that at pH values of 6 and greater, there is significant formation of insoluble hydroxides. Furthermore, above pH 3, vanadyl is susceptible to oxidation to

vanadium(V). This early hydrolysis and facile oxidation can be combated to some degree by appropriate ligand complexation. Some oxovanadium(IV) complexes for example, possess oxidation half-lives several times greater than vanadyl sulfate.^{81,82} The pH-metric chemical speciation of the vanadium compounds can be appropriately designed through the correct combination of donor atoms involved in the bidentate coordination of the ligands in order to achieve the requisite stabilization under the physiological pH range.

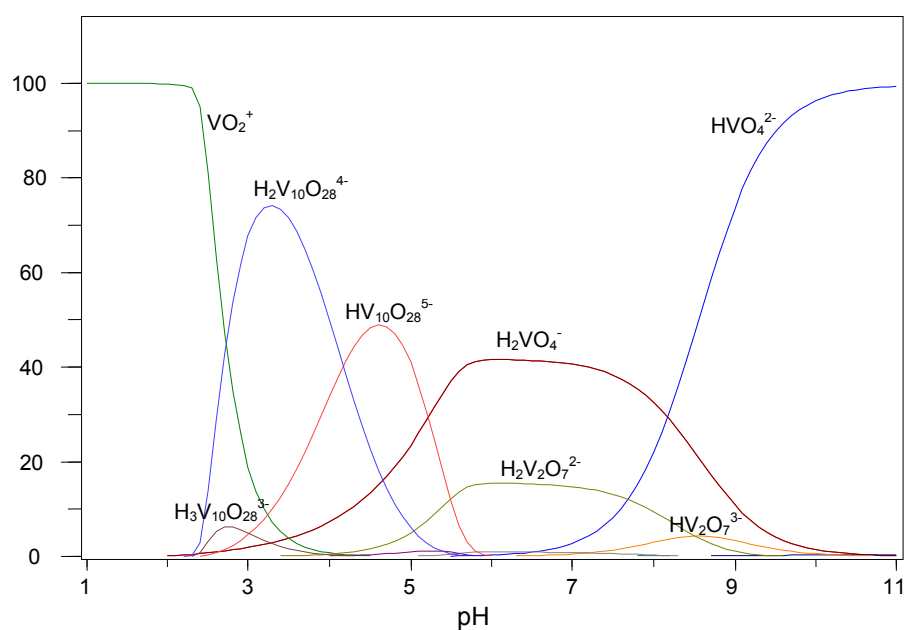


Figure 1.15 Speciation diagram for aqueous vanadate (VO_2^+). Concentration of $[\text{VO}_2^+] = 1.0 \text{ mM}$

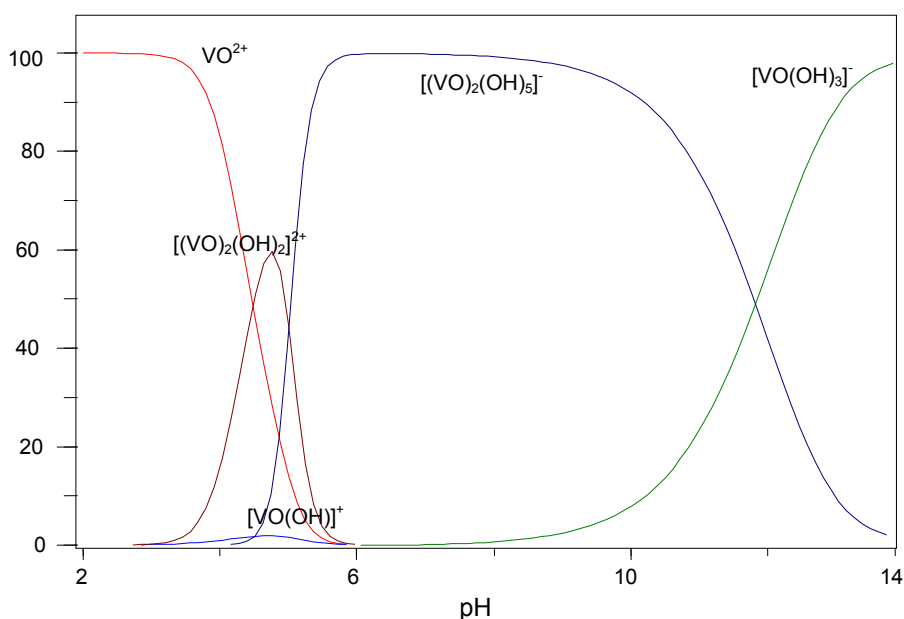


Figure 1.16 Speciation diagram for aqueous vanadyl (VO^{2+}). Concentration of $[\text{VO}^{2+}] = 10 \text{ mM}$

1.7 Vanadium in biology

Vanadium can be found in reasonably high quantities in many sea-dwelling animals. Ascidiaceans typically accumulate large quantities of vanadium, for example *Ascidia nigra* stores up to 14 500 ppm of vanadium. In humans vanadium is found in multiple organs and tissues, particularly the kidneys, bone, blood, liver, spleen and heart^{37,45,83} but has also been found in brain and muscle tissue in lower concentrations.⁸³ Vanadium is preferentially retained in the bone for longer periods, for example the residence time of ⁴⁸V-BMOV in the bone was 31 days compared to 7 mins in the blood for the same compound. Ultimately vanadium is excreted via the urine and faeces.³⁷ In healthy humans, vanadium blood concentrations were found to be between 0.18 and 0.22 ppm.⁸⁴ The main sources of vanadium in the diet include; mushroom, fish, black pepper, fresh fruits and parsley.⁸⁵

1.7.1 Biospeciation of vanadium

For any pharmaceutical drug, the absorption, distribution, metabolism and excretion (ADME) profiles are of considerable importance. The chelated oxovanadium(IV) complexes typically

undergo a similar, albeit relatively complex fate *in vivo*.⁸⁶⁻⁸⁹ After oral administration the complexes enter the acidic conditions of the stomach (pH ~2). Under these conditions a coordinated ligand is lost and ionic vanadium species predominate.^{87,90,91} This is not ideal considering that it is believed that these complexes should have a neutral charge to improve lipophilicity and hence cell membrane permeability.⁶⁵ Nevertheless, it seems enough of the complexes survive as they still display improved absorption and tissue accumulation profiles over the inorganic salts.³⁷ Of course these complexes can be protected from the harsh stomach conditions by tailoring the drug formulation, for example via the encapsulation technique, thereby protecting the complex from stomach acidity.^{92,93}

Once in the blood stream (after absorption), high molecular weight proteins including human serum albumin (HSA) and transferrin (Tf) as well as low molecular weight bioligands such as lactate, oxalate, citrate and phosphates, bind to vanadium.^{48,90,94,95} This is thought to be of critical importance since these bioligands protect vanadium from forming water-insoluble hydrolysis products which have very slow aqueous substitution kinetics and help transport vanadium to the relevant site of action.⁹⁶ An *in vitro* investigation by Chasteen and co-workers as well as Kiss and co-workers, revealed that apo-Tf binds vanadyl much more strongly than HSA, approximately 4 times more strongly in fact.^{48,97} Thus, even though HSA is found in significantly higher concentrations (~20 times more than Tf), most vanadyl remains bound to Tf making it the primary transport protein. Studies using blood circulated method electron paramagnetic resonance (BCM-EPR) confirmed these results, also indicating that the majority (~77%) of vanadium in the blood was bound by Tf, with the remainder presumably being bound by low molecular weight serum binders (citrate, lactate, etc). A latter study further showed that vanadium was bound to Tf in the +4 oxidation state regardless of the form of vanadium initially administered (either V⁴⁺ or V⁵⁺).⁹⁸

Several years back, Chasteen *et al.* showed that binding of vanadium to Tf occurred less rapidly in the absence of bicarbonate ions (HCO₃⁻). They subsequently demonstrated that in the absence of bicarbonate certain ligands could act synergistically, especially those containing carboxylic acid functional groups like citrate and lactate.^{97,99} It was therefore suspected that ligands such as 1,2-dimethyl-3-hydroxy-4(1*H*)-pyridinone (dhp) or maltol (mal) can substitute the synergistic anion and improve VO²⁺ binding. Kiss *et al.* showed by circular dichroism (CD) and EPR, that incubation of Tf with various *bis*-coordinated oxovanadium(IV) complexes resulted in the formation of ternary

complexes. The ternary complexes were in the form $(V^{4+}O)Tf(L)$, $(V^{4+}O)_2Tf(L)_2$ and $(V^{4+}O)_2hTf(L)$, where L was a bidentate carrier ligand, either maltol (mal) or 1,2-dimethyl-3-hydroxy-4-pyridinone (dhp). However a similar EPR study using $VO(pic)_2$ revealed that the EPR spectrum of VO^{4+} -apoTf was practically the same as that obtained after incubating $VO(pic)_2$ with apoTf, suggesting complete ligand displacement.⁴⁸ While it is certainly interesting to study and understand the possible species existing in the blood, how this affects the antidiabetic activity of these complexes remains unanswered, especially considering that HCO_3^- or other biological anions may substitute these ligands.⁹⁷

Despite the dominance of Tf as a binder of vanadium, the interactions of the low molecular weight bioligands such as citrate, lactate and phosphate with vanadium should not be neglected since these may displace the original ligand forming a binary complex, or coordinate to form ternary or quinary complexes. This may subsequently affect transport and delivery processes and possibly even the physiological activity.⁹¹

In summary, the transport mechanism of oxovanadium(IV) complexes seems similar regardless of the ligands used. Once in the blood, the strong binder Tf is capable of abstracting the vanadyl ion from the complex. Thus complexes such as $VO(mal)_2$, $VO(pic)_2$ and $VO(acac)_2$ (where mal = maltol; pic = picolinate; acac = acetylacetonate) as well as their derivatives are quite likely delivered to the target sites as a similar vanadium(IV)-serum protein complex.^{54,100} The ligands, therefore serve primarily as transporter molecules, assisting only by shuttling vanadyl from the gastro-intestinal tract into the blood stream. This was substantiated by a ^{48}V biodistribution study in which $^{48}VOSO_4$ and $^{48}V-BMOV$ were both administered orally to Wistar rats.³⁷ Both exhibited similar tissue distribution, however, BMOV accumulated in significantly higher concentrations despite the same administration dose.

1.8 Aims and objectives of this study

The main aim of this study was to prepare and characterize new oxovanadium(IV) complexes and evaluate their potential as possible antidiabetic drugs. As previously discussed, the primary function of the ligands is to shuttle vanadyl into the blood stream via the stomach and

gastrointestinal tract. New ligands are to be designed which are capable of stabilizing vanadyl under these conditions as well as imparting a balanced lipo/hydrophilicity to the complex, thus allowing for adequate absorption. The research objectives can be briefly summarized as follows:

1. Prepare nature-inspired bidentate ligands containing the N,O-donor atoms and the corresponding neutral *bis*-coordinated oxovanadium(IV) complexes.
2. Use glass electrode potentiometry to determine the ligand pK 's as well as the stability constants of the oxovanadium complexes. This may give an indication of the fate of the complexes not only in the stomach and intestine, but also in the blood.
3. Prepare species distribution diagrams to evaluate the different species existing over the biological pH range and use these results to improve the ligand design.
4. Determine the *in vitro* cytotoxicity and glucose-lowering effects of the synthesized vanadium complexes using three cell culture lines; muscle (C2C12), fat (3T3-L1) and liver (Chang) cells.
5. Investigate the effect of the prepared complexes on the coagulation process using the PT, and APTT clotting time assays as well as monitoring the fibrin and D-Dimer formation.

1.9 References

- (1) Wild, S.; Roglic, G.; Green, A.; Sicree, R.; King, H. *Diabetes Care* **2004**, *27*, 1047.
- (2) World Health Organization, W. H. "Preventing chronic diseases: a vital investment," 2005.
- (3) Zimmet, P.; Alberti, K. G. M. M.; Shaw, J. *Nature* **2001**, *414*, 782.
- (4) Saatchi, K.; Thompson, K. H.; Patrick, B. O.; Pink, M.; Yuen, V. G.; McNeill, J. H.; Orvig, C. *Inorg. Chem.* **2005**, *44*, 2689.
- (5) Butler, P. C.; Kryshak, E. J.; Schwenk, W. F.; Haymond, M. W.; Rizza, R. A. *Diabetes* **1990**, *39*, 217.
- (6) Burger, A. *Burger's Medicinal Chemistry*; 4th ed.; Wiley-Interscience: Canada, 1981.
- (7) Panunti, B.; Jawa, A. A.; Fonseca, V. A. *Drug Discovery Today* **2004**, *1*, 151.
- (8) Goc, A. *Cent. Euro. J. Biol.* **2006**, *1*, 314.
- (9) Nicholson, G.; Hall, G. M. *Brit. J. Anaesth.* **2011**, *107*, 65.
- (10) Sunayama, S.; Watanabe, Y.; Ohmura, H.; Sawano, M.; Shimada, K.; Mokuno, H.; Daida, H.; Yamaguchi, H. *Atherosclerosis* **1999**, *146*, 187.
- (11) Sung, B. H.; Izzo Jr, J. L.; Dandona, P.; Wilson, M. F. *Hypertension* **1999**, *34*, 83.
- (12) Kruszynska, Y. T.; Yu, J. G.; Olefsky, J. M.; Sobel, B. E. *Diabetes* **2000**, *49*, 633.
- (13) Cheng, A. Y. Y.; Fantus, I. G. *CMAJ*. **2005**, *172*, 213.
- (14) Phillippe, H. M.; Wargo, K. A. *Ann. Pharmacother.* **2010**, *44*, 1615.
- (15) Skamagas, M.; Breen, T. L.; LeRoith, D. *Oral Dis.* **2008**, *14*, 105.
- (16) Erem, C.; Hacıhasanoğlu, A.; Çelik, Ş.; Ovalı, E.; Önder Ersöz, H.; Ukinç, K.; Deger, O.; Telatar, M. *Med. Princ. Pract.* **2005**, *14*, 22.
- (17) Mackman, N.; Tilley, R. E.; Key, N. S. *Arterioscler. Thromb. Vasc. Biol.* **2007**, *27*, 1687.
- (18) Davie, E. W.; Fujikawa, K.; Kisiel, W. *Biochemistry* **1991**, *30*, 10363.
- (19) Carr, M. E. *J. Diabetes Complicat.* **2001**, *15*, 44.
- (20) Beckman, J. A.; Creager, M. A.; Libby, P. *JAMA*. **2002**, *287*, 2570.
- (21) White, J. R. *Diabetes Spectr.* **2011**, *24*, 47.
- (22) Schwietert, C. W.; McCue, J. P. *Coord. Chem. Rev.* **1999**, *184*, 67.
- (23) Raymond, E.; Chaney, S. G.; Taamma, A.; Cvitkovic, E. *Ann. Oncol.* **1998**, *9*, 1053.
- (24) Zhang, C. X.; Lippard, S. J. *Curr. Opin. Chem. Biol.* **2003**, *7*, 481.
- (25) Clayton, E. H.; Tahiliani, A. G.; McNeill, J. H. *Science* **1985**, *227*, 1474.

-
- (26) Lo, K. K.-W.; Louie, M.-W.; Zhang, K. Y. *Coord. Chem. Rev.* **2010**, *254*, 2603.
- (27) Bottrill, M.; Kwok, L.; Long, N. J. *Chem. Soc. Rev.* **2006**, *35*, 557.
- (28) Hofmann, M. H.; Maecke, H. M.; Börner, A. B.; Weckesser, E. W.; Schöffski, P. S.; Oei, M. O.; Schumacher, J. S.; Henze, M. H.; Heppeler, A. H.; Meyer, G. M.; Knapp, W. K. *Eur. J. Nucl. Med. Mol. Imaging* **2001**, *28*, 1751.
- (29) Boros, E.; Ferreira, C. L.; Patrick, B. O.; Adam, M. J.; Orvig, C. *Nucl. Med. Biol.* **2011**.
- (30) Butler, A.; Carrano, C. J. *Coord. Chem. Rev.* **1991**, *109*, 61.
- (31) Tolman, E. L.; Barris, E.; Burns, M.; Pansini, A.; Partridge, R. *Life Sciences* **1979**, *25*, 1159.
- (32) Degani, H.; Gochin, M.; Karlsh, S. J. D.; Shechter, Y. *Biochemistry* **1981**, *20*, 5795.
- (33) Heyliger, C. E.; Tahiliani, A. G.; McNeill, J. H. *Science* **1985**, *227*, 1474.
- (34) Willsky, G. R.; Chi, L.-H.; Godzala Iii, M.; Kostyniak, P. J.; Smee, J. J.; Trujillo, A. M.; Alfano, J. A.; Ding, W.; Hu, Z.; Crans, D. C. *Coord. Chem. Rev.* **2011**, *255*, 2258.
- (35) Thompson, K. H.; Lichter, J.; LeBel, C.; Scaife, M. C.; McNeill, J. H.; Orvig, C. *J. Inorg. Biochem.* **2009**, *103*, 554.
- (36) Cohen, M. D. *Toxicol. Ecotoxicol. News* **1996**, *3*, 132.
- (37) Setyawati, I. A.; Thompson, K. H.; Yuen, V. G.; Sun, Y.; Battell, M.; Lyster, D. M.; Vo, C.; Ruth, T. J.; Zeisler, S.; McNeill, J. H.; Orvig, C. *J. Appl. Physiol.* **1998**, *84*, 569.
- (38) Broadhurst, C. L.; Domenico, P. *Diabetes Technol. Ther.* **2006**, *8*, 677.
- (39) Mulyani, I.; Levina, A.; Lay, P. A. *Angew. Chem. Int. Ed.* **2004**, *43*, 4504.
- (40) Levina, A.; McLeod, A. I.; Seuring, J.; Lay, P. A. *J. Inorg. Biochem.* **2007**, *101*, 1586.
- (41) Thompson, K. H.; Chiles, J.; Yuen, V. G.; Tse, J.; McNeill, J. H.; Orvig, C. *J. Inorg. Biochem.* **2004**, *98*, 683.
- (42) Hiramura, M.; Adachi, Y.; MacHida, M.; Hattori, M.; Sakurai, H. *Metallomics* **2009**, *1*, 92.
- (43) Rehder, D. *Bioorganic vanadium chemistry*; John Wiley and Sons Ltd.: West Sussex, 2008.
- (44) Shukla, R.; Bhonde, R. R. *BioMetals* **2008**, *21*, 205.
- (45) Thompson, K. H.; Orvig, C. *J. Inorg. Biochem.* **2006**, *100*, 1925.
- (46) Peters, K. G.; Davis, M. G.; Howard, B. W.; Pokross, M.; Rastogi, V.; Diven, C.; Greis, K. D.; Eby-Wilkens, E.; Maier, M.; Evdokimov, A.; Soper, S.; Genbauffe, F. *J. Inorg. Biochem.* **2003**, *96*, 321.
-

-
- (47) McLauchlan, C. C.; Hooker, J. D.; Jones, M. A.; Dymon, Z.; Backhus, E. A.; Greiner, B. A.; Dorner, N. A.; Youkhana, M. A.; Manus, L. M. *J. Inorg. Biochem.* **2010**, *104*, 274.
- (48) Kiss, T.; Jakusch, T.; Hollender, D.; Dörnyei, A.; Enyedy, E. A.; Pessoa, J. C.; Sakurai, H.; Sanz-Medel, A. *Coord. Chem. Rev.* **2008**, *252*, 1153.
- (49) Tsiani, E.; Fantus, I. G. *Trends Endocrinol. Metab.* **1997**, *8*, 51.
- (50) Ramanadham, S.; Mongold, J. J.; Brownsey, R. W.; Cros, G. H.; McNeill, J. H. *Am. J. Physiol. Heart Circ. Physiol.* **1989**, 257.
- (51) Mongold, J. J.; Cros, G. H.; Vian, L.; Tep, A.; Ramanadham, S.; Siou, G.; Diaz, J.; McNeill, J. H.; Serrano, J. J. *Pharmacol. Toxicol.* **1990**, *67*, 192.
- (52) Ramanadham, S.; Cros, G. H.; Mongold, J. J.; Serrano, J. J.; McNeill, J. H. *Can. J. Physiol. Pharmacol.* **1990**, *68*, 486.
- (53) McNeill, J. H.; Yuen, V. G.; Hoveyda, H. R.; Orvig, C. *J. Med. Chem.* **1992**, *35*, 1489.
- (54) Sakurai, H.; Fujii, K.; Watanabe, H.; Tamura, H. *Biochem. Biophys. Res. Comm.* **1995**, *214*, 1095.
- (55) Thompson, K. H.; Orvig, C. *Coord. Chem. Rev.* **2001**, 219-221, 1033.
- (56) Liboiron, B. D.; Thompson, K. H.; Hanson, G. R.; Lam, E.; Aebischer, N.; Orvig, C. *J. Am. Chem. Soc.* **2005**, *127*, 5104.
- (57) Barrand, M. A.; Callingham, B. A.; Hider, R. C. *J. Pharm. Pharmacol.* **1987**, *39*, 203.
- (58) Thompson, K. H.; Orvig, C. *Dalton Trans.* **2006**, 761.
- (59) Rangel, M.; Tamura, A.; Fukushima, C.; Sakurai, H. *J. Biol. Inorg. Chem.* **2001**, *6*, 128.
- (60) Buglyó, P.; Kiss, T.; Kiss, E.; Sanna, D.; Garribba, E.; Micera, G. *J. Chem. Soc., Dalton Trans.* **2002**, 2275.
- (61) Passadouro, M.; Metelo, A. M.; Melão, A. S.; Pedro, J. R.; Faneca, H.; Carvalho, E.; Castro, M. M. C. A. *J. Inorg. Biochem.* **2010**, *104*, 987.
- (62) Nick, H. *Curr. Opin. Chem. Biol.* **2007**, *11*, 419.
- (63) Scott, L. E.; Orvig, C. *Chem. Rev.* **2009**, *109*, 4885.
- (64) Melchior, M.; Thompson, K. H.; Jong, J. M.; Rettig, S. J.; Shuter, E.; Yuen, V. G.; Zhou, Y.; McNeill, J. H.; Orvig, C. *Inorg. Chem.* **1999**, *38*, 2288.
- (65) Thompson, K. H.; McNeill, J. H.; Orvig, C. *Chem. Rev.* **1999**, *99*, 2561.
- (66) Thompson, K. H.; Barta, C. A.; Orvig, C. *Chem. Soc. Rev.* **2006**, *35*, 545.
-

-
- (67) Greenwood, N. N.; Earnshaw, A. *Chemistry of the Elements*; Elsevier: New York, 2005; Vol. 2nd.
- (68) Tracey, A. S., Willsky, G. R., Takeuchi, E. S. *Vanadium: Chemistry, Biochemistry, Pharmacology and Practical Applications*; CRC Press: Boca Raton, 2007.
- (69) Selbin, J.; Holmes Jr, L. H. *J. Inorg. Nucl. Chem.* **1962**, *24*, 1111.
- (70) Selbin, J. *Chem. Rev.* **1965**, *65*, 153.
- (71) Ballhausen, C. J.; Gray, H. B. *Inorg. Chem.* **1962**, *1*, 111.
- (72) Selbin, J.; Holmes Jr, L. H.; McGlynn, S. P. *J. Inorg. Nucl. Chem.* **1963**, *25*, 1359.
- (73) Selbin, J. *Coord. Chem. Rev.* **1966**, *1*, 293.
- (74) Page, E. M. *Coord. Chem. Rev.* **1998**, *172*, 111.
- (75) Selbin, J.; Manning, H. R.; Cessac, G. *J. Inorg. Nucl. Chem.* **1963**, *25*, 1253.
- (76) Back, D. F.; Manzoni de Oliveira, G.; Ballin, M. A.; Corbellini, V. A. *Inorg. Chim. Acta.* **2010**, *363*, 807.
- (77) Fites, R. J.; Yeager, A. T.; Sarvela, T. L.; Howard, W. A.; Zhu, G.; Pang, K. *Inorg. Chim. Acta.* **2006**, *359*, 248.
- (78) Elvingson, K.; González Baró, A.; Pettersson, L. *Inorg. Chem.* **1996**, *35*, 3388.
- (79) Henry, R. P.; Mitchell, P. C. H.; Prue, J. E. *J. Chem. Soc., Dalton Trans.* **1973**, 1156.
- (80) Komura, A., Hayashi, H., Imanaga, H. *Bull. Chem. Soc. Jpn.* **1977**, *50*, 2927.
- (81) Sun, Y.; James, B. R.; Rettig, S. J.; Orvig, C. *Inorg. Chem.* **1996**, *35*, 1667.
- (82) Amin, S. S.; Cryer, K.; Zhang, B.; Dutta, S. K.; Eaton, S. S.; Anderson, O. P.; Miller, S. M.; Reul, B. A.; Brichard, S. M.; Crans, D. C. *Inorg. Chem.* **2000**, *39*, 406.
- (83) Mukherjee, B.; Patra, B.; Mahapatra, S.; Banerjee, P.; Tiwari, A.; Chatterjee, M. *Toxicol. Lett.* **2004**, *150*, 135.
- (84) Agrawal, Y. K.; Sant, M. S. *Bioorg. Chem.* **1978**, *9*, 369.
- (85) Barceloux, D. G. *J. Toxicol. Clin. Toxicol.* **1999**, *37*, 265.
- (86) Sanna, D.; Micera, G.; Buglyó, P.; Kiss, T.; Gajda, T.; Surdy, P. *Inorg. Chim. Acta.* **1998**, *268*, 297.
- (87) Kiss, E.; Garribba, E.; Micera, G.; Kiss, T.; Sakurai, H. *J. Inorg. Biochem.* **2000**, *78*, 97.
- (88) Buglyó, P.; Kiss, E.; Fábíán, I.; Kiss, T.; Sanna, D.; Garribba, E.; Micera, G. *Inorg. Chim. Acta.* **2000**, *306*, 174.
-

-
- (89) Rangel, M.; Leite, A.; Amorim, M. J.; Garribba, E.; Micera, G.; Lodyga-Chruscinska, E. *Inorg. Chem.* **2006**, *45*, 8086.
- (90) Jakusch, T.; Hollender, D.; Enyedy, E. A.; Gonzalez, C. S.; Montes-Bayon, M.; Sanz-Medel, A.; Pessoa, J. C.; Tomaz, I.; Kiss, T. *Dalton Trans.* **2009**, 2428.
- (91) Kiss, T.; Kiss, E.; Micera, G.; Sanna, D. *Inorg. Chim. Acta.* **1998**, *283*, 202.
- (92) Fugono, J.; Yasui, H.; Sakurai, H. *J. Pharm. Pharmacol.* **2005**, *57*, 665.
- (93) Sakurai, H.; Fugono, J.; Yasui, H. *Mini Rev. Med. Chem.* **2004**, *4*, 41.
- (94) Kiss, T.; Jakusch, T.; Bouhsina, S.; Sakurai, H.; Enyedy, É. A. *Eur. J. Inorg. Chem.* **2006**, 3607.
- (95) Jakusch, T.; Costa Pessoa, J.; Kiss, T. *Coord. Chem. Rev.* **2011**, *255*, 2218.
- (96) Baes, C. F., Mesmer, R. E. *The Hydrolysis of Cations*; Kreiger Publishing Company: Malabar, FL, 1986.
- (97) Chasteen, N. D.; Grady, J. K.; Holloway, C. E. *Inorg. Chem.* **1986**, *25*, 2754.
- (98) Sakurai, H.; Shimomura, S.; Fukuzawa, K.; Ishizu, K. *Biochem. Biophys. Res. Comm.* **1980**, *96*, 293.
- (99) Chasteen, N. D.; *Coord. Chem. Rev.* **1977**, *22*, 1.
- (100) Woo, L. C. Y.; Yuen, V. G.; Thompson, K. H.; McNeill, J. H.; Orvig, C. *J. Inorg. Biochem.* **1999**, *76*, 251.

This page has been left blank intentionally

Chapter 2

Experimental materials and methods

2.1 General reagents

Vanadyl sulfate hydrate was obtained from BDH Limited (England). Methylsalicylate, ethylenediamine, *N*-ethanoethylenediamine, *N*-ethylethylenediamine, imidazole-4-carboxylic and methylimidazole were purchased from Sigma-Aldrich (SA). Unless otherwise stated, all complexation reactions were performed under an inert atmosphere of argon. Tetramethylammonium chloride (97%) and tetramethylammonium hydroxide (10% solution in H₂O) were purchased from Sigma-Aldrich (SA). Analytical grade hydrochloric acid (1 N) was purchased from Merck (SA). All solvents were obtained from Merck Chemicals (SA) and were of reagent grade and used without further purification. Other reagent grade chemicals were also obtained from commercial sources and used as received. *N*-butyllithium (BuLi) (2.5 M, in hexane) was purchased from Sigma-Aldrich and stored at 4 °C. Anhydrous diethyl ether was prepared by addition of sodium wire. Aqueous hydrogen peroxide (30%) was obtained from Merck and stored at 4 °C.

2.2 Techniques and instrumentation

2.2.1 General instrumentation

The infrared spectra were recorded on either a Perkin Elmer 2000 FTIR spectrometer in the mid-IR range (4000 – 400 cm⁻¹) as KBr pellets or a Perkin Elmer 100 ATR-TIR (4000 – 650 cm⁻¹) as neat compounds. Melting points were determined using Galenkamp Melting point apparatus equipped with a thermometer (0 – 400 °C). ¹H and ¹³C NMR spectra of all ligands were recorded on a Bruker AMX 400 NMR MHz spectrometer and reported relative to tetramethylsilane (δ 0.00). Electronic spectra were recorded on either a Perkin Elmer Lambda 25 UV-V or Varian Cary 500 Scan UV-Vis spectrophotometer using 1 cm quartz cells. Microanalysis was carried out using a

Vario Elementar Microcube ELIII. Cyclic voltammetry was performed using a BAS CV 100 Cyclic Voltammogram. Potentiometric studies were performed using either a Metrohm 794 Titrino or a Metrohm 888 Titrando equipped with a Metrohm LL Ecotrode. The temperature of the jacketed vessel was maintained at 25 °C using a Thermo Scientific Haake water circulator. A Bio-Tek KC4 powerwave XS microtiter plate reader was used to measure absorbance for 3-(4,5-dimethylthiazol-2-yl)-2,5-diphenyl tetrazolium bromide (MTT) and Glucose assays.

2.2.2 Cyclic voltammetry

Cyclic voltammograms were recorded using a glassy carbon electrode as the working electrode, platinum wire as the counter electrode and silver chloride-coated silver wire as the reference electrode (when using DMF as the solvent) or a silver-silver chloride combination electrode (aqueous). Tetrabutylammonium perchlorate or potassium chloride was used as a supporting electrolyte. Argon was bubbled through the solutions for 5 minutes before each run. A scan rate of 100 mV.s⁻¹ was used.

2.2.3 Potentiometric studies

The protonation and stability constants for the ligands and oxovanadium(IV) complexes were determined by potentiometric titration of approximately 25 mL samples. All solutions were prepared using freshly boiled and degassed deionized milli-Q water to ensure the removal of dissolved oxygen and carbon dioxide. The ligand concentration was 1 mM and metal-to-ligand ratios of 1:1, 1:5 and 1:10 were used. Titrations were performed over the pH range of 2-11 under a continuous flow of purified nitrogen using HCl and tetramethylammonium hydroxide (TMAOH). The vanadium stock solution containing 0.10 M HCl was standardized by titration with permanganate. The ionic strength of the titration solutions was kept constant at 0.10 M tetramethylammonium chloride (TMACl). Titrations were controlled using Tiamo 2.0 software. The glass electrode was calibrated for a strong acid-base reaction by the Gran-method¹ using GLEE,² which allows one to determine the standard potential E° . The ionic product of water (pK_w) of 13.83(1) at 25.0±0.1 °C in 0.10 M TMACl was used in all calculations.³ The hydrolysis model of a

vanadyl system was included in the model; $[\text{VO}(\text{OH})]^+$ ($\log\beta_{1-1} = -5.94$), $[(\text{VO})_2(\text{OH})_2]^{2+}$ ($\log\beta_{2-2} = -6.95$), $[\text{VO}(\text{OH})_3]$ ($\log\beta_{1-3} = -18.0$)⁴ AND $[(\text{VO})_2(\text{OH})_5]$ ($\log\beta_{2-5} = -22.0$).⁵ Where relevant, the Davies equation was used when taking into consideration different ionic strengths.⁶ The concentration stability constants $\beta_{\text{pqr}} = [\text{M}_p\text{L}_q\text{H}_r]/[\text{M}]^p[\text{L}]^q[\text{H}]^r$ were calculated by using the computer program HYPERQUAD.⁷ The final values of the constants were obtained from an average of six independent titrations using an average of 400 data points in total for each refinement.

2.2.4 X-ray crystal structure resolution and refinement

Intensity data for $[\text{VO}(\text{pimin})_2]$ and $[\text{VO}_2(\text{pimin})(\text{piminH}')]^+$ (**Part 1, Chapter 3**) were collected on a Bruker APEX II CCD area detector diffractometer with graphite monochromated Mo K_α radiation (50 kV, 30 mA) using the APEX 2 data collection software.⁸ The collection method involved ω -scans of width 0.5° and 512x512 bit data frames. Data reduction was carried out using the program SAINT⁹ and absorption corrections were made using the program SADABS.⁹

The crystal structures were solved by direct methods using SHELXTL.¹⁰ Non-hydrogen atoms were first refined isotropically followed by anisotropic refinement by full matrix least-squares calculations based on F^2 using SHELXTL. Hydrogen atoms were first located in the difference map then positioned geometrically and allowed to ride on their respective parent atoms. Diagrams and publication material were generated using SHELXTL, PLATON¹¹ and ORTEP-3.¹²

2.2.5 Biological studies

(a) Maintenance of cells lines

3T3-L1 preadipocytes, were maintained in Dulbecco's modified eagle medium (DMEM) supplemented with 10% fetal bovine serum (FBS), while C2C12 mouse skeletal myoblasts and Chang liver cells were maintained in RPMI-1640 medium (Sigma) supplemented with 10% FBS. These were incubated at 37°C in a humidified incubator with 5% CO_2 . Cells were subcultured at 70% confluence and seeded at a density of 35 000 cells.mL⁻¹ (for 3T3-L1) and 25 000 cells.mL⁻¹ (for Chang and C2C12) in 24-well culture plates.

(b) MTT Cytotoxicity studies

Cells were seeded in 24 well plates (Nunc) at densities of 25 000 cells.mL⁻¹ for C2C12 and Chang liver cells, and 35 000 cells.mL⁻¹ for 3T3-L1. After overnight attachment, the culture medium was replaced with medium containing the test compounds at a range of concentrations (0.5-100 µM). Cells were incubated for 24 hours at 37 °C after which the MTT (Sigma) assay was performed.¹³

(c) Glucose uptake studies

The glucose uptake assay was performed using the GLUCOSE (Glu-cinet) kit (BAUER).¹⁴ Control cells were represented by untreated differentiated fat (3T3-L1), liver (Chang) and muscle (C2C12) cells (Con) incubated in culture media. Positive control cells (Met) were represented by untreated differentiated fat, liver and muscle cells exposed to metformin. Cells were then exposed for 48 hours to the test compounds. Thereafter glucose uptake was determined and the cell number was normalized using the MTT assay.¹³

(d) Anticoagulation studies

The effect of the various vanadium compounds on blood coagulation was investigated using a CL Coagulation Analyzer (Beckman). The assays used were the HemosIL[®] activated partial thromboplastin time (APTT), prothromin time (PT), Fibrinogen (Fib)-C, and D-Dimer as per the instructions which can be found on the manufacturers website.¹⁵ The APTT assays were performed by adding the test compounds, positive control or diluent, and APTT reagent to plasma. This was incubated for 3 minutes at 37 °C followed by addition of CaCl₂ to initiate coagulation. PT was performed by incubating PT reagent and treatments followed by the addition of plasma. Fib-C was performed by treating diluted plasma [1:4 (v/v)], incubating, and adding bovine thrombin. D-Dimer was performed by adding treatments and reaction buffer to plasma, hereafter D-Dimer latex reagent was added, the vial was mixed 1-2 times and the agglutination measured. Vanadium compounds were used at 10 µM for screening assays and 0.01 µM, 0.1 µM, and 10 µM for concentration dependence studies, positive control was heparin at 0.1 U.mL⁻¹.

(e) Statistical Analysis

Error bars indicate the standard error of the mean (SEM) unless specified otherwise ($n = 3$). The two-tail paired test was used to determine significance of results ($p < 0.05$) and ($p < 0.01$).

2.3 References

- (1) Gran, G. *Analyst* **1952**, *77*, 661.
- (3) Gans, P.; O'Sullivan, B. *Talanta* **2000**, *51*, 33.
- (3) Bazzicalupi, C.; Bencini, A.; Bianchi, A.; Danesi, A.; Giorgi, C.; Valtancoli, B. *Inorg. Chem.* **2009**, *48*, 2391.
- (4) Henry, R. P.; Mitchell, P. C. H.; Prue, J. E. *J. Chem. Soc., Dalton Trans.* **1973**, 1156.
- (5) Komura, A., Hayashi, H., Imanaga, H. *Bull. Chem. Soc. Jpn.* **1977**, *50*, 2927.
- (6) Davies, C. W.; *J. Chem. Soc.* 1938, 397, 2093.
- (7) Gans, P.; Sabatini, A.; Vacca, A. *Talanta* **1996**, *43*, 1739.
- (8) Bruker (2005a). APEX2. Version 2.0-1. Bruker AXS Inc., M., Wisconsin, USA.
- (9) Bruker (2005b). SAINT-NT. Version 6.0. (includes XPREP and SADABS) Bruker AXS Inc., M., Wisconsin, USA.
- (10) Bruker (1999). SHELXTL. Version 5.1. (includes XS, X., XP, XSHELL) Bruker AXS Inc., Madison, Wisconsin, USA.
- (11) Spek, A. L. *J. Appl. Crystallogr.* **2003**, *36*, 7.
- (12) Farrugia, L. J. *J. Appl. Crystallogr.* **1997**, *30*, 565.
- (13) Mossman, T. *J. Immunol. Met.* **1983**, *65*, 55.
- (14) Keston, A. S. In 129th Meeting American Chemistry Society 1956, p 31c.
- (15) APTT Testing. [http://www.instrumentationlaboratory.com/benelux/products services/Hemostasis diagnostics/reagents/general screening and anticoagulant monitoring.aspx](http://www.instrumentationlaboratory.com/benelux/products/services/Hemostasis%20diagnostics/reagents/general%20screening%20and%20anticoagulant%20monitoring.aspx).

This page has been left blank intentionally

Chapter 3

Oxovanadium(IV) complexes with 2-(2'-hydroxyphenyl)-1*R*-imidazoline ligands

3.1 Introduction

There have been several studies concerning the preparation and characterization of oxovanadium(IV) complexes with ligands containing N,O-donor atoms.¹⁻⁶ Many of these complexes have proven to be effective insulin-enhancers. The oxovanadium(IV)-picolinate complex, VO(pic)₂, probably the most successful of the lot, was capable of inhibiting free fatty acid release as well as lowering glucose levels.¹

The 2-(2'-hydroxyphenyl)-1*R*-imidazoline ligands prepared in this study are structurally related to the naturally occurring 2-(2'-hydroxyphenyl)-2-oxazoline and thiazoline ligating moieties found in siderophores – a class of microbial iron chelators.^{7,8} In terms of hard and soft acid base theory (HSAB), oxovanadium(IV) being a hard acid, should form a stable complex with the relatively hard phenol oxygen and imidazoline nitrogen bases. Furthermore, with the phenol group deprotonated each ligand holds a -1 charge. Thus, upon reaction of two of these ligands with vanadyl (VO²⁺), a neutral complex forms – a prerequisite for effective metallopharmaceuticals.⁹ The imidazoline moiety is also structurally similar to imidazole, a chemical functionality abundant in biological systems. Imidazole forms part of the side chain of the amino acid histidine and commonly plays a role in metal coordination in metalloenzymes.^{10,11} As shown in **figure 3.1**, the proposed binding modes for the binary vanadyl-apoTf species involve coordination of a proximal phenol group from a tyrosine residue (TYR92) and an imidazole group from a histidine residue (HIS253). The resultant ligation is thus quite similar to that of the 2-(2'-hydroxyphenyl)-1*R*-imidazoline ligand.

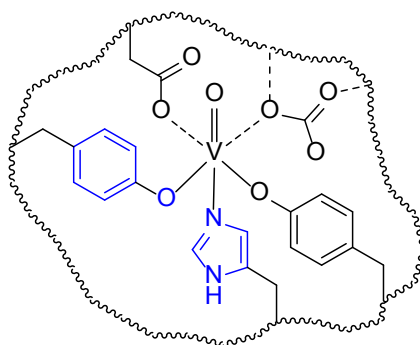


Figure 3.1 The proposed coordination environment of the vanadyl-transferrin binary complex

Other than stable complex formation, another important property to consider when designing metallopharmaceuticals includes imparting an optimal lipophilicity/hydrophilicity balance, such that the complexes while being water soluble, may still be sufficiently lipophilic to cross cell membranes.⁹ The ethyl substituted complex *bis*(ethylmaltolato)oxovanadium(IV), for example, demonstrated improved lipophilicity as well as hydrolytic stability, and as such this compound rather than the methyl derivative, *bis*(maltolato)oxovanadium(IV), was taken to clinical trials.¹²

Beyond optimizing the physico-chemical properties of the complexes, it may be beneficial to consider using ligands which exhibit certain therapeutic effects. This is by no means a novel idea.^{13,14} Vanadyl-biguanide complexes have been prepared and tested for antidiabetic activity and while there were no positive associative effects observed in this study, the possibility for using therapeutic ligands remains an exciting option.¹³ In this regard, several imidazole-containing compounds have in fact been shown to exhibit antihyperglycemic activity.¹⁵⁻¹⁸ The exact mechanism of action remains debatable; however they are thought to act either by α_2 -adrenoreceptor activation or via activation of I₁ imidazole receptors.¹⁵ While this is undoubtedly interesting, it should be noted that the antidiabetic activity of the ligands themselves is beyond the focus of this study but could be examined in the future.

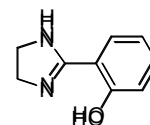
In this chapter, the synthesis and characterization of a small series of oxovanadium(IV) complexes with 2-(2'-hydroxyphenyl)imidazole, 2-(2'-hydroxyphenyl)-ethylimidazole and 2-(2'-hydroxyphenyl)-1-ethanolimidazole as coordinating ligands is presented. The protonation constants of 2-(2'-hydroxyphenyl)-ethylimidazole and 2-(2'-hydroxyphenyl)-1-ethanolimidazole

as well as the stability constants of these with oxovanadium(IV) were determined using glass electrode potentiometry. This gives an indication as to whether the complexes would stabilize vanadyl across a biological pH range. The anticoagulatory effect was evaluated by a range of assays while the antidiabetic potential of these complexes was assessed via an *in vitro* assay using 3T3-L1 adipocytes, C2C12 muscle cells and Chang liver cells.

3.2 Preparative work

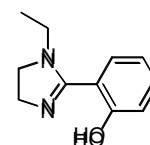
3.2.1 2-(2'-hydroxyphenyl)-1H-imidazole (piminH).

Methyl salicylate (1.84 g, 0.012 mol) was added to an excess of ethylenediamine (3.2 g, 0.053 mol) in a conical flask and heated in a microwave for 7 minutes at 180 W. Excess ethylenediamine was distilled off under reduced pressure until a solid material was left behind. This solid was then digested overnight in chloroform, filtered and then washed with cold chloroform to afford a cream solid. Yield: 78.1%. ^1H NMR (δ , 400 MHz, $\text{DMSO-}d_6$): 3.71 (s, 4H, Im- CH_2), 6.69 (t, 1H, Ar-H) 6.77 (d, 1H, Ar-H), 7.27 (t, 1H, Ar-H), 7.56 (d, 1H, Ar-H). ^{13}C NMR (δ , 100 MHz, $\text{DMSO-}d_6$): 46.5, 110.2, 115.5, 118.4, 127.2, 132.7, 163.5, 166.1; IR (cm^{-1} , KBr disk): 3217, $\nu(\text{N-H})$; 1618, $\nu(\text{C=N})$. *Anal.* Calcd (Found) for $\text{C}_9\text{H}_{10}\text{N}_2\text{O}$ (%): C, 66.65 (66.68); H, 6.21 (6.20); N, 17.27 (16.98).



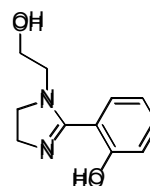
3.2.2 2-(2'-hydroxyphenyl)-1-ethylimidazole (EtpiminH).

This was prepared in a similar manner as above (3.2.1) except that *N*-ethylethylenediamine was used. Yield: 50.3%. ^1H NMR (δ , 400 MHz, CDCl_3): 1.26 (t, 3H, $\text{N-CH}_2\text{CH}_3$), 3.39-3.44 (q, 2H, N-CH_2), 3.48-3.53 (t, 2H, Im- CH_2), 3.89-3.94 (t, 2H, Im- CH_2), 6.76 (t, 1H, Ar-H), 6.98 (d, 1H, Ar-H), 7.27 (t, 1H, Ar-H), 7.36 (t, 1H, Ar-H). ^{13}C NMR (δ , 100 MHz, CDCl_3): 14.48, 45.52, 50.47, 50.92, 112.31, 117.11, 118.66, 127.31, 132.16, 162.19, 167.09. IR (cm^{-1} , KBr disk): 1608, $\nu(\text{C=N})$; *Anal.* Calcd (Found) for $\text{C}_{11}\text{H}_{14}\text{N}_2\text{O}$ (%): C, 69.45 (69.54); H, 7.42 (7.67); N, 14.73 (14.44).



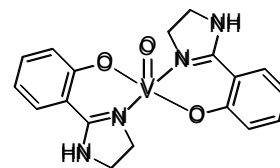
3.2.3 2-(2'-hydroxyphenyl)-1-ethanolimidazole (EtOHpiminH).

This was prepared in a similar manner as for piminH above (3.2.1), except that *N*-ethanoethylenediamine was used. Yield: 54.1%. ^1H NMR (δ , 400 MHz, D_2O): 3.56-3.59 (t, 2H, N-CH_2), 3.78-3.81 (t, 2H, $\text{N-CH}_2\text{CH}_2$), 4.03-4.19 (m, 4H, Im- CH_2), 6.67-6.71 (t, 1H, Ar-H), 6.75-6.77 (d, 1H, Ar-H), 7.26-7.28(d, 1H, Ar-H), 7.40-7.45 (t, 1H, Ar-H). ^{13}C NMR (δ , 100 MHz, D_2O): 43.13, 49.15, 49.19, 58.18, 112.21, 114.18, 121.81, 130.19, 134.93, 166.02, 169.49. IR (cm^{-1} , KBr disk): 3138 $\nu(\text{O-H})$; 1612, $\nu(\text{C=N})$. *Anal.* Calcd (Found) for $\text{C}_{11}\text{H}_{14}\text{N}_2\text{O}_2$ (%): C, 64.06 (64.31); H, 6.84 (6.55); N, 13.58 (13.44).



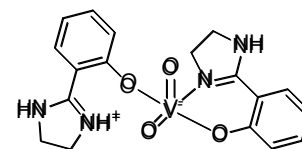
3.2.4 [VO(pimin)₂]

To a solution of piminH (0.25 g, 1.5 mmol) in methanol (5 mL) was added vanadyl sulfate (0.152 g, 0.70 mmol) in water (5 mL). A blue-green precipitate formed immediately. The reaction was allowed to proceed for a further 2 hours. The precipitate was collected, washed with water, then methanol and dried at 100 °C. Yield: 56.9%. IR (cm⁻¹, KBr disk): 944, ν(V=O); 3260, ν(N-H); 1609, ν(C=N). *Anal.* Calcd (Found) for C₁₈H₁₈N₄O₃V (%): C, 55.53 (55.43); H, 4.66 (4.74); N, 14.39 (14.16). UV/Vis (DMSO) λ_{max} (ε, M⁻¹cm⁻¹): 617 (55), 542 (44), 403sh (196).



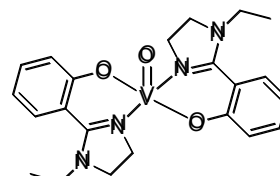
3.2.5 [VO₂(pimin)(piminH⁺)]

Upon standing the synthetic mother liquor of [VO(pimin)₂] at room temperature and under aerobic conditions, yellow crystals of [VO₂(pimin)(piminH⁺)] were obtained. Yield wrt V: 12.3%. IR (cm⁻¹, KBr disk): 913, 882, ν(V=O); 3346, ν(N-H); 1617, ν(C=N). *Anal.* Calcd (Found) for C₁₈H₁₉N₄O₄V (%): C, 53.21 (53.14); H, 4.71 (4.71); N, 13.79 (13.82).



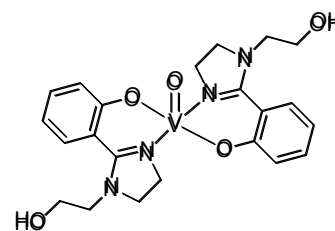
3.2.6 [VO(Etpimin)₂]

This was prepared in a similar manner as for [VO(pimin)₂] above except that EtpiminH was used. Yield: 47.6%. IR (cm⁻¹, KBr disk): 987, ν(V=O); 1602, ν(C=N). *Anal.* Calcd (Found) for C₂₂H₂₆N₄O₃V (%): C, 59.32 (59.04); H, 5.88 (5.88); N, 12.58 (12.27). UV/Vis (DMSO) λ_{max} (ε, M⁻¹cm⁻¹): 621 (120), 547 (99), 401sh (300).



3.2.7 [VO(EtOHpimin)₂]

This was prepared in a similar manner as for [VO(pimin)₂] except that EtOHpiminH was used. Yield: 52%. IR (cm⁻¹, KBr disk): 966, ν(V=O); 1603, ν(C=N). *Anal.* Calcd (Found) for C₂₂H₂₆N₄O₅V (%): C, 55.35 (55.30); H, 5.49 (5.63); N, 11.74 (11.66). UV/Vis (DMSO) λ_{max} (ε, M⁻¹cm⁻¹): 625 (84), 548 (66), 404sh (269).



3.3 Results and discussion

3.3.1 Synthesis and general considerations

The ligands were synthesized according to a modified method by Parik *et al.*¹⁹ with the main exception being the use of a conventional household microwave. The use of a microwave allowed us to reduce the reaction time from 11 hours to 7 mins, whilst increasing the yield from 50.3 to 78.1% for piminH. The 2-(2'-hydroxyphenyl)-1-ethylimidazoline (EtpiminH) and 2-(2'-hydroxyphenyl)-1-ethanolimidazoline (EtOHpiminH) ligands were prepared by substituting ethylenediamine with *N*-ethylethylenediamine and *N*-ethanolethylenediamine, respectively. The goal of including the ethyl and ethanol substituents, was to obtain a small range of compounds with different lipo/hydrophilicity, since a delicate balance is required for optimal absorption of these metallopharmaceuticals.²⁰

NMR spectroscopy was used as the primary tool to confirm the successful preparation of the ligands. In all ¹H NMR spectra, four peaks corresponding to the aromatic di-substituted benzene ring were found between 6.5 and 7.6 ppm. Of these four peaks, two were split into doublets and the remaining two into triplets (**figure 3.2**). This corresponds to the substitution pattern of the benzene ring (i.e. the two triplets corresponding to the protons at the 4 and 5 position of the benzene ring and the doublets corresponding to the protons at the 3 and 6 position). The methylene protons of the alkyl substituent's (EtpiminH and EtOHpiminH) as well as the methylene protons from the imidazoline ring, appear upfield from the aromatic region as expected. For piminH, the imidazoline CH₂s appear as a broad singlet, however substitution at the N-H position with either an ethyl or ethanol group, alters the chemical environment of the imidazoline CH₂s and thus separates these signals as shown for EtpiminH in **figure 3.2**. The ¹³C NMR spectrum shown in **figure 3.3** further confirmed the structure with all the expected carbon signals being accounted for. NMR analysis of the complexes was not performed due to the paramagnetic nature of d¹ VO(IV) metal ion.

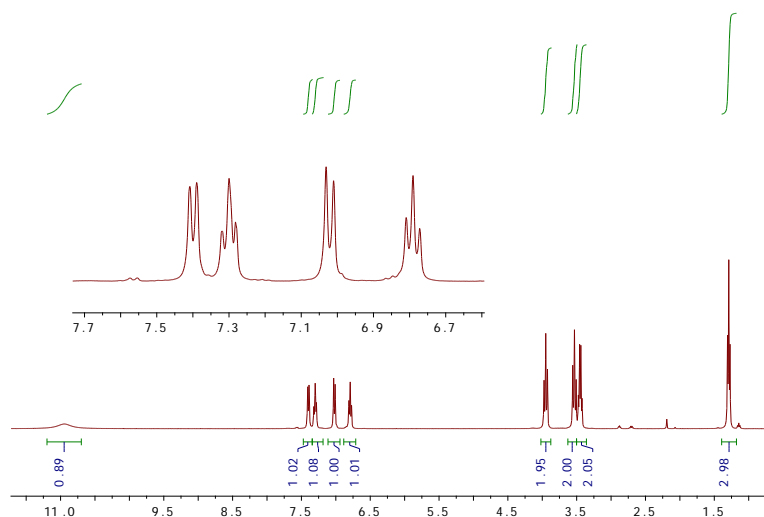


Figure 3.2 ^1H NMR spectrum of 2-(2'-hydroxyphenyl)-1-ethylimidazole (δ ppm). The insert shows an expanded view of the aromatic region

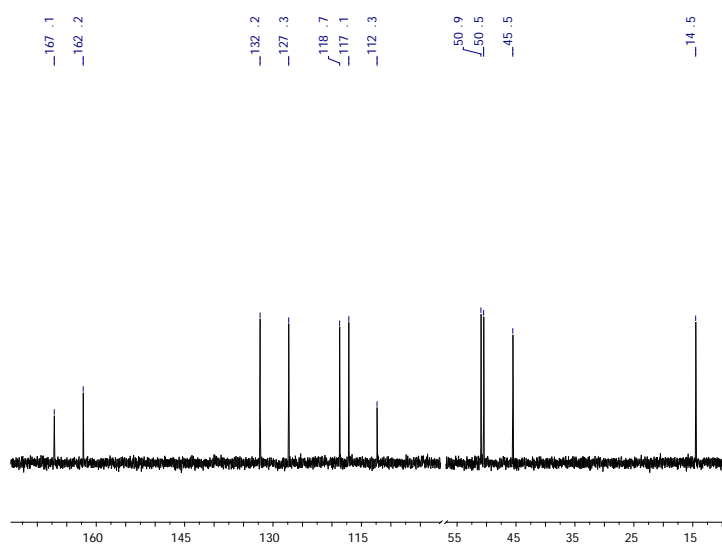
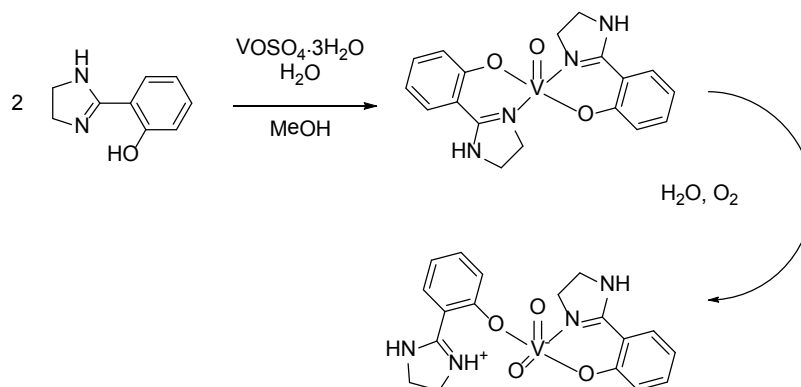


Figure 3.3 ^{13}C NMR spectrum of 2-(2'-hydroxyphenyl)-1-ethylimidazole (δ ppm). Solvent peak (CDCl_3) has been omitted

The oxovanadium(IV) complexes were synthesized by addition of an aqueous vanadyl sulfate solution to a methanolic solution of the corresponding ligand in a 1:2 (metal:ligand) molar ratio (**scheme 3.1**), under an argon atmosphere. The complexes which precipitated out of solution were easily collected by filtration. All of these complexes were soluble in various alcohols, DMF and DMSO. Both $[\text{VO}(\text{Etpimin})_2]$ and $[\text{VO}(\text{EtOHpimin})_2]$ were soluble in dichloromethane,

acetonitrile and slightly soluble in water. Upon standing the mother liquor of $[\text{VO}(\text{pimin})_2]$ in open air at room temperature, the colour of the solution changed from green (symbolic of V^{4+} in this case) to a yellow-green (possibly a mixture of V^{4+} and V^{5+}), due to hydrolysis and concurrent autooxidation. After a few days, yellow crystals deposited and were collected, filtered and dried. The yellow crystals were later identified as the dioxovanadium(V) species by single crystal X-ray crystallography.

This facile autooxidation incited us to study the oxidation potentials of these complexes which was carried out using cyclic voltammetry. The cyclic voltammograms are shown in **figure 3.4**. All of the complexes display irreversible $\text{V}^{4+} - \text{V}^{5+}$ oxidation peaks between 400 – 490 mV. The E_{pa} for $[\text{VO}(\text{pimin})_2]$, $[\text{VO}(\text{Etpimin})_2]$ and $[\text{VO}(\text{EtOHpimin})_2]$ appeared at 490, 440 and 400 mV, respectively. These low oxidation potentials correspond well to the observed facile autooxidation upon exposure to air.



Scheme 3.1 Preparation of $[\text{VO}(\text{pimin})_2]$ and $[\text{VO}_2(\text{pimin})(\text{piminH}^{\prime})]$. The other oxovanadium(IV) complexes were prepared in a similar fashion

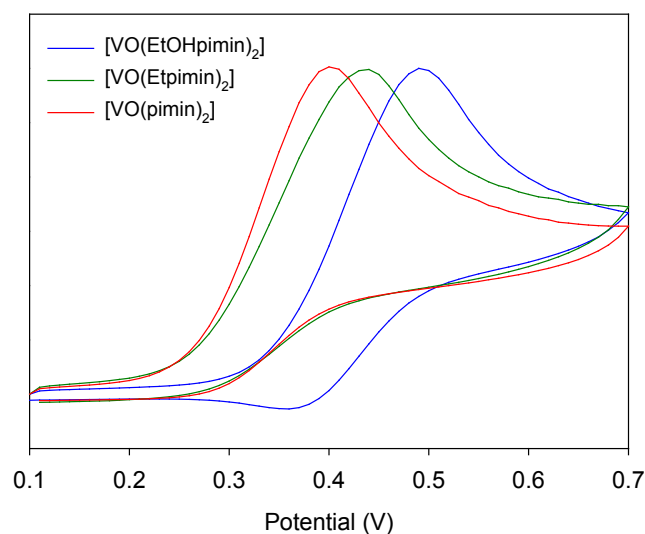


Figure 3.4 Cyclic voltammograms of complexes $[\text{VO}(\text{pimin})_2]$, $[\text{VO}(\text{Etpimin})_2]$ and $[\text{VO}(\text{EtOHpimin})_2]$ in DMSO

All of the ligands display infrared stretching frequencies between 1618 to 1608 cm^{-1} which can be assigned to the azomethine (C=N) stretch.^{19,21} The $\nu(\text{N-H})$ of piminH appears at 3346 cm^{-1} , and the alcohol stretch for EtOHpimin appears at 3125 cm^{-1} , the position of the latter band indicating strong intramolecular hydrogen bonding.²² Coordination to oxovanadium(IV) was evident from a $\sim 9\text{ cm}^{-1}$ shift of the (C=N) stretch to lower frequencies.²³ The uncoordinated ligands show phenolic $\nu(\text{C-O})$ stretches between 1287 - 1269 cm^{-1} which upon coordination shift to a higher wavelength of 1313 - 1319 cm^{-1} .²⁴ This suggested that coordination was likely taking place via the azomethine nitrogen and the phenolate group in a bidentate fashion. Furthermore, the $\nu(\text{V=O})$ bands appear at 941 , 987 and 965 cm^{-1} for $[\text{VO}(\text{pimin})_2]$, $[\text{VO}(\text{Etpimin})_2]$ and $[\text{VO}(\text{EtOHpimin})_2]$ respectively, and are within the reported range for V=O stretches of 930 - 1030 cm^{-1} .²⁵ For the dioxovanadium(V) complex $[\text{VO}_2(\text{pimin})(\text{piminH}^+)]$, two $\nu(\text{V=O})$ bands appear at 913 and 881 cm^{-1} . The higher energy band is assigned to the ν_{as} stretch and the lower energy band is assigned to the ν_{s} stretch of the *cis*- VO_2^+ moiety.²⁶ The IR spectra of the oxovanadium(IV) complexes are shown in **figure 3.5**.

In general, square-pyramidal oxovanadium(IV) complexes display three low intensity d-d transitions in the range of 330 - 1000 nm .²⁷ The high energy transition, ($a_1 \leftarrow b_2$), occurs between

401 - 404 cm^{-1} ($\varepsilon = 196 - 300$), while the ($b_1 \leftarrow b_2$) and ($e_\pi \leftarrow b_2$) transitions fall in the range 538-545 cm^{-1} and 617 - 625 cm^{-1} . As shown in **figure 3.6** for $[\text{VO}(\text{pimin})_2]$, the higher energy transition is much more intense as it appears as a shoulder to the charge transfer band.

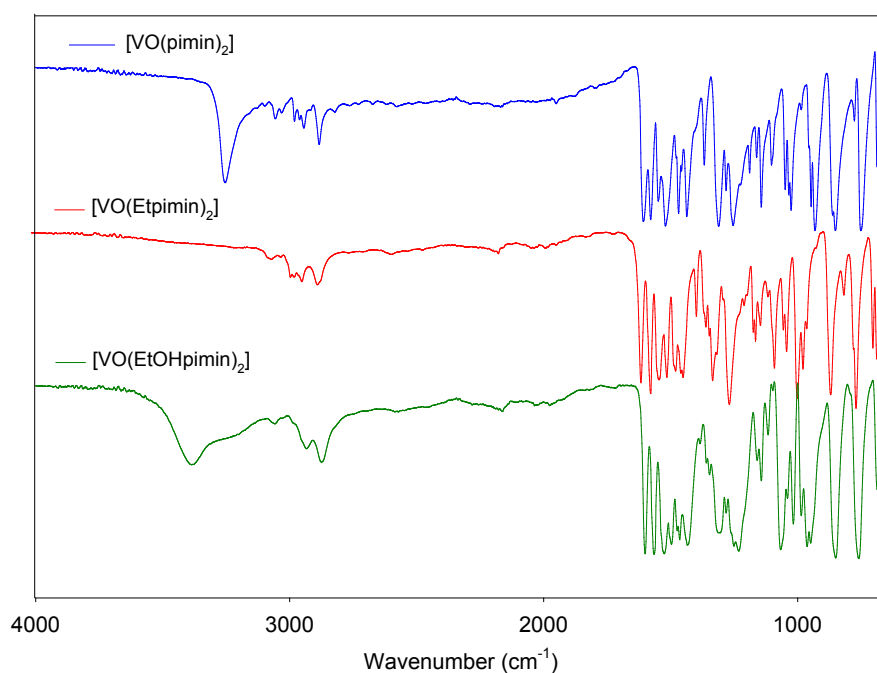


Figure 3.5 Stacked IR spectra of $[\text{VO}(\text{pimin})_2]$, $[\text{VO}(\text{Etpimin})_2]$ and $[\text{VO}(\text{EtOHpimin})_2]$, in the range 4000 – 650 cm^{-1}

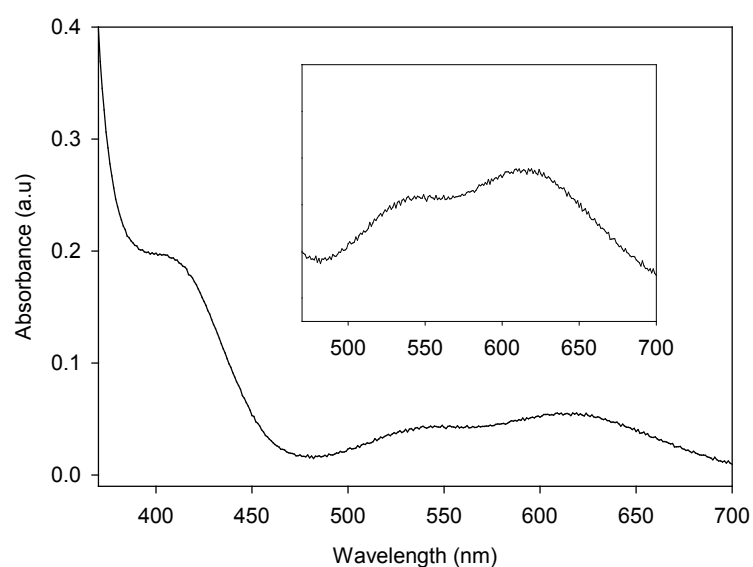


Figure 3.6 Electronic spectrum of $[\text{VO}(\text{pimin})_2]$, in DMSO. Insert shows an expanded view of the region between 450-700 nm

After several attempts blue-green crystals of [VO(pimin)₂] suitable for X-ray crystallography were obtained upon recrystallization of the compound in acetonitrile at -20 °C. If heating or sonication was used to assist dissolution of the compound, the solution rapidly turned yellow indicating oxidation had taken place. The yellow crystals of [VO₂(pimin)(piminH')] were obtained after standing a methanolic mother liquor of [VO(pimin)₂] at room temperature for 2-4 days. The ORTEP diagrams for the structures of [VO(pimin)₂] and [VO₂(pimin)(piminH')] are represented by **figures 3.7 and figure 3.8** respectively. The bond lengths and angles are presented in **table 3.1** and other selected crystallographic data in **table 3.2**.

For [VO(pimin)₂], the V=O bond length of 1.619(2) Å is slightly longer than those observed for similar compounds, which fall in the range of 1.591-1.605 Å.^{3,6} The geometry of [VO(pimin)₂] ($\tau = 0.49$)²⁸ falls between trigonal bipyramidal ($\tau = 1$) and square pyramidal ($\tau = 0$) and sits on a crystallographic two-fold axis. Vanadium is situated 0.550 Å above the plane defined by the N₂O₂ ligand donor atoms and the N(1)-V(1)-O(2) and O(1)-V(1)-O(2) angles are 99.12(6) and 113.92(6)° respectively. The N(1)-V(1)-N(1) and O(1)-V(1)-O(1) angles in the equatorial plane are 161.8(1) and 132.2(1)° respectively, showing marked deviations from an ideal of 180° expected for a square pyramidal geometry.

The bidentate ligand coordinates through the neutral imidazoline nitrogen and phenolate oxygen resulting in the formation of the neutral *bis*[(imidazolyl)phenolato]oxovanadium(IV) complex. The average bite angle of the ligands is 86.32(8)°. The V(1)-O(1) and V(1)-N(1) bond lengths have averages of 1.911(1) and 2.048(2) Å respectively. The imidazoline and phenyl rings are not coplanar, and have an average dihedral angle of 20.11° between them. As expected, the imidazoline ring is not planar with the torsion angles C(9)-C(8)-N(1)-C(7)=13.4(3)° and C(8)-C(9)-N(2)-C(7)=16.9(3)°.

The five-coordinate dioxovanadium(V) complex, [VO₂(pimin)(piminH')] adopts a highly distorted trigonal bipyramidal geometry ($\tau = 0.59$) with O(1), O(3) and O(4) forming the trigonal plane. The deviations in this plane are given by O(1)-V(1)-O(3)=128.05(9)°, O(1)-V(1)-O(4)=123.40(9)° and O(3)-V(1)-O(4)=108.3(1)°. The N(1)-V(1)-O(2) at 159.02(8)° is also far from the ideal of 180°.

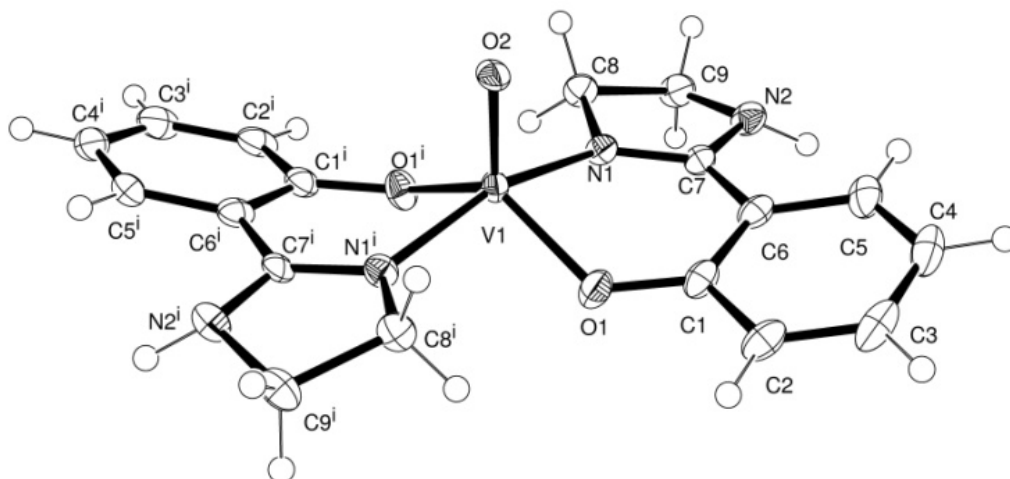


Figure 3.7 ORTEP diagram of $[\text{VO}(\text{pimin})_2]$, showing 50% thermal probability ellipsoids

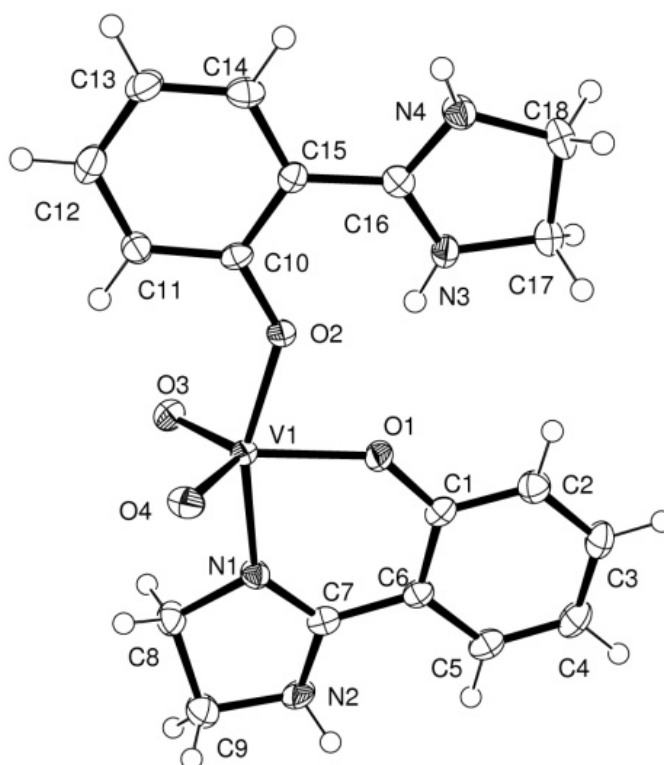


Figure 3.8 ORTEP diagram of $[\text{VO}(\text{pimin})(\text{piminH}')]$, showing 50% thermal probability ellipsoids

The V(1)-O(3) and V(1)-O(4) at 1.617(1) and 1.648(1) Å are within the lengths expected for a five-coordinate dioxovanadium(V) system.²⁶ One of the ligands attaches to the dioxovanadium(V) center in a monodentate fashion through the phenolate oxygen while the other ligand attaches in a bidentate manner through the imidazoline nitrogen (N1) and phenolate oxygen (O1) with a bite angle of 81.56(8)°. The imidazoline nitrogen (N3) of the mono-coordinated ligand is protonated to afford a positively charged species which neutralizes the extra negative charge resulting from the two phenolate oxygens and the two dioxo ligands, and the vanadium(V) center.

Table 3.1 Selected bond lengths (Å) and angles (°) for [VO(pimin)₂] and [VO₂(pimin)(piminH⁺)]

[VO(pimin)₂]		[VO₂(pimin)(piminH⁺)]	
V(1)-O(2)	1.619(2)	V(1)-O(3)	1.617(1)
V(1)-O(1)	1.911(1)	V(1)-O(4)	1.648(1)
V(1)-N(1)	2.048(2)	V(1)-O(1)	1.949(1)
O(1)-V(1)-O(1)	132.2(1)	V(1)-O(2)	1.932(1)
N(1)-V(1)-N(1)	161.8(1)	V(1)-N(1)	2.062(2)
O(1)-V(1)-O(2)	113.91(6)	O(3)-V(1)-O(4)	108.3(1)
N(1)-V(1)-O(2)	99.12(6)	O(1)-V(1)-O(3)	128.08(9)
N(1)-V(1)-O(1)	86.26(8)	O(1)-V(1)-O(4)	123.40(9)
N(1)-V(1)-O(1) ⁱ	86.37(8)	N(1)-V(1)-O(2)	159.07(8)

Table 3.2 Selected crystallographic data for [VO(pimin)₂] and [VO₂(pimin)(piminH⁺)]

Compound	[VO(pimin) ₂]	[VO ₂ (pimin)(piminH ⁺)]
empirical formula	C ₁₈ H ₁₈ N ₄ O ₃ V	C ₁₈ H ₁₉ N ₄ O ₄ V
formula weight	389.30	406.32
crystal color	Blue-green	Yellow
crystal system	Orthorhombic	Monoclinic
space group	<i>Fdd2</i>	<i>P2₁/c</i>
temperature	173(2) K	173(2) K
<i>a</i> , Å	12.4698(7)	8.9544(8)
<i>b</i> , Å	36.810(2)	22.6383(19)
<i>c</i> , Å	7.3123(4)	8.6648(7)
α , deg	90	90
β , deg	90	90.736(2)
γ , deg	90	90
<i>V</i> , Å ³	3356.5(3)	1756.3(3)
<i>Z</i>	8	4
ρ_{calc} , g/cm ³	1.541	1.537
wavelength, Å	0.71073	0.71073
total reflections	4875	12519
unique reflections	1827	4234
<i>R</i>	0.0384	0.0501
<i>R_w</i>	0.0735	0.0962

3.3.2 pH-Metric chemical speciation

As has been discussed, it is important to gain an understanding of the aqueous speciation of metallopharmaceuticals to predict what species may exist over a biological pH range. The stability

constants of the metal-ligand complexes may give further indication of the type of binding that might take place between the complexes and other bioligands, for example the formation of ternary complexes. Thus, in the context of V(IV) complexes, pH stability may provide a good indication of biological efficacy.

The protonation constants of EtpiminH and EtOHpiminH were determined using aqueous potentiometric titrations, from an average of six independent titrations. Solution studies with the ligand piminH were precluded due to the low water solubility of this ligand. The stability constants for the VO(IV) – EtpiminH and EtOHpiminH (VO:L ratio's of 1:1, 1:2, 1:5 and 1:10) systems were determined from an average of six titrations and are summarized in **table 3.3**. For the metal:ligand speciation, the best fitting experimental curves were obtained using higher metal-to-ligand ratios. At 1:5 and 1:10 metal-to-ligand ratios no precipitation occurred in the pH range examined. For the 1:1 ratio, only the first binding constants could be calculated. The species distribution diagrams were generated using the program HySS2009,²⁹ by inclusion of protonation, stability and hydrolysis constants.

Both EtpiminH and EtOHpiminH are basic ligands with p*K* values of 7.52 and 7.33, and 11.26 and 11.09 for the imidazoline nitrogen and phenolate oxygen, respectively. The relevant protonation reactions are shown in **scheme 3.2** and species distribution diagrams for EtpiminH and EtOHpiminH are shown in **figure 3.9** and **figure 3.10**, respectively, both being relatively similar. Under acidic conditions (pH < 4), the ligands remain fully protonated (both the imidazoline nitrogen as well as the phenolate oxygen). As the pH increases (pH > 4), the imidazoline nitrogen is deprotonated followed by deprotonation of the phenolate oxygen. Thus it is only at relatively high pH values that the ligand appears fully deprotonated. These p*K*_a values were slightly higher (more basic) than the structurally similar, fully aromatized derivative, 2-(2'-hydroxyphenyl)imidazole, which had reported p*K*_a values of 6.5 (imidazole protonation) and 9.25 (phenolate protonation).³⁰ Benzimidazole has a known p*K*_a of around 5.41³¹ and imidazole around 6.95.³² Thus one can see that the p*K*_a values are largely related to the extent of delocalization of the π-electron density on these rings. It is therefore no surprise that the non-conjugated imidazoline ligands have slightly higher first protonation values than the imidazoles.

As a consequence of the ligand basicity, coordination to vanadyl begins at relatively higher pH values making way for hydrolysis at a low pH ($3 < \text{pH} < 5$). However, as the pH increases a single fully deprotonated ligand binds ($3.5 < \text{pH} < 7$), followed by a second fully deprotonated ligand ($\text{pH} > 5$) to form a neutral complex which is stable at a relatively high pH (**scheme 3.3**). The binary hydroxyl species $[(\text{VO})_2(\text{OH})_5]^-$ and $[\text{VO}(\text{OH})_3]^-$ did not fit within the model and no hydrolysis was detected up to a pH of 9. The overall stability constants for these VO-ligand systems are high at 17.13(3) and 16.66(3) for VO-EtpiminH (**figure 3.11**) and VO-EtOHpiminH (**figure 3.12**) systems, respectively. Both systems (VO-EtpiminH and VO-EtOHpiminH) show good overall stability, but are however, subject to hydrolysis at acidic pH values due to the basic nature of the ligands.

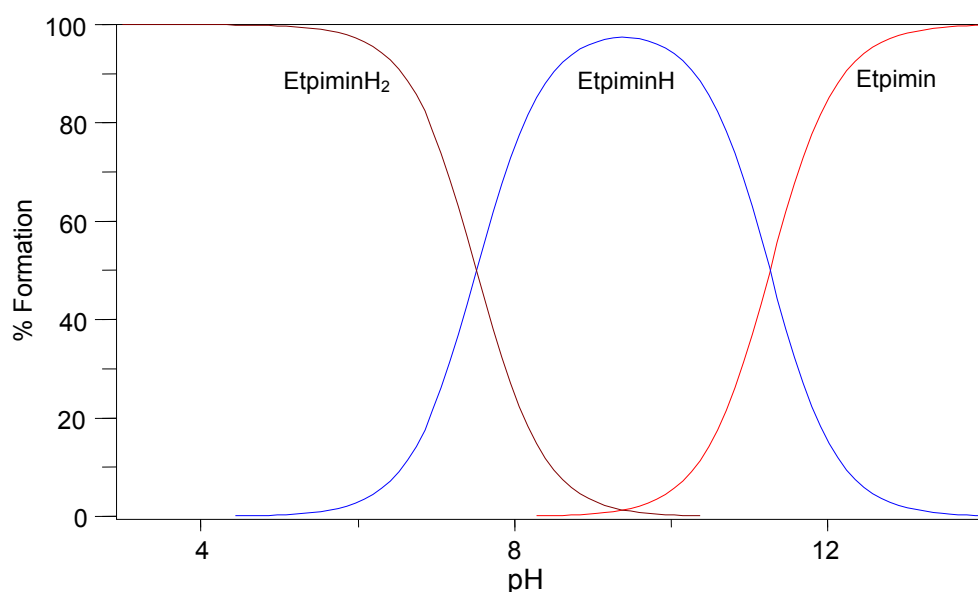


Figure 3.9 Species distribution as a function of pH for 2-(2'-hydroxyphenyl)-1-ethylimidazoline

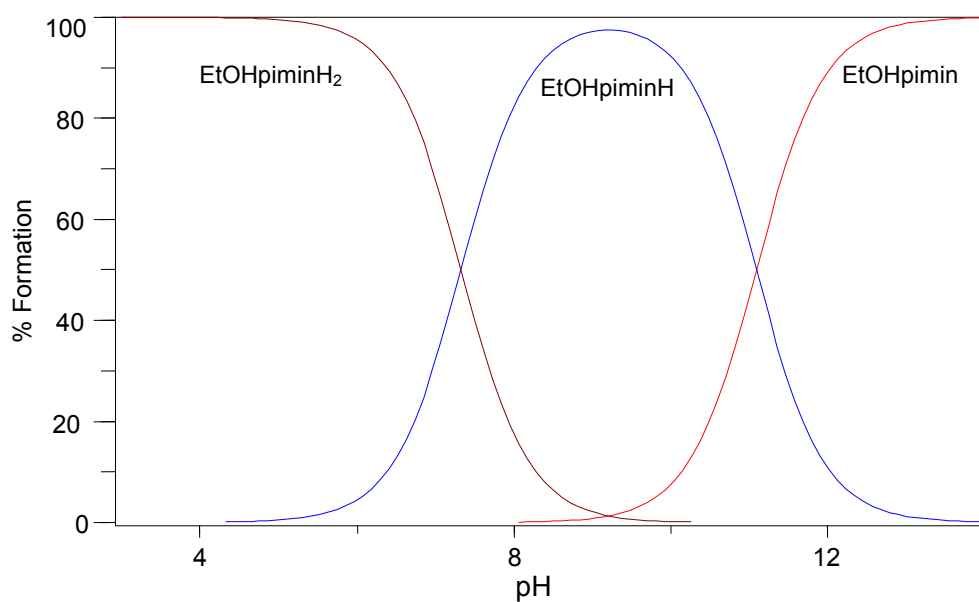
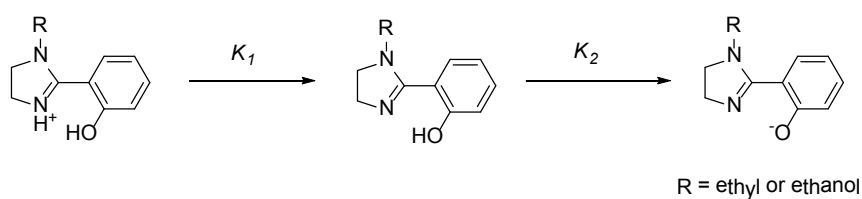


Figure 3.10 Species distribution as a function of pH for 2-(2'-hydroxyphenyl)-1-ethanolimidazoline

Table 3.3 Protonation ($\log K$) and complex formation constants ($\log \beta$) for VO(IV)-ligand systems at 25 ± 0.1 °C and $I = 0.10$ M (TMACI)

	Reaction	Ligand		
		<i>EtpiminH</i>	<i>EtOHpiminH</i>	<i>MaltoI</i> ³³
pK_1	$LH_2^+ \rightleftharpoons H^+ + LH$	7.52(1)	7.33(1)	-
pK_2	$LH \rightleftharpoons H^+ + L^-$	11.26(1)	11.09(1)	8.44(2)
$\log \beta_{110}$	$VO^{2+} + L^- \rightleftharpoons [VO(L)]^+$	10.73(1)	10.53(2)	8.80(2)
$\log \beta_{120}$	$VO^{2+} + 2L^- \rightleftharpoons [VO(L)_2]$	17.13(3)	16.66(3)	16.29(2)



Scheme 3.2 Deprotonation steps for the 2-(2'-hydroxyphenyl)-1*R*-imidazoline ligands. H^+ have been omitted from the equilibria

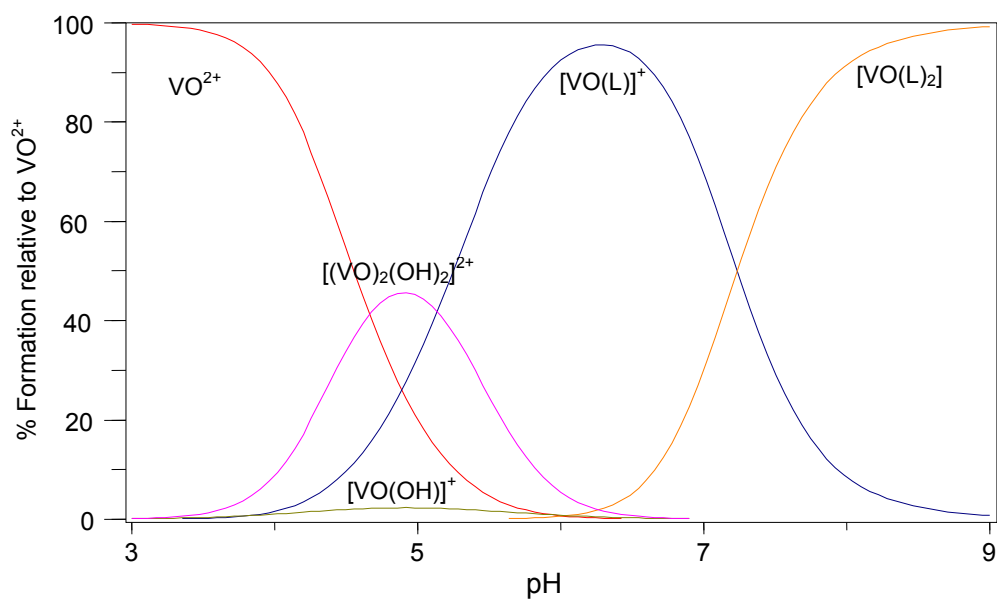


Figure 3.11 Species distribution diagram for the complexation of VO(IV) with EtpiminH (LH), $c_{VO} = 0.002 \text{ mol.L}^{-1}$ and $c_{ligand} = 0.004 \text{ mol.L}^{-1}$

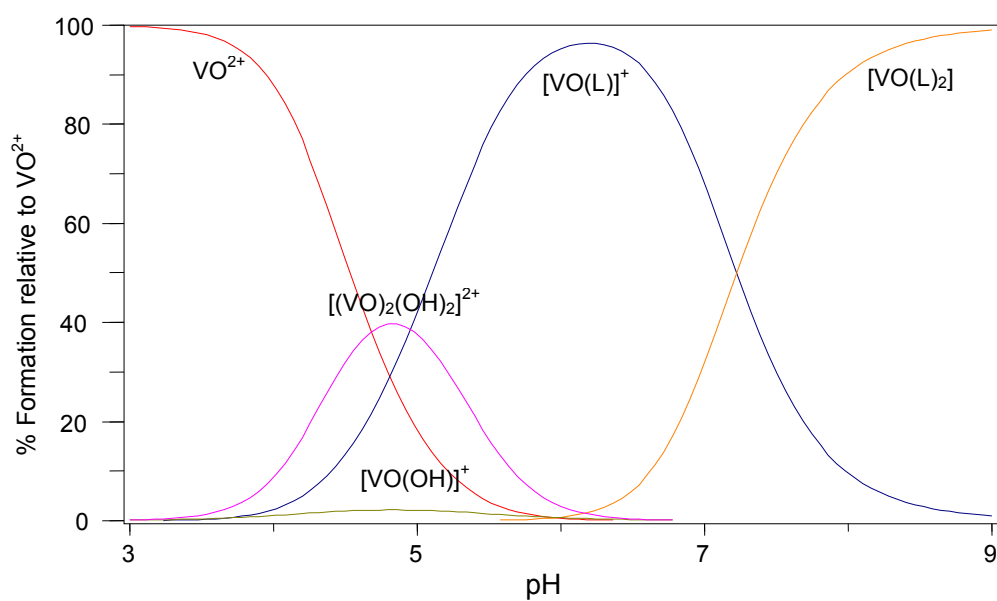
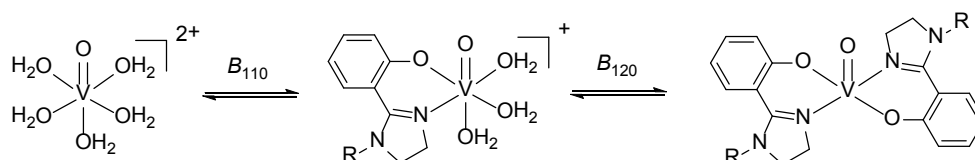


Figure 3.12 Species distribution diagram for the complexation of VO(IV) with EtOHPiminH (LH), $c_{VO} = 0.002 \text{ mol.L}^{-1}$ and $c_{ligand} = 0.004 \text{ mol.L}^{-1}$



Scheme 3.3 The stepwise formation of oxovanadium(IV) complexes. LH and L^- are omitted in the complexation equilibria as are the hydrolysis equilibria

In summary, the basicity of these 2-(2'-hydroxyphenyl)-1*R*-imidazolines make them less than ideal ligands for stabilizing vanadyl at acidic pH, such as that experienced in the stomach. However, this could be circumvented by improving the drug formulation, for example by using a drug encapsulation technique.^{34,35} The speciation studies suggest that in more alkaline conditions (such as the intestine), the ligands may help to prevent the formation of hydrolysis species which may consequently improve absorption of vanadyl into the bloodstream.

3.3.3 In vitro glucose uptake studies

The vanadium compounds [VO(pimin)₂], [VO(Etpimin)₂], [VO(EtOHpimin)₂] and VOSO₄ showed no cytotoxicity between 0.5-10 μM in the 3T3-L1, Chang and C2C12 cell lines tested as determined by an MTT-assay. At concentrations above 10 μM, however, the vanadium compounds proved to be cytotoxic (less than 80% cell viability). Similar toxicity profiles were reported by Rehder *et al.*, in SV-3T3 mice fibroblasts for a range of oxovanadium(IV) complexes.³⁶ Thus, the glucose uptake ability of the vanadium compounds, at non-cytotoxic pharmacologically relevant concentrations of 0.5, 1 and 10 μM, was screened.

Generally at 1 μM concentrations of the oxovanadium(IV) compounds, the highest and most consistent glucose uptake activity was observed across all three cell lines tested, once again a similar trend to that observed by Rehder and co-workers.³⁶ The results at this concentration are presented in **figure 3.13**, while the results for all concentrations tested can be found in **table 3.4**.

In the 3T3-L1 adipocytes (**figure 3.13**), the oxovanadium(IV) compounds (VOSO₄, [VO(pimin)₂], [VO(Etpimin)₂], [VO(EtOHpimin)₂]) enhanced glucose uptake significantly, either equalling or surpassing the effects observed for metformin, a drug commonly used in the treatment of type II diabetes.³⁷ The uptake of glucose in C2C12 muscle cells was not as significant as that observed in the other cell lines (**figure 3.13**). Nevertheless, vanadyl sulfate as well as compounds [VO(pimin)₂] and [VO(Etpimin)₂] improved glucose uptake relative to the control. The Chang liver cells exhibited the greatest response to the tested compounds compared to the other cell lines tested, however activity was slightly lower than the positive control, metformin.

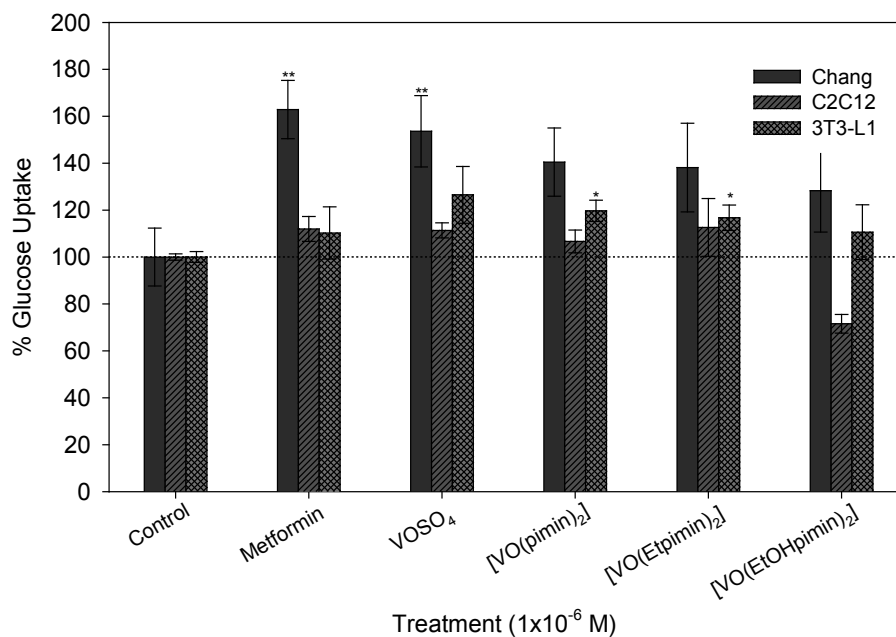


Figure 3.13 The effects of metformin (Met), vanadyl sulfate (VOSO₄), [VO(pimin)₂], [VO(Etpimin)₂] and [VO(EtOHpimin)₂] (at 1 μM concentration) on Chang, C2C12 and 3T3-L1 glucose uptake. The basal glucose uptake, is represented as 100% (Control). Error bars indicate SEM (n=3), * (p < 0.05) and ** (p < 0.01) relative to the (Con)

Vanadyl sulfate proved to be the most effective of the oxovanadium(IV) compounds in stimulating the uptake of glucose. This can be attributed to the fact that an *in vitro* model does not take into account that uncomplexed vanadyl (VOSO₄) may be simply oxidized to vanadate, the active species for PTP-inhibition, whilst compounds [VO(pimin)₂], [VO(Etpimin)₂] and [VO(EtOHpimin)₂], must first undergo oxidation and ligand dissociation. This extra ligand dissociation step may be the reason for the decreased *in vitro* activity of the synthesized compounds.³⁸ However, the increased stability of the organovanadium compounds, imparted by the organic ligands, may allow vanadium to survive the harsh conditions of the digestive system unlike VOSO₄ which undergoes facile hydrolysis and subsequent excretion. It has also been shown that the intestinal cell permeability of complexed vanadium compounds far exceeds that of the inorganic salt (VOSO₄).²⁰ The effect of the R-substituents (R = H, Et, EtOH) in compounds [VO(pimin)₂], [VO(Etpimin)₂] and [VO(EtOHpimin)₂], makes little difference to the *in vitro* activity, but would perhaps become important in an *in vivo* model when considering the lipophilicity/hydrophilicity of the complexes. Although the *in vitro* model used may have certain shortcomings, in that it does not exactly

replicate *in vivo* conditions,⁵ it does provide a simple and ethical platform for the rapid assessment of new complexes.

Table 3.4 The effects of metformin (Met), VOSO₄, [VO(pimin)₂], [VO(Etpimin)₂] and [VO(EtOHpimin)₂] on 3T3-L1, Chang and C2C12 cells at 0.5, 1.0 and 10 μM concentrations. Basal glucose uptake is represented as 100%

Compound	3T3-L1 adipocytes			Chang hepatocytes			C2C12 myoblasts		
	0.5	1	10	0.5	1	10	0.5	1	10
	Concentration (μM)								
Metformin	-	110±11.1	-	-	163±17.2	-	-	112±5.3	-
VOSO ₄	123±10.2	126±28.7	129±4.9	131±12.4	154±24.7	122±20.4	235±15.9	111±3.2	50±19.5
[VO(pimin) ₂]	122±3.2	120±3.2	121±9.7	109±7.2	141±27.0	116±22.3	88±45.2	107±4.8	87±2.8
[VO(Etpimin) ₂]	115±11.1	117±0.9	122±20.2	126±26.1	138±32.7	117±31.3	87±4.8	113±31.0	96±8.8
[VO(EtOHpimin) ₂]	124±4.7	111±11.6	117±3.7	163±7.2	128±31.0	124±31.9	114±8.42	72±3.9	24±3.5

3.3.4 Anticoagulation studies

Diabetes mellitus sufferers are at a higher risk of thrombotic associated fatalities and as such quite often benefit from anticoagulatory medication. Despite this, there has been very little investigation into the anticoagulatory effects of oxovanadium(IV) complexes. We therefore decided to investigate whether or not [VO(pimin)₂] a representative example of the compounds in this class, displayed any activity in this regard.

The prothrombin time (PT) is the screening test for the extrinsic coagulation pathway, which is initiated by tissue factor. In the PT test, the time required for plasma to clot following conversion of prothrombin to thrombin upon addition of CaCl₂ is measured. The activated partial thromboplastin time (APTT) assay investigates the intrinsic pathway. In an APTT reagent, negatively charged particles such as silica are mixed with phospholipids and buffers providing an ideal environment for activation of intrinsic plasma proteins. After incubation of the APTT reagent with plasma, CaCl₂ is added which initiates multiple steps of the intrinsic pathway penultimately leading to a fibrin clot. The time from addition of the calcium salt until the clot formation is measured in seconds. D-dimer fragments are contained in the soluble derivatives formed upon plasmin degradation of Factor XIIIa crosslinked fibrin. Plasmin, a serine protease, is capable of digesting the insoluble fibrin producing a variety of soluble derivatives. These soluble products contain neoantigen (D-dimer domain) which is not present on the original fibrinogen molecule. In the D-Dimer assay, elevated levels of fibrin reflect a state of activated coagulation and fibrinolysis (hypercoagulation state). The Fibrinogen-C (Fib-C) screening test uses an excess of thrombin to convert fibrinogen to fibrin in diluted plasma. High levels of fibrinogen are associated with an increased risk of cardiovascular disease.

For the APTT and PT screening tests, only heparin (positive control) significantly increased clotting times relative to the control (**figure 3.14**). Thus, [VO(pimin)₂] did not affect the intrinsic or extrinsic pathways. For the Fib-C test, there was a very slight reduction in fibrin formation when the oxovanadium(IV) complex was administered, however compared to heparin the effect was not too significant. The D-Dimer test showed the most promising results, with [VO(pimin)₂] reducing D-Dimer formation comparably to that of heparin thereby reducing the state of hypercoagulation.

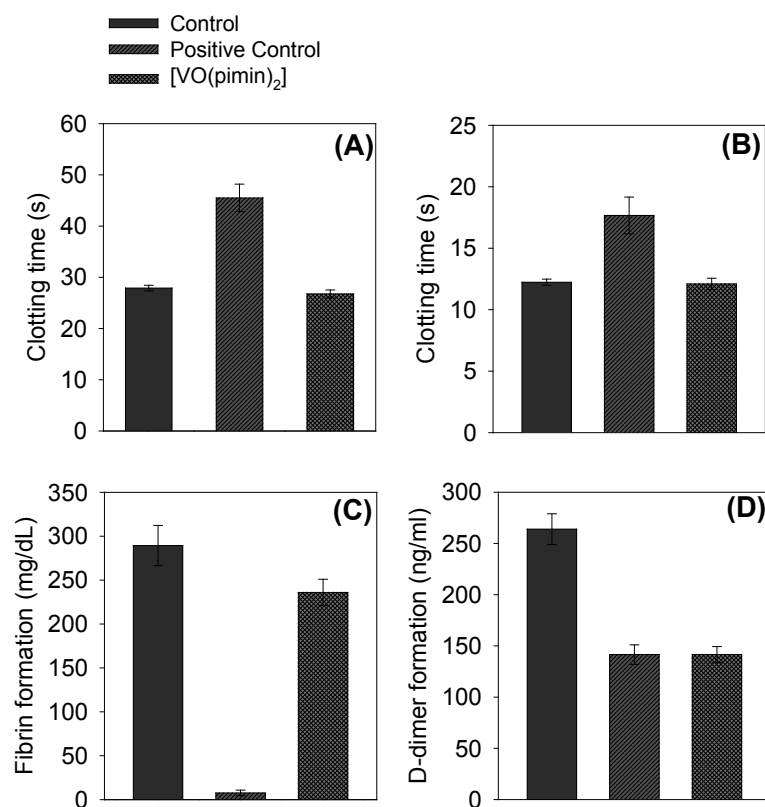


Figure 3.14 The effect of [VO(pimin)₂] (10 μM) on APTT (A) and PT (B) clotting times, on fibrin formation (C) and D-Dimer formation. The control represents untreated sample while the positive control represents the anticoagulant heparin (0.1 U.mL⁻¹) (n = 3)

3.4 Conclusions

A range of neutral oxovanadium(IV) complexes with bidentate imidazoliny-phenolato ligands were successfully prepared and characterized. Aqueous potentiometry was used to determine the pK values for the ligands as well as the stability constants for the formation of the corresponding oxovanadium(IV) complexes. The highly basic character of the ligands prevented vanadyl hydrolysis in basic conditions, such as that experienced in the intestine. In more acidic conditions however, ligand dissociation was prevalent as was the formation of hydrolysis species, an obstacle which could be remedied by drug encapsulation. The oxovanadium(IV) complexes showed promising glucose lowering properties *in vitro* in liver, muscle and fat cells. Improvements could however be made by increasing complex stability over a broader pH range. In addition to the antidiabetic properties, [VO(pimin)₂] displayed anticoagulative activity as evidenced by inhibition of D-Dimer formation. This effect of oxovanadium(IV) complexes has barely, if at all, been studied and represents an additional therapeutic avenue for the treatment of diabetes.

3.5 References

- (1) Sakurai, H.; Fujii, K.; Watanabe, H.; Tamura, H. *Biochem. Biophys. Res. Commun.* **1995**, *214*, 1095.
- (2) Williams, P.; Baran, E. *Transition Met. Chem.* **1997**, *22*, 589.
- (3) Bolm, C.; Luongb, T. K. K.; Harms, K. *Chem. Ber.* **1997**, *130*, 887.
- (4) Sanna, D.; Micera, G.; Buglyó, P.; Kiss, T.; Gajda, T.; Surdy, P. *Inorg. Chim. Acta.* **1998**, *268*, 297.
- (5) Nejo, A. A.; Kolawole, G. A.; Opoku, A. R.; Wolowska, J.; O'Brien, P. *Inorg. Chim. Acta.* **2009**, *362*, 3993.
- (6) Melchior, M.; Thompson, K. H.; Jong, J. M.; Rettig, S. J.; Shuter, E.; Yuen, V. G.; Zhou, Y.; McNeill, J. H.; Orvig, C. *Inorg. Chem.* **1999**, *38*, 2288.
- (7) Hersman, L.; Lloyd, T.; Sposito, G. *Geochim. Cosmochim. Acta* **1995**, *59*, 3327.
- (8) Hoveyda, H. R.; Karunaratne, V.; Orvig, C. *Tetrahedron* **1992**, *48*, 5219.
- (9) Thompson, K. H.; Orvig, C. *Coord. Chem. Rev.* **2001**, *219-221*, 1033.
- (10) McCracken, J.; Peisach, J.; Dooley, D. M. *J. Am. Chem. Soc.* **1987**, *109*, 4064.
- (11) Bouwman, E.; Douziech, B.; Gutierrez-Soto, L.; Beretta, M.; Driessen, W. L.; Reedijk, J.; Mendoza-Díaz, G. *Inorg. Chim. Acta.* **2000**, *304*, 250.
- (12) Thompson, K. H.; Lichter, J.; LeBel, C.; Scaife, M. C.; McNeill, J. H.; Orvig, C. *J. Inorg. Biochem.* **2009**, *103*, 554.
- (13) Woo, L. C. Y.; Yuen, V. G.; Thompson, K. H.; McNeill, J. H.; Orvig, C. *J. Inorg. Biochem.* **1999**, *76*, 251.
- (14) Storr, T.; Mitchell, D.; Buglyó, P.; Thompson, K. H.; Yuen, V. G.; McNeill, J. H.; Orvig, C. *Bioconjugate Chem.* **2003**, *14*, 212.
- (15) Szabo, B. *Pharmacol. Ther.* **2002**, *93*, 1.
- (16) Efendic, S.; Efanov, A. M.; Berggren, P.-O.; Zaitsev, S. V. *Diabetes* **2002**, *51*, S448.
- (17) Proks, P.; Treinies, I.; Mest, H.-J.; Trapp, S. *Eur. J. Pharmacol.* **2002**, *452*, 11.
- (18) Crane, L.; Anastassiadou, M.; Hage, S. E.; Stigliani, J. L.; Baziard-Mouysset, G.; Payard, M.; Leger, J. M.; Bizot-Espiard, J.-G.; Ktorza, A.; Caignard, D.-H.; Renard, P. *Bioorg. Med. Chem.* **2006**, *14*, 7419.

-
- (19) Parík, P.; Senauerová, S.; Lisková, V.; Handlír, K.; Ludwig, M. *J. Heterocycl. Chem.* **2006**, *43*, 835.
- (20) Thompson, K. H.; Liboiron, B. D.; Sun, Y.; Bellman, K. D. D.; Setyawati, I. A.; Patrick, B. O.; Karunaratne, V.; Rawji, G.; Wheeler, J.; Sutton, K.; Bhanot, S.; Cassidy, C.; McNeill, J. H.; Yuen, V. G.; Orvig, C. *J. Biol. Inorg. Chem.* **2003**, *8*, 66.
- (21) Suydam, F. H. *Anal. Chem.* **1963**, *35*, 193.
- (22) Baikalova, L. V.; Domnina, E. S.; Skvortsova, G. G. *Russ. Chem. Bull.* **1977**, *26*, 1065.
- (23) Westland, A. D.; Tarafder, M. T. H. *Inorg. Chem.* **1981**, *20*, 3992.
- (24) Bhattacharya, S.; Ghosh, T. *Transition Met. Chem.* **2002**, *27*, 89.
- (25) Wilkinson, G.; Gillard, R. D.; McCleverty, J. A. *Comprehensive Coordination Chemistry*; Pergamon Press: New York, 1987.
- (26) Ligtenbarg, A. G. J.; Spek, A. L.; Hage, R.; Feringa, B. L. *J. Chem. Soc., Dalton Trans.* **1999**, 659.
- (27) Selbin, J. *Chem. Rev.* **1965**, *65*, 153.
- (28) Addison, A. W.; Rao, T. N.; Reedijk, J.; Van Rijn, J.; Verschoor, G. C. *J. Chem. Soc., Dalton Trans.* **1984**, 1349.
- (29) Alderighi, L.; Gans, P.; Ienco, A.; Peters, D.; Sabatini, A.; Vacca, A. *Coord. Chem. Rev.* **1999**, *184*, 311.
- (30) Rogers, G. A.; Bruice, T. C. *J. Am. Chem. Soc.* **1974**, *96*, 2463.
- (31) Donkor, K. K.; Kratochvil, B. *J. Chem. Eng. Data* **1993**, *38*, 569.
- (32) Sari, H.; Covington, A. K. *J. Chem. Eng. Data* **2005**, *50*, 1425.
- (33) Saatchi, K.; Thompson, K. H.; Patrick, B. O.; Pink, M.; Yuen, V. G.; McNeill, J. H.; Orvig, C. *Inorg. Chem.* **2005**, *44*, 2689.
- (34) Sakurai, H.; Fugono, J.; Yasui, H. *Mini Rev. Med. Chem.* **2004**, *4*, 41.
- (35) Fugono, J.; Yasui, H.; Sakurai, H. *J. Pharm. Pharmacol.* **2005**, *57*, 665.
- (36) Rehder, D.; Pessoa, J. C.; Geraldés, C. F. G. C.; Margarida, C. A.; Kabanos, C. T.; Kiss, T.; Meier, B.; Micera, G.; Pettersson, L.; Rangel, M.; Salifoglou, A.; Turel, I.; Wang, D. *J. Biol. Inorg. Chem.* **2002**, *7*, 384.
- (37) Davidson, M. D. M. B.; Peters, M. D. A. L. *Am. J. Med.* **1997**, *102*, 99.
-

-
- (38) Peters, K. G.; Davis, M. G.; Howard, B. W.; Pokross, M.; Rastogi, V.; Diven, C.; Greis, K. D.; Eby-Wilkens, E.; Maier, M.; Evdokimov, A.; Soper, S.; Genbauffe, F. *J. Inorg. Biochem.* **2003**, *96*, 321.

This page has been left blank intentionally

Chapter 4

Oxovanadium(IV) complexes with imidazole-carboxylic acid ligands

4.1 Introduction

Imidazole (**figure 4.1**) is a planar, 5-membered, aromatic molecule, consisting of a trigonal nitrogen atom with two electrons in the p-orbital of the N-1 “pyrrole” nitrogen and at position 3 (N-3), a heterocyclic, “imino” nitrogen containing a lone pair of electrons in a hybrid orbital and a single electron in the p-orbital.¹ The electrons in the unhybridised p-orbital of N-1 atom form part of the aromatic sextet. The N-1 electrons are not available for bonding since the aromaticity of the imidazole would be compromised. However, if deprotonation were to occur, a lone pair of electrons would be available for bonding.

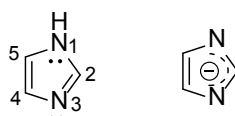


Figure 4.1 Structure of neutral imidazole (a), and the anionic form (b)

The net charges for imidazole and pyridine molecules have been calculated using *ab initio* methods^{2,3} and are reported in **table 4.1**. The N-3 σ and π electron charges are slightly negative indicating moderate σ -donating and weak π -accepting properties. The unshared electron pair on N-3 and the possibility of overlap between the d-orbitals of a metal ion and the imidazole π -orbitals, allow for the formation of stable metal complexes.

Nature certainly caught on to the idea of using imidazoles to bind metals, specifically the transition metals. The imidazole group which forms part of the side chain of histidine is found bound to nickel, iron and zinc whereas cobalt is coordinated to a similar benzimidazole group in vitamin B12.⁴ Functioning as biocatalysts, these imidazole-metal systems not only catalyze oxidation and

hydroxylation reactions, but can also function as electron storage sites and dioxygen transporters.⁴ More pertinently, vanadium has also been found bound to imidazoles in the naturally occurring vanadium-dependent haloperoxidases.⁵ Other than metal binding capabilities, imidazole compounds are well established in the field of medicinal chemistry with applications such as anticancer,⁶ antibacterial,⁷ antifungal⁸ and antidiabetic⁹ drugs, to name a few.

Table 4.1 Calculated net charges on the nitrogen atoms of imidazole and pyridine^{2,3}

Nitrogen Atom	σ	π
N1	-0.84	0.4
N3	-0.1	-0.1
Pyridine	-0.22	-0.01

This study explores the use of imidazole derivatives as a binding moiety to oxovanadium(IV) since imidazoles are known to play a significant role in a large variety of biological processes. It is therefore envisaged that these ligands should not pose a threat to the body once cleaved from the vanadium ion *in vivo*. The studies performed in **Part 1, Chapter 3** made us aware of the undesirable effects of using ligands with high basicity (ligand dissociation at low pH) and for this reason we have incorporated the acidic carboxylate group (instead of a phenol group) to provide stability in the low pH range. The combination of both the imidazole and carboxylate functionalities should therefore provide suitable stabilization of vanadyl over a biological pH range. In addition, alkylation at the “pyrrole” nitrogen allows for modification of the balance between lipophilicity and hydrophilicity of the resultant complexes.

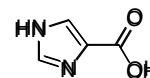
In this chapter, the synthesis and characterization of a small series of oxovanadium(IV) complexes with imidazole-4-carboxylic acid, imidazole-2-carboxylic acid and 1-methylimidazole-2-carboxylic acid, as coordinating ligands is presented. The protonation constants of the ligands as well as the stability constants of these with oxovanadium(IV) were determined using glass electrode potentiometry. This provided an indication as to whether the complexes would stabilize vanadyl across a biological pH range. The formation of ternary complexes with citric acid was also

investigated using potentiometry in the hope of gaining an understanding of the possible species that may exist in the bloodstream where bioligands are prevalent.

4.2 Preparative work

4.2.1 Imidazole-4-carboxylic acid (Im4COOH)

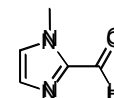
As discussed in section 2.2.1 this ligand was purchased from Sigma-Aldrich Chemical Company and used in subsequent steps without further purification.



4.2.2 1-Methylimidazole-2-carboxaldehyde (Melm2CHO)

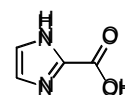
1-Methylimidazole-2-carboxaldehyde was prepared according to a literature method.¹⁰⁻

¹² To a suspension of 1-methylimidazole (2.20 g, 0.020 mol) in dry diethyl ether (50 mL) was added 2.5 M butyllithium (8.40 mL, 0.021 mol) at -78 °C. After stirring for an hour, DMF (2.33 mL, 0.030 mol) was added and this solution was stirred overnight. After completion of the reaction, 2 mL of water was added followed by 15 mL of 4 N HCl. The aqueous layer was made basic by addition of potassium carbonate following which the product was extracted into chloroform. This organic layer was concentrated and the product was distilled at 3.0×10^{-1} mBar and 80 °C to yield a brownish crystalline solid after cooling. Yield: 76.1%. ¹H (δ , 400 MHz, CDCl₃): 4.03 (s, 3H, NCH₃), 7.16-7.27 (m, 2H, Im-H), 9.81 (s, 1H, CHO); ¹³C NMR (δ , 100 MHz, CDCl₃): 35.20, 127.69, 131.74, 144.00, 182.37. IR (cm⁻¹, KBr disk): 3108(m), 2956(m), 2835(m), 1671(s), 1532(w), 1509(m), 1479(m), 1380(s), 1330(s), 1289(s), 1218(m), 1150(m), 1077(m), 920(s), 766(s), 682(s). *Anal.* Calcd (Found) for C₅H₆N₂O (%): C, 54.54 (54.25); H, 5.49 (5.65); N, 25.44 (25.19).



4.2.3 Imidazole-2-carboxylic acid.H₂O (Im2COOH)

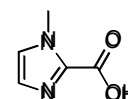
An aqueous 30% H₂O₂ (10 g) was added dropwise to a stirred solution of imidazole-2-carboxaldehyde (2.88 g, 0.030 mol) in water (10 mL). The reaction was allowed to proceed at room temperature for 72 hours, following which the water was removed *in vacuo* at room temperature to afford a white crystalline solid. This solid was washed with a mixture of diethyl ether/methanol/water (4:1:1) to remove the excess peroxide. *Note:* The product should be stored in an anhydrous environment since it is hygroscopic. Slow decarboxylation may occur at room temperature, thus refrigeration is suggested. Yield: 97.5%. Mp = 156-158 °C. ¹H NMR (δ , 400 MHz, D₂O): 7.56 (2H, s, Im-H); ¹³C NMR (δ , 100 MHz, D₂O): 158.86, 141.02, 120.49. IR (cm⁻¹, KBr disk): 3392(m), 3124(m), 2861(m), 1618(s), 1502(m), 1462(m), 1421(s), 1388(s), 1322(m),



1108(s), 925(s), 910(s), 819(m), 797(s), 774(m). *Anal.* Calcd (Found) for $C_4H_6N_2O_3$ (%): C, 36.92 (37.18); H, 4.65 (4.94); N, 21.53 (21.47).

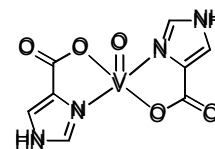
4.2.4 1-Methylimidazole-2-carboxylic acid.H₂O (Melm2COOH)

The procedure followed that of Im2COOH above except that 1-methylimidazole-2-carboxyaldehyde was used and the yield was quantitative after the removal of water under high vacuum (no washing with diethyl ether/water was necessary). *Note:* The product should be stored in an anhydrous environment since it is hygroscopic. Slow decarboxylation may occur at room temperature, thus refrigeration is suggested. Yield: 100%. Mp = 99-101 °C. ¹H NMR (δ , 400 MHz, D₂O): 7.42, 7.39 (2H, s, Im-H) and 4.08 ppm (3H, s, NCH₃); ¹³C NMR (δ , 100 MHz, D₂O): 158.67, 139.68, 125.83, 118.46, 36.73. IR (cm⁻¹, KBr disk): 3347(m) 3119(m), 2663(w), 1641(s), 1683(m), 1507(s), 1449(m), 1388(s), 1338(s), 1285(s), 1173(m), 1123(s), 961(m) 910(m), 776(s), 685(s). *Anal.* Calcd (Found) for $C_5H_8N_2O_3$ (%): C, 41.67 (41.28); H, 5.59 (5.23); N, 19.44 (19.12).



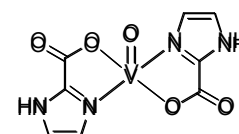
4.2.5 [VO(Im4COO)₂]

This complex was prepared according to a literature method but with slight modifications.¹⁰ To a stirred aqueous solution of Im4COOH (0.254 g, 2.26 mmol) in water (10 mL), was added 10% TMAOH (1.04 mL, 1.13 mmol). To this solution was added aqueous VOCl₂ (1.13 mmol), prepared by the reaction of VOSO₄ with BaCl₂. The reaction was allowed to stir overnight, following which the light blue precipitate was collected, washed with methanol and ether and dried in an oven at 100 °C. Yield: 64.6%. Mp > 300°C. ATR-IR (cm⁻¹, neat): 3129(m), 2992(m), 2856(m), 1606(s), 1573(s), 1499(m), 1439(m), 1356(s), 1209(m), 1080(m), 1012(m), 981(s), 878(m), 819(s), 780(s). *Anal.* Calcd (Found) for $C_8H_6N_4O_5V \cdot H_2O$ (%): C, 31.29 (31.20); H, 2.63 (2.67); N, 18.24 (18.14). UV/Vis (H₂O) λ_{max} (ϵ , M⁻¹cm⁻¹): 746 (25), 561 (10), 310sh (194). UV/Vis (solid reflectance), λ_{max} (nm): 712, 570, 339.



4.2.6 [VO(Im2COO)₂]

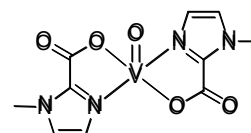
This complex was prepared in the same manner as [VO(Im4COO)₂], except that an aqueous solution of VOSO₄ was added to the ligand solution



instead of aqueous VOCl_2 . Yield: 69.9%. Mp > 300°C. ATR-IR (cm^{-1} , neat): 3448(m), 3129(w), 3008(m), 2906(m), 1625(s), 1558(m), 1487(m), 1398(s), 1338(m), 1277(m), 1171(m), 1112(s), 984(s), 908(m), 829(m), 769(s), 658(s) cm^{-1} . *Anal.* Calcd (Found) for $\text{C}_8\text{H}_6\text{N}_4\text{O}_5\text{V}\cdot\text{H}_2\text{O}$ (%): C, 31.29 (31.21); H, 2.63 (2.53); N, 18.24 (18.07). UV/Vis (H_2O) λ_{max} (ϵ , $\text{M}^{-1}\text{cm}^{-1}$): 749 (23), 550 (10), 317sh (191). UV/Vis (solid reflectance), λ_{max} (nm): 715, 559, 333.

4.2.7 $[\text{VO}(\text{MeIm}2\text{COO})_2]$

This complex was prepared similarly to $[\text{VO}(\text{Im}4\text{COO})_2]$. However, upon stirring overnight a blue precipitate did not form. The blue solution was then allowed to stand for 24 hours and a light blue precipitate formed,

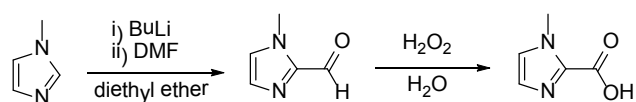


which was filtered and washed with methanol and then ether and dried in an oven at 100 °C. Yield: 62.3%. Mp = 218-220°C. ATR-IR (cm^{-1} , neat): 3134 (m), 1628(s), 1487(s), 1426(s), 1327(s), 1286(m), 1180(s), 1166(s), 963(s), 837(m), 797(s), 769(s), 698(s) cm^{-1} . *Anal.* Calcd (Found) for $\text{C}_{10}\text{H}_{10}\text{N}_4\text{O}_5\text{V}\cdot\text{H}_2\text{O}$ (%): C, 35.83 (36.01); H, 3.61 (3.47); N, 16.72 (16.67)%. UV/Vis (H_2O) λ_{max} (ϵ , $\text{M}^{-1}\text{cm}^{-1}$): 761 (23), 576 (10). UV/Vis (solid reflectance), λ_{max} (nm): 718, 578, 352.

4.3 Results and discussion

4.3.1 Synthesis and general considerations

The most common method for preparing 2-substituted *N*-alkylimidazoles involves lithiation typically using *n*-butyllithium (*n*-BuLi), followed by reaction with a suitable electrophile.^{11,12} The hydrogen at the 2-position of *N*-alkylimidazoles is the most acidic and therefore the carbanion is readily generated at this position. In our case, 1-methylimidazole was reacted with *n*-BuLi followed by formylation using DMF, giving 1-methylimidazole-2-aldehyde in good yield (**scheme 4.1**). The reaction was carried out under inert and anhydrous conditions to prevent the lithiated intermediate from decomposing upon reaction with air or water. Furthermore, we have noticed that an increase in temperature or rapid addition of *n*-BuLi can result in di-substitution, most likely at the 2 and 5-positions.¹³ 1-Methylimidazole-2-aldehyde was then converted to the carboxylic acid by oxidation with hydrogen peroxide (**scheme 4.1**). This novel reaction was 'green' in that water was generated as the only by-product. Additionally, it was also much simpler and higher yielding than other reported methods.^{14,15} At the end of this reaction, the product (1-methylimidazole-2-carboxylic acid) was recovered by removal of water under a high vacuum giving a high purity crystalline material. Importantly, removal of water was performed at room temperature. Increasing the temperature to facilitate solvent removal gave the decarboxylated product. This facile decarboxylation has also been acknowledged by others.^{14,16}



Scheme 4.1 Synthesis of 1-methylimidazole-2-carboxylic acid from the starting material 1-methylimidazole

Imidazole-2-carboxylic acid was prepared by the same method, however unlike 1-methylimidazole-2-carboxylic acid, this ligand seemed to contain peroxide impurities even after extensive drying under vacuum. This was first noticed after addition of a solution of vanadyl sulfate to an aqueous solution of imidazole-2-carboxylic acid resulted in a colour change from

blue (V^{4+}) to yellow/orange (V^{5+}). The peroxide was removed by thoroughly washing of the ligand with a solvent mixture consisting of cold diethyl ether/methanol/water. A methanolic vanadyl sulfate solution was added to the washings to ascertain when the peroxide had been completely removed (washings remained blue).

NMR spectroscopy (along with other techniques) was used to confirm the successful synthesis of the ligands. Shown in **figure 4.2** and **4.3** are the 1H NMR spectra of 1-methylimidazole-2-aldehyde and 1-methylimidazole-2-carboxylic acid. The most descriptive indicator of successful oxidation was the disappearance of the aldehyde proton which appeared at ~ 9.8 ppm in Melm2CHO. In the ^{13}C NMR spectrum (**figure 4.4**), the aldehyde carbon signal of MelmCHO appeared 182 ppm while the more shielded carboxylic acid carbon for MelmCOOH appeared further upfield at 159 ppm. In both spectra, all five carbon signals were accounted for.

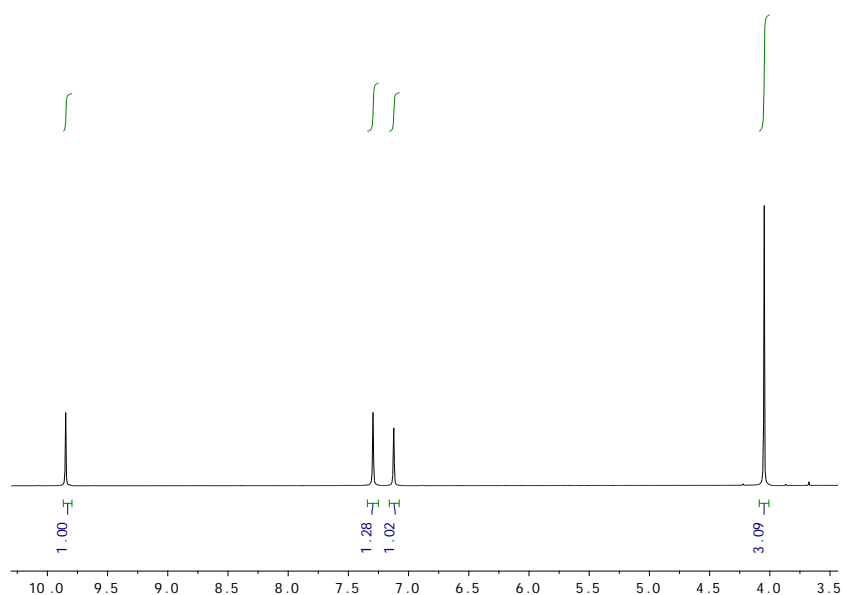


Figure 4.2 1H NMR spectrum of Melm2CHO (δ ppm). The solvent ($CDCl_3$) is responsible for the inflated integration at 7.3 ppm

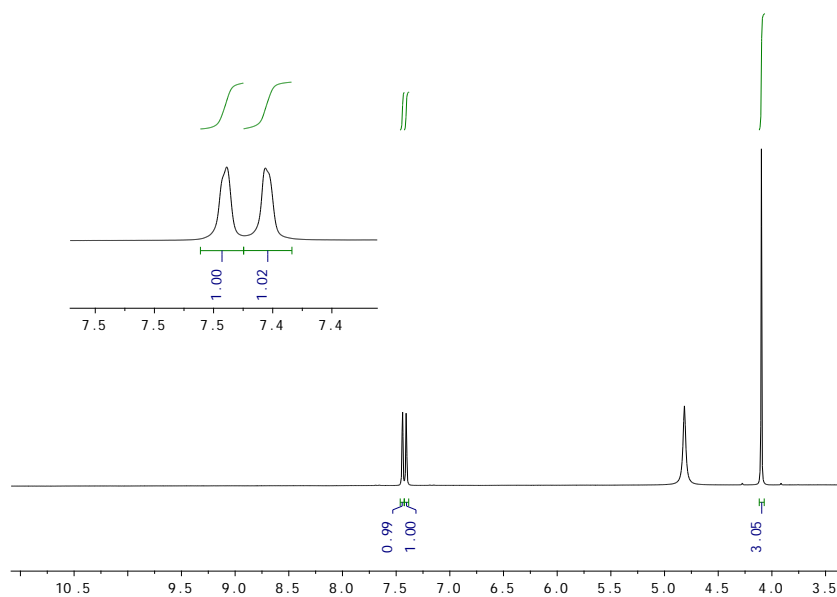


Figure 4.3 ^1H NMR spectrum of Melm2COOH (δ ppm). The solvent (D_2O) is left un-integrated

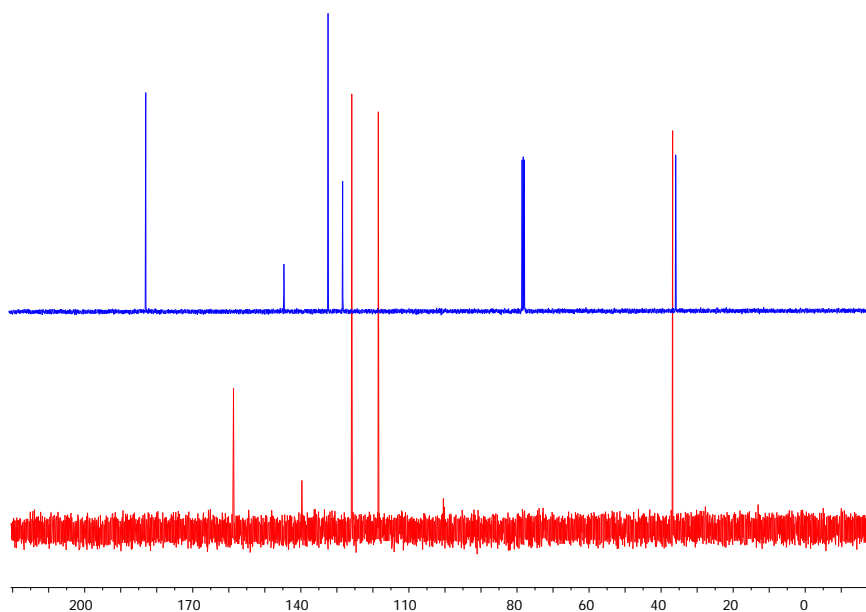
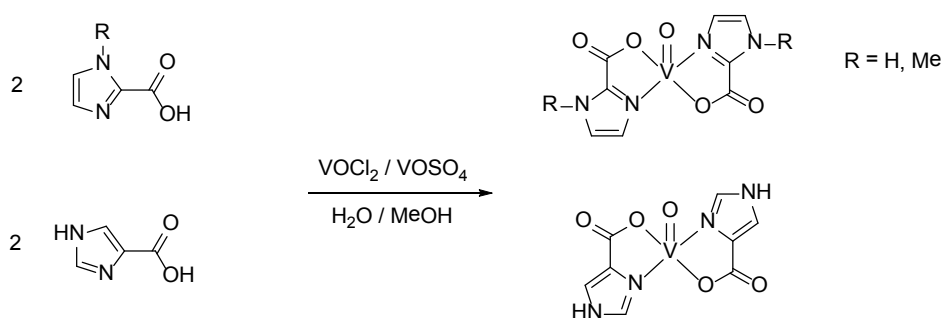


Figure 4.4 Comparison of the ^{13}C NMR spectra of Melm2CHO (top) (in CDCl_3 residual solvent peak at ~ 77 ppm) and Melm2COOH (bottom) (in D_2O)

The oxovanadium(IV) complexes were prepared using two slightly different procedures. Both $[\text{VO}(\text{Im4COO})_2]$ and $[\text{VO}(\text{Melm2COO})_2]$ were prepared by addition of an aqueous solution of

VOCl_2 to a two-fold excess of Im4COOH and MeIm2COOH , respectively (**scheme 4.2**). The vanadyl chloride (VOCl_2) was prepared separately by addition of one mole equivalent of BaCl_2 to VOSO_4 . Finally, the resultant VOCl_2 solution was filtered through a Millipore filter to remove precipitated BaSO_4 .¹⁰ $[\text{VO}(\text{Im2COO})_2]$ was prepared by the direct reaction with VOSO_4 rather than using VOCl_2 (**scheme 4.2**). It should be noted that either VOSO_4 or VOCl_2 can be used. The only reason for using VOCl_2 to prepare $[\text{VO}(\text{Im4COO})_2]$ and $[\text{VO}(\text{MeIm2COO})_2]$ was that the complexes precipitated out of solution quicker compared to when using VOSO_4 . The complexes were slightly soluble in water, but sparingly soluble in many common organic solvents such as DMSO, DMF, dichloromethane and methanol. Furthermore, after standing solutions of the oxovanadium(IV) complexes, the solutions gradually turned yellow indicating that oxidation had taken place. This was especially rapid when organic/aqueous mixtures were used or when the solution was heated or sonicated. This made crystal growth especially difficult, even when measures were taken to prevent aerial oxygen from entering the vessel.



Scheme 4.2 Preparation of oxovanadium(IV) imidazole-carboxylic acid complexes

Cyclic voltammetry was conducted to determine the oxidation potentials of these complexes. Quite interestingly, the methyl-substituted complex $[\text{VO}(\text{MeIm2COO})_2]$ displayed notably different electrochemical properties to the non-substituted complexes, $[\text{VO}(\text{Im4COO})_2]$ and $[\text{VO}(\text{Im2COO})_2]$ (**figure 4.5**). For $[\text{VO}(\text{MeIm2COO})_2]$, a reversible oxidation ($i_{pa}/i_{pc} = 1.1$) took place at a potential of 300 mV corresponding to the $\text{V}^{4+} - \text{V}^{5+}$ oxidation. The remaining two complexes $[\text{VO}(\text{Im4COO})_2]$ and $[\text{VO}(\text{Im2COO})_2]$ displayed irreversible oxidation peaks at higher potentials of 480 and 410 mV, respectively. This corresponded well to what was observed visually considering that an aqueous solution containing $[\text{VO}(\text{MeIm2COO})_2]$ turned yellow well before that of the other two complexes.

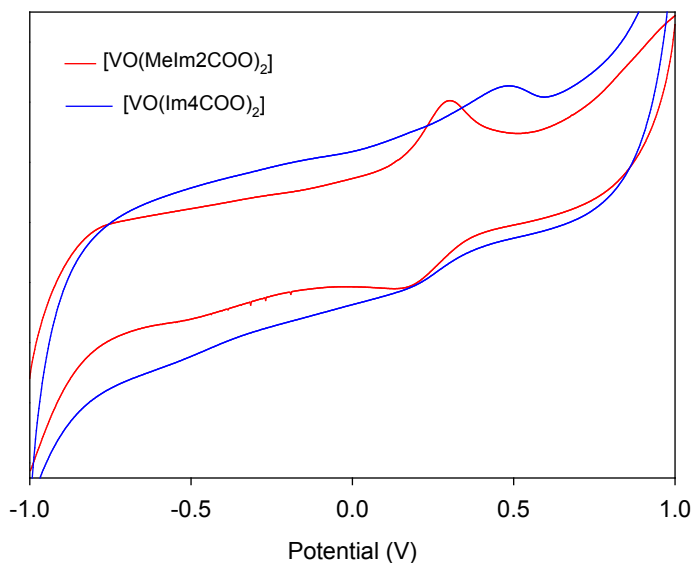


Figure 4.5 Cyclic voltammograms of complexes [VO(MeIm2COO)₂] and [VO(Im4COO)₂] in H₂O

4.3.2 Spectroscopic characterization

In the IR spectra of the ligands, the $\nu(\text{C}=\text{N})$ appeared in the range 1618-1641 cm^{-1} , shifting to lower values (1608 - 1628 cm^{-1}) after coordination to vanadium. The prominent vanadyl stretching vibration, $\nu(\text{V}=\text{O})$, appeared between 981 – 963 cm^{-1} , well within the range reported for oxovanadium(IV) complexes.¹⁷ Representative infrared spectra of Im2COOH and the corresponding oxovanadium(IV) complex have been illustrated in **figure 4.6**.

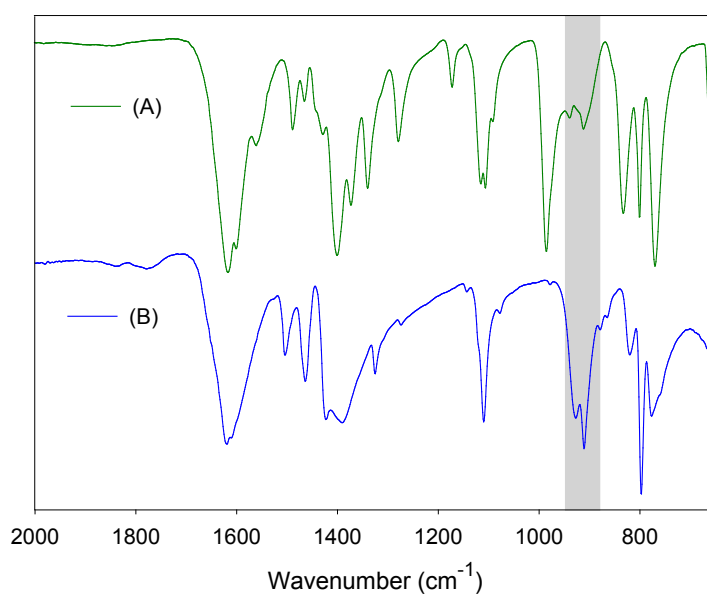


Figure 4.6 Infrared spectra of (A) [VO(Im2COO)₂] and (B) Im2COOH

The solution UV/Vis studies were performed using water as a solvent ($c = 1 \times 10^{-3}$ M) as well as in the solid state. In solution state, both $[\text{VO}(\text{Im}4\text{COO})_2]$ and $[\text{VO}(\text{Im}2\text{COO})_2]$ displayed three low intensity d-d transitions, while for $[\text{VO}(\text{Melm}2\text{COO})_2]$ only the two lower energy transitions were observed. In the former two complexes, the $(a_1 \leftarrow b_2)$ transition was comparatively intense ($\epsilon = 194 - 191 \text{ M}^{-1}\text{cm}^{-1}$) due to the effects of the neighbouring charge transfer band. These transitions appear at 310-317 nm. The $(b_1 \leftarrow b_2)$ and $(e_\pi \leftarrow b_2)$ transitions were found for all three complexes at wavelengths of 550-576 nm ($\epsilon = 10 \text{ M}^{-1}\text{cm}^{-1}$) and 746-761 nm ($\epsilon = 23 - 25 \text{ M}^{-1}\text{cm}^{-1}$) respectively. The representative solution state UV/Vis spectrum of $[\text{VO}(\text{Im}4\text{COO})_2]$ has been included in **figure 4.7**. Solid state UV/Vis studies gave similar results with all three d-d transitions once again being observed in all complexes. The high energy $(a_1 \leftarrow b_2)$ transition was however more clearly resolved as shown in **figure 4.8** for a representative example, $[\text{VO}(\text{Melm}2\text{COO})_2]$. This confirmed that all of the complexes were structurally similar, adopting a square-pyramidal geometry and d^1 electronic configuration.¹⁷

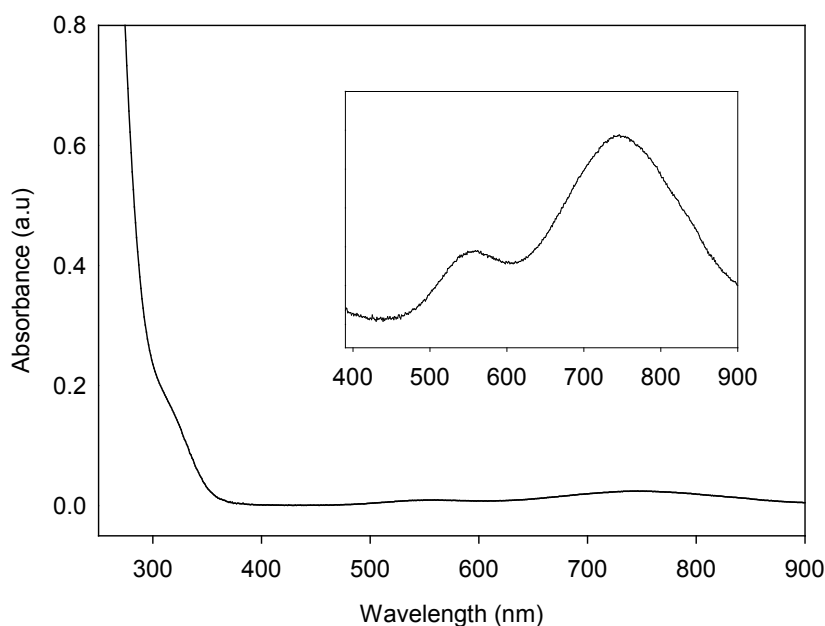


Figure 4.7 Solution electronic spectrum of $[\text{VO}(\text{Im}4\text{COO})_2]$ in water. Insert shows an expanded view of the region between 400-900 nm

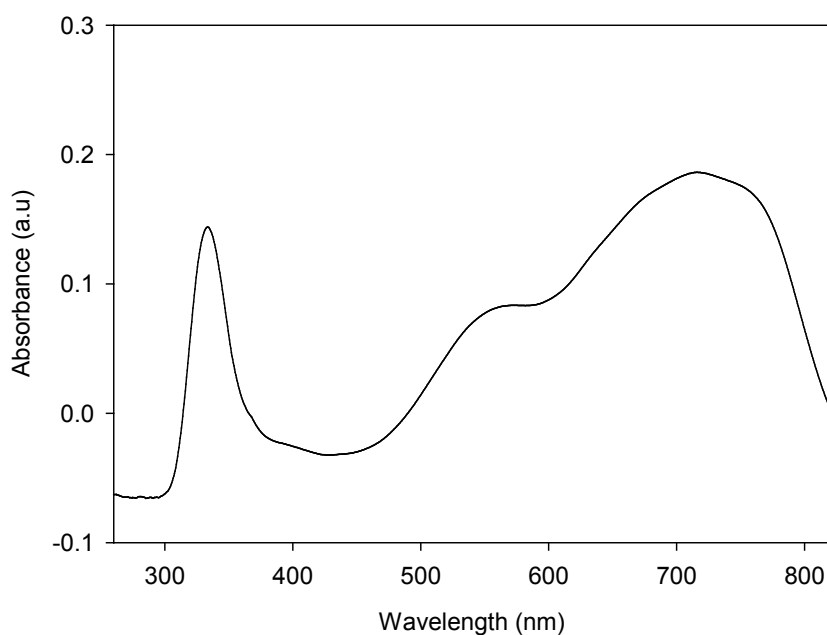


Figure 4.8 Solid state electronic spectrum of [VO(Melm2COO)₂]

4.3.3 pH-Metric chemical speciation

It is important, when dealing with metallopharmaceuticals, to gain a clear understanding of the various species that may exist over a biological pH range. In the previous chapter (**Part 1, Chapter 3**) it was shown that the 2-(2'-hydroxyphenyl)-1*R*-imidazoline ligands did not effectively stabilize vanadyl in the low pH range due to the high protonation constants of the donor groups. The consequence of this was that the ligands easily dissociated in acidic conditions releasing free vanadyl. The negative implications of this include an increased susceptibility to the formation of insoluble hydrolysis species (in more basic conditions) and poorer absorption into the bloodstream.¹⁸ Because of this, we decided to prepare ligands containing the imidazole as well as the carboxylic acid functional groups. The latter functional group we expected would provide additional stability in the acidic pH range.

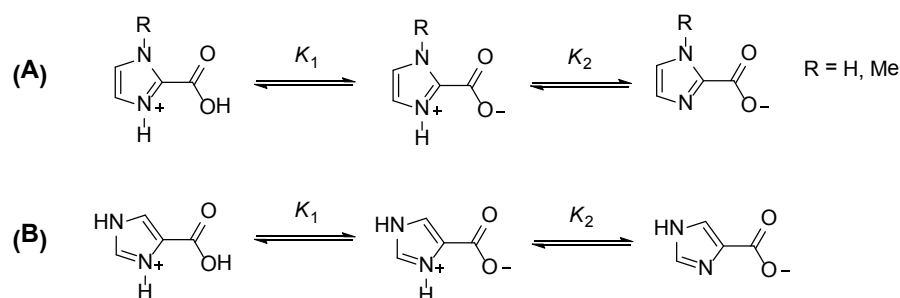
The protonation constants of Im4COOH, Im2COOH and Melm2COO were determined using aqueous potentiometric titrations from an average of six independent titrations each. The stability constants for the VO(IV) – Im4COOH, Im2COOH and Melm2COOH (VO:L ratio's of 1:1, 1:2, 1:5 and 1:10) systems were determined from an average of six titrations and are summarized in **table**

4.2. At a metal:ligand (M:L) ratio of 1:1, only the first binding constants could be calculated due to the formation of hydrolysis species. The species distribution diagrams were generated using the program HySS2009,¹⁹ by inclusion of protonation, stability and hydrolysis constants.

Table 4.2 Protonation ($\log K$) and complex formation constants ($\log \beta$) for VO(IV)-ligand systems at 25 ± 0.1 °C and $I = 0.10$ M (TMACl)

Reaction	Ligand			
	<i>Im4COOH</i>	<i>Im2COOH</i>	<i>Melm2COOH</i>	<i>pic</i> ²⁰
pK_1 $LH_2^+ \rightleftharpoons H^+ + LH$	2.70(3)	2.72(3)	1.3(1)	~1
pK_2 $LH \rightleftharpoons H^+ + L^-$	6.13(1)	6.44(2)	6.75(3)	5.19(2)
$\log\beta_{110}$ $VO^{2+} + L^- \rightleftharpoons [VO(L)]^+$	7.11(2)	7.53(3)	9.84(6)	6.66(2)
$\log\beta_{111}$ $VO^{2+} + H^+ + L^- \rightleftharpoons [VO(LH)]^{2+}$	-	-	14.85(7)	-
$\log\beta_{120}$ $VO^{2+} + 2L^- \rightleftharpoons [VO(L)_2]$	11.38(8)	11.62(6)	15.49(9)	12.11(2)

The relevant protonation/deprotonation reactions are shown in **scheme 4.3** and species distribution diagrams for *Im2COOH* and *Melm2COOH* are shown in **figures 4.9** and **4.10**, respectively. The species distribution diagram for *Im4COOH* was extremely similar to that of *Im2COOH* and as such has not been included. Unlike the 2-(2'-hydroxyphenyl)-1*R*-imidazoline ligands, these ligands exhibit deprotonation at much lower pH values – a property that we had expected to achieve by introducing the carboxyl functionality.



Scheme 4.3 Deprotonation steps of the *Im2COOH* and *Melm2COOH* (A) as well as *Im4COOH* (B) systems. H^+ have been omitted from the equilibria

The ligands Im4COOH and Im2COOH had similar pK_1 values of 2.70 and 2.71 respectively, while that of Melm2COOH was 1.3. Halina (2008),¹⁸ who was investigating the formation constants of V^{3+} with various imidazole carboxylic acids, found the pK_1 of Im4COOH to be slightly lower at 2.3, compared to 2.70 determined in this study. The pK_1 of Melm2COOH ($pK_1 = 1.3$) was comparable to that of picolinic acid (Hpic) ($pK_1 \sim 1$) (table 4.2).²⁰ The lower acidity of the carboxylic acid groups in Im4COOH and Im2COOH compared to Hpic and Melm2COOH may be due to additional stabilization by hydrogen bonding, since these ligands contain unsubstituted N-H groups.²¹ The pK_2 (N-deprotonation) for Im4COOH, Im2COOH and Melm2COOH were 6.13, 6.44 and 6.75 respectively, while that of free imidazole is around 6.95. The carboxylic acid functionality has been known to exert a base weakening effect on the parent heterocycle which explains why in all cases, the pK_2 for the imidazole group in the ligands was lower than that of free imidazole.²² The pK_2 of the N-methyl substituted derivative (Melm2COOH) (6.75) was more basic than the N-H analogues (Im4COOH and Im2COOH) and quite similar to that reported by Franz (6.88).¹⁴ This increased basicity observed upon N-methylation follows the same trend seen for imidazole ($pK = 6.95$) and 1-methylimidazole ($pK = 7.20$).

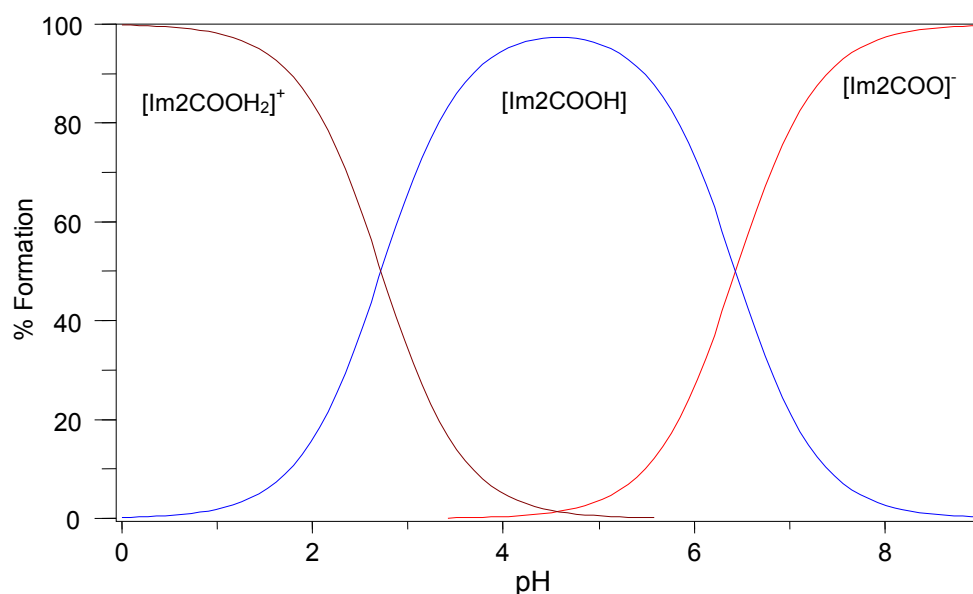


Figure 4.9 Species distribution as a function of pH for imidazole-2-carboxylic acid

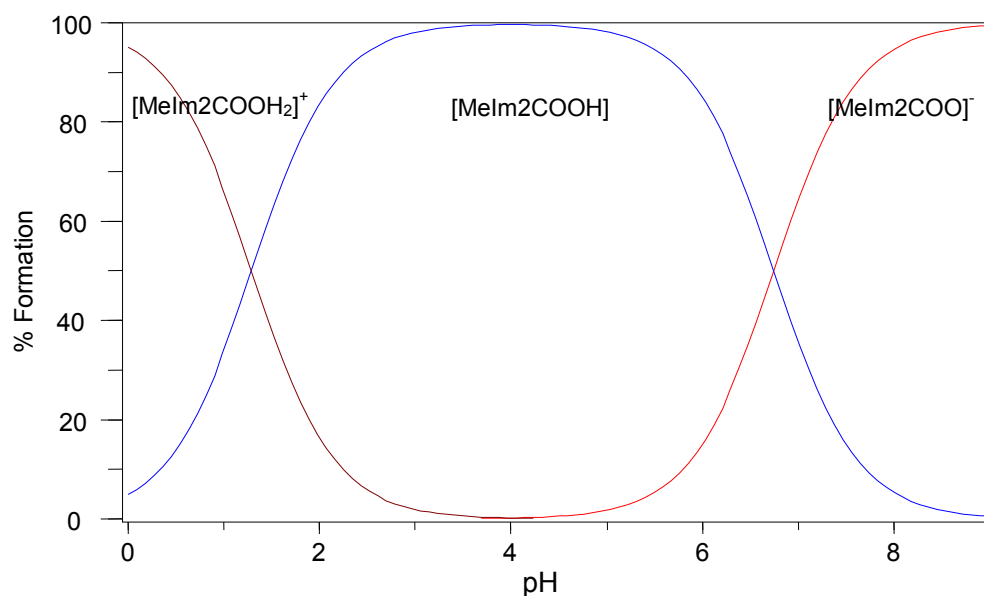
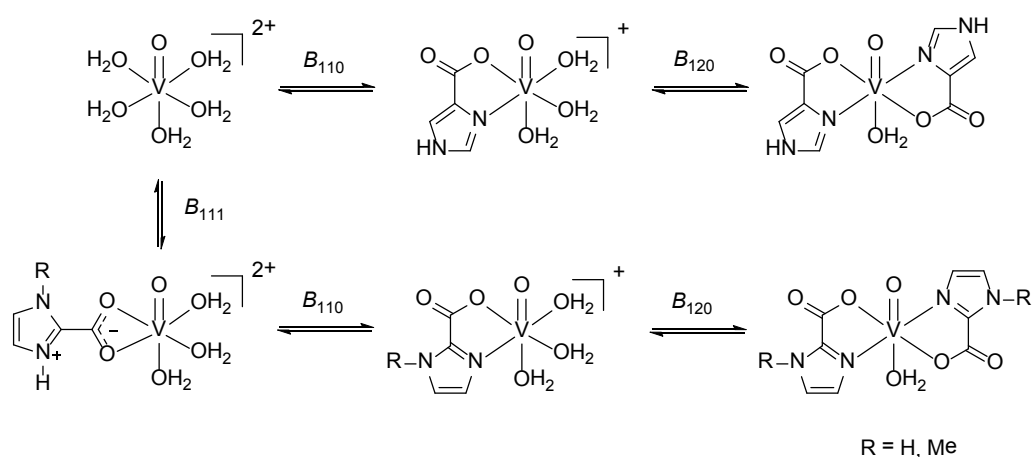


Figure 4.10 Species distribution as a function of pH for N-methylimidazole-2-carboxylic acid

The proposed interactions of these ligands in aqueous solutions with oxovanadium(IV) are represented by **scheme 4.4**. The ligand imidazole-2-carboxylic acid (Im2COOH) shows similar interactions and stability with vanadyl as imidazole-4-carboxylic acid (Im4COOH). The species distribution diagrams are represented by **figures 4.11** and **4.12** for the ($V^{IV}O$)-imidazole-2-carboxylic acid and ($V^{IV}O$)-1-methylimidazole-2-carboxylic acid systems, respectively.



Scheme 4.4 The stepwise formation of oxovanadium(IV) complexes with Im4COOH and MeIm2COOH (R = Me) or Im2COOH (R = H). LH and L^- are omitted in the complexation equilibria as are the hydrolysis equilibria

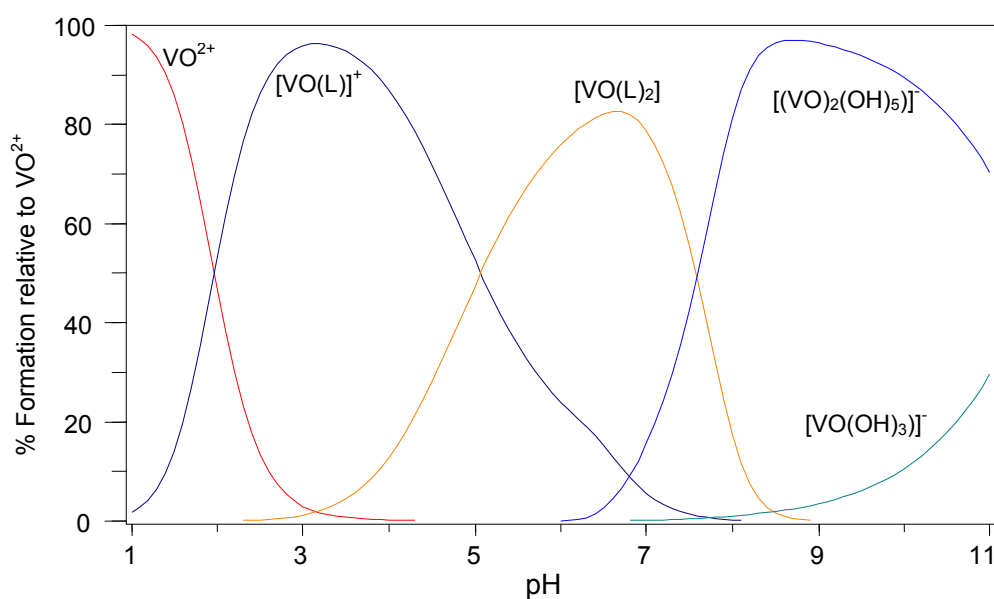


Figure 4.11 Species distribution diagram for the complexation of VO(IV) with Im2COOH (LH), $c_{VO} = 0.002 \text{ mol.L}^{-1}$ and $c_{ligand} = 0.004 \text{ mol.L}^{-1}$

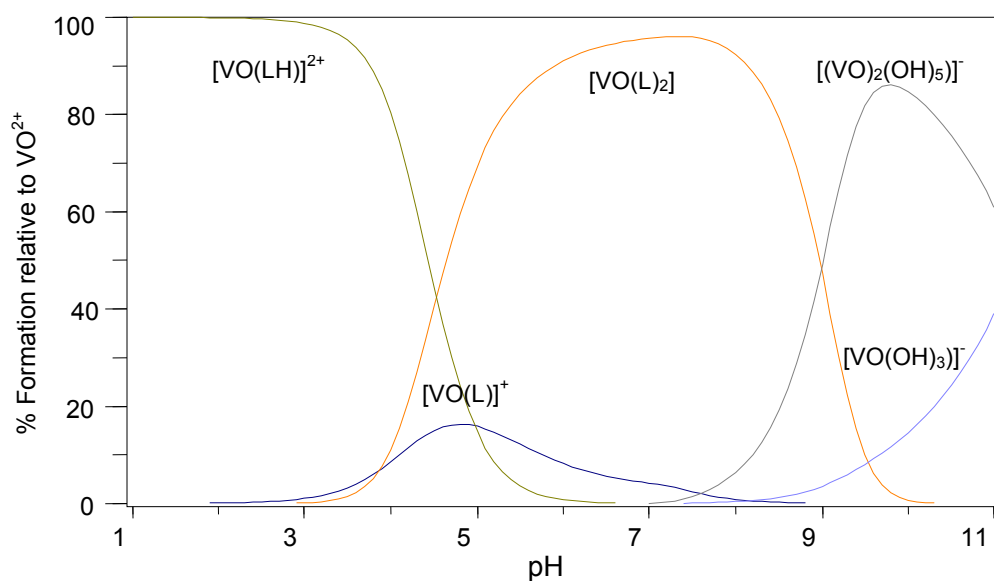


Figure 4.12 Species distribution diagram for the complexation of VO(IV) with Melm2COOH (LH), $c_{VO} = 0.002 \text{ mol.L}^{-1}$ and $c_{ligand} = 0.004 \text{ mol.L}^{-1}$

The first binding constants could be calculated with a 1:1 metal-to-ligand ratio (M:L), however at low M:L ratio's (1:1 and 1:2) hydrolysis occurred, preventing accurate determination of the second binding constants. Thus a high ligand excess (10-fold), was utilized and this allowed for the

determination of the second binding constant. The fitting of the titration data supports the formation of monomeric $[\text{VO}(\text{L})]^+$ and $[\text{VO}(\text{L})_2]$ species as well as the monomeric protonated species, $[\text{VO}(\text{LH})]^{2+}$, for MeIm_2COOH . As shown in **figures 4.11** and **4.12** the presence of the carboxylic acid group on the ligands allowed for coordination at much lower pH values. Considering the $\text{VO-Im}_2\text{COOH}$ system as an example; at pH 3 the main species existing in solution was $[\text{VO}(\text{Im}_2\text{COOH})]^+$ while for the VO-EtpiminH system the $[\text{VO}(\text{EtpiminH})]^+$ species predominated at pH 6 (**Part 1, Chapter 3**). Certainly, looking at the $\text{VO-MeIm}_2\text{COOH}$ system (**figure 4.12**) one can see the predominance of ligand-bound vanadyl species existing over a biological pH range, with hydrolysis products being observed only at relatively high pH values (pH >7.2). The imidazole-carboxylic acid ligands used in this study compared favourably with the structurally similar pyridine-2-carboxylic acid (or picolinic acid) ligand. This was promising considering that the oxovanadium complex of picolinic acid (pic), $\text{VO}(\text{pic})_2$, has been shown to exhibit reasonable antidiabetic activity.²³ The protonation and stability constants can be found in **table 4.2**.

Once the oxovanadium(IV) complexes have passed through the digestive tract and have been absorbed into the bloodstream, they may encounter numerous metal-binding bioligands. These bioligands may completely displace the original ligands or partially displace them to form ternary complexes. This may subsequently affect the transport, absorption and biological activity of the drug. Thus, studying ternary complex formation can be of significant importance. Of the low molecular weight bioligands, citric acid has proven to be one of the strongest binders of the hard vanadyl ion. For this reason, the ternary complex formation between vanadyl, the imidazole-carboxylic acid ligands (Im_4COOH , Im_2COOH and MeIm_2COOH) and citrate has been performed. In this context, the imidazole-carboxylic acid ligands may be interchangeably and collectively referred to as ligand A, while citric acid may be referred to as ligand B. The titrations were performed using different ratios of VO:A:B including; 1:1:1, 1:2:1, 1:2:2 and 1:4:4. Pertinent data regarding citric acid protonation and vanadyl complex formation has been included in **table 4.3** and were considered (along with the metal hydrolysis constants) when fitting the experimental data.

Table 4.3 Proton ($\log K$) and VO^{2+} stability constants ($\log \beta$) for the complexes of citric acid (B) at 25.0 ± 0.1 °C and $I = 0.2$ M (KCl)²⁴

Complex	$\log K / \log \beta$
HB	5.57(2)
H ₂ B	4.27(2)
H ₃ B	2.87(3)
VOBH	10.65(6)
VOB	7.85(7)
(VO) ₂ B ₂ H ₋₁	15.71(7)
(VO) ₂ B ₂ H ₋₂	10.73(4)
(VO) ₂ B ₂ H ₋₃	1.6(2)
VOB ₂ H ₋₂	-2.89(7)
VOBH ₋₂	-5.7(2)

As illustrated in **figure 4.13 - 4.15**, the formation of ternary complexes with citric acid is highly favoured with VOABH, VOAB and VOABH₋₁ dominating over a wide pH range. Starting from an acidic pH, the unsubstituted imidazole-carboxylic acid systems Im2COOH and Im4COOH share similar stability constants for the monoprotonated ternary complex (designated 1,1,1 in **table 4.4**) of 19.82 and 19.67, respectively. These values were comparable to that of maltol and slightly less than kojic acid (dhp) (**table 4.4**). The *N*-methylated analogue, MeIm2COOH, displayed a significantly higher stability constant (22.71) for the formation of this species and was comparable to kojic acid (dhp). For all systems, as the pH increased ($4 < \text{pH} < 6$), the fully ligand-deprotonated ternary species predominated. Finally, under more basic conditions, the mixed hydroxo species [VOAB(OH)]⁻ begins to form ($\text{pH} > 6$). The stability constant for the formation of this species was significantly higher than that of maltol (mal) and picolinic acid (pic) and slightly more comparable to kojic acid (dhp) (**table 4.4**). One may initially suspect that this may be due to the more acidic nature ligands used in this study, especially considering that the stability constant for the formation of this species using dhp (which is structurally similar to mal) was higher than that for mal, and dhp is slightly more acidic than mal ($\text{p}K_{\text{mal}} = 8.44$; $\text{p}K_{\text{dhp}} = 7.67$). However, picolinic acid

which is more acidic than the imidazole-carboxylic acid ligands (**table 4.4**) has a lower stability constant for this process.

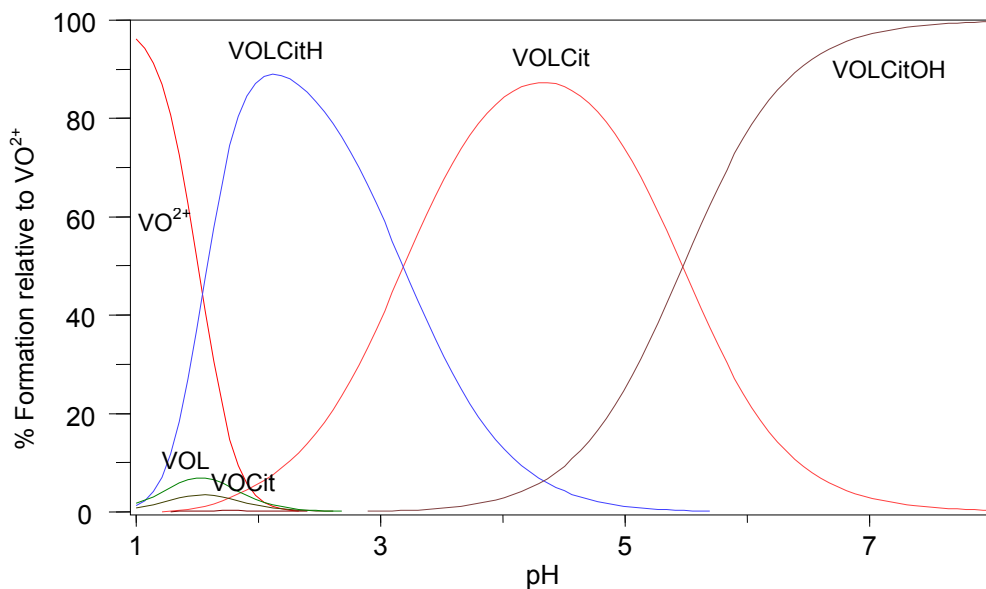


Figure 4.13 Species distribution diagram for the complexation of VO(IV) with Im4COOH (LH) and citric acid (Cit), $c_{\text{VO}} = 0.002 \text{ mol.L}^{-1}$, VO:A:B (1:2:2)

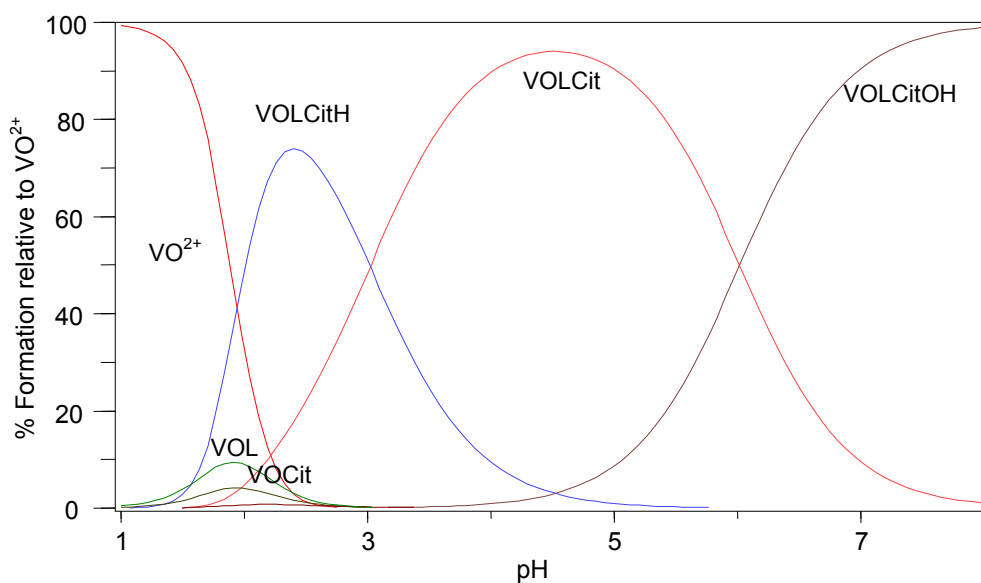


Figure 4.14 Species distribution diagram for the complexation of VO(IV) with Im2COOH (LH) and citric acid (Cit), $c_{\text{VO}} = 0.002 \text{ mol.L}^{-1}$, VO:A:B (1:2:2)

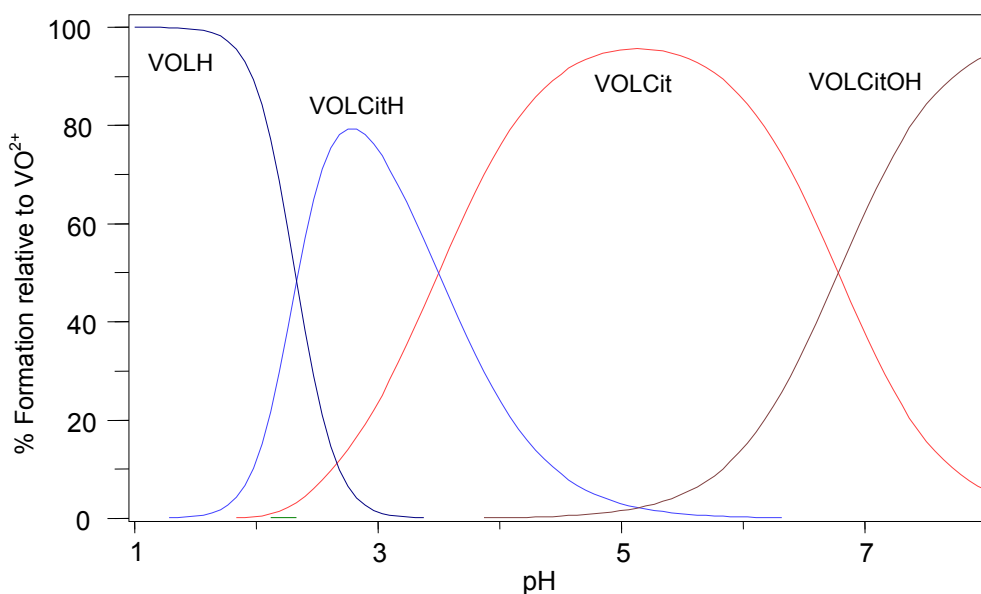


Figure 4.15 Species distribution diagram for the complexation of VO(IV) with Melm2COOH (LH) and citric acid (Cit), $c_{VO} = 0.002 \text{ mol.L}^{-1}$, VO:A:B (1:2:2)

Table 4.4 Stability constants of mixed ligand VO^{2+} complexes of Im2COOH, Im4COOH and Melm2COOH with citric acid at $25 \pm 0.1 \text{ } ^\circ\text{C}$. P,q,r represents ligand A, ligand B and protons/hydroxides, respectively

p,q,r	Im2COOH*	Im4COOH*	Melm2COOH*	mal ²⁵ †	dhp ²⁶ †	pic ²⁷ †
1,1,1	19.82(2)	19.67(3)	22.71(1)	18.85(6)	22.28(3)	16.96(4)
1,1,0	16.78(2)	16.48(3)	19.21(2)	15.41(3)	18.66(2)	13.33(4)
1,1,-1	10.72(4)	11.01(5)	12.43(5)	7.54(3)	10.25(3)	7.57(3)

*This work, $I = 0.10 \text{ M}$ (TMACl); † $I = 0.20 \text{ M}$ (KCl)

4.3.4 In vitro glucose uptake studies

The vanadium compounds $[VO(\text{Im}4\text{COO})_2]$, $[VO(\text{Im}2\text{COO})_2]$, $[VO(\text{Melm}2\text{COO})_2]$ and the simple vanadium salt, VOSO_4 , showed no cytotoxicity (>80% cell viability) between 0.5-10 μM in the 3T3-L1, Chang and C2C12 cell lines tested as determined by an MTT-cell viability assay. Similar to the vanadium compound prepared in the previous chapter (**Part 1, Chapter 3**), at concentrations

over 10 μM , the vanadium compounds proved to be too cytotoxic (<80% cell viability). Thus, the glucose uptake ability of the vanadium compounds, at non-cytotoxic concentrations of 0.5, 1 and 10 μM , was screened. The results for the 1 μM concentrations are presented in **figure 4.16**, while the results for all concentrations tested can be found in **table 4.5**.

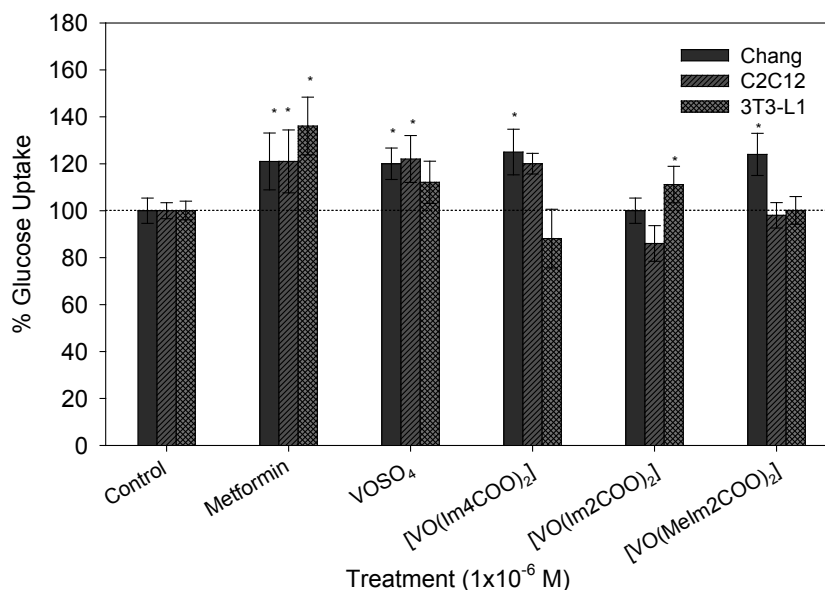


Figure 4.16 The effects of metformin (Met), vanadyl sulfate (VOSO₄), [VO(lm4COO)₂], [VO(lm2COO)₂] and [VO(MeIm2COO)₂] (at 1 μM concentration) on Chang, C2C12 and 3T3-L1 glucose uptake. The basal glucose uptake, is represented as 100% (Control). Error bars indicate SEM (n=3), * (p < 0.05) relative to the (Con).

There were varying effects observed in the 3T3-L1 adipocytes (**figure 4.16**). Metformin, along with vanadyl sulfate and [VO(lm2COO)₂] improved glucose uptake. However for [VO(lm4COO)₂] and [VO(MeIm2COO)₂], less than basal glucose uptake was observed. For the Chang cells, enhanced glucose uptake was observed for all (besides [VO(lm2COO)₂]) of the oxovanadium(IV) compounds. In the C2C12 cells, VOSO₄ and [VO(lm4COO)₂] enhanced glucose uptake to a level comparable to Metformin. When higher than 1 μM concentrations of the oxovanadium(IV) compounds were administered to the cells, the general trend was a slight drop in glucose uptake, possibly due to some cytotoxicity at these conditions (**table 4.5**).

Table 4.5 The effects of metformin (Met), VOSO_4 , $[\text{VO}(\text{Im4COO})_2]$, $[\text{VO}(\text{Im2COO})_2]$ and $[\text{VO}(\text{MeIm2COO})_2]$ on 3T3-L1, Chang and C2C12 cells at 0.5, 1.0 and 10 μM concentrations. Basal glucose uptake is represented as 100%

Compound	3T3-L1 adipocytes			Chang hepatocytes			C2C12 myoblasts		
	Concentration (μM)								
	0.5	1	10	0.5	1	10	0.5	1	10
Metformin	-	136 \pm 12.3	-	-	121 \pm 12.1	-	-	121 \pm 13.4	-
VOSO_4	100 \pm 7.5	112 \pm 9.1	109 \pm 5.5	102 \pm 6.6	120 \pm 6.7	91 \pm 5.0	92 \pm 12.1	122 \pm 10.0	99 \pm 3.2
$[\text{VO}(\text{Im4COO})_2]$	92 \pm 11.2	88 \pm 12.5	76 \pm 3.2	104 \pm 7.1	125 \pm 9.7	95 \pm 12.3	96 \pm 4.9	120 \pm 4.4	78 \pm 7.9
$[\text{VO}(\text{Im2COO})_2]$	96 \pm 12.4	111 \pm 7.8	79 \pm 11.1	99 \pm 7.2	100 \pm 5.4	101 \pm 13.4	102 \pm 6.2	86 \pm 7.6	65 \pm 4.1
$[\text{VO}(\text{MeIm2COO})_2]$	89 \pm 17.6	100 \pm 5.9	88 \pm 9.8	114 \pm 9.1	124 \pm 8.9	111 \pm 3.2	103 \pm 5.7	98 \pm 5.4	89 \pm 9.9

4.3.5 Anticoagulation studies

A similar trend was observed for these compounds as was observed for $[\text{VO}(\text{pimin})_2]$ as discussed in **Part 1, Chapter 3**. For the APTT and PT screening tests, only heparin (positive control) significantly increased clotting times relative to the control (**figure 4.17**). Thus, the oxovanadium(IV) complexes did not affect either the intrinsic or extrinsic pathways. No significant or conclusive results could be drawn from the Fib-C screening test either. $[\text{VO}(\text{Im4COO})_2]$ decreased Fibrin formation slightly however this was within error of the control (solvent vehicle) and certainly not as significant as the positive control, heparin. The D-Dimer test once again showed promising results, with all the oxovanadium(IV) complexes reducing D-Dimer formation comparably to that of heparin thereby suggesting a reduction in the state of hypercoagulation.

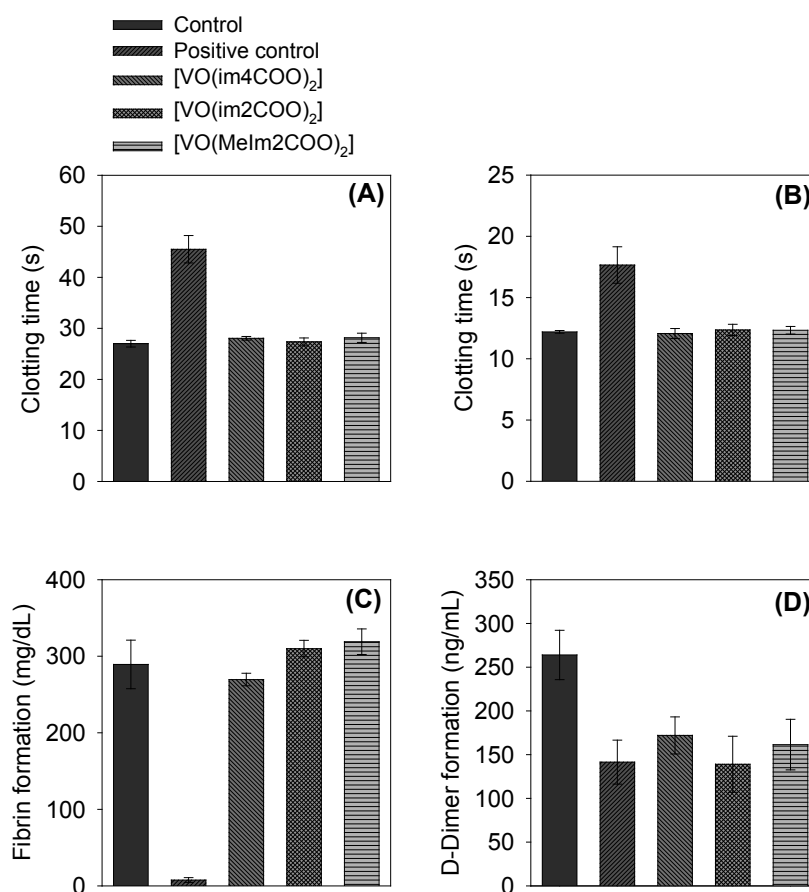


Figure 4.17 The effect of $[\text{VO}(\text{Im4COO})_2]$, $[\text{VO}(\text{Im2COO})_2]$ and $[\text{VO}(\text{Melm2COO})_2]$ (10 μM) on APTT (A) and PT (B) clotting times, on fibrin formation (C) and D-Dimer formation (D). The control represents untreated sample while the positive control represents the anticoagulant heparin (0.1 $\text{U}\cdot\text{mL}^{-1}$) ($n = 3$)

4.4 Conclusions

A range of oxovanadium(IV) complexes with bidentate imidazolyl-carboxylato ligands were successfully prepared and characterized. Aqueous potentiometric titrations revealed that incorporation of the acidic carboxylic acid group did indeed improve stability at low pH values compared to the 2-(2'-hydroxyphenyl)-1*R*-imidazoline ligands in **Part 1, Chapter 3**. Additionally, when including citric acid in the titrations, ternary complex formation of vanadyl with the imidazole-carboxylic acid and citric acid was highly favoured. The prepared complexes exhibited minimal toxicity in the concentration range tested as well as glucose lowering activity in an *in vitro* assay using muscle, liver and fat cells. In addition, all of the complexes displayed anticoagulative activity as evidenced by inhibition of D-Dimer formation. The prepared oxovanadium(IV) complexes may represent an alternative and competitive option to the well studied BMOV and V O(pic)₂ complexes, however *in vivo* studies would be required to unequivocally confirm this.

4.5 References

- (1) Martinez-Carrera, S. *Acta Cryst.* **1966**, *20*, 783.
- (2) Berthier, G., Praud, L., Serre, J.; Bergman, E. D., Pullman, B. *Quantum aspects of heterocyclic compounds in chemistry and biochemistry*, Israel Academy of Science: Jerusalem, 1970.
- (3) Clementi, E. *J. Chem. Phys.* **1967**, *46*, 4751.
- (4) Bouwman, E.; Douziech, B.; Gutierrez-Soto, L.; Beretta, M.; Driessen, W. L.; Reedijk, J.; Mendoza-Díaz, G. *Inorg. Chim. Acta.* **2000**, *304*, 250.
- (5) Arber, J. M.; De Boer, E.; Garner, C. D.; Hasnain, S. S.; Wever, R. *Biochemistry* **1989**, *28*, 7968.
- (6) Congiu, C.; Cocco, M. T.; Onnis, V. *Bioorg. Med. Chem. Lett.* **2008**, *18*, 989.
- (7) Khabnadideh, S.; Rezaei, Z.; Khalafi-Nezhad, A.; Bahrinajafi, R.; Mohamadi, R.; Farrokhoz, A. A. *Bioorg. Med. Chem. Lett.* **2003**, *13*, 2863.
- (8) Göker, H.; Ertan, R.; Akgün, H.; Yulung, N. *Arch. Pharm.* **1991**, *324*, 283.
- (9) Crane, L.; Anastassiadou, M.; Hage, S. E.; Stigliani, J. L.; Baziard-Mouysset, G.; Payard, M.; Leger, J. M.; Bizot-Espiard, J.-G.; Ktorza, A.; Caignard, D.-H.; Renard, P. *Bioorg. Med. Chem. Lett.* **2006**, *14*, 7419.
- (10) McLauchlan, C. C.; Hooker, J. D.; Jones, M. A.; Dymon, Z.; Backhus, E. A.; Greiner, B. A.; Dorner, N. A.; Youkhana, M. A.; Manus, L. M. *J. Inorg. Biochem.* **2010**, *104*, 274.
- (11) Kirk, K. L. *J. Org. Chem.* **1978**, *43*, 4381.
- (12) Tertov, B. A.; Koshchienko, Y. V. *Chem. Heterocycl. Compd.* **1988**, *24*, 117.
- (13) Lipshutz, B. H.; Huff, B.; Hagen, W. *Tetrahedron Lett.* **1988**, *29*, 3411.
- (14) Franz, R. G. *AAPS J.* **2001**, *3*, XI.
- (15) Shirley, D. A. *J. Am. Chem. Soc.* **1957**, *79*, 4922.
- (16) Franz, R. G., MSc Thesis, Lehigh University, 1999.
- (17) Selbin, J.; Holmes Jr, L. H.; McGlynn, S. P. *J. Inorg. Nucl. Chem.* **1963**, *25*, 1359.
- (18) Setyawati, I. A.; Thompson, K. H.; Yuen, V. G.; Sun, Y.; Battell, M.; Lyster, D. M.; Vo, C.; Ruth, T. J.; Zeisler, S.; McNeill, J. H.; Orvig, C. *J. Appl. Physiol.* **1998**, *84*, 569.
- (19) Alderighi, L.; Gans, P.; Ienco, A.; Peters, D.; Sabatini, A.; Vacca, A. *Coord. Chem. Rev.* **1999**, *184*, 311.

-
- (20) Kiss, E.; Petrohán, K.; Sanna, D.; Garribba, E.; Micera, G.; Kiss, T. *Polyhedron* **2000**, *19*, 55.
- (21) Sanna, D.; Micera, G.; Buglyó, P.; Kiss, T.; Gajda, T.; Surdy, P. *Inorg. Chim. Acta.* **1998**, *268*, 297.
- (22) Schofield, K., Grimmett, M. R., Keene, B. R. T. *Heteroaromatic nitrogen compounds : the azoles*; Cambridge University Press: Cambridge, 1976.
- (23) Melchior, M.; Thompson, K. H.; Jong, J. M.; Rettig, S. J.; Shuter, E.; Yuen, V. G.; Zhou, Y.; McNeill, J. H.; Orvig, C. *Inorg. Chem.* **1999**, *38*, 2288.
- (24) Kiss, T.; Buglyó, P.; Sanna, D.; Micera, G.; Decock, P.; Dewaele, D. *Inorg. Chim. Acta.* **1995**, *239*, 145.
- (25) Kiss, T.; Kiss, E.; Micera, G.; Sanna, D. *Inorg. Chim. Acta.* **1998**, *283*, 202.
- (26) Buglyó, P.; Kiss, T.; Kiss, E.; Sanna, D.; Garribba, E.; Micera, G. *J. Chem. Soc., Dalton Trans.* **2002**, 2275.
- (27) Kiss, E.; Garribba, E.; Micera, G.; Kiss, T.; Sakurai, H. *J. Inorg. Biochem.* **2000**, *78*, 97.

This page has been left blank intentionally

Chapter 5

Conclusions and future work

5.1 Conclusions

The first set of oxovanadium(IV) complexes with 2-(2'-hydroxyphenyl)-1*R*-imidazoline ligands were successfully prepared and characterized. The solution model predicted that in the acidic pH-range, these complexes would dissociate and thus, when administered orally would require the use of a drug encapsulation technique. Conversely, the excellent stability of the complexes under basic conditions would mitigate the formation of insoluble vanadyl hydrolysis species in the intestine and therefore improve uptake into the blood stream and subsequently cause less gastrointestinal stress. A series of imidazole-carboxylic acid ligands and the corresponding oxovanadium(IV) complexes were then prepared. The carboxylic acid group was significantly more acidic than the phenol group of the 2-(2'-hydroxyphenyl)-1*R*-imidazoline ligands, which had the desired effect of improving low pH stability. All of the complexes demonstrated mild antihyperglycemic activity along with anticoagulation activity *via* D-Dimer inhibition.

5.2 Future work

It became very clear while undertaking this work that although the *in vitro* assay may be a useful indicator for antidiabetic activity, it does not accurately mimic the biological system, especially considering that the proposed mechanism of action of these vanadium drugs is not a typical drug-receptor interaction (where the drug remains in-tact). Rather, it has been proposed that the main function of the ligands is to transport vanadium into the blood stream and prevent hydrolysis, after which they may be replaced partially or completely by bioligands.

Thus rat-model studies (eg. STZ, Zucker or Cafeteria diabetic rats), which account for the digestive system and the interaction of the vanadium complexes with transport proteins in the blood, would be important to make any reasonable comparisons with current lead compounds. On

that note, the interaction of these complexes with transferrin in particular may provide further information, especially considering that there has been few, if any, studies relating the formation of ternary complexes to toxicity or antidiabetic activity. Thus an in-depth study comparing a range of different oxovanadium(IV) complexes, each coordinated to ligands which fall under the categories of weak, intermediate or strong carrier, may provide insight into a different or parallel mechanism of cellular uptake or antidiabetic action.

This page has been left blank intentionally

Part 2

Catalytic properties of heterogeneous oxovanadium(IV) complexes

Chapter 1

Introduction

1.1 Catalysis

The term catalysis, first coined in 1836 by Berzelius, refers to a process in which a substance (the catalyst) influences the rate of a reaction without being consumed.¹ Since then, the field of catalysis has expanded rapidly especially with the advent of 'green chemistry'. The chemical industry is arguably the most successful sector of the manufacturing industry. Within this industry approximately 75% of chemicals are produced with the aid of catalysts.² Catalysts can be subdivided into two main types namely; homogeneous and heterogeneous catalysts. These names refer to the phase in which they exist with the reaction medium.

The value of homogeneous catalysts cannot be understated, especially under laboratory scale conditions. However, the industrial applicability of these catalysts is quite limited compared to the heterogeneous counterparts. The main reason for this can be linked primarily to the difficulties associated with separation of homogeneous catalysts from the reaction solution. Not only does this lead to increased costs, but also environmental concerns. The very nature of these catalysts also limits their use to batch rather than continuous flow reactions, another negative for industrial application.³ A table comparing these two types of catalysts has been included (**table 1.1**).

Table 1.1 Comparison of homogeneous and heterogeneous catalysts²

Heterogeneous Catalysts	Homogeneous Catalysts
Simple separation and recyclability	Often difficult to separate
Diverse process applicability	Limited process applicability (batch only)
Diffusion controlled	Diffusion limitations practically absent
Lower selectivity	Generally high selectivity
Thermally stable	Lower thermal stability
Well defined structure	Structure can be difficult to identify

1.2 Vanadium in catalysis

Vanadium is one of the most abundant metals in the earth's crust, found in over a hundred different minerals as well as in crude oils bound by porphyrins.⁴ The majority of vanadium is extracted from titaniferrous magnetite ores, with about 38 000 tonnes being produced annually. Most of this is used as a steel additive (80%) or in combination with other metals to form strong light weight alloys, commonly used in the aerospace industry.

Other than the metallurgical applications, the most common use of vanadium is in the field of catalysis, accounting for about 5% of the annual production of this metal.⁵ Vanadium catalysts are used in the manufacture of a number of important chemicals, the most commonly known of these probably being the production of sulfuric acid by the Contact process. Other industrial applications include the production of phthalic and maleic anhydride,⁶ oxidation of sulfur dioxide⁷ as well as the removal of nitrogen oxides which are of environmental concern.⁸ The catalytic capabilities of vanadium go far beyond these few reactions. To name a few, supported vanadium catalysts have been used for the selective oxidation of alkanes and alkenes, oxidation of methanol to formaldehyde, photo-oxidation of CO, oxidation of H₂S, polymerization of olefins and the oxidative coupling of methane.⁵ A brief description of some of the reactions in which vanadium based heterogeneous catalyst are utilized has been included (**table 1.2**).

Table 1.2 Overview of a few reactions catalyzed by supported vanadium catalysts

Catalytic Reaction	References
Oxidation of alkanes, alkenes and alcohols	9,10
Olefin polymerization	11
Oxidative halogenation	12
Oxidation of methanol to formaldehyde	13
Epoxidation of alkenes	14
Hydroxylation of benzene and phenol	15,16
Oxidation of H ₂ S to S	17
Hydroamination and oxidative amination	18,19
Asymmetric epoxidations and oxidations	20
Addition of propargyl alcohols and imines	21
Biginelli condensation of an aldehyde β -keto ester and urea	22
Enantioselective oxidative coupling of 2-naphthols	23

Many of these processes utilize the heterogeneous forms of vanadium catalysts. Commonly, a vanadium oxide phase is deposited on the surface of an oxide support such as, SiO₂, Al₂O₃, TiO₂ and ZrO₂. Other than the silica, alumina and other metal oxides; organic polymers, zeolites and carbon have been used as supports for immobilization of homogeneous catalysts. The four main methods for preparing heterogeneous catalysts or immobilizing (heterogenization) homogeneous catalysts are listed below and include;

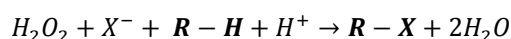
1. Adsorption
2. Encapsulation
3. Covalent linking
4. Electrostatic interactions.

In the first method (adsorption), predominantly van der Waals interactions keep the catalyst bound to the support. This is typically a weak interaction which may be improved by hydrogen bonding or other interactions such as π -stacking. Encapsulation does not rely on bonding interactions but

rather on pore sizes of the support. Of course the catalyst must be larger than these pores to prevent leaching. The advantage of this technique is that it probably best represents the original homogeneous catalyst since there are no bonding interactions that could affect the electronic properties of the metal. Conversely, techniques such as covalent linking and immobilization via electrostatic interactions have obvious ramifications in terms of the catalysts' electronic properties. The latter technique relies on the same concept as ion exchange with silicates and zeolites commonly used as supports in this regard. Covalent linking, as the name suggests, utilizes strong covalent bonds to immobilize the catalysts resulting in a fairly stable material.

1.2.1 Naturally occurring vanadium-dependent haloperoxidases

As is so often the case, 'mother nature' was the first to discover the oxidative catalytic potential of vanadium. The class of enzymes known as vanadium-dependent haloperoxidases (VHPO's) are capable of oxidising halides (iodide, bromide, chloride) in the presence of hydrogen peroxide to form halogenated organic compounds which are thought to provide chemical defence for the associated organisms.²⁴ These enzymes are further classified based on the most electronegative halogen oxidized. Thus, vanadium chloroperoxidases (V-CIPOs) can oxidize chloride, bromide and iodide, while vanadium bromoperoxidase can oxidize bromide and iodide.²⁵ The general reaction that these enzymes catalyze is shown below:



VHPO's catalyze the two electron oxidation of a halide (X^-) using H_2O_2 as an oxidant to afford a halogen intermediate (such as Br^+ or biological equivalent).²⁶ Following this, the halogen intermediate can react with either an organic substrate to afford the halogenated organic molecules, or with another equivalent of hydrogen peroxide, producing singlet state diatomic oxygen ($^1O_2^*$).^{27,28}

These enzymes are quite robust, capable of withstanding temperatures of up to 70 °C as well as surviving in organic solvents and excess H_2O_2 . VHPO's are commonly found in marine algae such as *A. nodosum*, *C. pilulifera*, *Cor. officinalis* to name a few (**figure 1.1**).²⁶ Several single crystal X-ray structures of these enzymes have been solved and while some differences between them

exist, the vanadium binding sites are relatively conserved.^{24,29} As the name suggests, the enzymes contain a vanadium atom located in the active site which adopts a five-coordinated trigonal-bipyramidal geometry. This centre is coordinated to four oxygen atoms, three hydroxyl oxygens in equatorial positions and an oxo group in an axial position. Interestingly, in the binding site of all VHPOs, vanadium is bound by an imidazole group of a histidine residue coordinated to the remaining axial position *trans* to the oxo group in the trigonal-bipyramid (**figure 1.2**).^{24,29}

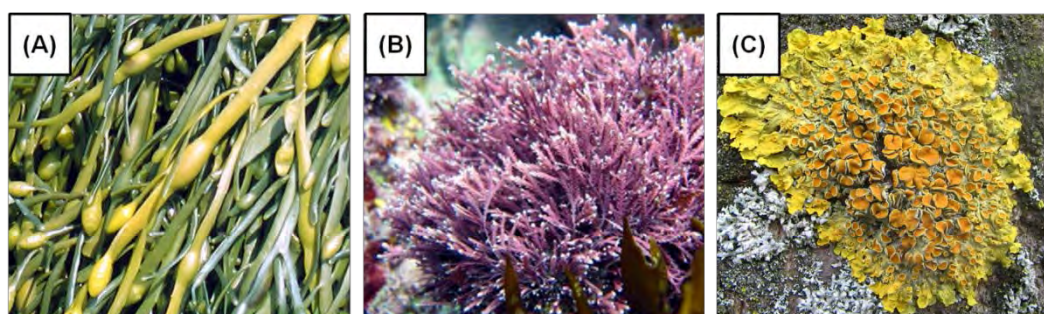


Figure 1.1 Bromoperoxidases are found in *A. nodusum* (A), *Cor. officinalis* (B) and *X. parietina* (C)^{30,31}

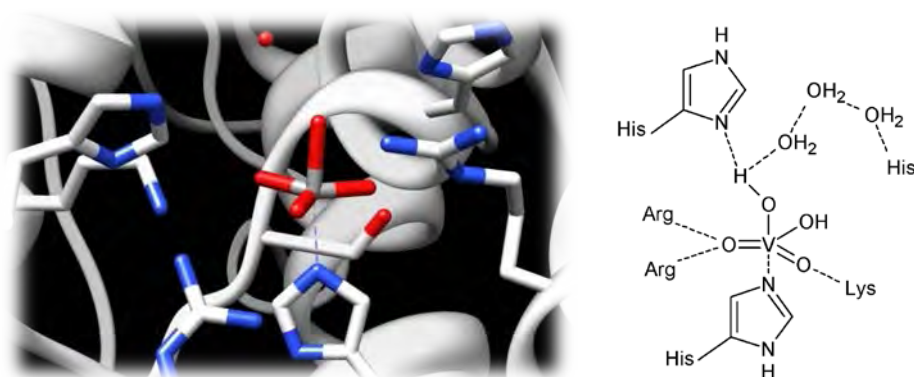


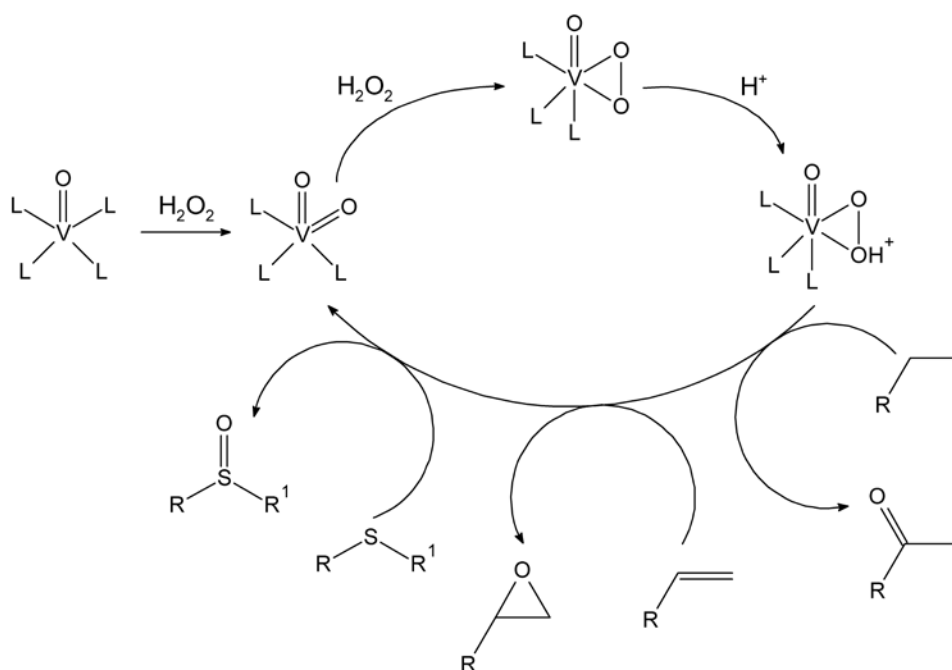
Figure 1.2 The active site of the bromoperoxidase from *Ascophyllum nodusum* showing vanadium coordinated to the imidazole group of a histidine residue (HIS 486) and the close proximity of two other histidine residues (HIS 418 and HIS 411). PDB ID: 1QI9, illustrated using UCSF Chimera²⁹

The discovery of these enzymes has incited the development of structural and functional VHPO model complexes.³² Many of these complexes contain imidazole^{33,34} and benzimidazole-based ligands,^{35,36} and all have shown promising catalytic activity. Despite this, there is still a need for

further perfection of these complexes in terms of geometrical similarity and activity.³⁷ In addition, the activity of these VHPO models is not limited to halogenation reactions and encompasses numerous oxidation reactions including sulfides, alkanes, alkenes and alcohols.^{36,38}

1.2.2 Catalytic mechanism of oxovanadium(IV) oxidations

Several studies have been performed focusing on the determination of the catalytic mechanism of these so called 'VHPO-inspired' catalysts.³⁶ Comprehensive ⁵¹V NMR,³⁹ UV/Vis³³ and EPR³⁹ studies suggest initial oxidation of oxovanadium(IV) to dioxovanadium(V) followed by addition of the peroxide to form the oxoperoxo-species (**scheme 1.1**). Furthermore, in an acidic medium, the peroxy may protonate to form the hydroxyl-peroxovanadium(V) species.⁴⁰ These peroxovanadium species are more reactive than the original hydrogen peroxide and react with the substrate to afford the oxidation product.²⁴



Scheme 1.1 Simplified catalytic mechanism for the vanadium-peroxide oxidation of alkenes, alkanes and sulfides. Here L may refer to an adjacent donor atom or a solvent molecule.

1.3 Support materials for immobilization of homogeneous catalysts

The support material influences the performance of the catalysts significantly and as such should be developed with a sound understanding of the chemical processes being investigated. Thermal, chemical and mechanical stability along with large surface areas are just a few of the desirable components that make for a useful support.³ Silica-based resins have become an extremely popular choice as catalytic support materials due to the low cost, wide availability, mechanical stability and high porosity.⁴¹ The group of crystalline aluminosilicates known as zeolites form another popular choice. The well-defined pore shape and size of these materials offers the advantage of shape/size selective catalysis, in which only molecules smaller than the pore diameter will take part in the reaction.⁴² This thesis focuses on the use of polymers as support materials.

1.3.1 The basics of polymerization

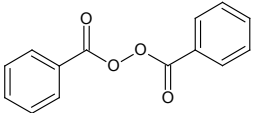
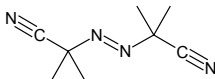
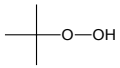
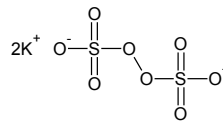
Polymer supports have only recently (the last few decades) begun to gain popularity. The initial lack of interest was possibly due to the underlying suspicion that being organic themselves, these supports could take part in the reaction, for example by being oxidized, thus eventually leading to deterioration of the support. Although this is a valid concern, it has proven to be less of a problem than initially suspected.⁴³ As will be shown in this section, there are a vast number of chemical modifications that can be performed on polymers, producing unique materials with interesting functionalities.

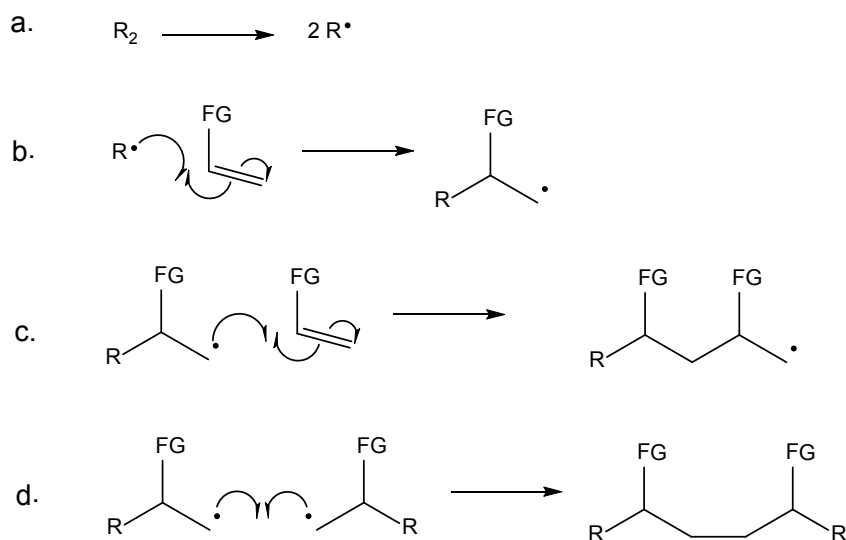
Perhaps the most popular method of producing polymeric material is that of radical initiated polymerization. This is probably due to the wide variety of monomers that lend themselves to this type of reaction. Certain vinyl monomers may undergo polymerization on heating even in the absence of an initiator; however most require an initiator of some kind. Radical initiators may be divided into four major groups; peroxides and hydroperoxides, azo compounds, redox initiators and photoinitiators. The most popular of these are benzoyl peroxide, *tert*-butyl hydroperoxide, 2,2'-azobisisobutyronitrile, potassium persulfate and benzophenone respectively (**table 1.3**).

These initiators provide the initial radical which then reacts with the vinylic monomer. This radical containing monomer reacts with another monomer to form a dimer radical species. This process

is known as chain propagation and continues until terminated by radical coupling, combination or disproportionation (**scheme 1.2**). Chain transfer in radical polymerization refers to the process whereby the propagating radical combines with a transfer agent yielding a dead polymer and a small radical. Should this radical be unstable, it may combine with the monomer to initiate chain growth of a new polymer. The general effect of a chain transfer agent is a reduction in the degree of polymerization and hence shorter polymer chains are produced.⁴⁴

Table 1.3 Some common thermal free radical initiators for polymerization of vinyl monomers

Name	Structure	Name	Structure
Benzoyl peroxide (BPO)		2,2-Azobisisobutyronitrile (AIBN)	
<i>Tert</i> -butyl hydroperoxide (TBHP)		Potassium persulfate (KPS)	



Scheme 1.2 Radical initiation (a), propagation (b-c) and termination (d)

1.3.2 Soluble polymer supports

The use of polymers as support materials is widespread.^{45,46} Soluble (linear) polymers have been used as support materials for catalysts, the aim of these being to bridge the gap between heterogeneous and homogeneous catalysts. Diffusion limitations associated with heterogeneous catalysts are reduced due to the polymer solubility, but the polymers may be collected by precipitation using a non-solvent however, this method can result in sticky polymers that are difficult to work with. Other methods of recovery include tedious micro and ultrafiltration. Then there are the solution problems, the polymer must dissolve in the reaction solvent, but should not be used at high concentrations that make the solution too viscous. For this reason, the concern from here on will be on purely heterogeneous polymer supports.

1.3.3 Techniques for producing polymer beads

Polymers can be made insoluble by the addition of a crosslinking agent. The crosslinker typically contains two or more sites for polymerization thereby linking different polymer chains to make a highly branched but interconnected network. The most frequently used crosslinkers are divinylbenzene (DVB) and ethylene glycol dimethacrylate (EGDMA), however there are many others (**table 1.4**). Different forms of these insoluble polymers can be obtained depending on the type of polymerization used. Probably the simplest method is that of bulk polymerization, in which the functionalized monomer, crosslinker and initiator are polymerized in the absence of a solvent. The resultant monolith can be crushed and sieved to obtain particles with relevant diameters.

In this study we are primarily concerned with the forms of polymerization that produce particles with specific morphologies since irregularly shaped particles may, for instance, break down to form fine particles. A number of different polymerization techniques exist which are capable of meeting these requirements, the most popular being emulsion, dispersion and suspension polymerization. Emulsion polymerization typically gives uniform sized particles with diameters of less than 1 μm . Dispersion and suspension polymerization produce larger beads but with a broad particle size distribution.⁴⁷

Table 1.4 Structures and names of some common crosslinking agents

Name	Structure	Name	Structure
Divinylbenzene (DVB)		<i>N,N'</i> - <i>m</i> -phenylenebis-(methacrylamide)	
<i>m</i> -Diisopropenylbenzene (DIP)		<i>N,N'</i> - <i>m</i> -phenylenebis-acrylamide	
Ethylene glycol dimethacrylate (EGDMA)		<i>N,N'</i> -Bisacrylylcystamine	
Tetramethylene glycol dimethacrylate (TDGMA)		Trimethylolpropane trimethacrylate (TRIM)	
<i>N,N'</i> -ethylenebisacrylamide (EBAAM)		Pentaerythritol triacrylate (PETRA)	
<i>N,N'</i> -hexamethylenebisacrylamide (HMEBAAM)		Pentaerythritol tetraacrylate (PETRA)	

(a) Emulsion polymerization

First developed in the 1920's by the Goodyear Tire and Rubber Company, emulsion polymerization accounts for a huge amount of the total polymer production, more than 20 million tons per year.⁴⁸ In this technique, a hydrophobic monomer is dispersed in an aqueous phase by use of a surfactant (often termed emulsifying agent). Unlike suspension polymerization, a water-soluble radical initiator is used. The radicals diffuse from the aqueous phase into the swollen monomer containing micelles and as the monomer is depleted, more migrates into the micelles (**figure 1.3**)⁴⁹ allowing for the formation of very large molecular weight polymers. Much smaller

diameter spheres (compared to suspension polymerization) can be obtained using this method.⁴² The main disadvantage of this type of polymerization is contamination of the product with surfactants and additives. Although these resins are much smaller and consequently may have high surface area-to-volume ratios, they can become difficult to separate from solution and often centrifugation is required.

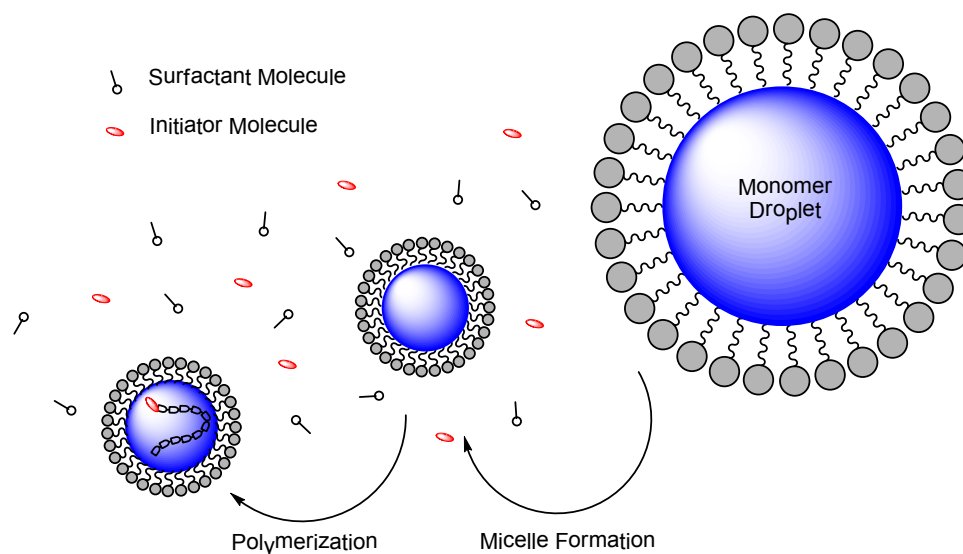


Figure 1.3 Illustration of the process of emulsion polymerization

(b) *Dispersion and precipitation polymerization*

In dispersion and precipitation polymerization a monomer, initiator and often a stabilizer are dissolved in a solvent. As the polymer grows it becomes insoluble in the solvent and precipitates out as discrete particles. The stabilizer, often a polymer modifier, helps to prevent agglomeration by providing a steric barrier. This technique produces spheres with sizes between those produced by emulsion and suspension polymerization (0.1 – 10 μm). In dispersion polymerization the polymer particles formed early on are the main locus of polymerization. On the other hand in precipitation polymerization the locus of polymerization is the continuous phase because of the lack of swelling of the precipitated polymer. This means that polymer particles continue to grow during polymerization and diameters from nanometer to low micrometer can be obtained.^{42,50}

(c) *Suspension polymerization*

The relative simplicity and reproducibility of suspension polymerization make it a practical, frequently exploited option under both lab and industrial scales. In normal suspension polymerization, the monomers and the polymerization initiator are dissolved in an organic solvent which is immiscible with water. This organic phase is added to an aqueous phase containing stabilizing agents. Small droplets containing the monomers and initiator form upon mixing. The mixture is then heated to initiate polymerization (for thermal based initiators). Since the kinetics during this type of polymerization are essentially identical to bulk, one could regard the droplets as minibulk polymerization reactors. However, unlike bulk polymerization the heat is more effectively controlled by the surrounding aqueous phase. For normal phase suspension polymerization, the monomers should be insoluble in the aqueous phase, while reverse phase suspension polymerization as the name suggest, is essentially the inverse (monomer soluble in water). The stabilizing agents maintain stable droplets, prevent droplet coalescence and adhesion of partially polymerized particles so that beads with similar spherical morphology can be obtained.

The process has been illustrated in **figure 1.4**. Flask (A) contains an organic phase consisting of a monomer, initiator (I^*) and organic solvent as well as an aqueous phase containing a stabilizer. After mixing and heating (B), polymer beads form. These beads are coated by the stabilizing agent (C) which can be removed by washing. Some examples of stabilizing agents include; poly(vinylalcohol) (PVA), poly(vinyl pyrrolidone) (PVP), cellulose derivatives and gelatine.

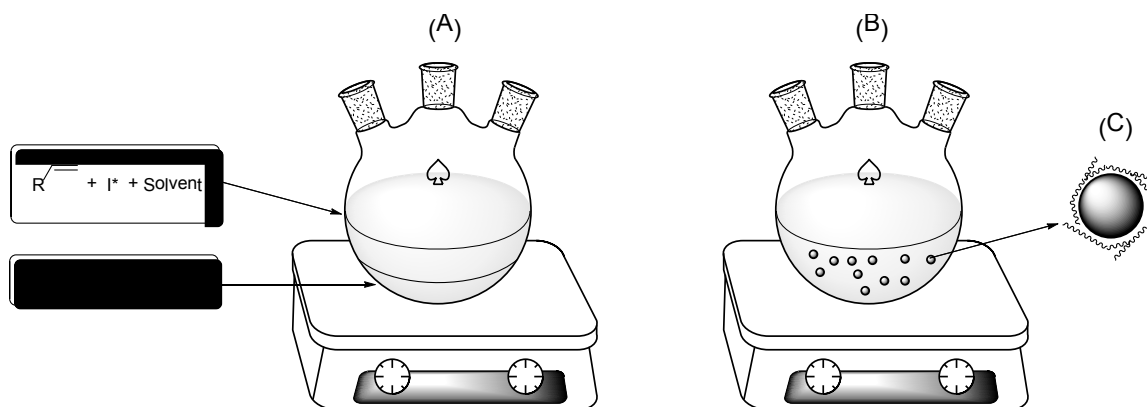


Figure 1.4 A schematic of a typical suspension polymerization procedure

The bead size depends on several factors including; stirring speed, ratio of water to monomer, concentration and type of stabilizer and solution viscosities. Typically, beads with sizes in the micrometer range are prepared by this method. These beads can be easily collected and separated by filtration and sieving, respectively. Porosity is another important property which depends primarily on the amount of crosslinker as well as the type of solvent, in this context referred to as the porogen. Beads obtained when using a low amount of crosslinker (typically less than 8%) are referred to as gel type resins which may swell significantly in certain solvents. This swelling ensures efficient diffusion of reactants and products. The swelling is highly dependent on the solvent used as well as any chemical modifications made to the polymer. Using a gel-type chloromethylated polystyrene resin as an example, the resin swells significantly in toluene but completely collapses in water (due to the hydrophobic nature of the material) but after reacting this resin with trimethylamine to form the benzyltrimethylammonium groups, the resin swells in water and collapses in toluene.⁵¹ These gel type resins are soft and compressible and as such unsuitable for many robust applications. Higher amounts of crosslinker can produce macroporous resins. These resins typically have higher surface areas in the dry state, are more resistant to osmotic shock and do not need to be swelled in a solvent since the pores are rigid.

The particle/bead diameters that can be obtained using the above mentioned and other techniques have been illustrated in the figure below (**figure 1.5**).

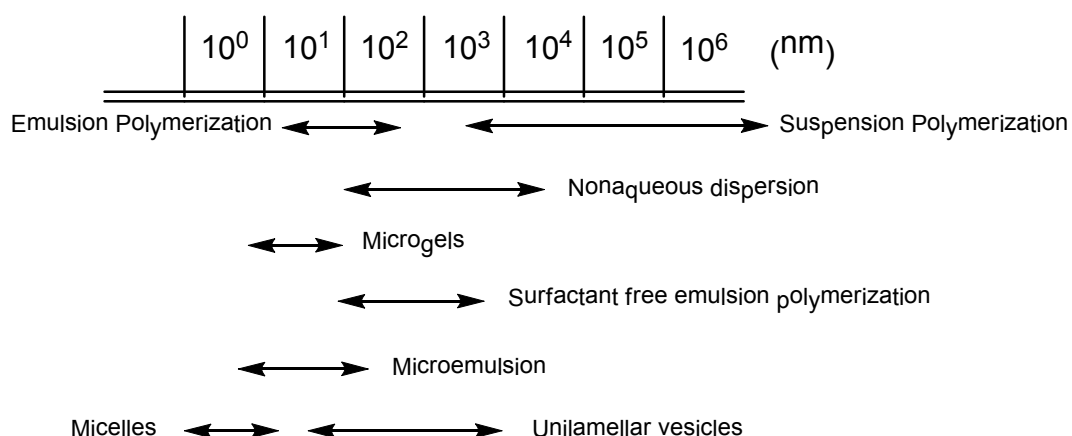


Figure 1.5 Typical particle sizes obtained using different polymerization techniques⁴²

1.3.4 Techniques for producing polymer fibers

Fibers may be produced by a variety of methods including; drawing,⁵² template synthesis,⁵³ deposition on a substrate, thermally induced phase separation and spinning. Of the spinning methods, electrospinning allows for fabrication of extremely fine (low nanometer) fibers⁵⁴ and will be discussed in greater detail below. Each of these methods have their associated advantages and disadvantages as summarized below (**table 1.5**).

1. **Drawing:** This method is very similar to dry spinning. Fibers are drawn from a microdroplet of polymer solution by dipping an object, for example a micropipette, into the droplet and withdrawing at a certain speed. This discontinuous process requires viscoelastic materials and has a lower limit for fiber diameters of 100 nm.⁵²
2. **Template Synthesis:** Template synthesis, as the name suggests, utilizes a nanoporous template through which the polymer solution is pushed. The resultant polymer fibers solidify in a suitable solvent. The diameter of the fibers is directly related to the diameter of the pores of the template and as such, excellent reproducibility can be obtained.⁵⁵
3. **Phase Separation:** There are several steps to this process including; polymer dissolution, gelation, solvent extraction, freezing and freeze drying to finally give a porous nanofibrous structure. The formation of fibers occurs due to physical incompatibility.⁵⁶
4. **Self Assembly:** This method provides ultrafine fibers with diameters typically less than 100 nm. Unlike the other methods, this is a 'bottom-up' approach in which atoms and molecules arrange via weak non-covalent interactions into well defined structures.⁵⁷

Table 1.5 Advantages and disadvantages of various fiber processing techniques^{66,67}

Process	Advantages	Disadvantages
Electrospinning	<ul style="list-style-type: none"> - Up-scalable - Repeatable - Convenient (and cheap) - Can control fiber size and orientation to an extent - Well established technique - Cost effective - Long continuous fibers produced 	<ul style="list-style-type: none"> - Difficult to control porosity and pore shape - Has lower limit to fiber diameter - Jet instability - Difficult to fabricate 3D shapes - Can be time consuming - Harmful solvent vapours
Self Assembly	<ul style="list-style-type: none"> - Simple fabrication - Repeatable - Excellent control of 3D shape - Good for obtaining smaller nanofibers 	<ul style="list-style-type: none"> - Inconvenient/complex process - Poor control of fiber diameters - Difficult to control pore size and shape
Phase Separation	<ul style="list-style-type: none"> - Excellent control over pore shape and size - Excellent control over 3D shape - Good consistency 	<ul style="list-style-type: none"> - Little control over fiber diameter and orientation - Longer fabrication times (many steps involved) - Limited to specific polymers
Template Synthesis	<ul style="list-style-type: none"> - Repeatable - Convenient - Good control of diameters – different diameters obtained using different templates 	<ul style="list-style-type: none"> - Limited fiber length - Difficult to upscale process
Drawing	<ul style="list-style-type: none"> - Repeatable - Convenient - Minimum equipment required 	<ul style="list-style-type: none"> - Poor control of fiber diameters - Discontinuous process

(a) *Electrospinning*

One of the great draw cards of electrospinning is the low cost and relative simplicity of the equipment needed. Perhaps the most sophisticated piece would be the high voltage DC power supply. This is connected to an electrode in contact with a suitably viscous polymer solution or melt. Fibers can be collected on a grounded or oppositely charged surface.⁵⁸ Commonly the collector used is a rotating drum or a piece of grounded foil, however several interesting variations exist.⁵⁹ Charge is commonly introduced to the polymer solution by connecting a needle (through which the polymer flows) to the power supply.⁶⁰ Another simple method involves immersing a copper wire connected to the power supply into a polymer solution contained within a simple glass pipette.^{61,62} The typical electrospinning set-up used in this study has been illustrated in **figure 1.6**.

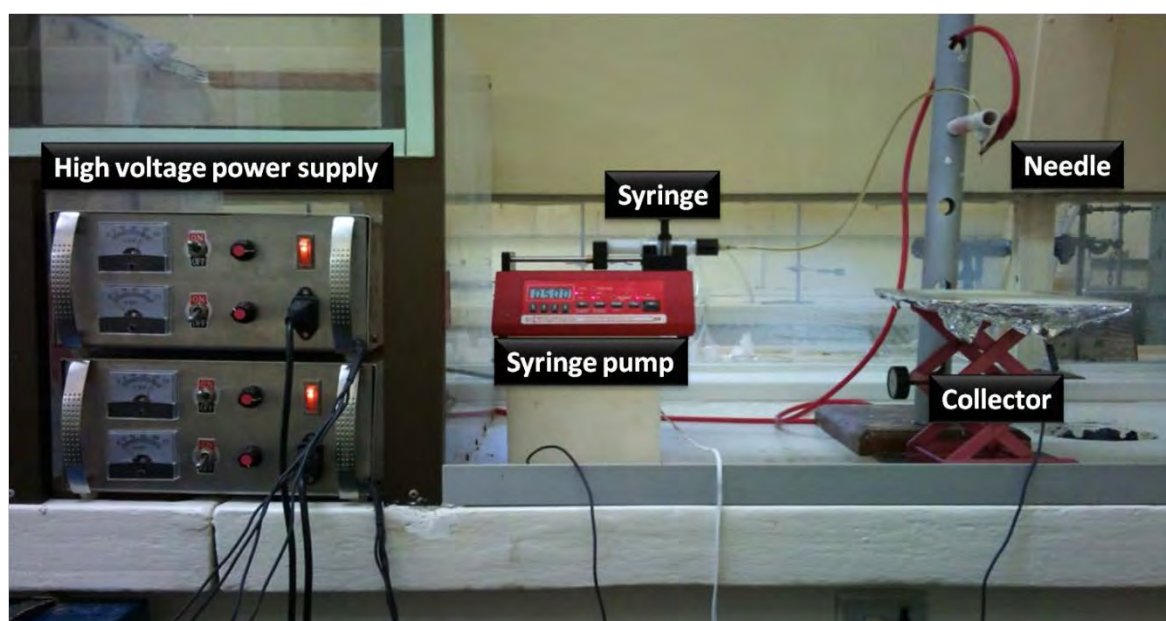


Figure 1.6 The electrospinning equipment used for the fabrication of polymer fibers for this thesis

The first electrospinning apparatus was developed over a century ago by Cooley (**figure 1.7**)⁶³ but Anton Formhals was the first to describe the electrospinning of plastics in 1934.⁶⁴ While there were some developments after this, the technique only became widely popularized with the advent of nanotechnology. One can see a huge increase in the number of publications relating to electrospinning - in 1994 there were just 3 and in 2010 there were over 2,500 publications (**figure**

1.8). The research into this field seemed to grow almost exponentially after the publication of a review on the topic by Huang and co-workers entitled; “A review on polymer nanofibers by electrospinning and their applications in nanocomposites”, in 2003.⁶⁵

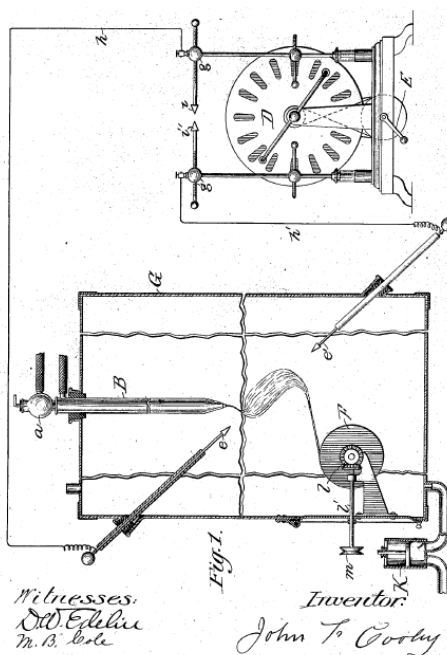


Figure 1.7 Drawing of the first recorded electrospinning apparatus as described by Cooley in 1902⁶³

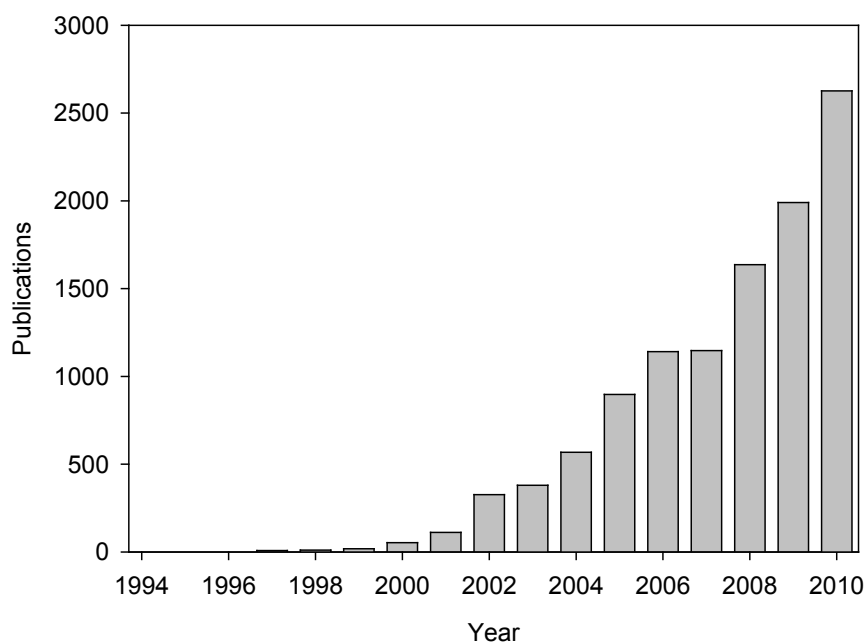


Figure 1.8 Scifinder Scholar® publication frequency analysis for the search term “electrospinning” or “electrospun” between 1994 and 2010

(b) *The process of electrospinning*

The viscous polymer (composite or sol-gel) solution, or melt forms a drop at the spinneret, typically a blunt end needle or pipette. The electric field draws this droplet into a structure known as the Taylor cone.⁶⁸ The surface tension is overcome when there is sufficient electrostatic repulsion resulting in the formation of a polymer jet. As the jet accelerates towards a counter electrode (typically ground) it undergoes bending and elongation and at the same time solvent evaporates until a fine solid fiber forms.⁶⁹ Although electrospinning seems simple from an instrumentation point of view, there are several parameters that influence this process. These parameters can be roughly divided into three groups; polymer solution, process and ambient conditions.⁷⁰

- i) **Polymer solution properties** include parameters surrounding the type and *molecular weight* of the polymer.^{68,70} *Viscosity* is an extremely important property to consider when conducting electrospinning. An increase in the molecular weight or concentration of polymer results in an increase in chain entanglements in the polymer solution, a critical property for effective electrospinning.⁵⁸ Too low a viscosity and fibers will not form due to insufficient chain entanglement. Typically bead-on-string or electro spraying occurs under these conditions. Increasing the viscosity, on the other hand, generally results in an increase in fiber diameters up to a critical point, after which interactions between polymer chains become too significant to be overcome by the applied electric field. Other polymer solution parameters include; *type of solvent* used, *conductivity of the polymer solution* and the *dielectric constant* of the solvent.^{68,70} Of course it is important that the polymer be soluble in the solvent, however, rate of evaporation and surface tension of the solvent should also be considered. The rate of evaporation dictates the solidification of the fibers, however, premature solidification which results in clogging, may take place should evaporation occur too rapidly. *Surface tension* along with solution viscosity influences the critical voltage required to begin the electrospinning process. This follows considering that the polymer jet erupts from the hanging polymer solution drop. The stretching of a polymer jet is caused primarily by the build up and repulsion of charges at its surface. A higher solution conductivity assists with

the accumulation of charge and thus assists the formation of fibers and further promotes stretching of fibers. The effect of this is to decrease the resultant fiber diameters. The limited conductivity of organic solvents is commonly remedied by introducing a salt such as lithium chloride into the solution. Finally, a high dielectric constant of a solvent concentrates the electrostatic flux lines leading to better stretching of the polymer jet.^{68,70}

- ii) **Process parameters** include the *applied voltage*, the *polymer solution feed rate*, the *tip-to-collector distance*.^{68,70} The applied voltage which provides the charges necessary to overcome surface tension and subsequently produce the polymer jet, drives the electrospinning process. The polymer solution feed rate or flow rate, is the speed at which the polymer solution is delivered to the needle tip. For example, too high a flow rate may result in deposition of wet fibers and the flow rate also has a definite effect on the resultant fiber diameters. Increasing the tip-to-collector distance increases the flight time of the polymer jet and provides time for solvent evaporation as well as time for stretching of the jet. The net result is typically a decrease in diameter of the fibers with an increase in tip-to-collector distance.^{68,70}
- (iii) **Ambient parameters** include *temperature*, *humidity*, and *atmospheric* conditions. The effect of temperature has an effect on several other parameters.^{68,70} An increase in temperature decreases the polymer solution viscosity and surface tension, while increasing polymer solubility, conductivity and rate of solvent evaporation. The humidity also affects solvent evaporation which consequently affects the solidification process of the polymer jet. Finally, the atmospheric conditions also affect electrospinning. The rate of evaporation for a pure liquid from a free surface is proportional to the difference between the saturated and the surrounding vapour pressure. Thus, the solvent will evaporate slower if the same solvent is present in the atmosphere. Since solvent evaporation takes place continually throughout electrospinning, this may result in a change in atmosphere which consequently results in non-homogeneous fiber characteristics.^{68,70}

1.4 Functionalization of polymer supports

Three of the main methods for functionalizing a polymer with a desired ligand are listed below:

1. Attachment of a ligand, which contains an appropriate functional group, to a pre-prepared polymer which also contains a suitable functionality. This strategy will be referred to as the *ligand-immobilization* strategy.
2. *Graft polymerization* of a suitable ligand monomer to a prepared polymer.
3. Addition of a polymerizable group to a ligand (monomerization) followed by *(co)polymerization*.

The first method is probably the simplest and most commonly used. Merrifield resin, a chloromethylated polystyrene resin crosslinked with divinylbenzene, contains the “reactive” chloromethyl groups which readily undergo substitution reactions in the presence of a nucleophile. Therefore, any ligand which contains a suitable nucleophilic group (eg. N-H, O-H, S-H, COOH etc.) will form a covalent bond ‘locking’ itself to the polymer backbone.⁷¹

Graft polymerization involves connecting a polymerizable ligand, for example a vinyl containing molecule, to the surface of a preformed polymer. Reactive radicals on the polymer surface can be introduced using a chemical or radiation (UV, γ -irradiation, etc) based approach. Following this, radical polymerization may proceed thereby ‘coating’ the surface of the polymer.

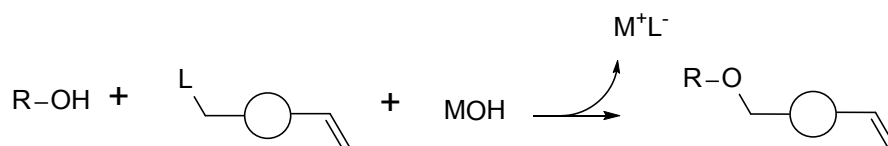
The third method is not as simple since it combines both synthetic organic chemistry with polymer chemistry. Some of the synthetic strategies for producing monomerized ligands have been discussed below. Unlike radiation-induced graft polymerization (2), however, both copolymerization (1) and ligand-immobilization methods (3) do not require additional equipment.

1.4.1 Monomerization

As mentioned above, there are a few approaches to prepare ligand-functionalized polymers. The copolymerization strategy relies on the availability of a polymerizable ligand and the process of preparing such ligands is commonly referred to as monomerization. One of the simplest methods for achieving this involves alkylating the ligand with a suitable polymerizable precursor. This

procedure has been illustrated in **scheme 1.3**. In this scheme, an alcohol containing compound (this could also be any other nucleophile such as amine or thiol) is reacted with a polymerizable group which contains a good leaving group (L). This alkylation is promoted by addition of a base such as a metal hydroxide (MOH). This final result of this procedure is the production of a new polymerizable ligand.

A few of these polymerizable starting materials have been included below (**table 1.6**). To use vinylbenzyl chloride (VBC) as an example; this commercially available reagent, reacts with nucleophiles by a substitution reaction, thereby connecting the ligand to the styryl group. Typically these reactions are carried out in polar aprotic solvents such as acetonitrile or DMF in the presence of a base like triethylamine, potassium carbonate, or potassium hydroxide.⁴⁷ Catalytic amounts of potassium iodide (KI) are often added because iodide, which is a better leaving group than chloride for example, may exchange with the chloride thereby improving reaction rates and yields.⁷²



Scheme 1.3 Introduction of a polymerizable group by alkylation reaction

Table 1.6 Names and structures of some common polymerizable groups used to make polymerizable ligands

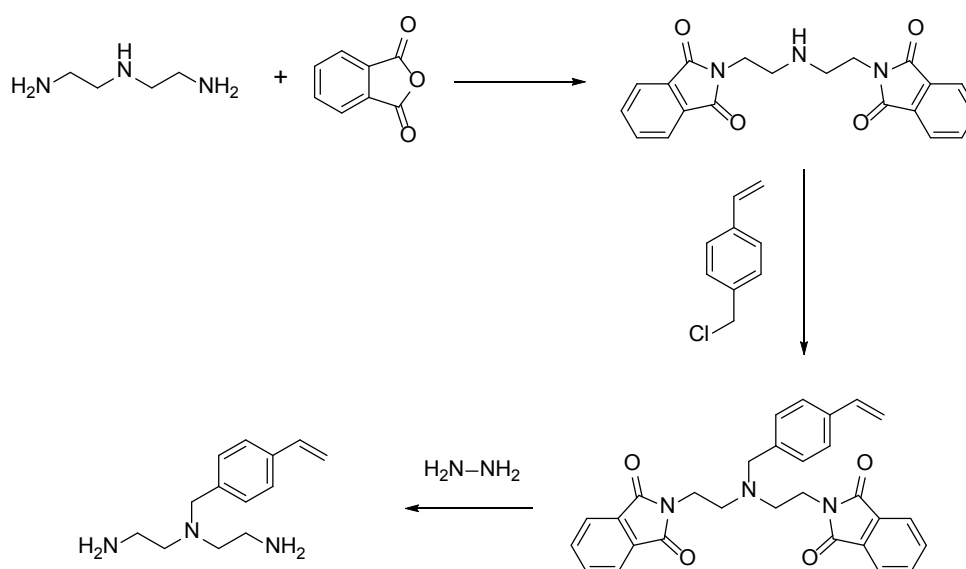
Name	Structure	Name	Structure
4-Vinylbenzyl chloride		2-Chloroethyl acrylate	
Allylbromide		Methacryloyl chloride	
Acryloyl chloride		2-Chloroethyl-2-methylacrylate	

There are two main questions that ought to be considered when adopting this approach of ligand functionalization:

1. Firstly, does the ligand contain a suitable nucleophilic group for attachment of the polymerizable group?
2. Secondly, are there other nucleophilic centers which may also react with the polymerizable group?

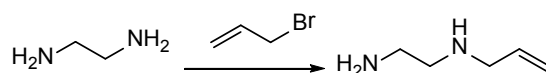
The first question is relatively straight forward, either the ligand has the correct nucleophilic group or not. If not, it could be introduced by a set of reactions, for example by hydroxylation (O-H)⁷³ or amination (N-H). The second question introduces some challenges and is especially important considering that ligands designed for metal coordination often contain reactive hydroxyl, amine, thiol and carboxylic acid functionalities – alkylation of the donor atoms has obvious negative ramifications. Regioselective alkylation can be challenging⁷⁴ and thus the typical approach for overcoming this issue involves the use of protecting group chemistry.

To illustrate this concept in use, the ‘tri-functional’ molecule diethylenetriamine was monoalkylated with vinylbenzyl chloride with the aid of phthalic anhydride as a protecting group. The triamine was reacted with phthalic anhydride which protected both primary amines leaving the secondary amine free for reaction with vinylbenzyl chloride. This product was then deprotected using hydrazine to afford the vinylbenzyl functionalized ligand (**scheme 1.4**).⁷⁵

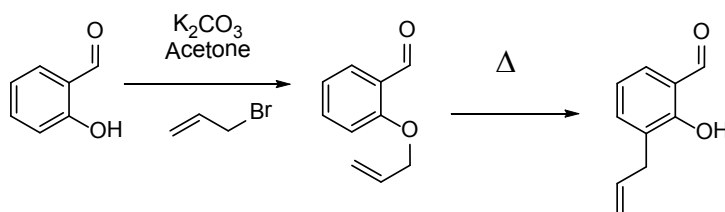


Scheme 1.4 Synthesis of polymerizable diethylenetriamine

As was the case for the styryl group, the allyl group has been introduced via typical nucleophilic substitution reactions using allyl bromide. Monosubstituted N-allylethylenediamine has been achieved under careful conditions, using a large excess of ethylenediamine to help prevent dialkylation (**scheme 1.5**).⁷⁶ Similarly, an allyl ether may be formed by reaction of allylbromide with salicylaldehyde under basic conditions. A commonly employed reaction at this point is the Claisen rearrangement to form the corresponding allylphenol – 2-hydroxy-3-allylbenzaldehyde (**scheme 1.6**).⁷⁷ This type of rearrangement is crucial from a coordination chemistry perspective since the phenol group remains available for coordination to a metal center.



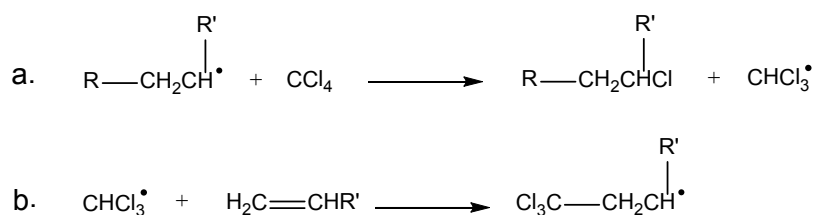
Scheme 1.5 Synthesis of monosubstituted N-allylethylenediamine⁷⁶



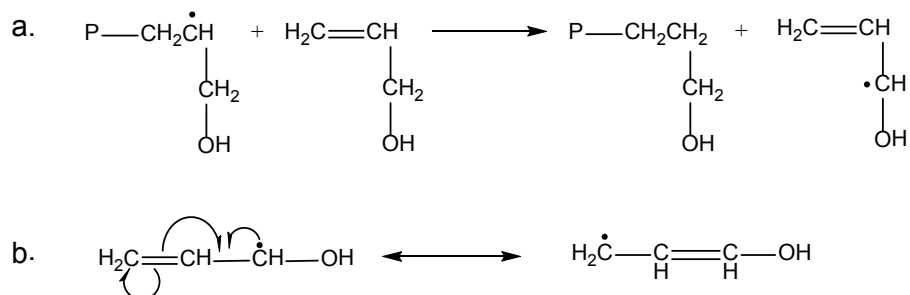
Scheme 1.6 Preparation of allyl functionalized monomer by alkylation and Claisen rearrangement⁷⁷

The 3-allyl substituted salicylaldehyde provides a foundation for the synthesis of numerous polymerizable ligands since the salicylaldehydes are widely used to prepare metal chelating salen ligands.⁷⁷ It has however been reported that allyl monomers do not undergo polymerization as readily as vinyl monomers. The reason for this is reported to be due to the chain termination process known as degradative chain transfer.⁷⁸ As mentioned earlier, a solvent may react with a growing radical rather than a monomer molecule. In **scheme 1.7** for example, a growing radical reacts with the solvent (carbon tetrachloride) resulting in the formation of a solvent radical (a). This radical may then initiate chain propagation with a new monomer (b). In this context the expression ‘termination’ is somewhat misleading, since the solvent which now contains a free

radical may start a new chain. If the solvent radical was inactive, for example due to resonance stabilization, and did not combine with a new monomer, the chain reaction would be terminated. This same process may occur with the allyl monomer as shown below (**scheme 1.8**). Here, the growing radical reacts with an allyl alcohol (a) which is resonance stabilized (b) and hence unreactive towards further propagation. The result of this would be not only termination of the growing chain but also termination of the chain reaction.⁷⁸



Scheme 1.7 Chain transfer in solvent radical polymerization



Scheme 1.8 Degradative chain transfer in the polymerization of allyl alcohol

The acryloyl and methacryloyl groups are also typically introduced by the alkylation method using acryloyl and methacryloyl chloride respectively.⁷⁹⁻⁸¹ The reason for using different polymerizable groups are vast, but typically the choice is based on ease of functionalization and characterization, the solubility of the resultant material and the reactivity ratio's if copolymerization is to be used. With respect to the latter point, the general rule is that like goes with like. So if using styrene as a co-monomer, the ligand ought to be functionalized with a styryl group and if using methyl methacrylate, the ligand should be functionalized with a methacryloyl group. Although this

is by no means a hard and fast rule, it generally ensures that the monomerized ligand is adequately incorporated into the resultant polymer.⁴⁷

The vinyl group cannot be directly introduced as simply as the above mentioned examples since vinyl chloride does not typically undergo nucleophilic substitution reactions. Thus, direct introduction of the vinyl group requires different synthetic methods. Coupling reactions have become generally popular, especially with the 2010 Nobel Prize for chemistry being awarded to the chemists behind these reactions. These reactions are also commonly used to introduce vinyl groups. Once again, protecting group chemistry should be considered since certain nucleophiles may hinder carbon coupling reactions by coordinating to the catalyst.⁸² Sellergren *et al.*, discovered that directed Pd-catalyzed coupling of the vinyl group with 2-(2'-hydroxy-5-bromophenyl)imidazole was not possible due to the presence of the basic nitrogen.⁸³ For this reason, benzoyl protecting groups were introduced (by a reaction with benzoyl chloride), followed by introduction of the vinyl group via the Stille coupling using tributyl vinyl tin and tetrakis(triphenylphosphine)palladium(0) (**table 1.7**).⁸³ Other than the Stille reaction, vinyl groups may also be introduced by Suzuki,⁸⁴ Grignard,⁸⁰ Wittig-type,⁸⁵ elimination⁸⁶ or decarboxylation reactions.⁸⁷ A few examples of these reactions have been summarized in **table 1.7**.

As has already been mentioned, care should be taken when choosing to functionalize the ligand of choice by alkylation with a polymerizable group and protecting group chemistry is often used to ensure the polymerizable group is connected to the desired position of the ligand. Other than synthetic challenges, there are also the issues of side reactions associated with some of these polymerizable groups. Acrylates and acrylamides, for example, tend to undergo conjugate addition while the other common side reaction is premature polymerization, which may be either radical induced or ionic. It may thus be necessary to perform purification steps as well as any subsequent reactions under "low risk conditions" - this may include decreased temperatures and elimination of light. Several radical inhibitors are available and may be used as additives to prevent premature polymerization. Most of these inhibitors are hindered phenols or hindered amine light stabilizers and are typically added in 0.01-0.1% concentrations.⁴⁷

Of course once the ligands have been functionalized with a vinyl group, they may be incorporated into the polymer backbone by a radical polymerization procedure. A crosslinking agent is often

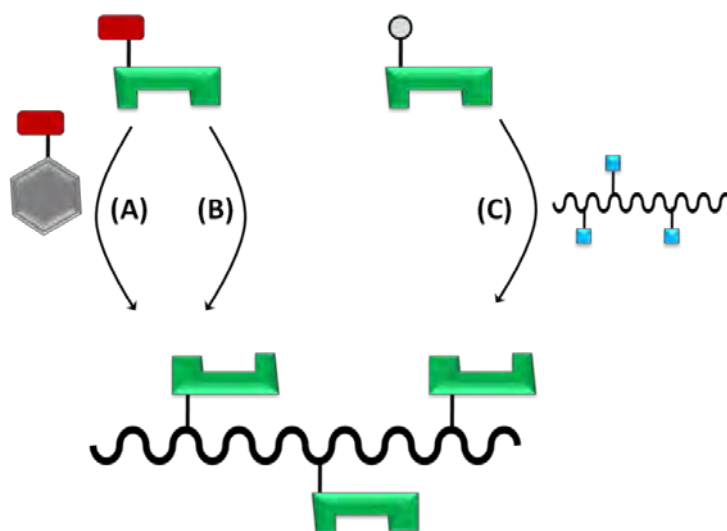
used to increase robustness and reduce solubility (an important property of heterogeneous catalysts) of the resultant polymer. This method, although more complicated than the Merrifield approach, allows for a greater degree of freedom since the amount of crosslinker and monomer can be altered along with many other properties of the polymer.

Table 1.7 Examples of reaction used for the introduction of the vinyl group

Reaction type	Example of reaction in use
Stille Coupling ⁸³	
Suzuki Coupling ⁷²	
Grignard ⁸⁰	
Elimination ⁸⁶	
Decarboxylation ⁸⁷	
Wittig ⁸⁵	

In summary, the commercial availability and simplistic functionalization of chloromethylated polystyrene resins makes them a common choice as catalyst supports. However, the ability to control the size, porosity, degree of crosslinking and degree of functionalization using the (co)polymerization techniques offers intrinsic advantages. A scheme summarizing the different methods for immobilizing homogeneous catalysts is shown in **scheme 1.9**. In route (A) of

scheme 1.9, a ligand containing a polymerizable group is copolymerized with a co-monomer (often a crosslinker). In route (B), a polymerizable ligand is polymerized in the absence of a co-monomer (the ligand itself may act as a crosslinker). Finally in route (C), a ligand is reacted with a pre-formed polymer; both contain appropriate functionality to allow for the formation of a covalent bond



Scheme 1.9 A schematic showing some of the different approaches used for obtaining ligand-functionalized polymer-supports

1.5 Aims and objectives

The principal aim of this study (and this Part in particular) was to prepare heterogeneous oxovanadium(IV) oxidation catalysts. As discussed herein, the active site of the VHPO's all contain vanadium bound by the imidazole group of a histidine residue. It was thus decided to connect imidazole and imidazoline based ligands (some of which were prepared in Part 1 of this thesis) to a polymer support followed by functionalization with oxovanadium(IV). Methods for the production of polymer supports, as well as their effectiveness as support materials will be investigated. The research objectives can be broken down as follows:

1. Prepare imidazoline/imidazole functionalized Merrifield resins and the corresponding polymer-bound oxovanadium(IV) catalysts and assess their catalytic activity.

2. Prepare imidazole functionalized polymer beads by using suspension polymerization and assess the catalytic activity of the oxovanadium(IV) functionalized beads.
3. Prepare imidazole-based electrospun polymer fibers and the corresponding oxovanadium(IV) functionalized derivatives and assess their catalytic activity.

1.6 References

- (1) Thomson, S. J.; Webb, G. *Heterogeneous Catalysis*; Oliver and Boyd LTD, 1968.
- (2) Hagen, J. *Industrial Catalysis: A Practical Approach*; 2nd ed.; Wiley-VCH Verlag, Weinheim, 2006.
- (3) Benaglia, M. *Recoverable and Recyclable Catalysts*; John Wiley & Sons, Ltd: West Sussex, 2009.
- (4) Magee, J. S.; Mitchell Jr, M. M. *Studies in Surface Science and Catalysis*; John, S. M., Maurice, M. M., Eds.; Elsevier, London 1993.
- (5) Weckhuysen, B. M.; Keller, D. E. *Catal. Today* **2003**, *78*, 25.
- (6) Wainwright, M. S.; Foster, N. R. *Catal. Rev.* **1979**, *19*, 211.
- (7) Livbjerg, H.; Villadsen, J. *Chem. Eng. Sci.* **1972**, *27*, 21.
- (8) Blanco, J.; Avila, P.; Barthelemy, C.; Bahamonde, A.; Odriozola, J. A.; De La Banda, J. F. G.; Heinemann, H. *Appl. Catal.* **1989**, *55*, 151.
- (9) Maurya, M. R.; Kumar, A.; Costa Pessoa, J. *Coord. Chem. Rev.* **2011**, *255*, 2315.
- (10) Schultz, M. J.; Sigman, M. S. *Tetrahedron* **2006**, *62*, 8227.
- (11) Wu, J.-Q.; Li, Y.-S. *Coord. Chem. Rev.* **2011**, *255*, 2303.
- (12) Ligtenbarg, A. G. J.; Hage, R.; Feringa, B. L. *Coord. Chem. Rev.* **2003**, *237*, 89.
- (13) Vining, W. C.; Strunk, J.; Bell, A. T. *J. Catal.* **2011**, *281*, 222.
- (14) Rigutto, M. S.; van Bekkum, H. *J. Mol. Catal.* **1993**, *81*, 77.
- (15) Alsalim, T. A.; Hadi, J. S.; Al-Nasir, E. A.; Abbo, H. S.; Titinchi, S. J. J. *Catal. Lett.* **2010**, *136*, 228.
- (16) Guo, Z. W.; Gu, Y. Y.; Zhou, S. L.; Ren, C. H. *Adv. Mater. Res.* **2011**, *233*, 1575.
- (17) Li, K. T.; Shyu, N. S. *Ind. Eng. Chem. Res.* **1997**, *36*, 1480.
- (18) Lorber, C.; Choukroun, R.; Vendier, L. *Organomet.* **2004**, *23*, 1845.
- (19) Maurya, M. R.; Kumar, U.; Correia, I.; Adão, P.; Pessoa, J. C. *Eur. J. Inorg. Chem.* **2008**, *577*.
- (20) Bolm, C. *Coord. Chem. Rev.* **2003**, *237*, 245.
- (21) Trost, B. M.; Chung, C. K. *J. Am. Chem. Soc.* **2006**, *128*, 10358.
- (22) Sabitha, G.; Reddy, G. S. K. K.; Reddy, K. B.; Yadav, J. S. *Tetrahedron Lett.* **2003**, *44*, 6497.

-
- (23) Chu, C. Y.; Hwang, D. R.; Wang, S. K.; Uang, B. J. *Chem. Comm.* **2001**, 980.
- (24) Rehder, D. *Bioorganic vanadium chemistry*; John Wiley and Sons Ltd.: West Sussex, 2008.
- (25) Butler, A.; Carter-Franklin, J. N. *Nat. Prod. Rep.* **2004**, *21*, 180.
- (26) Soedjak, H. S.; Walker, J. V.; Butler, A. *Biochemistry* **1995**, *34*, 12689.
- (27) Everett, R. R.; Soedjak, H. S.; Butler, A. *J. Biol. Chem.* **1990**, *265*, 15671.
- (28) Everett, R. R.; Kanofsky, J. R.; Butler, A. *J. Biol. Chem.* **1990**, *265*, 4908.
- (29) Weyand, M.; Hecht, H. J.; Kieß, M.; Liaud, M. F.; Vilter, H.; Schomburg, D. *J. Mol. Biol.* **1999**, *293*, 595.
- (30) http://en.wikipedia.org/wiki/Ascophyllum_nodusum, Accessed November, 2011.
- (31) <http://www.recif-france.com/Database/384.htm>, Accessed November, 2011.
- (32) Mba, M.; Pontini, M.; Lovat, S.; Zonta, C.; Bernardinelli, G.; Kündig, P. E.; Licini, G. *Inorg. Chem.* **2008**, *47*, 8616.
- (33) Maurya, M. R.; Arya, A.; Kumar, A.; Pessoa, J. C. *Dalton Trans.* **2009**, 2185.
- (34) Maurya, M. R.; Kumar, M.; Arya, A. *Catal. Comm.* **2008**, *10*, 187.
- (35) Maurya, M. R.; Kumar, A.; Ebel, M.; Rehder, D. *Inorg. Chem.* **2006**, *45*, 5924.
- (36) Maurya, M. R.; Arya, A.; Adao, P.; Pessoa, J. C. *J. Appl. Catal., A* **2008**, *351*, 239.
- (37) Schneider, C. J.; Penner-Hahn, J. E.; Pecoraro, V. L. *J. Am. Chem. Soc.* **2008**, *130*, 2712.
- (38) Maurya, M. R.; Chandrakar, A. K.; Chand, S. *J. Mol. Catal. A: Chem.* **2007**, *278*, 12.
- (39) Maurya, M. R.; Arya, A.; Kumar, A.; Kuznetsov, M. L.; Avecilla, F.; Costa, P. J. *Inorg. Chem.* **2011**, *49*, 6586.
- (40) Samuni, A.; Meisel, D.; Czapski, G. *J. Chem. Soc., Dalton Trans.* **1972**, 1273.
- (41) Zhao, X. S.; Bao, X. Y.; Guo, W.; Lee, F. Y. *Mater. Today* **2006**, *9*, 32.
- (42) Maurya, M. R.; Chandrakar, A. K.; Chand, S. *J. Mol. Catal. A: Chem.* **2007**, *274*, 192.
- (43) Sherrington, D. C. *Pure. Appl. Chem.* **1987**, *60*, 401.
- (44) Matyjaszewski, K.; Davis, T. P. *Handbook of Radical Polymerization*; John Wiley and Sons, Inc.: New York, 2002.
- (45) Toy, P. H.; Janda, K. D. *Acc. Chem. Res.* **2000**, *33*, 546.
- (46) Zhang, J.-L.; Che, C.-M. *Org. Lett.* **2002**, *4*, 1911.
- (47) Yan, M.; Ramstrom, O.; Dekker, M. *Molecularly Imprinted Materials. Science and Technology*; New York, 2005.
-

-
- (48) Asua, J. M. *J. Polym. Sci., Part A: Polym. Chem.* **2004**, *42*, 1025.
- (49) Stevens, P. M. *Polymer Chemistry. An Introduction*; Oxford University Press: New York, 1999.
- (50) Kawaguchi, S.; Ito, K. In *Polymer Particles*; Okubo, M., Ed.; Springer Berlin / Heidelberg: 2005.
- (51) Sherrington, D. C. *Chem. Comm.* **1998**, 2275.
- (52) Ondarçuhu, T.; Joachim, C. *Europhys. Lett.* **1998**, *42*, 215.
- (53) Martin, C. R. *Chem. Mater.* **1996**, *8*, 1739.
- (54) He, J.-H.; Liu, Y.; Mo, L.-F.; Wan, Y.-Q.; Xu, L. *Electrospun Nanofibers and Their Applications*; iSmithers: Shopshire, 2008.
- (55) Feng, L.; Li, S.; Li, H.; Zhai, J.; Song, Y.; Jiang, L.; Zhu, D. *Angew. Chem. Int. Ed.* **2002**, *41*, 1221.
- (56) Ma, P. X.; Zhang, R. *J. Biomed. Mater. Res.* **1999**, *46*, 60.
- (57) Liu, G.; Qiao, L.; Guo, A. *Macromolecules* **1996**, *29*, 5508.
- (58) *Science and Technology of Polymer Nanofibers*; Andradý, A. L., Ed.; John Wiley and Sons, Inc: New Jersey, 2008.
- (59) Katta, P.; Alessandro, M.; Ramsier, R. D.; Chase, G. G. *Nano Lett.* **2004**, *4*, 2215.
- (60) Carnell, L. S.; Siochi, E. J.; Holloway, N. M.; Stephens, R. M.; Rhim, C.; Niklason, L. E.; Clark, R. L. *Macromolecules* **2008**, *41*, 5345.
- (61) Smit, E.; Buttner, U.; Sanderson, R. D. *Polymer* **2005**, *46*, 2419.
- (62) Zhu, Z.; Zhang, L.; Howe, J. Y.; Liao, Y.; Speidel, J. T.; Smith, S.; Fong, H. *Chem. Comm.* **2009**, 2568.
- (63) Cooley, J. F. US Patent number 692631, 1902.
- (64) Formhals, A. US Patent number 1,975,504, 1934.
- (65) Huang, Z. M.; Zhang, Y. Z.; Kotaki, M.; Ramakrishna, S. *Compos. Sci. Technol.* **2003**, *63*, 2223.
- (66) Holzwarth, J. M.; Ma, P. X. *J. Mater. Chem.* **2011**, *21*, 10243.
- (67) De Vrieze, S., PhD Thesis, Universiteit Gent, 2010.
- (68) Dzenis, Y. *Science* **2004**, *304*, 1917.
- (69) Greiner, A.; Wendorff, J. H. *Angew. Chem. Int. Ed.* **2007**, *46*, 5670.
-

-
- (70) Kumar, A. *Nanofibers*; Intech: Vukovar, 2010.
- (71) Deng, J.; Wang, L.; Liu, L.; Yang, W. *Prog. Polym. Sci.* **2009**, *34*, 156.
- (72) De, B. B.; Lohray, B. B.; Sivaram, S.; Dhal, P. K. *J. Polym. Sci. Part A: Polym. Chem.* **1997**, *35*, 1809.
- (73) Mizuno, N.; Kamata, K.; Yamaguchi, K. *Catal. Today*. In Press, Corrected Proof.
- (74) Savall, B. M.; Fontimayor, J. R.; Edwards, J. P. *Tetrahedron Lett.* **2009**, *50*, 2490.
- (75) Striegler, S. *Tetrahedron* **2001**, *57*, 2349.
- (76) Linsker, F.; Evans, R. L. *J. Am. Chem. Soc.* **1945**, *67*, 1581.
- (77) Tobiasz, A.; Walas, S.; Trzewik, B.; Grzybek, P.; Zaitz, M. M.; Gawin, M.; Mrowiec, H. *Microchem. J.* **2009**, *93*, 87.
- (78) Laible, R. C. *Chem. Rev.* **1958**, *58*, 807.
- (79) Denizli, A.; Garipcan, B.; Karabakan, A.; Say, R.; Emir, S.; Patır, S. *Sep. Purif. Technol.* **2003**, *30*, 3.
- (80) Zhou, G.; Harruna, I. I. *Tetrahedron Lett.* **2003**, *44*, 4617.
- (81) Guo, Z.; Zhu, W.; Tian, H. *Macromolecules* **2009**, *43*, 739.
- (82) Krolski, M. E.; Renaldo, A. F.; Rudisill, D. E.; Stille, J. K. *J. Org. Chem.* **1988**, *53*, 1170.
- (83) Sellergren, B.; Karmalkar, R. N.; Shea, K. J. *J. Org. Chem.* **2000**, *65*, 4009.
- (84) Sellner, H.; Karjalainen, J. K.; Seebach, D. *Chem. Eur. J.* **2001**, *7*, 2873.
- (85) Kee, C. H.; Ariffin, A.; Awang, K.; Takeya, K.; Morita, H.; Hussain, S. I.; Chan, K. M.; Wood, P. J.; Threadgill, M. D.; Lim, C. G.; Ng, S.; Weber, J. F. F.; Thomas, N. F. *Org. Biomol. Chem.* **2010**, *8*, 5646.
- (86) Abruna, H. D.; Breikss, A. I.; Collum, D. B. *Inorg. Chem.* **1985**, *24*, 987.
- (87) Overberger, C. G.; Vorchheimer, N. *J. Am. Chem. Soc.* **1963**, *85*, 951.

This page has been left blank intentionally

Chapter 2

Experimental materials and methods

2.1 General reagents

Vanadyl sulfate hydrate was obtained from BDH Limited (England). Standard concentrations of vanadium for ICP calibration were prepared from a 1002 ppm ($\pm 2 \text{ mg.L}^{-1}$) stock solution (Teknolab, South Africa). Ultrapure TraceSelect 65% nitric acid (Sigma-Aldrich) was used when digesting samples for ICP. The substrates used in the oxidation reactions, styrene, ethylbenzene and thioanisole (Sigma-Aldrich) and oxidant 30% aqueous hydrogen peroxide (Merck) were stored refrigerated ($4 \text{ }^\circ\text{C}$). The latter was standardized every few weeks by titration with potassium permanganate.¹ Merrifield polymer (also called chloromethylated polystyrene) crosslinked with divinylbenzene (5.5% crosslinked, $\sim 5.5 \text{ mmol Cl/g}$ resin and 16-50 mesh) was purchased from Aldrich Chemical Company. Phenol red, 10% tetramethylammonium hydroxide (TMAOH), ethyleneglycol dimethacrylate (97%, EGDMA), divinylbenzene (80% remainder ethylbenzene, DVB) and benzoyl peroxide (70% remainder water) were purchased from Sigma-Aldrich. $\text{Pd}(\text{PPh}_3)_4$ (Sigma) and radical initiators azobisisobutyronitrile (AIBN) (Sigma) were stored in a refrigerator at $4 \text{ }^\circ\text{C}$. Polystyrene ($M_w = 192,000$) and polyvinylalcohol (88% hydrolyzed, $M_w = 130,000$) were purchased from Sigma-Aldrich and Merck, respectively. All solvents and general chemicals including *N,N*-dimethylformamide, toluene, ethanol, methanol, ethyl acetate, diethyl ether, triethylamine (97%), *N*-vinylimidazole, hydroxyethylcellulose, hydrochloric acid, allylbromide, ethylenediamine, salicylaldehyde, methyl salicylate, sodium chloride and lithium chloride were purchased from commercial sources (either Sigma or Merck) and used without further purification unless otherwise stated.

2.2 Techniques and instrumentation

2.2.1 General instrumentation

The infrared spectra were recorded on either a Perkin Elmer 2000 FTIR spectrometer in the mid-IR range ($4000 - 400 \text{ cm}^{-1}$) as KBr pellets or as neat compounds with a Perkin Elmer 100 ATR-IR ($4000 - 650 \text{ cm}^{-1}$). Melting points were determined using Galenkamp Melting point apparatus equipped with a thermometer ($0 - 400 \text{ }^\circ\text{C}$). ^1H and ^{13}C NMR spectra of all ligands were recorded on a Bruker AMX 400 NMR MHz spectrometer and reported relative to tetramethylsilane (δ 0.00). Electronic spectra were recorded on a Perkin Elmer Lambda 25 UV-Vis spectrophotometer using 1 cm quartz cells. Microanalysis was carried out using a Vario Elementar Microcube ELIII. Mass spectra were obtained using a Thermo-Finnigan GC-MS fitted with an electron impact ionization mass selective detector.

2.3.2 Scanning electron microscopy

Samples were prepared for scanning electron microscopy (SEM) by coating them in gold using a Balzers' Sputtering device. The samples were viewed using a TESCAN Vega TS 5136LM typically at 20 kV at a working distance of 20 mm.

2.3.3 Atomic force microscopy

Atomic force microscopy (AFM) imaging was performed using a C P-11 Scanning Probe Microscope from Veeco Instruments (Carl Zeiss, South Africa) in non-contact mode at a scan rate of 1 Hz using a MP11123 cantilever. The images were obtained using a spring constant range of $20 - 80 \text{ N.m}^{-1}$, and resonant frequency range of $217 - 276 \text{ Hz}$.

2.3.4 X-ray photoelectron spectroscopy

X-ray photoelectron spectroscopy (XPS) measurements were performed with a Kratos Axis Ultra X-ray Photoelectron Spectrometer equipped with a monochromatic Al K_α source (1486.6 eV). The

base pressure of the system was below 3×10^{-7} Pa. XPS experiments were recorded with 75 W power source using hybrid-slot spectral acquisition mode and an angular acceptance angle of $\pm 20^\circ$. The analyzer axis made an angle of 90° with the specimen surface, with the specimen surface making an angle of 45° with the X-ray angle. Charge neutraliser was used due to the insulating surface used to prepare the sample. The elemental analysis and metal core level were recorded with a step of 1 eV and pass energy of 160 eV. XPS data analysis was performed with Kratos version 2 program.

2.3.5 Inductively coupled plasma – Optical emission spectroscopy

The vanadium content was determined using a Thermo Electron (iCAP 6000 Series) inductively coupled plasma (ICP) spectrometer equipped with Optical Emission Spectroscopy (OES) detector. Four wavelengths were chosen for vanadium detection (290.88 nm, 292.40 nm, 309.31 nm, 311.07 nm). These wavelengths were the most sensitive and had the minimum amount of interferences. Three runs were performed at each wavelength. Additional operating parameters have been listed in **table 2.1**. Calibration was performed using no less than seven standards typically; 0.01 ppm, 0.1 ppm, 1 ppm, 2 ppm; 5 ppm; 10 ppm and 20 ppm. The standards were prepared by appropriate dilution of a 1000 ppm stock solution. All solutions were filtered through 0.45 μ m Millipore® filters to prevent nebulizer blockages. The samples to be run were digested in ultrapure nitric acid or a mixture of nitric acid and hydrogen peroxide. Typically, these were heated at 50 °C for a period of 5 days to ensure total leaching of vanadium from the sample. After appropriate dilutions with triple distilled, deionised Millipore water, the samples were filtered and the vanadium content determined.

Table 2.1 ICP-OES method and operating parameters

Parameter	Setting
Plasma Ar gas flow rate	5.0 L.min ⁻¹
Auxiliary Ar gas flow rate	1.00 L.min ⁻¹
Nebulizer Ar gas flow rate	0.90 L.min ⁻¹
Sampling depth	8.5 mm
Pump rate	100 rpm
N ₂ addition flow rate	0.5 L.min ⁻¹
Cooled spraying chamber temperature	4 °C
Selected wavelengths	290.88 nm
	292.40 nm
	309.31 nm
	311.07 nm
Sample flush time	30 s
Points per peak	3
Time scan acquisition	50 ms/point
RF power	1150 W

2.3.6 Brunauer, Emmett, Teller (BET) surface area analysis

Nitrogen adsorption/desorption isotherms were measured at 77 K using a Micromeritics ASAP 2020 Surface Area and Porosity Analyzer. Prior to each measurement, samples were degassed for a minimum of one week to ensure complete removal of adsorbed impurities. Degassing was performed at 70 °C for the linear polymers and at 150 °C for crosslinked polymers, unless mentioned otherwise. Approximately 0.2 g of sample was used and an equilibration interval of 20 seconds was allowed during the run. The surface area (BET),² total pore volume and pore size distribution (BJH method)³ were calculated from these isotherms.

2.3.7 Gas chromatography

Progress of the catalysed reactions was monitored using either an Agilent 7890A gas chromatograph (GC) or an Agilent 6890, both fitted with a flame ionization detector (FID) and a Zebron, ZB-5MSi, capillary column (30 m x 0.25 mm x 0.25 μm). The product identities were confirmed using a Thermo-Finnigan GC-MS fitted with an electron impact ionization mass selective detector. The GC parameters have been summarized in **table 2.2**. The same conditions were used for analysis on the GC-MS

Table 2.2 GC temperature programs used identification of the oxidation products of styrene, ethylbenzene and thioanisole

	Substrate	
	Styrene/Ethylbenzene	Thioanisole
Initial Temperature	70 °C	60 °C
Hold Time	2 mins	2 mins
Ramp	20 °C.min ⁻¹	25 °C.min ⁻¹
	Until 270 °C	Until 260 °C
Hold Time	2 mins	2 mins

2.3.8 Thermogravimetric analysis

Thermogravimetric analysis (TGA) was performed using a TA Instruments SDT Q600. Typically the samples were heated at a rate of 10 °C.min⁻¹ under a constant stream of nitrogen gas. The temperature range differed depending on the sample used. The samples were contained in platinum pans. The onset of decomposition or mass loss (T_{onset}) was determined from the normal TG-curve, while the maximum temperature (T_{max}), was determined from the peak of differential TG (DTG) curve.

References

- (1) Reichert, J. S.; McNeight, S. A.; Rudel, H. W. *Ind. Eng. Chem.* **1939**, *11*, 194.
- (2) Brunauer, S.; Emmett, P. H.; Teller, E. *J. Am. Chem. Soc.* **1938**, *60*, 309.
- (3) Barrett, E. P.; Joyner, L. G.; Halenda, P. P. *J. Am. Chem. Soc.* **1951**, *73*, 373.

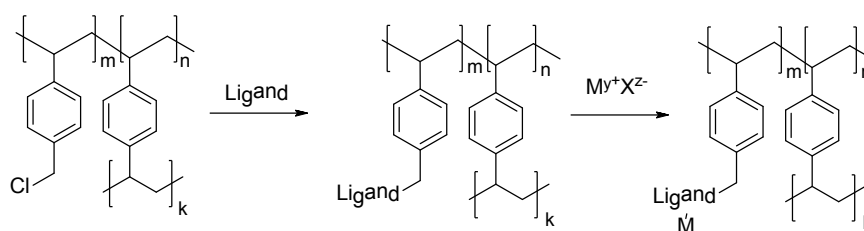
This page has been left blank intentionally

Chapter 3

Merrifield resin-based oxovanadium(IV) catalysts for oxidation reactions

3.1 Introduction

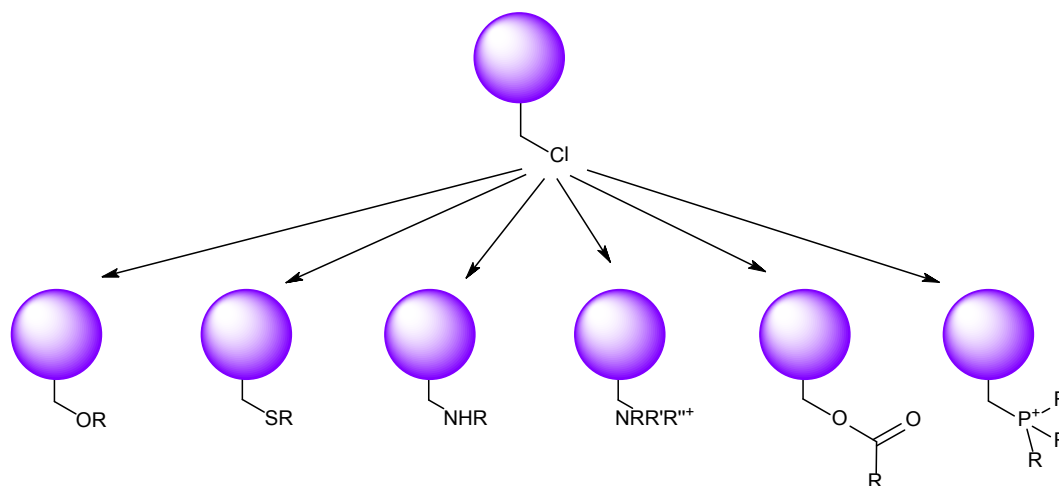
In the early 1960's Merrifield set out to design a solid support for peptide synthesis, an effort that earned him the Nobel Prize in Chemistry in 1984.¹ The requirement of the polymer support was that it should be insoluble in all relevant solvents, and that it should contain a functional group for amino acid attachment. The most suitable, he found, was a chloromethylated poly(styrene-co-divinylbenzene) copolymer in the form of 200-400 mesh beads.¹ This discovery, although certainly directed towards peptide synthesis, also led to significant advances in the field of heterogeneous catalysis. A typical method for producing the heterogeneous catalyst may be as follows; an organic molecule is covalently linked to Merrifield resin through a nucleophilic substitution reaction to afford the functionalized polymer. This may itself act as a catalyst (eg. chiral catalyst) or may act as a ligand and subsequently allow coordination with a metal. Should the latter be the case, the ligand functionalized polymer may be reacted with a metal salt yielding the metal containing heterogeneous catalyst (**scheme 3.1**).



Scheme 3.1 A Simplified reaction scheme for the immobilization of homogeneous catalysts onto Merrifield resin.

As Sherrington realised back in 1983, the use of polymer supports in the area of heterogeneous catalysis was an untapped resource. Since then the field has expanded significantly.² The

popularity of these polymer supports may be attributed to ease of chemical modification. Over 50 different functional groups including, but not limited to; carboxylic acids, amines, alcohols and thiols (**scheme 3.2**),³ have been attached to these supports.



Scheme 3.2 Functionalization of Merrifield-type resins³

Focusing only on polymer-supported oxidation catalysts, one can find several examples of this diversity being utilized. Attachment of amine related ligands to PS-Cl has been performed often in the presence of a base and at elevated temperatures. The electropositive carbon atom attached to the chlorine atom in PS-Cl is attacked by the nucleophilic amine from the ligand. Sherrington and co-workers have used this reaction to attach 2-(2'-pyridyl)imidazole (PIM) to PS-Cl and subsequently reacted this with molybdenyl acetylacetonate giving the heterogenized catalyst which was applied in epoxidation reactions.⁴ Maurya and co-workers have also published over 20 papers related to polymer-heterogenized oxidation catalysts. This group has immobilized several imidazole and benzimidazole ligands to chloromethylated polystyrene,⁵⁻⁹ some of which are shown in **figure 3.1**. The ligand-modified Merrifield resins were subsequently reacted with various metals including vanadium, molybdenum, tungsten, copper and nickel, and used as catalysts for epoxidation,¹⁰ oxidation^{8,9} and bromination reactions.^{6,11}

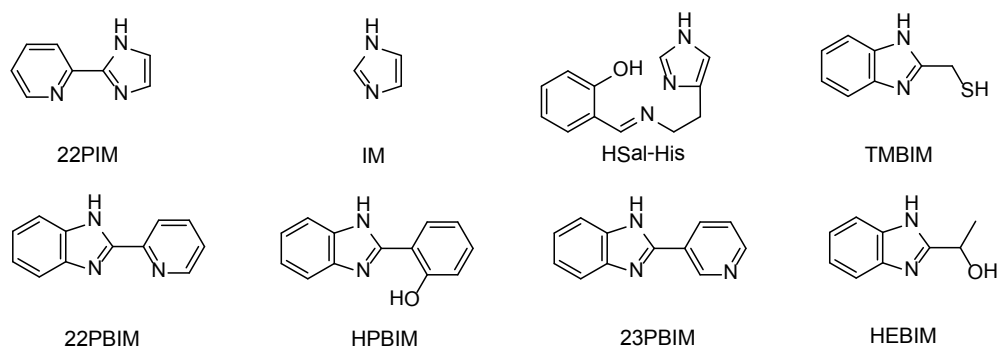


Figure 3.1 Structures of some imidazole-based ligands that have been anchored to PS-Cl⁵⁻⁹

In this chapter, the preparation of imidazole and imidazoline functionalized Merrifield resins is discussed. These ligand-functionalized microspherical polymer-based resins were then reacted with vanadyl sulfate to afford the oxovanadium(IV)-functionalized materials, which were used as heterogeneous catalysts. The surface chemistry was investigated using atomic force microscopy and scanning electron microscopy. The catalysts were further characterized by microanalysis and infrared spectroscopy. The catalytic potential of these complexes was demonstrated by studying the oxidation of methyl phenyl sulfide (thioanisole), styrene, ethylbenzene and briefly the oxidative halogenation of phenol red. Several factors affecting selectivity and overall oxidation including; amount of peroxide, temperature and amount of catalyst were investigated.

3.2 Preparative work

3.2.1 Synthesis of the ligands

The ligands 2-(2'-hydroxyphenyl)imidazole (piminH), 1-methylimidazole-2-carboxylic acid (Melm2COOH) and imidazole-4-carboxylic acid (Im4COOH) were prepared as reported in **Part 1, Chapter 3** of this thesis. Pertinent characterization data of these ligands can be found within the same section.

3.2.2 PS-pimin

Chloromethylated polystyrene (1.0 g, 5.5 mmol Cl) was allowed to swell in DMF (15 mL) overnight. To this was added piminH (0.93 g, 5.7 mmol) followed by a solution of triethylamine (1.25 g) in ethylacetate (30 mL). The reaction mixture was then heated and stirred under reflux for 9 hours. Following this, the cream-coloured beads were allowed to cool and then filtered and washed with hot DMF followed by ethanol. The beads were dried in the oven overnight at 60 °C. Due to some degradation from mechanical stirring the beads were first passed through sieves of various mesh sizes such that only the largest beads remained (>15 mesh). ATR-IR (cm^{-1} , neat): 3407, 2927, 2162, 1648, 1594, 1447, 1294, 1231, 1104, 1014, 808, 761 cm^{-1} . *Anal.* Found (%): C, 69.80; H, 6.93; N, 5.79.

3.2.3 PS-Im4COO

These were prepared in a similar fashion to PS-pimin (**3.2.2**) except that Im4COOH (1.2 mol eq. wrt to Cl) The resultant white beads were filtered, washed several times with DMF and then methanol. The beads were dried in an oven overnight at 60 °C. IR (cm^{-1} , KBr pellet): 3377, 3103, 2929, 1711, 1634, 1543, 1512, 1446, 1423, 1378, 1352, 1333, 1218, 1151, 1105, 976, 817, 767 cm^{-1} . *Anal.* Found (%): C, 66.77; H, 6.88; N, 8.14.

3.2.4 PS-MelmCOO

These were prepared in a similar fashion to PS-pimin (**3.2.2**) except that Im4COOH (1.2 mol eq. wrt to Cl) was used. The resultant white beads were cleaned as mentioned above (**3.2.3**). IR (cm^{-1} , KBr pellet): 3426, 1711, 1604, 1574, 1512, 1465, 1427, 1334, 1262, 1160, 1019, 814 cm^{-1} . *Anal.* Found (%): C, 56.7; H, 7.37; N, 9.48.

3.2.5 PS-[VO(pimin)_x]

PS-pimin (0.5 g) was allowed to swell in DMF for 2 hours. A DMF solution of vanadyl sulfate (0.6 g, 2.75 mmol) was added to the above mixture which was stirred and heated at 90 °C for 8 hours. The green beads were collected by filtration and rinsed with warm DMF and methanol and then dried in the oven overnight at 60 °C. ATR-IR (cm⁻¹, neat): 3393, 2924, 2162, 1677, 1594, 1447, 1288, 1225, 1159, 1043, 978, 819 cm⁻¹. *Anal.* Found (%): C, 62.12; H, 5.99; N, 4.63; S, 2.11; V, 4.7.

3.2.3 PS-[VO(Im4COO)_x]

These were prepared in a similar fashion as PS-[VO(pimin)_x] (3.2.5) except that PS-Im4COO was used (0.5 g). IR (cm⁻¹, KBr pellet): 3124, 2923, 1721, 1652, 1512, 1451, 1385, 1332, 1259, 1160, 1114, 1039, 1020, 972, 822 cm⁻¹. *Anal.* Found (%): C, 56.9; H, 5.89; N, 7.47; S, 2.62; V, 4.11.

3.2.6 PS-[VO(MelmCOO)_x]

This polymer was prepared as for PS-[VO(pimin)_x] (3.2.5) except that PS-Melm2COO (0.5 g) was used. IR (cm⁻¹, KBr pellet): 3431, 1631, 1572, 1512, 1451, 1424, 1261, 1159, 1110, 983, 806 cm⁻¹. *Anal.* Found (%): C, 49.31; H, 6.60; N, 6.99; S, 4.20; V, 4.60.

3.3 Catalytic activity studies

3.3.1 Oxidation of styrene, ethylbenzene and thioanisole

In a typical catalytic oxidation experiment, 20 mL of acetonitrile was added to a 100 mL round bottom flask fitted with a glass condenser. The temperature of the oil bath was regulated to ± 1 °C using an external temperature probe. The stirring rate was kept constant at 300 rpm for all reactions. Hereafter, styrene (1.04 g, 10 mmol), ethylbenzene (1.06 g, 10 mmol) or thioanisole (1.24 g, 10 mmol) was added followed by the required moles of hydrogen peroxide. Immediately after addition of hydrogen peroxide, the catalyst was added and this was considered the start of the reaction. The reaction progress was monitored using gas chromatography at specific time intervals.

3.3.2 Oxidative bromination

The oxidative bromination reactions were carried out in 25 mL of a pH 5.5 phosphate buffer (50 mM). Phenol red (20 μ M) and H₂O₂ (10 mM) were added to KBr (2.0 M). The reaction was initiated by addition of the required mass of the solid catalyst. The temperature during the reaction was maintained at ~ 20 °C and the stirring rate was kept constant at 700 rpm. The reaction progress was monitored spectrophotometrically. Phenol red shows two small absorption maxima at 268 nm and 557 nm and a high absorption maximum at 436 nm.¹² The oxidation bromination of phenol red can be followed by the disappearance of the peak at 436 nm and the appearance of a new peak at 590 nm corresponding to bromophenol blue, the tetrabrominated derivative.¹²

3.4 Results and discussion

3.4.1 Synthesis

The synthesis of piminH was similar to that performed by Parik¹³ with some slight modifications. These have been discussed in an earlier section (**Part 1, Chapter 3**). The same holds true for the synthesis of Melm2COOH, while Im4COOH was purchased from Sigma-Aldrich.

Both piminH and Im4COOH contain two nucleophilic groups both capable of taking part in nucleophilic substitution reactions, while Melm2COOH contains only the free carboxylic acid. For piminH these are the imidazoline-NH and the phenol groups, while for Im4COOH these are the carboxylic acid and the imidazole-NH groups. Thus reaction of these ligands with PS-Cl can be expected to give two possible products – the nitrogen bound or the oxygen bound derivatives. This simple consideration has been largely neglected in the field of heterogeneous catalysis. For example, the ligand 2-(2'-hydroxyphenyl)benzimidazole was reacted with PS-Cl in basic conditions and attachment was assumed to occur 100% via the benzimidazole-NH leaving the imine-nitrogen and phenol-oxygen free for coordination to the metal (in a bidentate fashion). While this indeed may occur, one cannot assume 100% selectivity since the pK_a s of the benzimidazole and the phenol are quite similar¹⁴ and in addition the relative order of acidity may switch depending on the solvent used.¹⁵ The consequence of this being that the actual coordination environment on the polymer is quite different to that of the neat complex.

It has been shown for Im4COOH, that the significantly more acidic carboxylic acid group directs alkylation to this position rather than the NH under mildly basic conditions.¹⁶ Thus one can expect the resultant coordination to be monodentate via the imidazole group (**scheme 3.3**). Similarly, alkylation of piminH provides predominantly the O-alkylated product. We demonstrated this by reacting piminH with benzyl chloride, affording the 2-(2'-benzyloxyphenyl)-1H-imidazoline product which was characterized by NMR and IR. The N-H signal remained in the ¹H NMR spectrum (**figure 3.2**) and the $\nu(\text{C-O-C})$ band at 1232 cm^{-1} in the infrared spectrum both confirmed O-alkylation. As for 1-methylimidazole-2-carboxylic acid, the methylated amine nitrogen ensures alkylation via the carboxyl group.

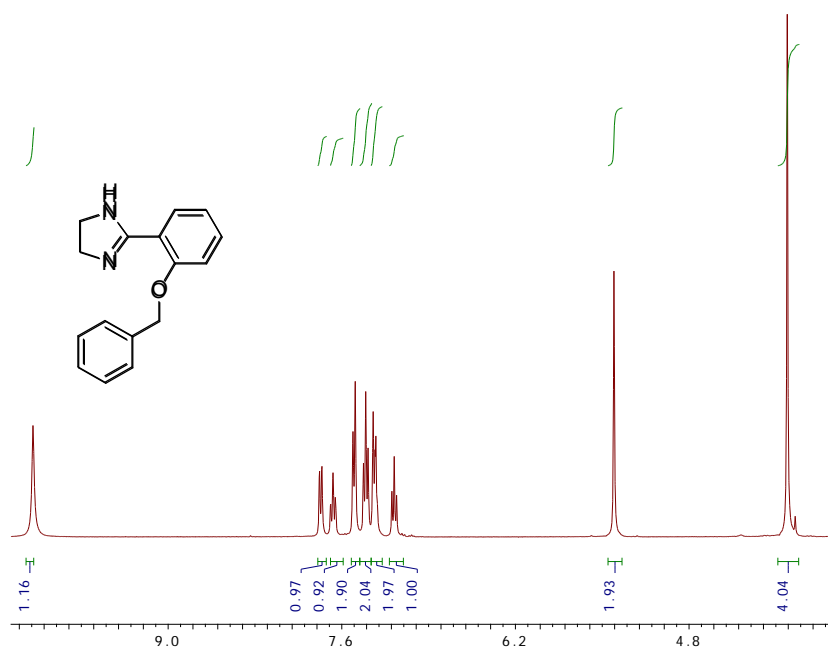
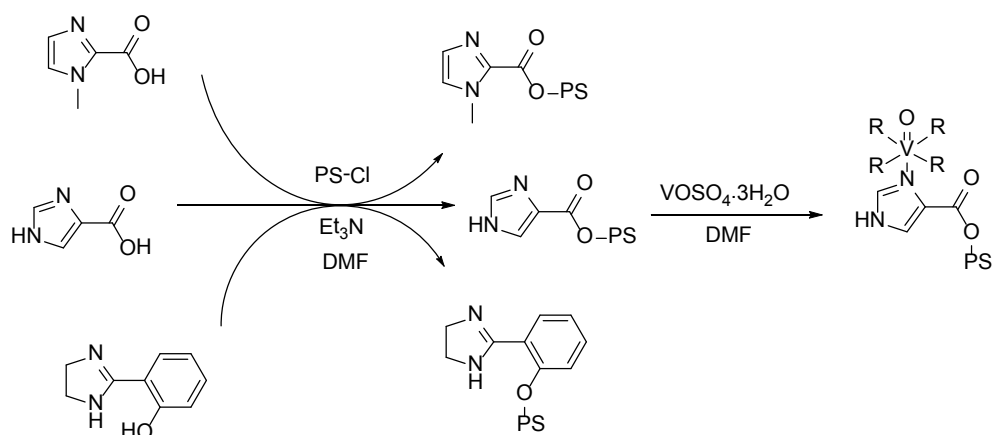


Figure 3.2 ¹H NMR spectrum of 2-(2'-benzyloxyphenyl)-1H-imidazole (δ ppm). The N-H proton signal appears at 10.1 ppm

The ligand bound polymers were then reacted with vanadyl sulfate, providing the heterogeneous oxovanadium(IV) catalysts. As a result of the above mentioned ligand attachment, the subsequent complex formation step may be expected to yield an oxovanadium(IV) complex with a different stereochemistry to that of the neat complexes; [VO(pimin)₂], [VO(Im4COO)₂] and [VO(MeIm2COO)₂]. The synthesis of these polymer-anchored catalysts has been described in **scheme 3.3**. The logic behind this synthesis was that by having free imidazole/imidazoline groups within the cross-linked polymer a coordination environment similar to the active site of VHPOs might be produced.



Scheme 3.3 Immobilization of oxovanadium(IV) onto imidazoline and imidazole functionalized PS-Cl. Only PS-[VO(Im4COO)_x] has been shown as a representative example. R represents a solvent molecule or a nearby ligand

3.4.2 Characterization

The infrared spectrum of chloromethylated polystyrene (PS-Cl) shows a band at 670 cm^{-1} corresponding to $\nu(\text{C-Cl})$,¹⁷ and the attachment of piminH, to polystyrene was confirmed by its disappearance and the appearance of a new band at 1615 cm^{-1} corresponding to the $\nu(\text{C=N})$. In the spectrum of the free ligand, a medium and broad band for the stretching frequency of the hydrogen bonded O-H appears at 2694 cm^{-1} ,¹⁸ but disappears in the spectrum of PS-pimin. This along with the appearance of the $\nu(\text{C-O-C})$ at 1233 cm^{-1} confirms that alkylation occurs predominantly *via* the phenol group.¹³ Similarly, for Melm2COOH and Im4COOH, the $\nu(\text{C=O})$ at 1614 cm^{-1} and 1655 , respectively, shift to 1711 cm^{-1} upon attachment to PS-Cl confirming attachment via the carboxylic acid group to form ester linkages.

Upon reaction of the ligand-functionalized Merrifield beads with vanadyl sulfate, PS-[VO(pimin)_x] displayed a medium intensity band in the IR spectrum at 978 cm^{-1} corresponding to the $\nu(\text{V=O})$ of the oxovanadium unit (**figure 3.3**).¹⁹ For PS-[VO(im4COO)_x] and PS-[VO(Melm2COO)_x] (**figure 3.4**), the $\nu(\text{V=O})$ appeared at 972 and 983 cm^{-1} respectively. In all instances, broadening of the $\nu(\text{C=N})$ made any meaningful conclusions regarding coordination via this group particularly unreliable. The position of the $\nu(\text{V=O})$ bands in the neat complexes was different to that of the functionalized polymers, with the $\nu(\text{V=O})$ for [VO(pimin)₂], [VO(Im4COO)₂] and [VO(Melm2COO)₂] appearing at 941 , 981 and 972 cm^{-1} respectively. These divergences can be expected since, as

already mentioned, the polymer-anchored and neat complexes were structurally dissimilar. For PS-[VO(pimin)_x], the bands appearing at 1225, 1159 and 1043 cm⁻¹ can be assigned to stretching vibrations of a coordinated sulfate ion (**figure 3.3**), while for the imidazole-based system this vibration appears as a very broad band from 1236 - 1060 cm⁻¹ (**figure 3.4**). This broadness was quite probably due to the presence of multiple overlapping bands. Thus, for all the polymer-anchored oxovanadium(IV) catalysts, the sulfate ion appears to be coordinated, with symmetry lower than T_d.²⁰ However, the exact mode of coordination, monodentate (C_{3v})²⁰ or bidentate (C_{2v})²⁰ remains questionable due to the complexity of the infrared spectra and presence of interfering vibrational bands. It is most likely, however, that the sulfate coordinates in a monodentate fashion as has been observed for vanadyl sulfate.²¹

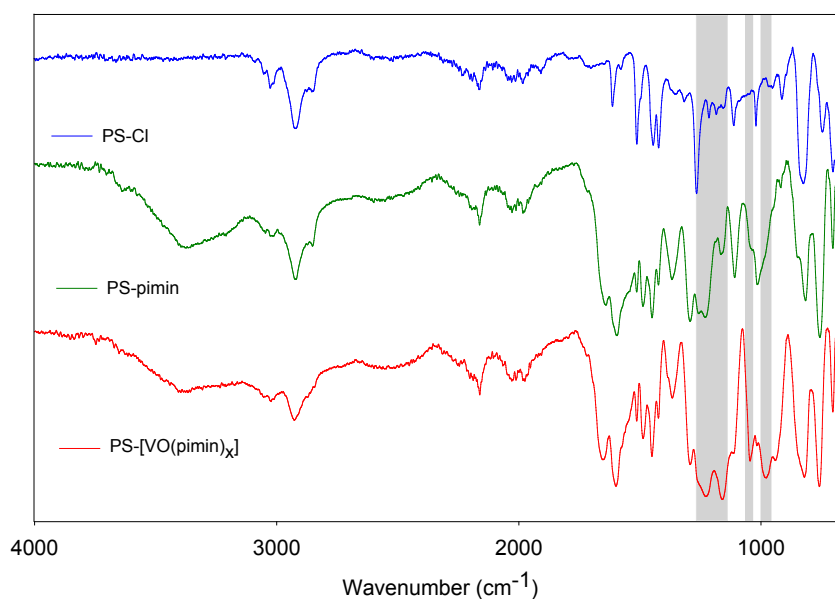


Figure 3.3 Stacked IR spectra of PS-Cl, PS-pimin and PS-[VO(pimin)_x] in the range 4000 – 650 cm⁻¹

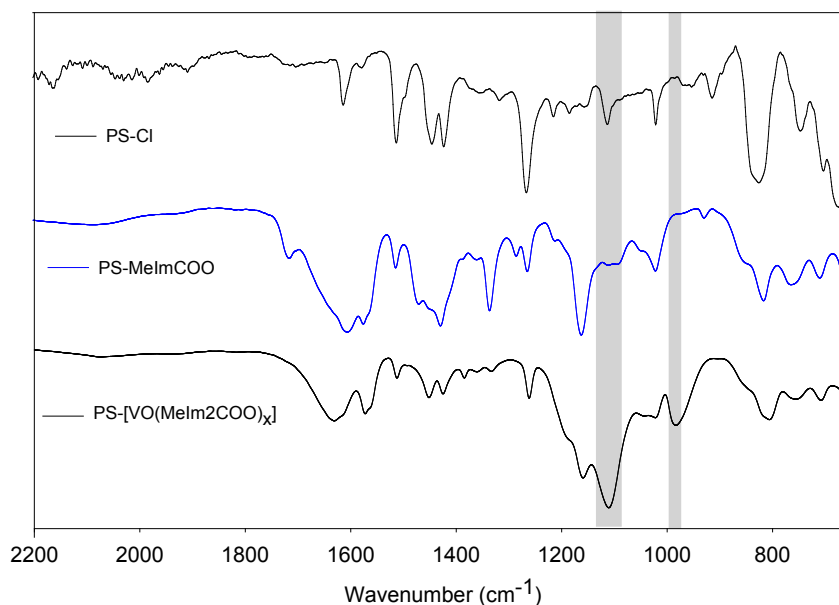


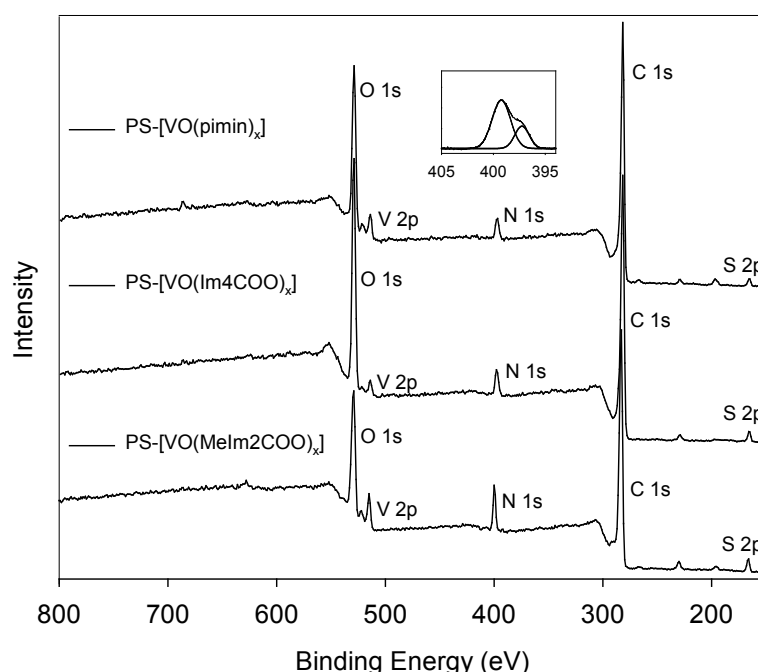
Figure 3.4 Stacked IR spectra of PS-Cl, PS-MelmCOO and PS-[VO(MelmCOO)_x] in the range 2200 – 650 cm⁻¹

Microanalysis results further confirmed that the polymer-bound vanadyl species was coordinated to sulfate, since sulfur was found in all heterogeneous catalysts. For each of the catalysts the sulfur/vanadium ratio was close to 1:1. The vanadium/nitrogen ratio for PS-[VO(pimin)_x] was 1:5 while for PS-[VO(Im4COO)_x] and PS-[VO(Melm2COO)_x] this changed to 1:6. This corresponds to 2.5 – 3 imidazoline/imidazole groups per vanadyl unit. It cannot be deduced, at least not without any great uncertainty, whether these are all bound to vanadium, or if there is a mixture of different species within the crosslinked polymer.

XPS was used to investigate the surface functionality of the heterogeneous catalysts (**figure 3.5**). The V 2p_{3/2} binding energy appeared at 514.9 eV confirming the presence of vanadium as well as the +4 oxidation state of the metal (**table 3.1**).²² The N 1s peak from the imidazole or imidazoline groups appeared at 399 eV (**table 3.1**) and the O 1s peak corresponding to oxygen in absorbed water, VO (vanadyl) and SO₄, appeared at 530 eV. In addition, the N 1s signal was comprised of two main peak due to the amine and imine nitrogen atoms (**figure 3.5**). The presence of sulfur as indicated by infrared and elemental analysis, was confirmed using XPS, with the S 2p_{3/2} peak appearing at 167 eV (**table 3.1**) for all catalysts.²³

Table 3.1 Elemental binding energies of Merrifield-based catalysts as determined by XPS

Polymer	Binding Energy (eV)					
	O 1s	N 1s	C 1s	V 2p _{3/2}	V 2p _{1/2}	S 2p _{3/2}
PS-[VO(pimin) _x]	530	399	285	515	522	167
PS-[VO(Im4COO) _x]	530	399	285	515	522	167
PS-[VO(MeIm2COO) _x]	530	399	285	515	522	167

**Figure 3.5** Wide scan XPS spectra of PS-[VO(pimin)_x], PS-[VO(Im4COO)_x] and PS-[VO(MeIm2COO)_x]. Insert shows an expanded view of the high resolution N 1s signals of PS-[VO(Im4COO)_x]

The various functionalization steps of the Merrifield beads (PS-Cl) was also investigated by thermogravimetric analysis (**figure 3.5**). Unmodified PS-Cl decomposed in two steps, the first beginning at 270 °C ($T_{\max} = 370$ °C) and the second at 400 °C ($T_{\max} = 444$ °C) quite similar to that observed by other researchers.²⁴ After ligand attachment, the TG curve changed significantly. An initial weight loss below 110 °C ($T_{\max} = 56$ °C) was observed for PS-pimin, probably due to absorbed water molecules. Another unique weight loss step began at 184 °C ($T_{\max} = 190$ °C), quite close to the melting point of the piminH. After functionalization with oxovanadium(IV), the latter weight loss step disappeared and a new one appeared at 250 °C ($T_{\max} = 300$ °C) possibly

due to complex decomposition (**figure 3.5**). This confirmed coordination of the ligand to oxovanadium(IV) within the polymer.

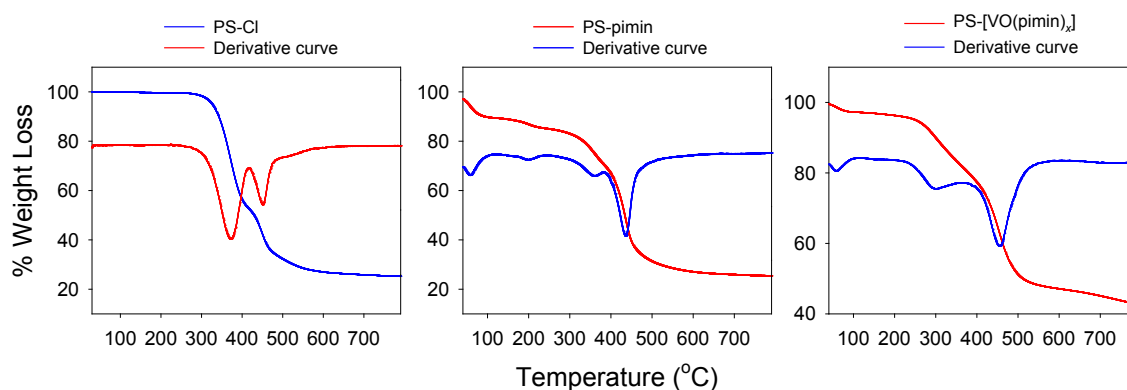


Figure 3.5 TG and DTG curves of PS-Cl, PS-pimin and PS-[VO(pimin)_x] at a heating rate of 10 °C.min⁻¹ under N₂

SEM and AFM were used to monitor the morphological changes occurring on the surface of the polymer beads after the various functionalization steps. For each of the different ligand systems, the SEM images showed the same trends. These changes are well illustrated in the representative example shown in **figure 3.6**, when Im4COOH was used as the ligand. Before modification the PS-Cl beads had an apparent smooth surface, whilst after reacting these with the ligand the surface roughness seemed to increase. After reacting these beads with vanadyl sulfate, the surface appeared 'coated' and was somewhat smoother than the ligand-functionalized beads. The abrasions shown on the surface of PS-[VO(Im4COO)_x] beads were likely due to the agitation of the mechanical stirrer. The average diameter for these beads was 612 μm.

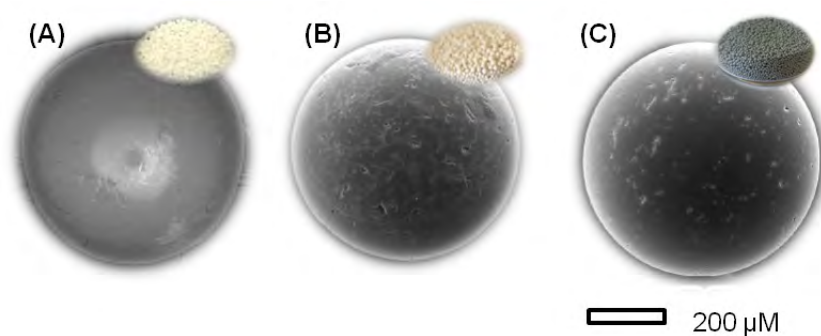


Figure 3.6 SEM images of a single bead and digital (right corner of bead) images of (A) PS-Cl, (B) PS-Im4COO and (C) PS-[VO(Im4COO)_x] (average diameter $\varnothing = 612 \mu\text{m}$)

The AFM studies agreed quite well with the above mentioned trends. Shown in **figure 3.7** are the atomic force micrographs of beads from the piminH ligand system at the various stages of synthesis. The unfunctionalized beads have a relatively amorphous surface. After reacting these with the ligand, the surface appeared significantly different. Even more significant were the changes that occurred after reaction with vanadyl sulfate, with small diamond-shaped structures appearing. The surface roughness (R_a nm) was determined from an average of five $10 \times 10 \mu\text{m}$ sections. The surface roughness for unmodified PS-Cl was 7.92 nm. For PS-pimin and PS-[VO(pimin)_x] the roughness values were 6.14 and 5.06 nm, respectively. For PS-Im4COO and PS-[VO(Im4COO)_x] they were 7.89 and 6.54 nm, respectively, and for PS-Melm2COO and PS-[VO(Melm2COO)_x] they were 7.56 and 6.12 nm, respectively. Once again these values corresponded relatively well with the trends observed visually. The slight exception may be the larger surface roughness of PS-Cl, which was not immediately evident from the SEM image (**figure 3.6**), but more visible at the higher resolution obtained using AFM.

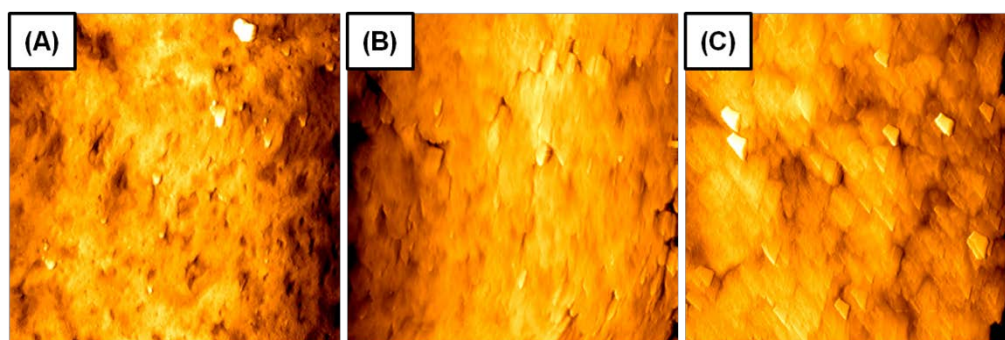


Figure 3.7 AFM images of (A) PS-Cl, (B) PS-pimin and (C) PS-[VO(pimin)_x] (scale = $10 \times 10 \mu\text{m}$)

The surface area of PS-Cl and a representative catalyst, PS-[VO(pimin)_x] was determined from nitrogen absorption/desorption isotherms (**figure 3.8**) using the BET method. The specific surface area of the PS-Cl beads was found to be $10.4 \text{ m}^2 \cdot \text{g}^{-1}$, while the average pore volume and size was $0.07 \text{ cm}^3 \cdot \text{g}^{-1}$ and 311 \AA , respectively. After functionalization of PS-Cl with piminH and oxovanadium(IV), the surface area dropped to $6.9 \text{ m}^2 \cdot \text{g}^{-1}$. The pore size remained relatively similar at 387 \AA and the pore volume dropped slightly to $0.05 \text{ cm}^3 \cdot \text{g}^{-1}$. The drop in surface area corresponds well with the observed drop in surface roughness shown using AFM. Additional loss

in surface area may be attributed to filling of pores by vanadium. This was corroborated by the above mentioned drop in pore volume from 0.07 to 0.05 cm³.g⁻¹.

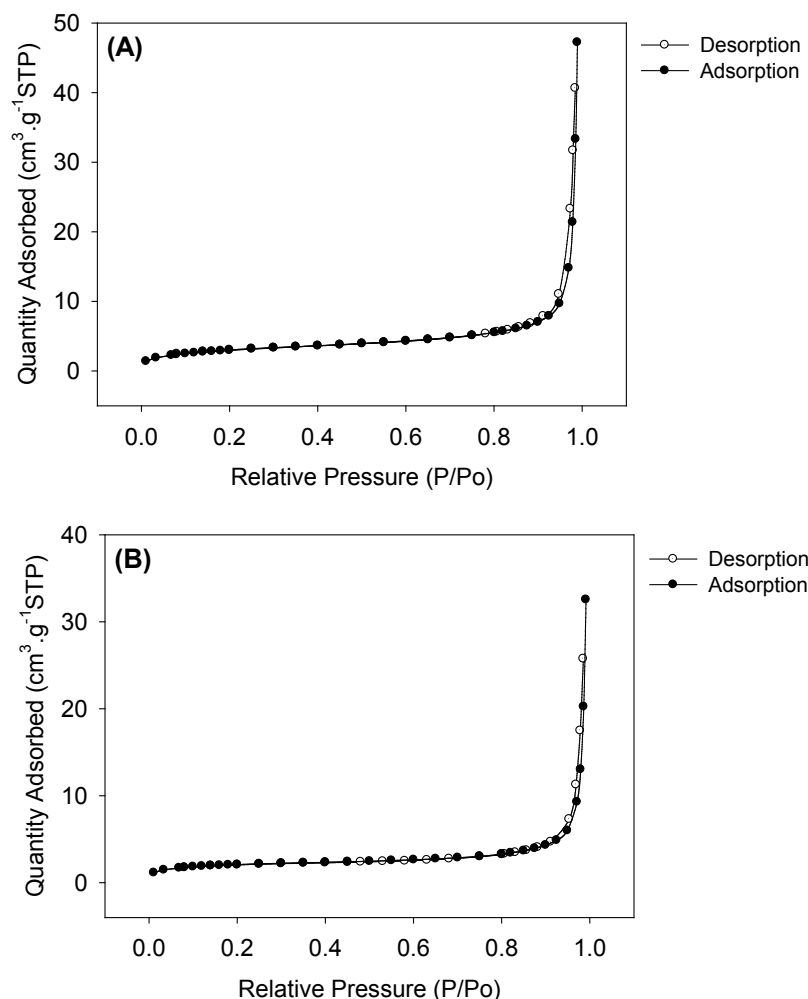


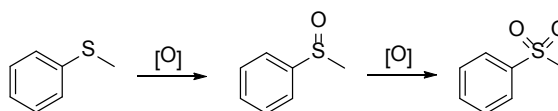
Figure 3.8 Nitrogen adsorption-desorption isotherms for (A) PS-Cl and (B) PS-[VO(pimin)_x]

3.4.3 Catalytic activity

The catalytic activity of the heterogeneous oxovanadium(IV) catalysts; PS-[VO(pimin)_x], PS-[VO(Im4COO)_x] and PS-[VO(MeIm2COO)_x], was investigated for the oxidation of thioanisole, styrene and ethylbenzene. The activity of these heterogeneous catalysts was compared to the non-geometrically equivalent homogeneous catalysts; [VO(pimin)₂], [VO(Im4COO)₂] and [VO(MeIm2COO)₂]. The reaction progress was monitored using GC by comparison of retention times to that of the pure standards. The product identities were also confirmed using GC-MS.

(a) Oxidation of thioanisole

The oxidation of sulfides has become a valuable reaction due to the use of sulfoxides (sulfide oxidation products) as intermediates in the synthesis of biologically active compounds.^{25,26} Additionally, oxidative desulfurization (ODS), a process used to remove sulfur from fuels, has recently received a renewed interest. The conventional hydrodesulfurization (HDS) process has been employed by refineries to remove organic sulfur from fuels for the past couple of decades with the lowest sulfur content achieved being around 500 ppm. Thus additional steps need to be developed in order to achieve the new criteria set for ultra-low sulfur fuels (<10 ppm, Euro standards). In this regard ODS has shown some promise.^{27,28} Thioanisole was chosen as the model sulfide to be used in this study. Although this compound does not form a large component of the problematic sulfide compounds in fuels, it is one of the most common reagents used to assess catalyst efficacy for sulfide oxidation reactions.²⁹⁻³² Upon oxidation, thioanisole is converted primarily to methyl phenyl sulfoxide which may be further oxidised to methyl phenyl sulfone according to **scheme 3.4**.



Scheme 3.4 Oxidation of methyl phenyl sulfide (thioanisole) gives primarily methyl phenyl sulfoxide and methyl phenyl sulfone ([O] represents an oxidizing agent)

The temperature and amount of catalyst were varied until optimal conditions were obtained. Additionally, the effect that these changes imposed on the overall conversion and product selectivity was monitored. According to the literature, the oxidation of sulfides invariably reaches a maximum conversion at a 2:1 peroxide-to-sulfide ratio⁶ and even less, and therefore in our study this ratio was kept constant. For the heterogeneous catalysts, the effect of temperature and catalyst amount in the range 0.0-0.035 g, on the rate of oxidation was studied as a function of time as shown in **figure 3.9** for PS-[VO(pimin)_x].

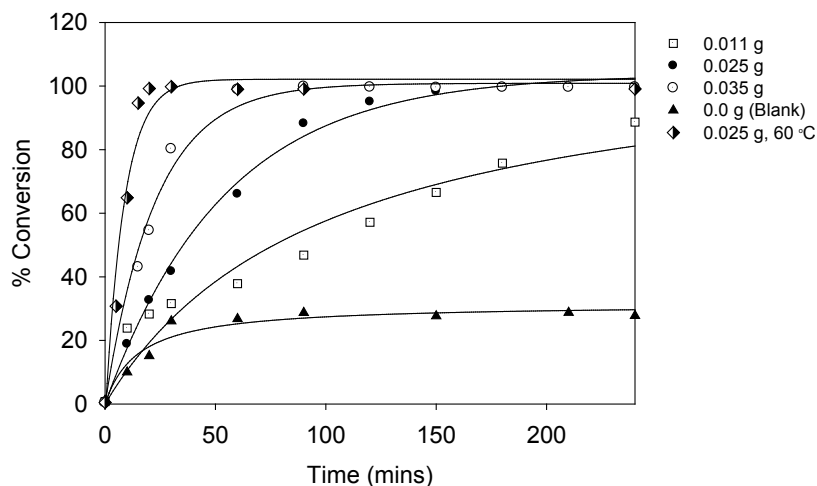


Figure 3.9 The effect of catalyst amount on thioanisole oxidation. Reaction conditions: PS-[VO(pimin)_x], thioanisole (10 mmol), H₂O₂ (20 mmol), acetonitrile (20 mL) and 25 °C

For a fixed amount of thioanisole (1.24 g, 10 mmol) in 20 mL of acetonitrile and 30% H₂O₂ (20 mmol) at room temperature, the rate of the oxidation reaction is fast for the highest catalyst amount of 0.035 g reaching 98.9% conversion within 1 h. When using 0.025 g of catalyst a maximum conversion of 99.6% was obtained within 3 h at room temperature. Using the same amount of catalyst and increasing the temperature from 25 °C to 60 °C (**table 3.1**) resulted in a significantly increased rate of oxidation – with near quantitative oxidation being attained in as little as 20 mins. When using 0.011 g a maximum of 88.8% was obtained after 4 hour reaction period. The overall activity of the imidazole-based catalysts, PS-[VO(Im4COO)_x] and PS-[VO(MeIm2COO)_x], was slightly lower than the imidazoline counterpart (**figure 3.10**). For example; after 4 hours, the maximum conversions recorded with these catalysts was 91.6 and 96.1% respectively, compared to >99% obtained with PS-[VO(pimin)_x].

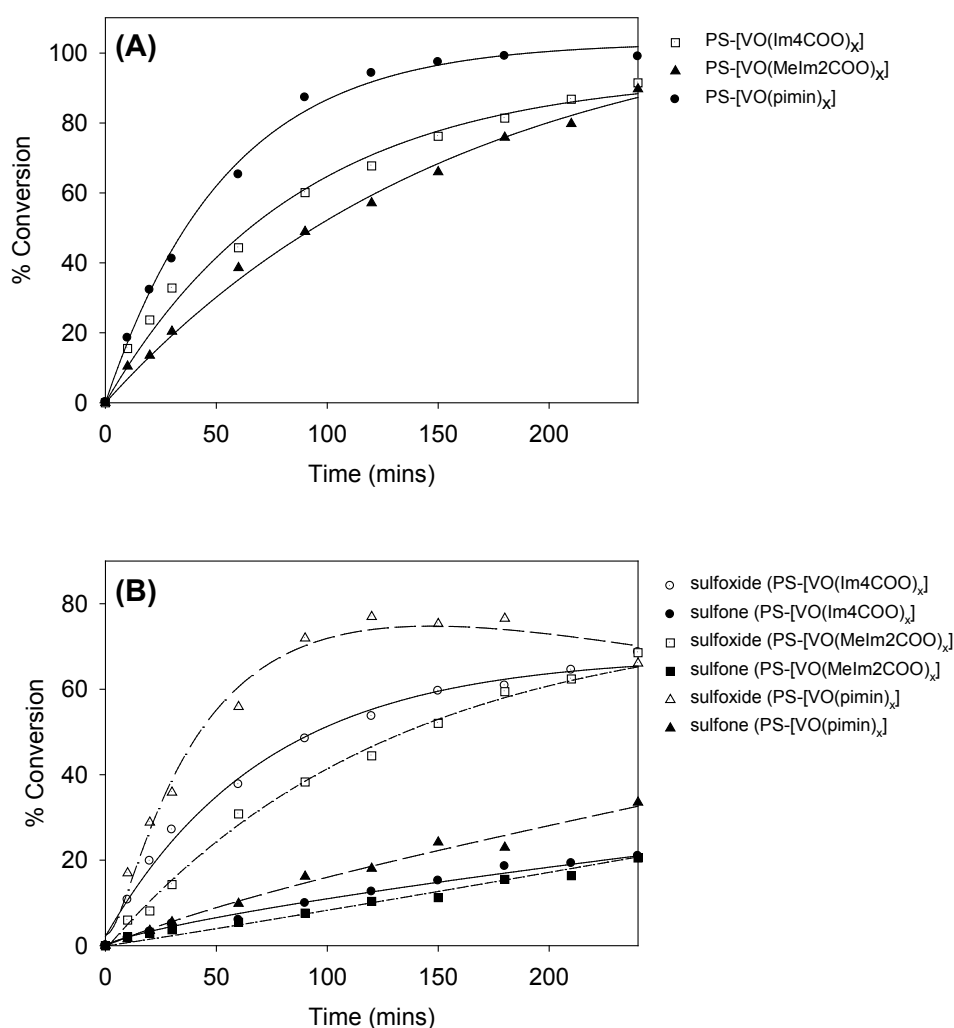


Figure 3.10 (A) Overall oxidation of thioanisole and (B) product selectivity for the catalysts PS-[VO(pimin)₂], PS-[VO(Im4COO)₂] and PS-[VO(Melm2COO)₂] (0.025 g, ~0.2 mol% of V, wrt thioanisole), thioanisole (10 mmol), H₂O₂ (20 mmol), acetonitrile (20 mL) and 25 °C

The product selectivity for all of the catalysts was relatively similar under the conditions tested. When using 0.025 g of any of the heterogeneous catalysts, the sulfoxide/sulfone ratio was maintained close to 2:1. Increasing the temperature, however, caused this ratio to change dramatically to 1:3 (sulfoxide/sulfone). This can be expected since under the harsher (more oxidizing) conditions, the sulfoxide may be converted to the sulfone via consecutive reactions as shown in **scheme 3.4**. A typical selectivity profile showing the formation of methyl phenyl sulfoxide and methyl phenyl sulfone, for each of the catalysts under identical conditions has been included in **figure 3.10**. Under these conditions (room temperature, 0.025 g of catalyst) the

sulfoxide formation increases rapidly and forms the major product along with a comparatively smaller amount of the sulfone. The consecutive conversion of the sulfoxide to sulfone is best illustrated at higher catalyst amounts, for example in **figure 3.11** which depicts a sharp initial increase in the formation of methyl phenyl sulfoxide, followed by a gradual decay associated with the steady conversion to the sulfone. Conversely, when using just 0.011 g of PS-[VO(pimin)_x] at room temperature gave a sulfoxide/sulfone a ratio of 5:1.

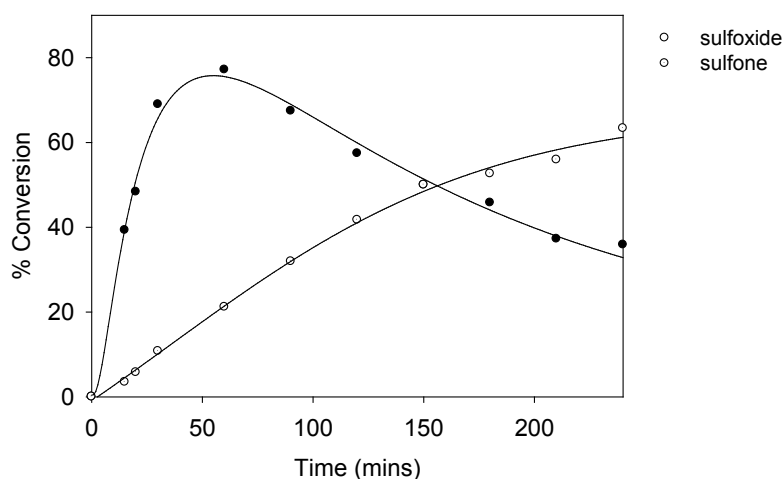


Figure 3.11 The product selectivity over time. Reaction conditions: PS-[VO(pimin)_x] (0.035 g), thioanisole (10 mmol), H₂O₂ (20 mmol), acetonitrile (20 mL) and 25 °C

Based on these observations, it can be deduced that the product selectivity may be altered by modifying the reaction conditions. Essentially, sulfoxide selectivity may be improved by using milder conditions such as a lower temperature or catalyst amount. The major disadvantage of this would be the increased reaction times for complete conversion. On the other hand, sulfone selectivity can be achieved more easily by increasing the reaction time, increasing catalyst amount or increasing reaction temperature.

One of the major draw cards of heterogeneous catalysts is that they can be separated and recycled from solution very easily. It is crucial then for the recyclability of the catalysts to be investigated. Both of the imidazole-based systems, PS-[VO(Im4COO)_x] and PS-[VO(MeIm2COO)_x], showed excellent recyclability. As shown in **figure 3.12**, there was in fact a reduced induction period after one catalytic cycle. This was quite possibly related to the first steps

of the catalytic mechanism. To recap this briefly; oxovanadium(IV) is first converted to the dioxovanadium(V) species which is subsequently converted to the oxoperoxovanadium(V) species. This conversion of V^{4+} to V^{5+} can be seen very easily with the naked eye - if the beads were removed from solution mid-reaction they retained a yellow-orange colour, however upon completion of the reaction, they returned to a colour *similar* to that of the original beads (a grey-blue). Closer examination of the latter using IR, revealed that the characteristic $\nu(V=O)$ was still present, but a shoulder to this band appeared at lower wavenumbers indicative of the dioxovanadium(V) species.³³ Thus one can conclude that the beads likely contain a mixture of the oxovanadium(IV) and dioxovanadium(V) species, rather than 100% of the oxovanadium(IV) species as originally presumed. This explains the reduced induction period upon recycling since the first oxidation step is no longer required as some dioxovanadium(V) species are present on the beads. However, the PS-[VO(pimin)_x] beads were comparably less successful in terms of recyclability, with an appreciable loss in activity being observed after successive cycles, probably due to leaching of vanadium (**figure 3.12**).

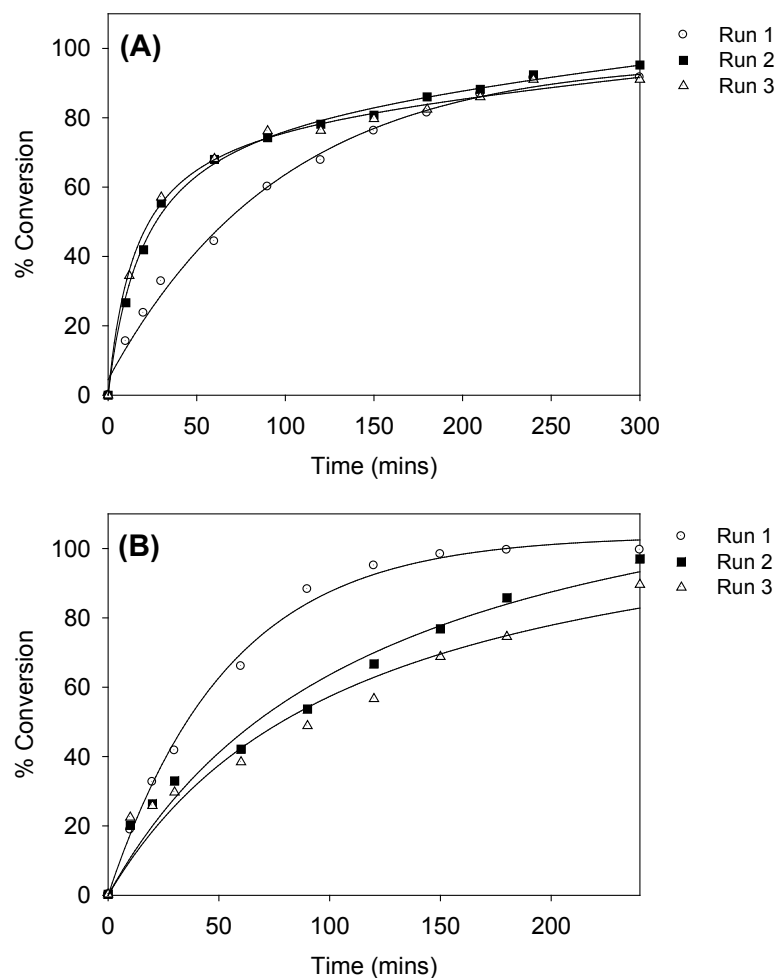


Figure 3.12 Catalyst recyclability for the oxidation of thioanisole. Reaction conditions: (A) PS-[VO(Im4COO)_x] (0.025 g), (B) PS-[VO(pimin)_x], thioanisole (10 mmol), H₂O₂ (20 mmol), acetonitrile (20 mL) and 25 °C

The catalytic activity of the non-geometrically equivalent homogeneous catalysts [VO(pimin)₂], [VO(Im4COO)₂] and [VO(MeIm2COO)₂] as well as the common vanadyl salt, VOSO₄, was also investigated. Specific masses of these complexes, which corresponded to approximately 0.025 g of the heterogeneous catalysts (0.2 mol% vanadium wrt. thioanisole), were taken to allow for comparison with the heterogeneous derivatives. As shown in **figure 3.13**, these homogeneous catalysts exhibit much higher activity, with >99% conversion being attained within 30 minutes. The vanadyl sulfate salt displayed the highest activity followed by [VO(pimin)₂] and then [VO(MeIm2COO)₂] and [VO(Im4COO)₂]. The activity in this case, was probably linked to the solubility of the complexes in acetonitrile. Vanadyl sulfate dissolved immediately and as

mentioned was the most active, while the imidazole based complexes dissolved quite slowly, only being completely dissolved after approximately 10 minutes. It is therefore quite clear that although some measures can be taken to increase the activity of the heterogeneous catalyst, by appropriate ligand design, the major improvements could be made by increasing the surface area of the catalyst support. A table summarizing the overall conversion, product selectivity and turnover frequencies (TOF) has been included (**table 3.2**).

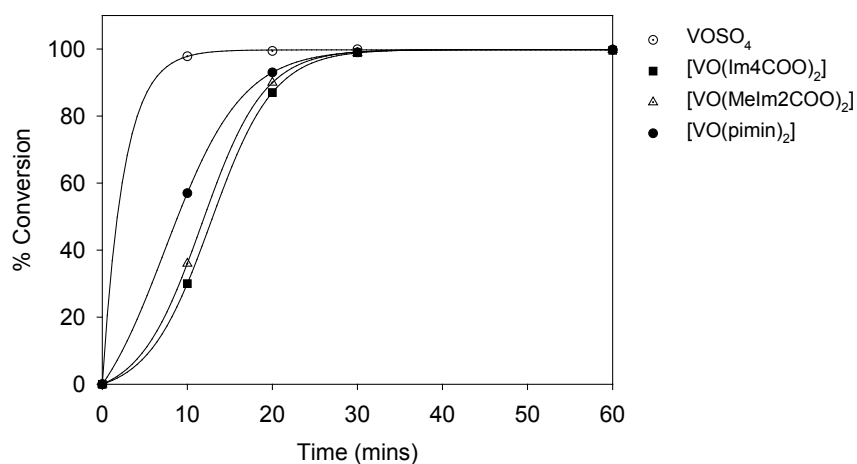


Figure 3.13 Oxidation of thioanisole by VOSO_4 , $[\text{VO}(\text{pimin})_2]$, $[\text{VO}(\text{Im}4\text{COO})_2]$ and $[\text{VO}(\text{MeIm}2\text{COO})_2]$. Reaction conditions: Catalyst (0.2 mol% wrt. thioanisole), thioanisole (10 mmol), H_2O_2 (20 mmol), acetonitrile (20 mL) and 25 °C

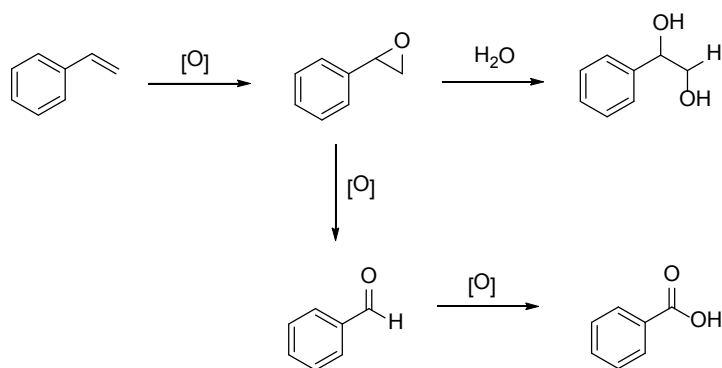
Table 3.2 Percentage conversion, turnover frequency (TOF) and product selectivity for the oxidation of thioanisole

Catalyst	Mass (g)	Temp (°C)	H ₂ O ₂ (eq) [†]	Conversion (%)	TOF ^a (h ⁻¹)	Sulfoxide (%)	Sulfone (%)
PS-[VO(pimin)_x]	0.011	25	2	88.8	156	74.2	14.3
	0.025	25	2	>99	169	66.1	33.5
	0.025 ^b	25	2	92.3	121	75.3	21.7
	0.025	60	2	>99	860	24.7	74.3
	0.035	25	2	>99	306	63.5	36.0
PS-[VO(Im4COO)_x]	0.025	25	2	91.6	88	65.8	29.9
	0.025 ^b	25	2	96.3	77	68.4	26.7
	0.025	60	2	>99	485	68.2	30.5
	0.035	25	2	99.5	57	65.5	27.8
PS-[VO(MeIm2COO)_x]	0.025	25	2	96.1	73	67.0	27.9
	0.025 ^b	25	2	96.6	74	61.9	33.8
	0.025	60	2	>99	911	65.7	33.0
	0.035	25	2	97.7	54	64.5	32.7

[†]mmol relative to thioanisole ^a Determined as moles of substrate converted/moles of catalyst/time (h); ^b After one catalytic cycle/reaction

(b) Oxidation of styrene

Catalytic oxidation of alkenes is an extremely important technology, frequently used for converting petroleum based feedstocks into useful (functional) chemicals such as alcohols, aldehydes, carboxylic acids and epoxides.³⁴ The test alkene used in this study was styrene, which upon oxidation, may be converted to styrene oxide, which may be subsequently converted to phenylethane-1,2-diol, or benzaldehyde. The latter product may be further oxidized to benzoic acid as outlined in **scheme 3.5**.



Scheme 3.5 The main products of the oxidation of styrene include styrene oxide, benzaldehyde, benzoic acid and phenylethane-1,2-diol ([O] represents an oxidizing agent)

The first parameter to be investigated was the effect of using the different catalysts as shown in **figure 3.14**. Under the conditions tested, PS-[VO(pimin)_x] and PS-[VO(Im4COO)_x] gave similar overall conversions and selectivity (see **table 3.3**), while the overall conversion obtained using PS-[VO(MeIm2COO)₂] was about 20% lower. The reason for this is not completely understood, but may be due to the electron donating methyl substituent. On the topic of selectivity, the general order was; benzaldehyde > phenylethane-1,2-diol > benzoic acid > styrene oxide as illustrated in **figure 3.15**.

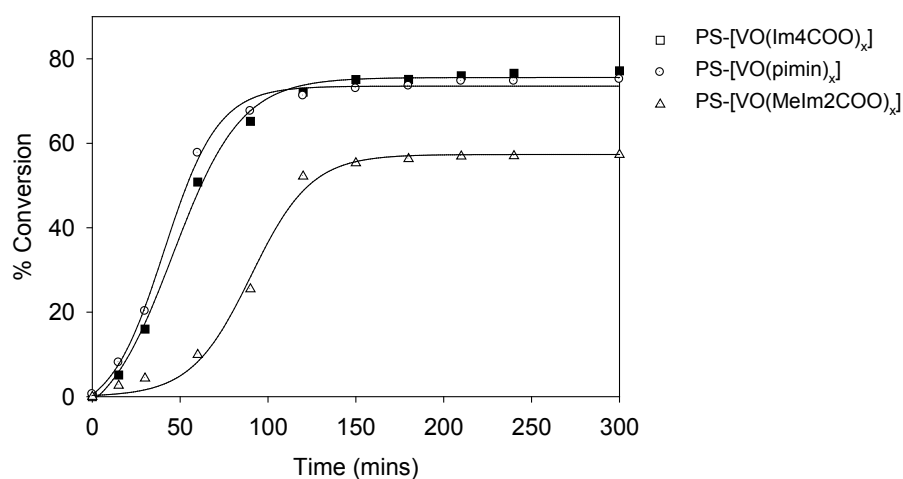


Figure 3.14 Oxidation of styrene by PS-[VO(pimin)_x], PS-[VO(Im4COO)_x] and PS-[VO(MeIm2COO)₂]. Reaction conditions: Catalyst (0.025 g), styrene (10 mmol), H₂O₂ (20 mmol), acetonitrile (20 mL) and 80 °C

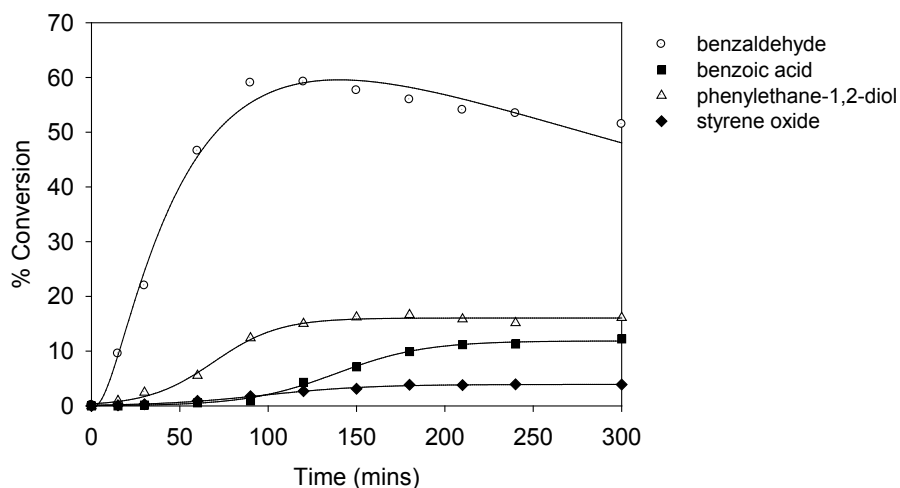


Figure 3.15 Product selectivity for the oxidation of styrene by PS-[VO(pimin)_x]. Reaction conditions: Catalyst (0.025 g), styrene (10 mmol), H₂O₂ (40 mmol), acetonitrile (20 mL) and 80 °C

The trends observed with increasing catalyst amount were not as predictable as those observed for thioanisole oxidation. As shown in **figure 3.16**, increasing the amount of catalyst improved the initial rate of reaction (reduced induction period), but resulted in a drop in overall activity. When 0.011 g, 0.025 g and 0.035 g of PS-[VO(pimin)_x] were used, the overall conversions after a 6 hour period were 85.4, 75.1 and 69.2%, respectively. A similar trend was observed for the imidazole-based catalysts (**table 3.3**).

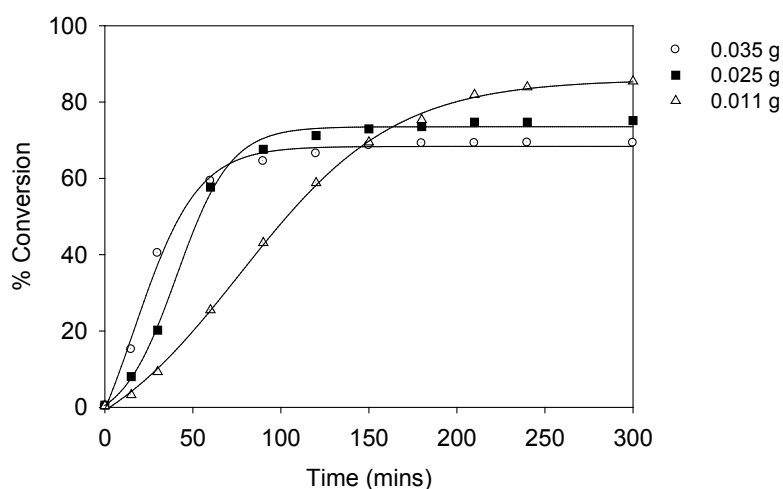


Figure 3.16 The effect of catalyst amount on the oxidation of styrene by PS-[VO(pimin)_x]. Reaction conditions: Styrene (10 mmol), H₂O₂ (20 mmol), acetonitrile (20 mL) and 80 °C

The next parameter investigated was the effect of oxidant concentration. As shown in **figure 3.17**, increasing the amount of H_2O_2 improved the overall conversion by approximately 20%, with no marked difference on the selectivity. The necessity for additional peroxide has been captured sufficiently well in **figure 3.18**. In this instance, the homogeneous catalyst, $[\text{VO}(\text{pimin})_2]$ was initially combined with two-equivalents of peroxide. The conversion began to plateau at 56.5% after 1.5 hours. When additional peroxide was added however (one equivalent wrt. styrene), the conversion rapidly increased to 91.6% where it then stabilized. Four-equivalents of peroxide was sufficient to achieve >99% conversions when using the homogeneous catalyst, $[\text{VO}(\text{pimin})_2]$.

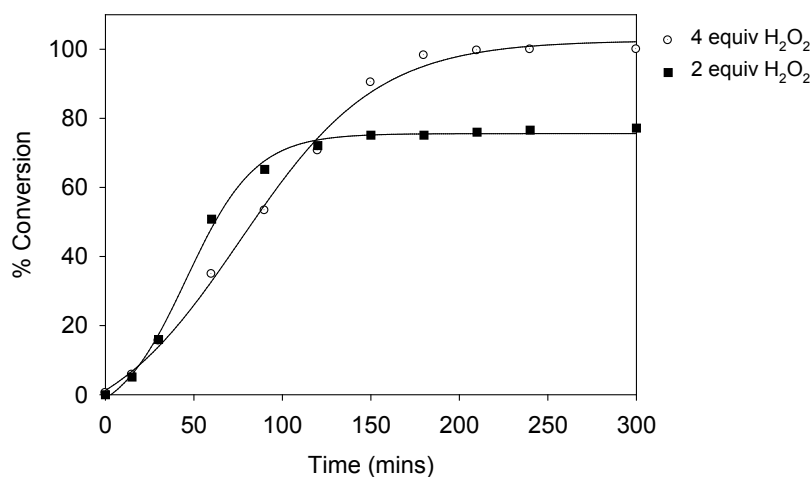


Figure 3.17 The effect of peroxide amount on the oxidation of styrene by $\text{PS}[\text{VO}(\text{Im}4\text{COO})_x]$. Reaction conditions: Catalyst (0.025 g), styrene (10 mmol), acetonitrile (20 mL) and 80°C

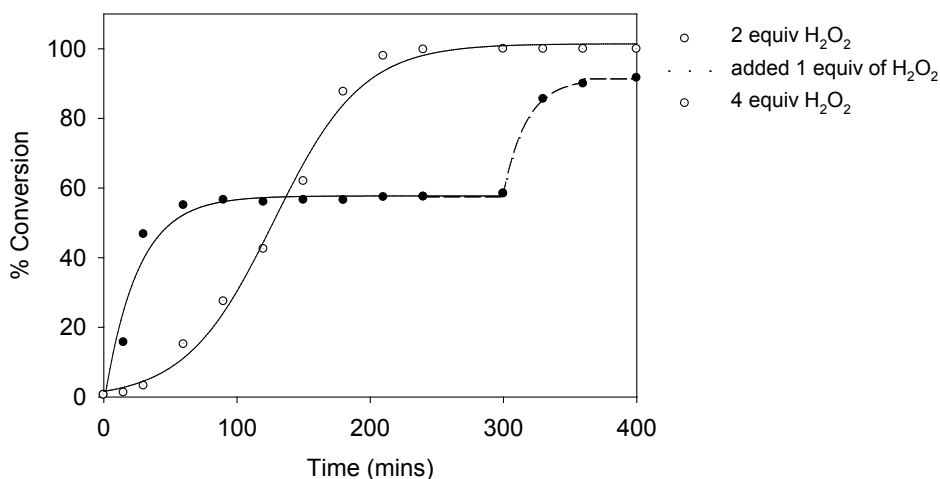


Figure 3.18 The effect of the amount of oxidant for the homogeneous oxidation of styrene by $[\text{VO}(\text{pimin})_2]$. Reaction conditions: Catalyst (0.2 mol%, equiv to 0.025 g of heterogeneous), styrene (10 mmol), acetonitrile (20 mL) and 80 °C

The optimal conditions for maximum styrene oxidation were obtained when using four-equivalents of peroxide with the reaction temperature being maintained at 80 °C. However, under these conditions the beads became fragile and subsequent deterioration made recycling experiments difficult. An AFM image of the surface of a PS- $[\text{VO}(\text{pimin})_x]$ beads after such a reaction has been included in **figure 3.19** to illustrate this point. The corresponding digital images also clearly show the development of surface cracks on the beads.

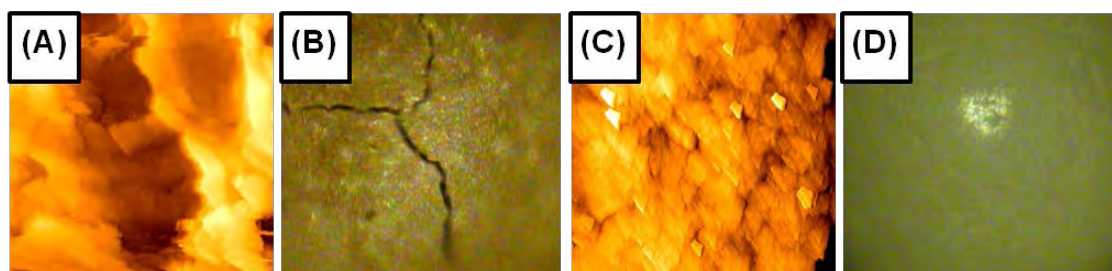


Figure 3.19 An AFM image (A) and digital image (B) of the surface of a PS- $[\text{VO}(\text{pimin})_x]$ bead after a catalytic reaction using styrene as the substrate, at 80 °C and with four-equivalents of H_2O_2 , along with the AFM (C) and digital (D) image of the same beads before a catalytic reaction

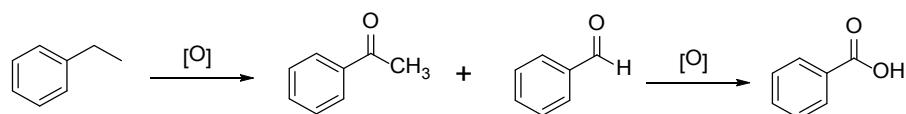
Table 3.3 Percentage conversion, turnover frequency (TOF) and product selectivity (for the two major products) for the oxidation of styrene (Benzal = benzaldehyde, Phen-1,2-diol = phenylethane-1,2-diol)

Catalyst	Mass (g)	Temp (°C)	H ₂ O ₂ (eq) [†]	Conversion (%)	TOF ^a (h ⁻¹)	Benzal (%)	Phen-1,2-diol (%)
PS-[VO(pimin) _x]	0.011	80	2	85.4	194	50.12	16.4
	0.025	80	2	75.1	129	49.4	17.2
	0.035	80	2	69.2	85	47.6	16.5
	0.025	80	4	>99	173	51.5	16.1
	0.025	60	2	69.3	119	50.8	15.2
PS-[VO(Im4COO) _x]	0.025	80	4	>99	138	43.3	17.3
	0.025	80	2	77.1	174	41.1	15.4
	0.035	80	2	67.2	145	36.6	14.8
	0.025	60	4	66.2	53	41.3	7.5
PS-[VO(MeIm2COO) _x]	0.025	80	2	57.3	119	28.6	14.7
	0.025	60	4	49.2	62	34.0	9.3
	0.035	80	2	60.1	129	33.0	14.1

[†]mmol relative to thioanisole; ^a Determined as moles of substrate converted/moles of catalyst/time (h)

(c) Oxidation of ethylbenzene

The transition metal catalyzed conversion of alkanes to oxygen-containing compounds is one of the most important and fundamental transformations in the chemical industry, and there is therefore a constant need for improving current systems.^{35,36} The test alkane used in this study was ethylbenzene which upon oxidation may be converted primarily to acetophenone, benzaldehyde and benzoic acid as outlined in **scheme 3.6**.



Scheme 3.6 The main products of the oxidation of ethylbenzene include acetophenone, benzaldehyde and benzoic acid ([O] represents some oxidizing agent)

Compared to alkene oxidation, the oxidation of alkanes is a significantly more difficult process due to the absence of empty orbitals and available lone pairs coupled with the strong bonding between C and H.³⁷ This resistance to oxidation was noticed by the generally low conversions obtained even under harsh conditions. As shown in **figure 3.20**, a maximum conversion of 30.3% was obtained for PS-[VO(pimin)_x] when four-equivalents of peroxide were used and the temperature was maintained at 80 °C. The two main oxidation products were found to be acetophenone and benzaldehyde. The mechanism of formation of acetophenone proposed by Hoshino *et al.*³⁸ involves the abstraction of an α-hydrogen from ethylbenzene to form 1-phenylethyl radicals, followed by a reaction with oxygen to produce acetophenone while the formation of benzaldehyde is believed to occur *via* the decomposition of 1-phenylethoxyl radicals.

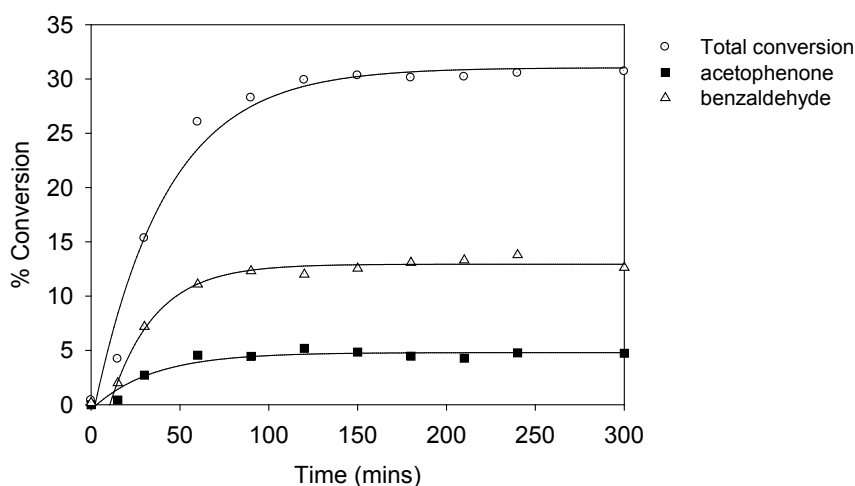


Figure 3.20 Selectivity for the oxidation of ethylbenzene using PS-[VO(pimin)_x]. Reaction conditions: Catalyst (0.025 g), ethylbenzene (10 mmol), H₂O₂ (40 mmol), acetonitrile (20 mL) and 80 °C

As mentioned earlier, these harsh conditions result in gradual disintegration of the catalyst beads, and thus milder conditions (lower temperature or peroxide amount) were adopted to limit this problem. Considering PS-[VO(pimin)_x] first, when the temperature was kept at 80 °C and the peroxide was dropped from four to two-equivalents the overall conversion dropped from 30.3% to 13.8%. As illustrated in **figure 3.21**, when the peroxide was kept at two-equivalents and the temperature reduced to 60 °C, the conversions dropped once again. For example, for PS-

[VO(Im4COO)_x], the conversion dropped from 10.6% (at 80 °C) to 8.2% (at 60 °C) even though the amount of catalyst was increased from 0.025 g to 0.035 g.

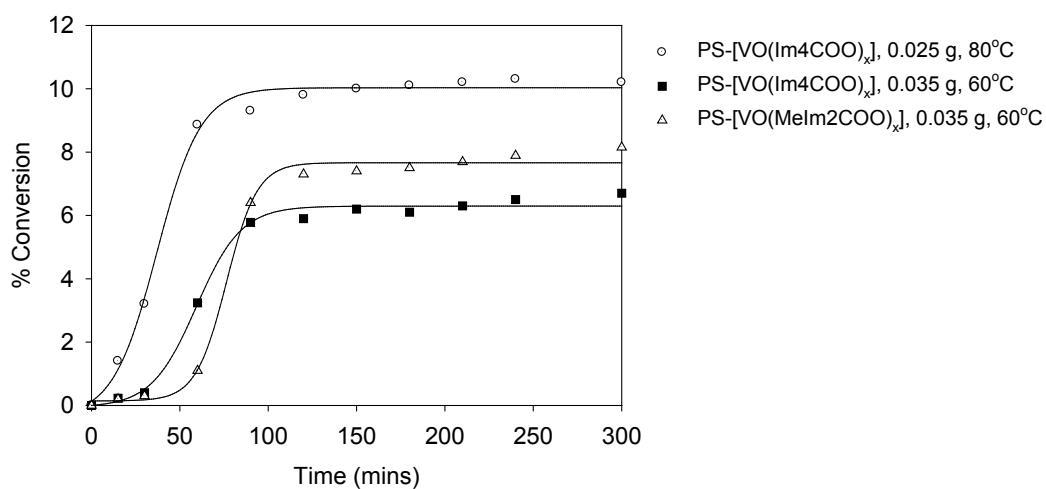


Figure 3.21 The effect of temperature and catalyst on the oxidation of ethylbenzene using PS-[VO(Melm2COO)_x] and PS-[VO(Im4COO)_x] at 60 and 80 °C. Reaction conditions: Catalyst (0.025 g and 0.035 g), ethylbenzene (10 mmol), H₂O₂ (20 mmol), acetonitrile (20 mL)

It is evident that in order to obtain better conversions, the amount of peroxide needs to be increased, even beyond four-equivalents, whilst keeping temperatures high. However, the tendency of the crosslinked chloromethylated polystyrene beads to break down under these conditions makes them less than ideal for such applications. The summary of the results obtained for the oxidation of ethylbenzene is presented in **table 3.4**.

Table 3.4 Percentage conversion, turnover frequency (TOF) and product selectivity (for the two major products) for the oxidation of ethylbenzene (Benzal = benzaldehyde, Acetophen = acetophenone)

Catalyst	Mass (g)	Temp (°C)	H ₂ O ₂ (eq) [†]	Conversion (%)	TOF ^a (h ⁻¹)	Acetophen (%)	Benzal (%)
PS-[VO(pimin) _x]	0.025	80	4	30.3	53	15.1	4.7
	0.025	80	2	13.8	24.1	12.6	5.0
PS-[VO(Im4COO) _x]	0.025	80	2	10.6	23	5.6	1.2
	0.035	60	2	8.15	10	4.7	1.1
PS-[VO(MeIm2COO) _x]	0.035	60	2	6.77	10	3.9	0.6

[†]mmol relative to thioanisole ^a Determined as moles of substrate converted/moles of catalyst/time (h)

(d) Mechanism of oxidation

As has been discussed previously, in the presence of hydrogen peroxide, vanadium(IV) readily converts to vanadium(V) along with the formation of monoperoxo and diperoxovanadium(V) complexes even when less than stoichiometric amounts of hydrogen peroxide are used.³⁹ All the reactions in this study were carried out in the presence of at least two-equivalents of H₂O₂ and so it is likely that mainly peroxo species exist. The peroxovanadium species are more reactive than H₂O₂ and are integral in the proposed catalytic mechanism.^{8,39} The first step involves the oxidation of vanadium(IV) followed by the formation of a peroxovanadium species which in acid media can form a reactive hydroxyl-peroxyvanadium(V) species, which subsequently oxidises the substrate. For the homogeneous catalysts we were able to confirm the first step of this process by spectrophotometric titrations of the complexes with H₂O₂ as shown in **figure 3.22** for [VO(pimin)₂] and **figure 3.23** for [VO(Im4COO)₂]. Before the addition of H₂O₂, three low-intensity peaks corresponding to the d-d transitions of a five-coordinate oxovanadium system were observed for each of the complexes.⁴⁰

The solution electronic spectrum for [VO(pimin)₂] displayed three d-d transitions at 617, 542 and 403 nm. Diluted hydrogen peroxide was added to this solution and the UV spectrum recorded after each successive 1-drop portions. The result, as shown in **figure 3.22**, was the gradual

disappearance of the d-d transition along with the appearance of an intense peak at around 350 nm corresponding to the peroxo-vanadium charge transfer band ($\pi_V^* \rightarrow d\sigma^*$).^{41,42}

For the imidazole-based systems, $[\text{VO}(\text{Im}4\text{COO})_2]$ was used since the d-d transitions of this complex were distinct and easily visible, whereas the high energy d-d transition of $[\text{VO}(\text{MeIm}2\text{COO})_2]$ was not easily observed. For this complex the d-d transitions appear at 742, 541 and 314 nm. Upon addition of H_2O_2 , these transitions disappeared and a charge transfer band appeared at 380 nm due to the formation of the d^0 dioxovanadium(V) species (**figure 3.22**) which was not as easily observed for $[\text{VO}(\text{pimin})_2]$. Further addition of H_2O_2 , produced a new band appearing at 325 nm which may be assigned the peroxo-vanadium charge transfer band ($\pi_V^* \rightarrow d\sigma^*$).^{41,42}

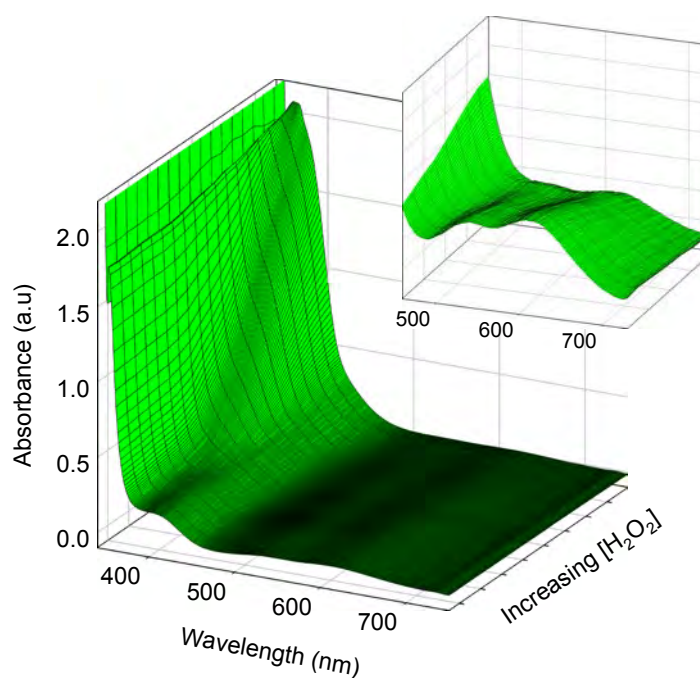


Figure 3.22 Spectrophotometric titration of $[\text{VO}(\text{pimin})_2]$ (1×10^{-4} mM, DMSO) with one-drop portions of H_2O_2 (5×10^{-2} mM) in water. The insert shows two of the d-d transitions which disappear upon addition of H_2O_2

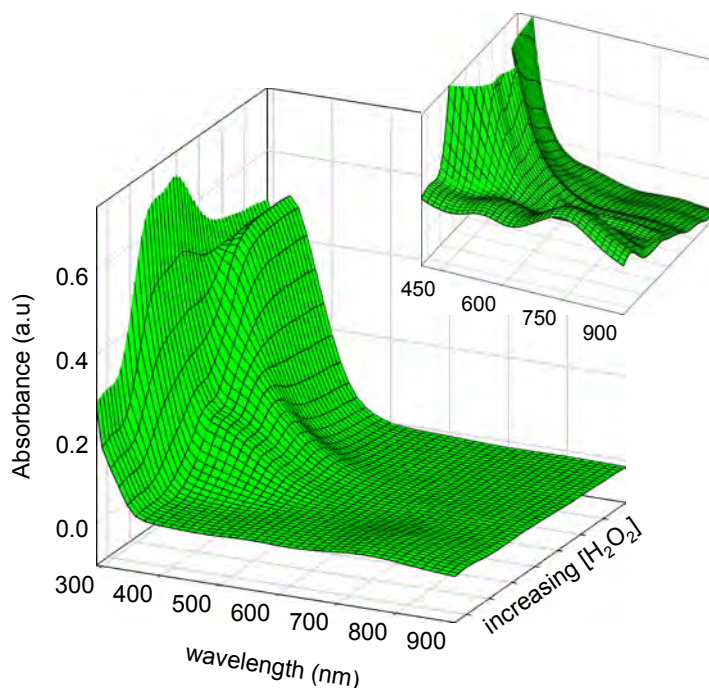


Figure 3.23 Spectrophotometric titration of $[\text{VO}(\text{Im4COO})_2]$ (1×10^{-4} mM, H_2O) with one-drop portions of H_2O_2 (5×10^{-2} mM) in water. The insert shows two of the d-d transitions which disappear upon addition of H_2O_2

(e) Oxidative bromination

Since the design of prepared catalysts was inspired by the active site of the naturally occurring vanadium-dependent haloperoxidases, we thought it would be logical to check if these catalysts did indeed display oxidative halogenation properties. Other than the naturally occurring counterparts, synthetic vanadium compounds have been shown to catalyze the oxidative bromination of several organic molecules including; salicylaldehyde,¹¹ anisole,⁴³ 1,3,5-trimethoxybenzene⁴⁴ and phenol red,⁴⁵ to name a few. We briefly investigated the oxybromination of phenol red due to the simplicity of this method. This was by no means an exhaustive study but served merely to investigate briefly if these catalysts would work for such reactions.

The bromination reaction was done by monitoring the formation of tetrabrominated bromophenol blue spectrophotometrically at 590 nm (**figure 3.24**). The reaction was performed at a pH of 5.5 since it has been shown that acidic conditions assist vanadium-catalyzed brominations.⁴⁴ The concentrations of KBr and H_2O_2 were kept constant at 2.0 M and 10 mM, respectively. In the absence of catalyst the reaction was extremely slow (**figure 3.25**). However, addition of either of

the heterogeneous catalysts resulted in the formation of bromophenol blue, albeit rather slow (**figure 3.25**). There was only very minor differences in activity between the various heterogeneous catalysts, with PS-[VO(pimin)_x] showing the greatest activity and PS-[VO(lm4COO)_x] the lowest (**figure 3.25**). The neat oxovanadium(IV) complexes [VO(lm4COO)₂], [VO(MeIm2COO)₂] and [VO(pimin)₂] showed improved activity over the heterogeneous counterparts (**figure 3.26**). In this instance [VO(pimin)₂] showed the lowest activity of the lot, probably due to the lower water solubility of this complex. The reduced activity for the heterogeneous catalysts is likely to be due to the slow diffusion of reagents to the catalyst surface.

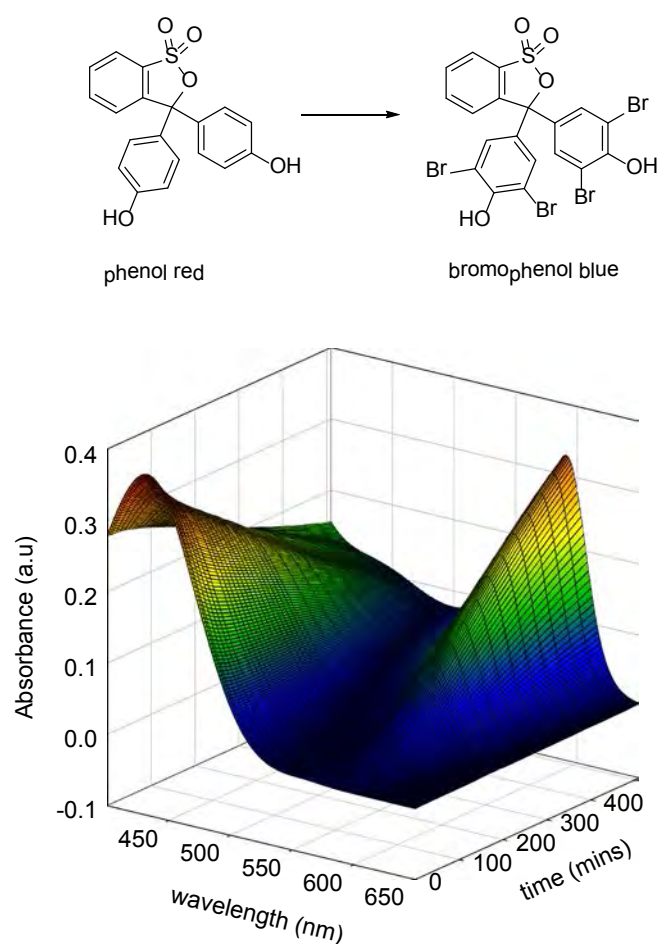


Figure 3.24 The reaction scheme for (top) and the change in the absorbance spectrum of phenol red due to the formation of bromophenol blue (below). Reaction conditions: PS-[VO(MeIm2COO)₂] (0.010 g), 25 mL of pH 5.5 phosphate buffer (50 mM), H₂O₂ (10 mM), KBr (1 M), phenol red (20 μM)

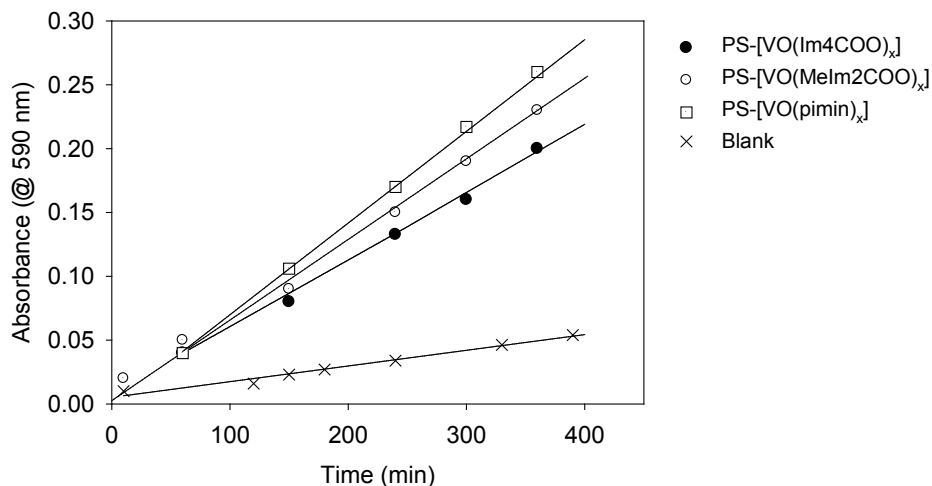


Figure 3.25 Plot of absorbance at 590 nm corresponding to the formation of bromophenol blue vs. time for heterogeneous catalysts. Reaction conditions: Catalyst (0.010 g), 25 mL of pH 5.5 phosphate buffer (50 mM), H₂O₂ (10 mM), KBr (1 M), phenol red (20 μM)

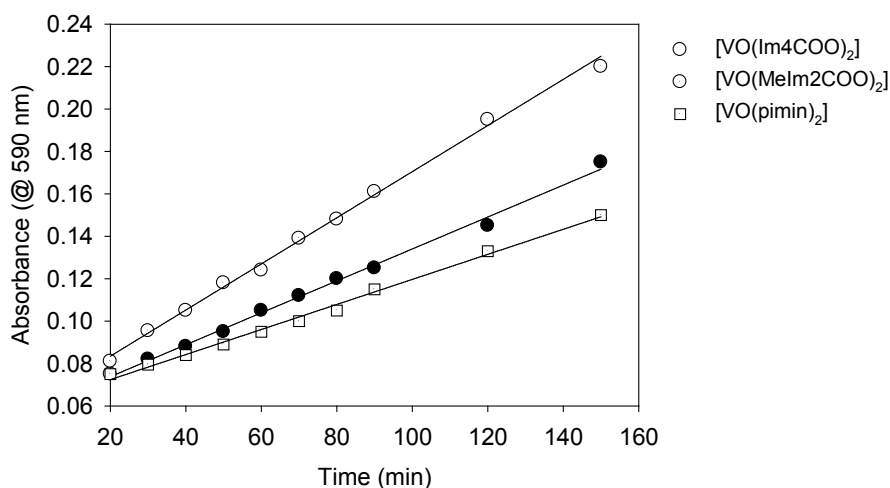


Figure 3.26 Plot of absorbance at 590 nm corresponding to the formation of bromophenol blue vs. time for the homogeneous catalysts. Reaction conditions: [VO(Im4COO)₂] (1.05 mg), [VO(MeIm2COO)₂] (1.15 mg) or [VO(pimin)₂] (1.33 mg) (equivalent to 0.010 g of corresponding heterogeneous catalyst), 25 mL of pH 5.5 phosphate buffer (50 mM), H₂O₂ (10 mM), KBr (1 M), phenol red (20 μM)

3.5 Conclusions

The Merrifield resin provides an excellent platform for immobilization of homogeneous oxovanadium catalysts. Functionalization with both the ligands and the metal was simple and the covalent linkage to the polymer-support ensured leaching of the metal was kept to a minimum as evidenced by recycling experiments. The heterogeneous catalysts successfully oxidized styrene nearly quantitatively; however under the conditions used for this reaction the polymer was susceptible to degradation. Oxidation of ethylbenzene was more challenging with a maximum of 31% conversion being attained. As mentioned in a recent review by da Silva *et al.*,⁴⁶ these catalysts provide the maximum conversion of styrene and ethylbenzene compared to others prepared in the same fashion. The heterogeneous catalysts proved ideal for the oxidation of thioanisole, which was conducted successfully under comparatively milder conditions. Rather than focusing on tuning the active site, more significant improvements could possibly be made by improving the support material. For example by increasing the mechanical strength and increasing the surface area.

3.6 References

- (1) Merrifield, R. B. *J. Am. Chem. Soc.* **1963**, 85, 2149.
- (2) Sherrington, D. C. *Pure Appl. Chem.* **1987**, 60, 401.
- (3) Clark, J.; Macquarrie, D. *Handbook of Green Chemistry and Technology*, Blackwell Science: Oxford, 2002.
- (4) Sherrington, D. C. *Catal. Today* **2000**, 57, 87.
- (5) Maurya, M. R.; Kumar, M.; Kumar, U. *J. Mol. Catal. A: Chem.* **2007**, 273, 133.
- (6) Maurya, M. R.; Kumar, M.; Arya, A. *Catal. Comm.* **2008**, 10, 187.
- (7) Maurya, M. R.; Arya, A.; Adao, P.; Pessoa, J. C. *Appl. Catal., A* **2008**, 351, 239.
- (8) Maurya, M. R.; Arya, A.; Kumar, A.; Pessoa, J. C. *Dalton Trans.* **2009**, 2185.
- (9) Maurya, M. R.; Kumar, A.; Costa Pessoa, J. *Coord. Chem. Rev.* **2011**, 255, 2315.
- (10) Miller, M. M.; Sherrington, D. C. *J. Catal.* **1995**, 152, 368.
- (11) Maurya, M. R.; Kumar, U.; Manikandan, P. *Dalton Trans.* **2006**, 3561.
- (12) Terrón, M. C.; Verhagen, F. J. M.; Franssen, M. C. R.; Field, J. A. *Chemosphere* **1998**, 36, 1445.
- (13) Parík, P.; Senauerová, S.; Lisková, V.; Handlír, K.; Ludwig, M. *J. Heterocycl. Chem.* **2006**, 43, 835.
- (14) Savall, B. M.; Fontimayor, J. R.; Edwards, J. P. *Tetrahedron Lett.* **2009**, 50, 2490.
- (15) Bordwell, F. G. *Acc. Chem. Res.* **1988**, 21, 456.
- (16) Moutevelis-Minakakis, P.; Papavassilopoulou, E.; Michas, G.; Georgikopoulou, K.; Ragoussi, M.-E.; Neophytou, N.; Zoumpoulakis, P.; Mavromoustakos, T.; Hadjipavlou-Litina, D. *Bioorg. Med. Chem.* **2011**, 19, 2888.
- (17) Lü, C.; Gao, B.; Liu, Q.; Qi, C. *Colloid Polym. Sci.* **2008**, 286, 553.
- (18) Lane, T. J.; Nakagawa, I.; Walter, J. L.; Kandathil, A. J. *Inorg. Chem.* **1962**, 1, 267.
- (19) Maurya, M. R.; Arya, A.; Adão, P.; Pessoa, J. C. *Appl. Catal., A* **2008**, 351, 239.
- (20) Nakamoto, Z. *Infrared and raman spectra of inorganic and coordination compounds*, John Wiley and Sons, New York, 1978.
- (21) Greenwood, N. N.; Earnshaw, A. *Chemistry of the elements*, Pergamon Press, Oxford, 1997.

-
- (22) Groenenboom, C. J.; Sawatzky, G.; de Liefde Meijer, H. J.; Jellinek, F. J. *Organomet. Chem.* **1974**, *76*, C4.
- (23) Moulder, J. F.; Stricle, W. F.; Sobol, K. D.; Bomben, K. D. *Handbook of X-ray photoelectron spectroscopy*, Perkin-Elmer Corporation, Physical Electronic, 1995.
- (24) Udapa, M. R.; *Thermochim. Acta* **1981**, *51*, 169.
- (25) Kaczorowska, K.; Kolarska, Z.; Mitka, K.; Kowalski, P. *Tetrahedron* **2005**, *61*, 8315.
- (26) Pellissier, H. *Tetrahedron* **2006**, *62*, 5559.
- (27) Sampanthar, J. T.; Xiao, H.; Dou, J.; Nah, T. Y.; Rong, X.; Kwan, W. P. *Appl. Catal., B.* **2006**, *63*, 85.
- (28) Song, C.; Ma, X. *Appl. Catal., B.* **2003**, *41*, 207.
- (29) Ando, R.; Yagyū, T.; Maeda, M. *Inorg. Chim. Acta.* **2004**, *357*, 2237.
- (30) Ando, R.; Inden, H.; Sugino, M.; Ono, H.; Sakaeda, D.; Yagyū, T.; Maeda, M. *Inorg. Chim. Acta.* **2004**, *357*, 1337.
- (31) Ando, R.; Mori, S.; Hayashi, M.; Yagyū, T.; Maeda, M. *Inorg. Chim. Acta.* **2004**, *357*, 1177.
- (32) Saito, B.; Katsuki, T. *Tetrahedron Lett.* **2001**, *42*, 3873.
- (33) Ligtenbarg, A. G. J.; Spek, A. L.; Hage, R.; Feringa, B. L. *J. Chem. Soc., Dalton Trans.* **1999**, 659.
- (34) Punniyamurthy, T.; Velusamy, S.; Iqbal, J. *Chem. Rev.* **2005**, *105*, 2329.
- (35) Fabrizio, C. *Catal. Today* **2010**, *157*, 8.
- (36) Hermans, I.; Spier, E.; Neuenschwander, U.; Turrà, N.; Baiker, A. *Top. Catal.* **2009**, *52*, 1162.
- (37) Joyner, R. W., van Santen, R. A. *Elementary reaction steps in heterogeneous catalysis*. Kluwer Academic Publishers: Dordrecht, 1993.
- (38) Hoshino, M., Akimoto, H., Okuda, M. *Bull. Chem. Soc. Jpn.* **1978**, *51*.
- (39) Samuni, A.; Meisel, D.; Czapski, G. *J. Chem. Soc., Dalton Trans.* **1972**, 1273.
- (40) Selbin, J. *Chem. Rev.* **1965**, *65*, 153.
- (41) Keramidas, A. D.; Miller, S. M.; Anderson, O. P.; Crans, D. C. *J. Am. Chem. Soc.* **1997**, *119*, 8901.
- (42) Bhattacharjee, M.; Chaudhuri, M. K.; Islam, N. S.; Paul, P. C. *Inorg. Chim. Acta.* **1990**, *169*, 97.
-

-
- (43) Rothenberg, G.; Clark, J. H. *Org. Process Res. Dev.* **2000**, 4, 270.
- (44) Kikushima, K.; Moriuchi, T.; Hirao, T. *Tetrahedron Lett.* **2010**, 51, 340.
- (45) Totaro, R. M.; Williams, P. A. M.; Apella, M. C.; Blesa, M. A.; Baran, E. *J. Chem. Soc., Dalton Trans.* **2000**, 4403.
- (46) da Silva, J. A. L.; Fraústo da Silva, J. J. R.; Pombeiro, A. J. L. *Coord. Chem. Rev.* **2011**, 255, 2232

This page has been left blank intentionally

Chapter 4

Polymer-supported oxovanadium(IV) catalysts prepared by suspension polymerization

4.1 Introduction

Suspension polymerization has become a popular method for producing functional polymer microspheres. The procedure involves mixing an organic phase and an aqueous phase resulting in small droplets in which polymerization takes place. Generally, the organic phase contains the initiator, monomers and crosslinker, while the aqueous phase contains the stabilizers.^{1,2}

The microspherical beads prepared by this approach have been used for various applications including catalyst supports³ and sorbents for metal ion removal.^{4,5} Vinylimidazole and vinylpyridine are the most common functional monomers used when preparing metal coordinating polymers, since they both contain a lone pair of electrons on the nitrogen atom which can take part in metal coordination. As for the imidazole-based resins, typically *N*-vinylimidazole is used in preference to 4(5)-vinylimidazole or 2-vinylimidazole, probably due to its commercial availability. However, despite the structural simplicity, ease of availability and strong metal binding capacity of imidazole, there have been no reports involving the use of vinylimidazole based polymer microspheres, prepared by suspension polymerization, for oxovanadium(IV) immobilization.

In the previous chapter (**Chapter 3**), we discovered that simple imidazole-containing resins prepared by functionalization of Merrifield beads, effectively immobilized oxovanadium(IV). Not only did these heterogeneous catalysts prove to be effective specifically in the oxidation of thioanisole, but they also showed excellent recyclability. In this chapter, we have used suspension polymerization to produce imidazole-containing polymer microspheres. This method allows for a greater degree of freedom in terms of degree of functionalization, bead diameters and degree of crosslinking, when compared to Merrifield modification. These imidazole-containing beads, as well as the oxovanadium(IV)-functionalized derivatives, were thoroughly characterized using AFM, SEM, BET and XPS among several other techniques. The focus of this chapter was directed

towards the synthetic and characterization aspects of the polymer support since this remains an area in which significant improvements could be made. Thus, the catalytic reactions investigated in this chapter were focused on the oxidation of thioanisole as this provided a good indicator of the catalytic activity.

4.2 Preparative work

4.2.1 p(VIM-co-EGDMA) beads

The functional monomer *N*-vinylimidazole (2 g, 0.021 mol), crosslinker ethyleneglycol dimethacrylate (EGDMA) (7 mL, 0.035 mol) and initiator azobisisobutyronitrile (AIBN) (0.15 g, 0.9 mmol) were stirred in an organic phase consisting of a toluene/cyclohexanol (7 mL/2 mL) mixture. In a separate 250 mL round bottom flask, an aqueous phase containing polyvinylalcohol (PVA) (0.28 g) and NaCl (0.7 g) in 80 mL of water was stirred at 300 rpm. This solution was warmed to 60 °C to facilitate the dissolution of PVA. The organic phase was added dropwise to the aqueous phase under constant stirring. The temperature was increased to 70 °C and the reaction was allowed to proceed for 24 hours under an argon atmosphere. The mixture was left to cool to room temperature and the beads were collected by filtration, washed several times with hot water followed by hot methanol and then dried in an oven at 60 °C overnight. These beads were then sieved and only the larger beads were retained (<25 mesh). ATR-IR (cm^{-1} , neat): 2946, 1721, 1654, 1452, 1390, 1232, 1142, 750, 665. *Anal.* Found (%): C, 59.95; H, 7.80; N, 6.52.

4.2.2 p(VIM-co-EGDMA)-VO beads

A mass of 2 g of the p(VIM-co-EGDMA) beads (4.2.1) were swollen in 20 mL of DMF for 2 hours. To this was added excess VO_2SO_4 (1 g, 4.6 mmol) in DMF (50 mL). The mixture was heated to 60 °C and stirred overnight. The resultant blue-green beads were filtered and washed several times with DMF, water, methanol and finally diethyl ether and dried in an oven at 60 °C overnight. ATR-IR (cm^{-1} , neat): 2951, 1720, 1655, 1456, 1390, 1230, 1140, 960, 753, 665. *Anal.* Found (%): C, 47.50; H, 6.78; N, 5.74; S, 1.98; V, 2.80.

4.2.3 Attempted synthesis imidazole-2-carboxylic acid containing beads

p[(*N*-vinylimidazole-2-aldehyde)-co-divinylbenzene]. An aqueous phase consisting of water (70 mL), hydroxyethylcellulose (HEC) (0.01 g) and gelatine (0.03 g) was stirred at 50 °C until the solids were completely dissolved. In a separate beaker, an organic phase consisting of *N*-vinylimidazole-2-carboxaldehyde⁶ (4 g, 0.033 mol), 80% divinylbenzene (5 g, 0.031 mol), toluene (9 mL) and 75% benzoyl peroxide (0.25 g, 0.77 mmol) was stirred. The organic phase was added to the aqueous phase at a constant stirring rate of 350 rpm and the temperature was increased to

70 °C. The reaction was carried out under a constant stream of argon for a period of 20 hours and then allowed to cool to room temperature. The beads were collected by filtration, washed several times with warm water, then methanol and finally diethyl ether. The beads were dried in an oven (60 °C) and sieved. ATR-IR (cm^{-1} , neat): 2929, 2172, 1692, 1605, 1452, 1275, 991, 906, 712. *Anal.* Found (%): C, 86.47; H, 7.69; N, 3.16.

p[(*N*-vinylimidazole-2-carboxylic acid)-co-divinylbenzene]. A vial containing p[(*N*-vinylimidazole-2-aldehyde)-co-divinylbenzene] microspheres (1.0 g) were allowed to swell in acetonitrile and water (10 mL/10 mL). To this was added aqueous hydrogen peroxide (5 mL, 30%) and this was stirred gently for one week at room temperature. The beads were filtered, washed several times with water, then methanol and ether and dried *in vacuo*. ATR-IR (cm^{-1} , neat): 2929, 2172, 1692, 1605, 1452, 1275, 991, 906, 712. *Anal.* Found (%): C, 81.37; H, 7.42; N, 2.91.

4.2.4 Attempted synthesis 2-(2'-hydroxyphenyl)imidazol(in)e containing beads

The allyl functionalized ligands, 2-(2'-hydroxyphenyl)-*N*-allylimidazoline⁷ and 2-allyl-6-(2'-hydroxyphenyl)imidazoline,⁸ were successfully synthesized. However, due to limited solubility in various organic solvents including toluene, chloroform, dichloromethane, cyclohexanol, octanol and ethylacetate (since these solvents are immiscible with water) suspension polymerization could not be conducted. In an attempt to improve monomer solubility the *N*-ethyl derivative, 2-allyl-6-(1-ethyl-2'-hydroxyphenyl)imidazoline, was prepared, but it was still not sufficiently soluble. We also prepared the vinyl imidazole derivative, 2-(2'-hydroxy-4-vinylphenyl)imidazole but once again the lack of solubility made it unsuitable for suspension polymerization. The synthesis of this ligand will be discussed in a later chapter (**Part 2, Chapter 5**). Nevertheless, since the ligand-functionalized polymers prepared in the previous chapter (**Part 2, Chapter 3**), were only monodentate with either an imidazole/imidazoline group available for coordination, we settled upon using *N*-vinylimidazole which produced a similar coordination environment.

4.3 Catalytic activity studies

4.3.1 Batch oxidation of thioanisole using p(VIM-co-EGDMA)-VO beads

In a typical reaction, 20mL of acetonitrile was added to a 100 mL round bottom flask fitted with a glass condenser and placed in an oil bath. The temperature of the oil bath was regulated to ± 1 °C by using an external temperature probe. The stirring speed was kept constant at 300 rpm for all reactions. Thioanisole (1.24 g, 10 mmol) was added followed by the required moles of aqueous H₂O₂ and then the catalytic beads which signalled the start of the reaction.

4.4 Results and discussion

4.4.1 Synthesis

Several attempts were carried out before imidazole-containing polymer beads of the desired size and morphology were obtained. The use of different crosslinking agents, stabilizers, stirring rate and, type and ratio of porogens (or organic solvents) was investigated and found to have a considerable effect on the resultant bead morphology. A few examples are further discussed to illustrate the effects of these parameters.

Initially toluene was used as a porogen and divinylbenzene as a crosslinker since this combination has frequently been used to prepare styrene-co-divinylbenzene microspheres.^{10,11} We also used this method to produce the p[(*N*-vinylimidazole-2-aldehyde)-co-divinylbenzene] beads (**4.2.3**). However, when *N*-vinylimidazole was used as the monomer rather than styrene (or *N*-vinylimidazole-2-aldehyde), the more hydrophilic *N*-vinylimidazole monomer transferred into the aqueous layer rather than remaining in the organic phase where polymerization occurs resulting in poor incorporation of the monomer in the polymer beads. This problem was also reported by Fontanals and co-workers,¹² and overcome by increasing the reaction time and adding the organic phase in two portions. However, since we were not restricted to using divinylbenzene, we substituted this with ethyleneglycol dimethacrylate. The result of this was that the *N*-vinylimidazole was retained in the monomer phase but very large non-spherical lumps were produced (**figure 4.1**). Cyclohexanol was used as a porogen by Uğuzdoğan and co-workers, who also prepared vinylimidazole-co-ethyleneglycol dimethacrylate beads.¹³ However, when we tried using this porogen only a powdery material formed (**figure 4.1**), probably due to the different stabilizer mixture used.

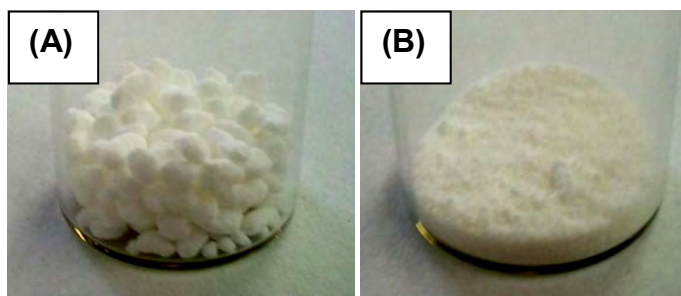


Figure 4.1 Images of two attempts at producing polyvinylimidazole-co-ethyleneglycol dimethacrylate beads using toluene (A) and (B) cyclohexanol as the only solvent (porogen)

Since only excessively large beads formed when toluene was used and only very fine powder formed when using cyclohexanol, we suspected that a combination of the two would provide the balance and yield the desired microspherical product, which was indeed the case. An optimal ratio of toluene/cyclohexanol of 7:2 (v/v) was eventually settled upon as it produced the most monodisperse set of beads (**figure 4.2**). Using these conditions, the stirring speed was adjusted until droplets of the desired size were attained with 300 rpm proving to be optimal. The corresponding vanadyl-functionalized beads (**figure 4.2**) were prepared by reacting these imidazole-containing beads with vanadyl sulfate. The synthetic scheme for the preparation of both p(VIM-co-EGDMA) and p(VIM-co-EGDMA)-VO is shown below (**scheme 4.1**)

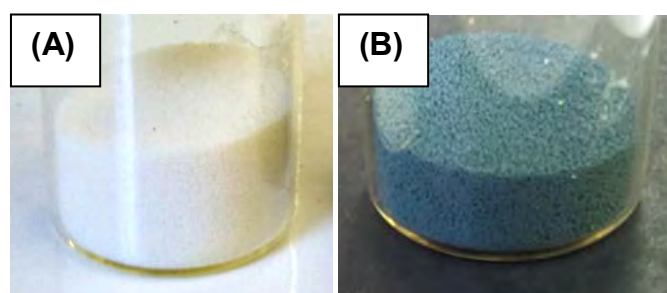
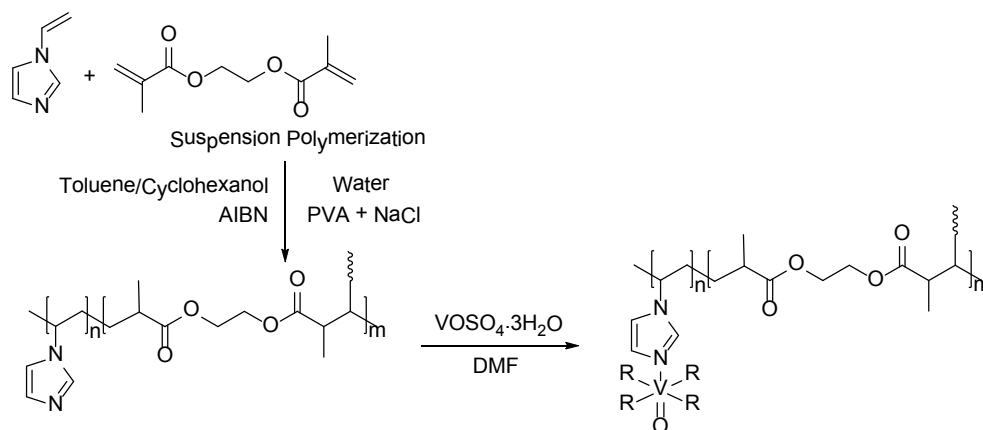


Figure 4.2 Poly(vinylimidazole-co-ethyleneglycol dimethacrylate) before (A) and after functionalization with vanadium (B)



Scheme 4.1 Synthetic scheme for the preparation of p(VIM-co-EGDMA) microspheres. R represents a solvent molecule or a nearby ligand

4.4.2 Attempted syntheses

There were several attempts at making imidazole-2-carboxylic acid and 2-(2'-hydroxyphenyl)imidazoline functionalized beads, to try and keep the ligand theme from the previous chapter consistent (**Part 2, Chapter 3**). This proved more challenging than initially expected. For the imidazole-2-carboxylic acid system, we firstly attempted to prepare *N*-vinylimidazole-2-carboxylic acid by reacting *N*-vinylimidazole with BuLi followed by carbonylation using dry ice (CO_{2(s)}). However the product proved difficult to extract into the organic phase and was thermally unstable. At this point this strategy was abandoned since normal phase suspension polymerization requires that the monomers are sufficiently soluble in the organic phase and not transfer into the aqueous phase. The next strategy involved using *N*-vinylimidazole-2-carboxaldehyde since this monomer was soluble in organic solvents. We were successful in preparing the *N*-vinylimidazole-aldehyde functionalized beads by suspension polymerization using divinylbenzene as a crosslinker. We were hopeful that oxidation using aqueous hydrogen peroxide would then convert the aldehyde to a carboxylic acid group as had been done before in homogeneous solution (**Part 1, Chapter 4**). Initially the results suggested success because the microanalysis showed a drop in C and N percentages indicative of addition of the OH from the carboxylic acid and the colour of the beads became clearer (**figure 4.3**). However, neither the $\nu(\text{C}=\text{O})$ nor any other bands in the infrared spectrum shifted at all (**figure 4.4**) indicating that no

reaction occurred at this position. Several other oxidizing agents including oxone and KMnO_4 were used to no avail.

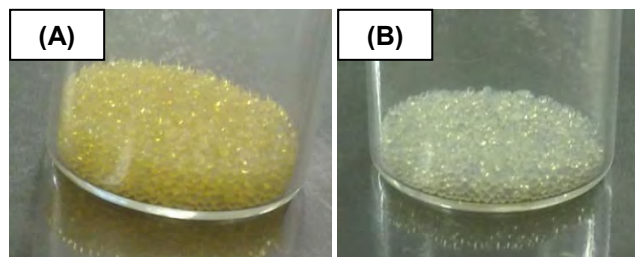


Figure 4.3 Images of poly[(vinylimidazole-2-carboxyaldehyde)-co-divinylbenzene] beads (A) before and (B) after reaction with hydrogen peroxide

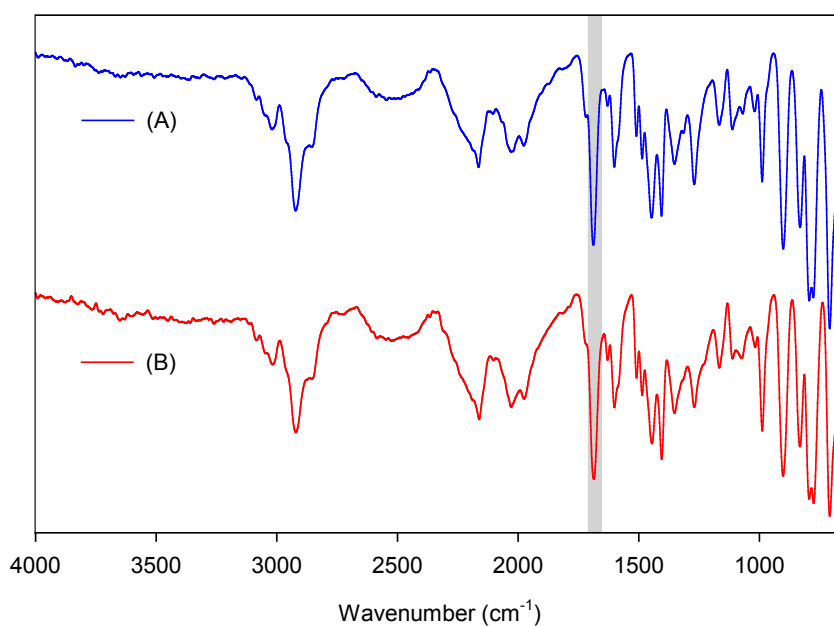


Figure 4.4 Infrared spectra of poly[(vinylimidazole-2-carboxyaldehyde)-co-divinylbenzene] beads (A) before and (B) after reaction with hydrogen peroxide. Highlighted region confirms no shift of the $\nu(\text{C}=\text{O})$

Synthesis of beads containing the bidentate 2-(2'-hydroxyphenyl)imidazoline ligand also proved unsuccessful. In this instance, the main problem was solubility of the monomerized ligands (of which a few variations were prepared in attempts to improve solubility). None of these dissolved

sufficiently in several of the organic solvents tested, showing solubility only in DMSO and DMF which are unfortunately miscible with water and thus unsuitable for use in suspension polymerization.

The above mentioned attempts certainly illustrate one of the major problems associated with suspension polymerization which is monomer solubility. Unlike the Merrifield functionalization approach, in which almost any solvent can be used to dissolve the ligand, direct incorporation of a monomerized ligand by suspension polymerization commands a fine balance of ligand hydrophobicity/hydrophilicity.

4.4.3 Characterization

In the infrared spectrum of the p(VIM-co-EGDMA) beads, an intense band appeared at 1721 cm^{-1} corresponding to the $\nu(\text{C}=\text{O})$ from EGDMA, while imidazolyl ring stretches were found at 1452 , 1232 and 665 cm^{-1} .^{5,14,15} After reacting these beads with vanadyl sulfate a band at 960 cm^{-1} appeared corresponding to the vanadyl $\nu(\text{V}=\text{O})$ stretch (**figure 4.5**).¹⁶ The sulfate ion stretching vibrations were not obviously apparent, probably being hidden beneath the polymer bands in the region of $1250 - 1025\text{ cm}^{-1}$ as there was some broadening in this region.

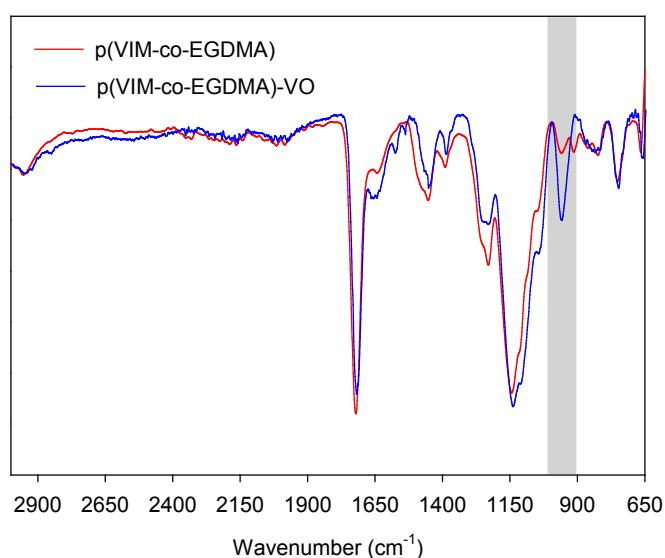


Figure 4.5 Overlaid infrared spectra of p(VIM-co-EGDMA) and p(VIM-co-EGDMA)-VO in the range $3000-650\text{ cm}^{-1}$

The sulfate was however detectable by microanalysis, which indicated a sulfur content of 9.98% in the p(VIM-co-EGDMA)-VO beads. The nitrogen content, a direct indicator of the quantity of imidazole incorporated, was found to be 6.52% for p(VIM-co-EGDMA) beads, which corresponds to an imidazole-to-EGDMA ratio of roughly 2:3. After vanadium functionalization, the nitrogen content dropped slightly to 5.74%, due to the incorporation of the vanadium salt. The total vanadium content was determined by ICP-OES after thorough leaching from the polymer using concentrated nitric acid. The 2.80% vanadium content determined translates to an imidazole-to-vanadium ratio of close to 4:1 and a sulfur-to-vanadium ratio of close to 1:1. The latter corresponds well to the expected 1:1 ratio of the divalent vanadyl cation and divalent sulfate anion. As for the imidazole-to-vanadium ratio, one should be cautious of extrapolating too far and presuming that all of the available imidazole groups are bound to vanadium.

Investigation of the surface chemistry of these beads was performed using XPS. In the p(VIM-co-EGDMA) beads, the N 1s peak representative of imidazole and the O 1s peak from EGDMA (C=O) appeared at 399 and 530 eV (**figure 4.6** and **table 4.1**) respectively, and within the reported ranges for these groups.¹⁷ These peaks were also observed for p(VIM-co-EGDMA)-VO along with additional peaks appearing at 515 and 522 eV corresponding to the V 2p_{3/2} and V 2p_{1/2}, respectively (**figure 4.6**). The latter not only confirmed the presence of vanadium on the surface of the beads but also confirmed the +4 oxidation state of vanadium.¹⁷ The proximity of the V 2p peak to the comparatively large O 1s peak and the low intensity of the N 1s and S 2p peaks made quantitative surface composition analysis unreliable and so comparative total-versus-surface composition could not be accurately performed.

Table 4.1 Elemental binding energies of p(VIM-co-EGDMA) and p(VIM-co-EGDMA)-VO as determined by XPS

Polymer	Binding Energy (eV)					
	O 1s	N 1s	C 1s	V 2p _{3/2}	V 2p _{1/2}	S 2p _{3/2}
p(VIM-co-EGDMA)	530	399	285	-	-	-
p(VIM-co-EGDMA)-VO	530	399	285	515	522	167

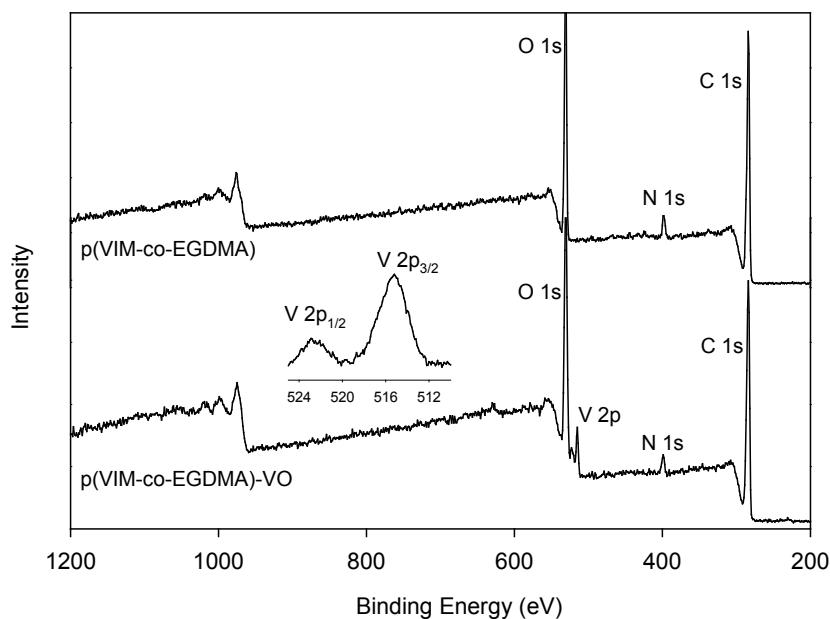


Figure 4.6 Wide scan XPS spectra of p(VIM-co-EGDMA) and p(VIM-co-EGDMA)-VO. The insert shows the expanded V $2p_{3/2}$ and V $2p_{1/2}$ signals

The general thermal stability of the p(VIM-co-EGDMA) and p(VIM-co-EGDMA)-VO beads was determined using TG. For both polymers an early weight loss step was observed below 110 °C probably due to absorbed water (**figure 4.7**). Onset of a multistep decomposition (T_{onset}) process for p(VIM-co-EGDMA) began at 250 °C (**figure 4.7**), while after functionalization with oxovanadium(IV), a new weight loss process was observed beginning at 368 °C ($T_{\text{max}} = 421$ °C), probably due to oxovanadium(IV) decomposition.

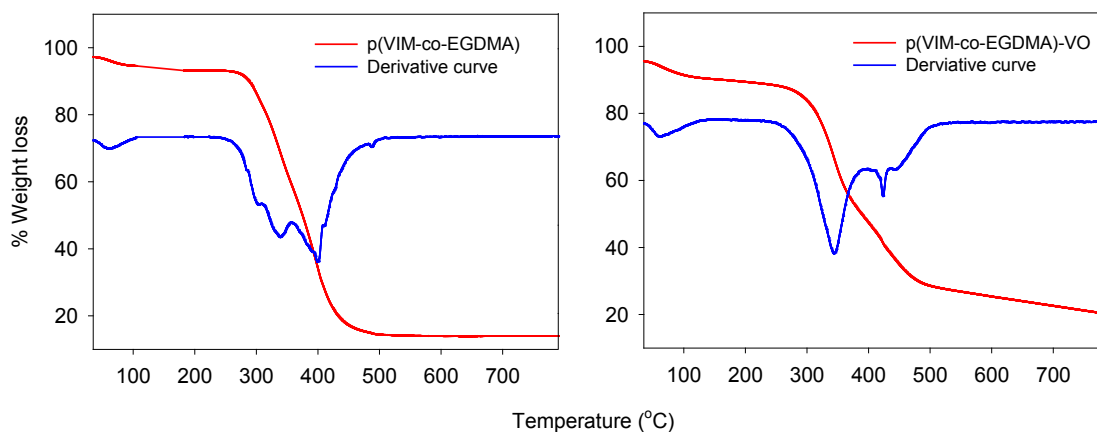


Figure 4.7 TG and DTG curves of p(VIM-co-EGDMA) (left) and p(VIM-co-EGDMA)-VO (right) at a heating rate of 10 °C.min⁻¹ under N₂

SEM and AFM were used to monitor the morphology of the beads. The SEM images of the p(VIM-co-EGDMA) and p(VIM-co-EGDMA)-VO beads are shown in **figure 4.8**. Both sets of beads had rough surfaces, whilst the oxovanadium(IV) functionalized beads displayed a greater level of surface homogeneity. Diameter measurements were performed using the measureIT software from Olympus Soft Imaging Solutions. For both sets of beads, the diameters of no less than 25 individual beads were measured. The p(VIM-co-EGDMA) beads had an average diameter of 314 μm with a size distribution range of 251 - 372 μm . The average diameter of the vanadium-functionalized beads was slightly larger (but within error of the non-metallated variety) at 322 μm with a range of 274 - 408 μm . These beads were considerably rougher and smaller than the Merrifield beads used in the previous chapter (**Part 2, Chapter 1**) which had an average diameter of 612 μm .

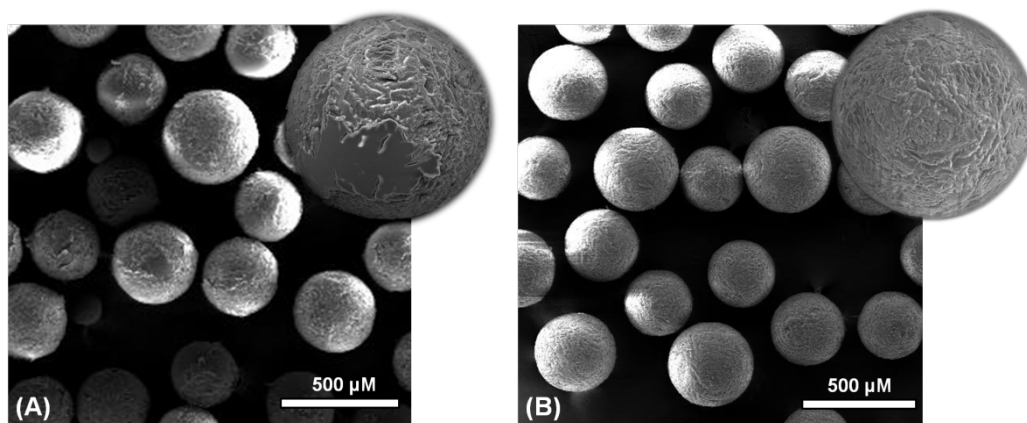


Figure 4.8 SEM images of (A) p(VIM-co-EGDMA) and (B) the oxovanadium(IV) functionalized derivative p(VIM-co-EGDMA)-VO. The insert shows an expanded view of a single bead

AFM also proved to be a useful tool for probing the surface morphology of the beads after the various synthetic steps. As shown in **figure 4.9**, the non-metallated p(VIM-co-EGDMA) beads have a bumpy surface, which after reaction with vanadyl sulfate appears significantly more ordered with a 'diamond-like' pattern emerging. The surface roughness of the p(VIM-co-EGDMA) beads decreased from 41.64 nm to 21.01 nm after reacting them with vanadyl sulfate. This trend was similar to that observed for the Merrifield beads from **Part 2, Chapter 3** and may be due to the formation of a vanadyl coating on the surface. The Merrifield-based beads were significantly

smoother than the beads prepared in this chapter (by approximately 10 fold), a property perhaps even more easily seen in the SEM images.

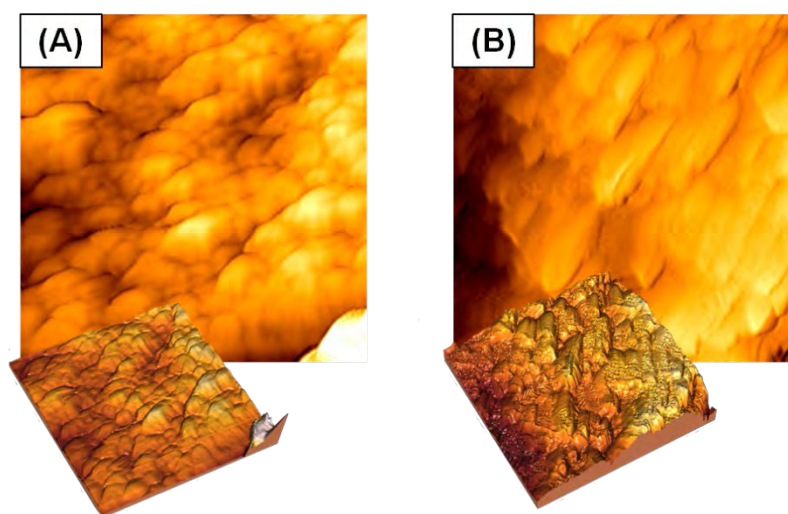


Figure 4.9 Selected 2D and 3D (1x1 μm sections) of (A) p(VIM-co-EGDMA) and (B) p(VIM-co-EGDMA)-VO

The surface area of the beads was determined from nitrogen absorption/desorption isotherms (**figure 4.10**) using the BET method. The specific surface area of the p(VIM-co-EGDMA) beads was found to be $151 \text{ m}^2 \cdot \text{g}^{-1}$, while the average pore volume and size was $0.31 \text{ cm}^3 \cdot \text{g}^{-1}$ and 82 \AA respectively. This surface area was slightly higher than the polyvinylimidazole-co-ethyleneglycol dimethacrylate beads reported by Kara *et al.*, who reported a surface area of $59.8 \text{ m}^2 \cdot \text{g}^{-1}$ for their 150-200 μm sized beads.⁵ The increased surface area observed in this study may be due to the larger amount of crosslinker used, since it has been observed that an increase in crosslinker may result in greater surface areas due to the formation of rigid pores.¹⁷ After reaction with vanadyl sulfate, the surface area dropped to $99 \text{ m}^2 \cdot \text{g}^{-1}$, while the average pore volume and diameter remained relatively similar ($0.21 \text{ cm}^3 \cdot \text{g}^{-1}$ and 87 \AA , pore volume and pore diameter respectively). The drop in surface area going from p(VIM-co-EGDMA) to p(VIM-co-EGDMA)-VO may be due to filling of the pores by vanadium, as evidenced by the slight drop in pore volume, as well as the decrease in surface roughness as measured by AFM. Despite this, the surface area of these beads was still considerably larger than the Merrifield beads used in the previous chapter (**Part 2, Chapter 3**) which had a surface area of $10.4 \text{ m}^2 \cdot \text{g}^{-1}$ with 311 \AA wide pores and an average pore volume of $0.051 \text{ cm}^3 \cdot \text{g}^{-1}$. This may once again be attributed to the combination of the increased

amount of crosslinker, roughness and the smaller size of the p(VIM-co-EGDMA) beads. It was hoped that the increased surface area of these beads would impact positively on the overall catalytic activity.

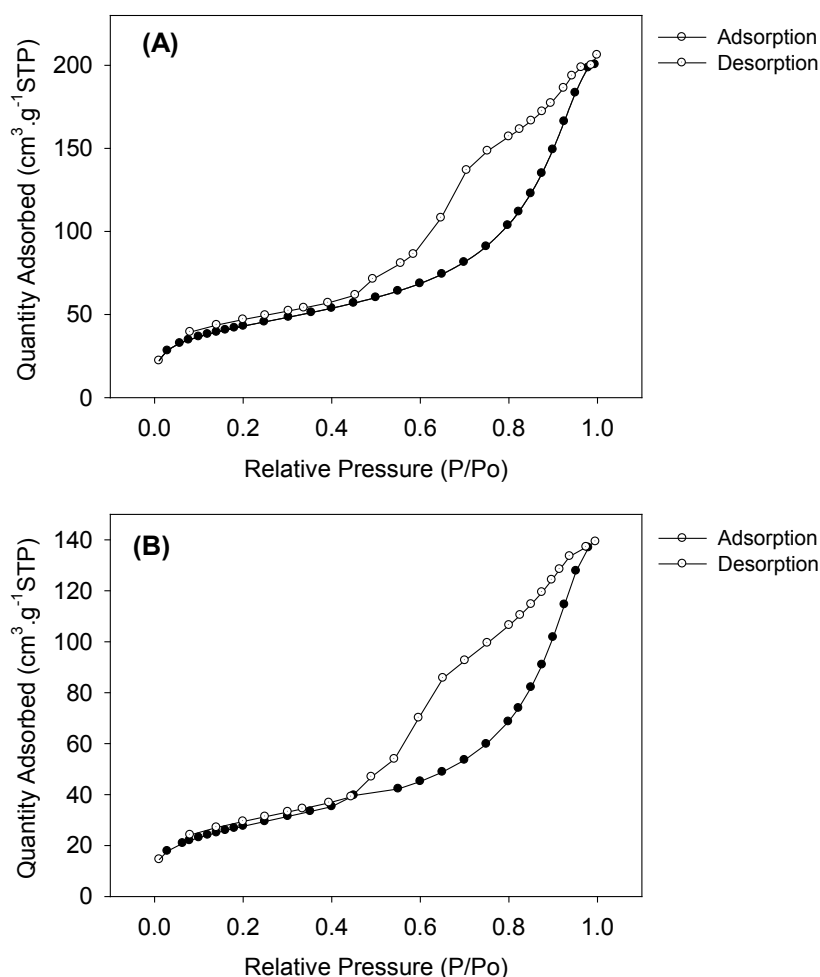


Figure 4.10 Nitrogen adsorption-desorption isotherms for (A) p(VIM-co-EGDMA) and (B) p(VIM-co-EGDMA)-VO

4.4.4 Catalytic activity

The catalytic activity of the p(VIM-co-EGDMA)-VO beads was assessed using the peroxide facilitated oxidation of thioanisole as a test reaction. From the previous chapter (**Part 2, Chapter 3**), we found this reaction to be a good indicator of catalytic activity. Furthermore, the higher temperatures and harsh oxidizing conditions required for effective oxidation of styrene and ethylbenzene was not well suited to the polymeric supports.

(a) Oxidation of thioanisole

The first parameter to be optimized for the oxidation of thioanisole was the amount of catalyst (**figure 4.11**). As expected, this had a noticeable effect on the rate of oxidation of thioanisole. When using 0.1, 0.2 and 0.3 g of catalyst the TOF's were 34.52, 35.69, 30.12 h⁻¹ respectively. For this reason further studies were performed using 0.2 g of catalyst. It should be noted that when using the un-metallated p(VIM-co-EGDMA) beads, a conversion of less than 17% was obtained reinforcing the catalytic properties of the oxovanadium-containing beads. At room temperature, all catalyst amounts gave greater quantities of the sulfoxide than the sulfone, but as the amount of catalyst increased and the reaction time progressed, the ratio of sulfoxide to sulfone began to decrease (**table 4.2**). For example, when using 0.1 g of p(VIM-co-EGDMA)-VO the ratio of sulfoxide-to-sulfone was 2:7 while when using 0.2 g and 0.3 g this ratio was 2:3 and 4:5, respectively.

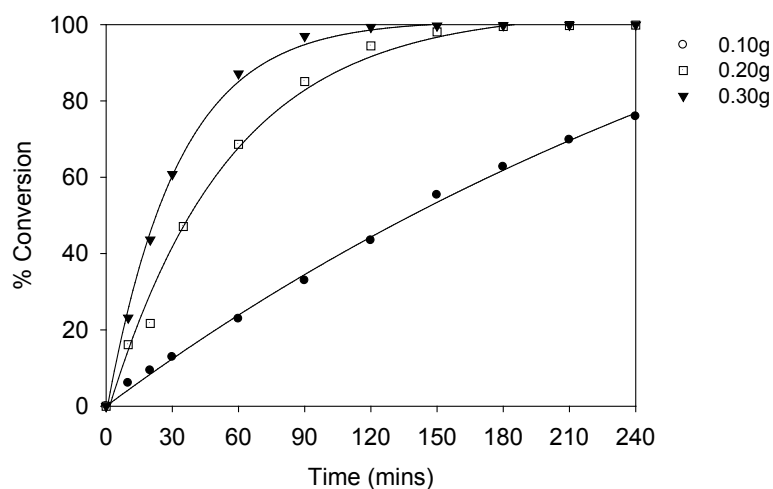


Figure 4.11 The effect of catalyst amount on thioanisole oxidation. Reaction conditions: H₂O₂ (20 mmol), thioanisole (10 mmol), acetonitrile (20 mL) and 25 °C

As has been observed before,¹⁸ an increase in temperature resulted not only in an increased rate of oxidation (**figure 4.12**) but also a greater quantity of methyl phenyl sulfone (**figure 4.13**). At 50 °C, there was a sharp increase in the formation of methyl phenyl sulfoxide, followed by a period of decay with an associated increase in the formation of the sulfone. For the same mass of catalyst, the TOF increased from 35.69 h⁻¹ at 25 °C to 268.53 h⁻¹ at 50 °C, while the conversions to the

sulfoxide were 59.6% (at 25 °C) and 31.2% (at 50 °C), and to the sulfone were 40.2% (at 25 °C) and 68.7% (at 50 °C).

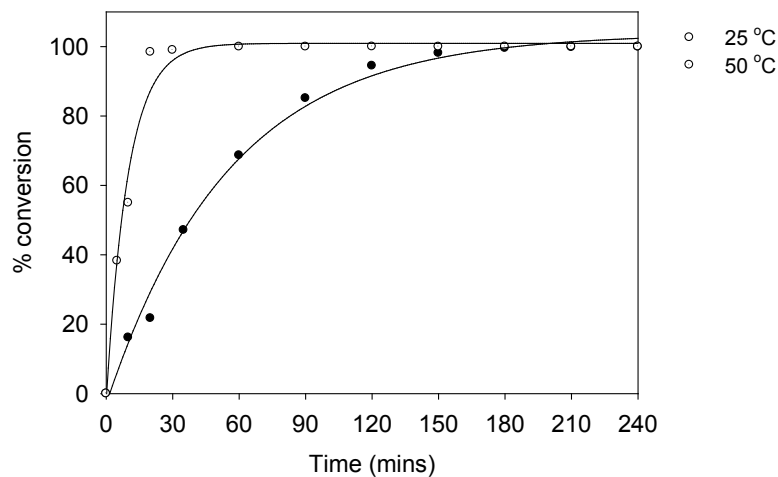


Figure 4.12 The effect of temperature on thioanisole oxidation. Conditions: p(VIM-co-EGDMA)-VO (0.20 g), H₂O₂ (20 mmol), thioanisole (10 mmol), acetonitrile (20 mL)

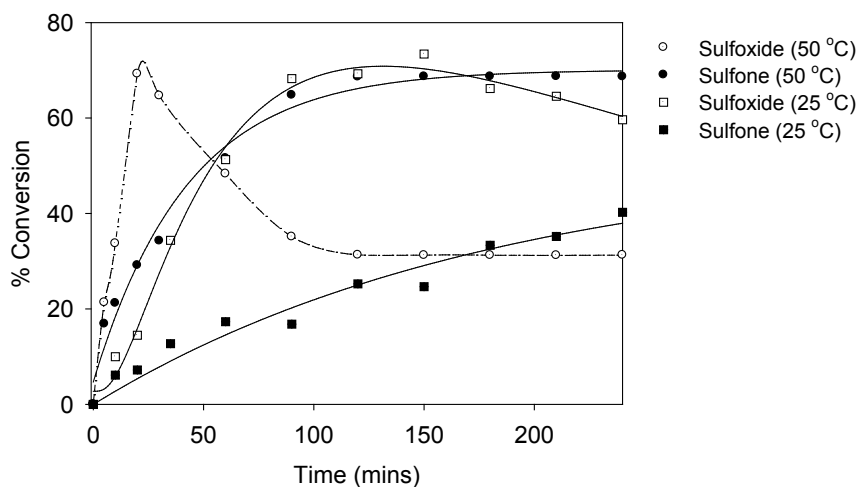


Figure 4.13 The effect of temperature on product selectivity. Conditions: p(VIM-co-EGDMA)-VO (0.20 g), H₂O₂ (20 mmol), thioanisole (10 mmol), acetonitrile (20 mL)

The catalytic beads showed good recyclability, an important property of heterogeneous catalysts. As shown in **figure 4.14** there was barely any drop in activity after subsequent catalyzed reactions demonstrating the excellent recyclability of these beads. In addition, there was barely

any significant damage to the surface of the beads after a catalytic reaction as illustrated in the AFM images in **figure 4.15**.

Substituting methanol for acetonitrile as the solvent resulted in a slight drop in activity (**figure 4.14**) which may be explained by the stabilization of the vanadium species by coordination of acetonitrile¹⁹ or due to the slightly higher dielectric constant of acetonitrile (37.5) compared to methanol (33). The reason for assessing the influence of the solvent will become more apparent in the next chapter (**Part 2, Chapter 5**). A summary of the results obtained using p(VIM-co-EGDMA)-VO appears in **table 4.2**.

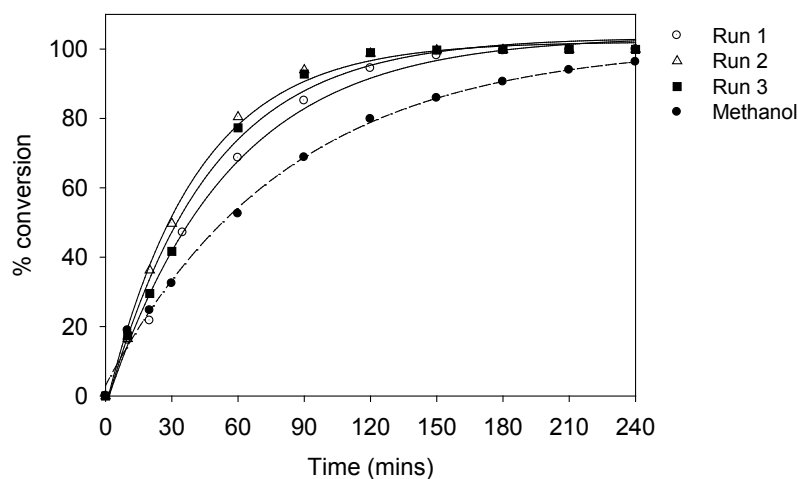


Figure 4.14 Recyclability of p(VIM-co-EGDMA)-VO beads at optimal conditions, and the effect of using methanol instead of acetonitrile as the solvent. Conditions: p(VIM-co-EGDMA)-VO (0.20 g), H₂O₂ (20 mmol), thioanisole (10 mmol), acetonitrile/methanol (20 mL) and 25 °C

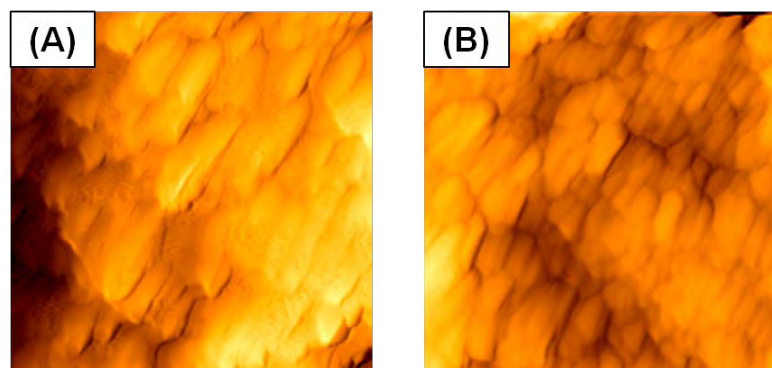


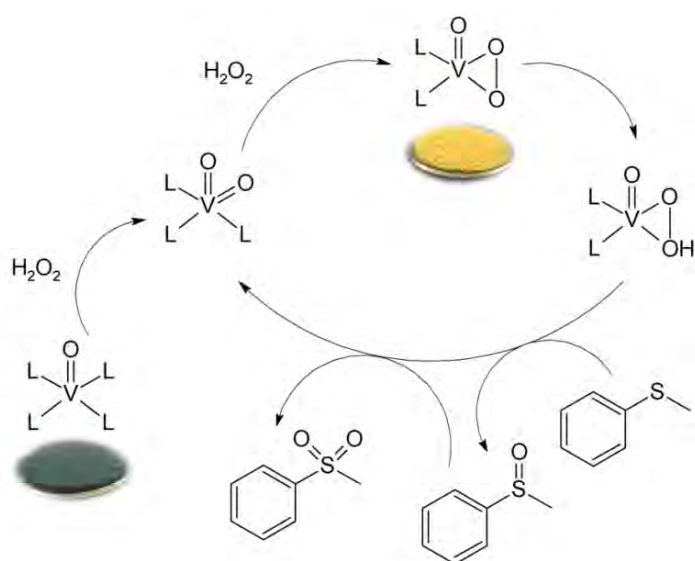
Figure 4.15 AFM images of (A) p(VIM-co-EGDMA)-VO and (B) p(VIM-co-EGDMA)-VO after one catalytic cycle

Table 4.2 Percentage conversion, turnover frequency (TOF) and product selectivity for the oxidation of thioanisole with hydrogen peroxide (20 mmol) using p(VIM-co-EGDMA)-VO as a catalyst

Mass (g)	Temp (°C)	Solvent	Conversion (%)	TOF ^a (h ⁻¹)	Sulfoxide (%)	Sulfone (%)
0.1	25	CH ₃ CN	75.9	34.52	59.3	16.6
0.2	25	CH ₃ CN	99.9	35.69	59.6	40.2
0.2*	25	CH ₃ CN	99.9	44.91	54.9	45
0.2**	25	CH ₃ CN	99.9	45.00	51.4	48.5
0.2	50	CH ₃ CN	99.9	268.53	31.2	68.7
0.2	25	MeOH	96.3	21.89	72.8	23.4
0.3	25	CH ₃ CN	99.9	30.12	55.5	44.4

^a Determined as moles of substrate converted/moles of catalyst/time (h); * After one cycle; ** After two cycles

During the catalytic reaction, the oxovanadium(IV) containing beads were oxidised to vanadium(V) species which was visibly noticed by a change in colour. As shown in **scheme 4.2**, the p-(VIM-co-EGDMA)-VO beads turn from a grey-blue colour to a yellow-orange colour, indicative of the change in oxidation state from +4 to +5 as proposed in the mechanism.



Scheme 4.2 The proposed catalytic mechanism for the oxidation of thioanisole by vanadium including photographs of beads before and during a reaction

In the infrared spectrum (**figure 4.16**), the yellow-coloured beads exhibit a strong band at 966 cm^{-1} consistent with the presence of a terminally bonded V=O group, while the band appearing at 870 cm^{-1} is tentatively assigned the peroxy O-O stretch, $\nu(\text{O-O})$.²⁰ It is therefore likely that the yellow-coloured beads consist predominantly of the oxoperoxovanadium(V) species as would be expected in conditions of excess peroxide.

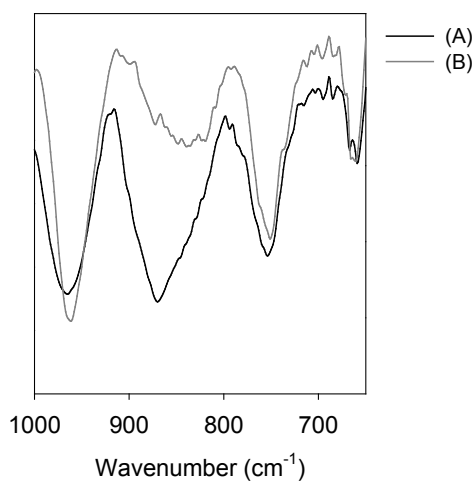


Figure 4.16 Overlaid infrared spectra of (A) p(VIM-co-EGDMA)-VO and (B) p(VIM-co-EGDMA)-VO recovered mid-reaction

4.5 Conclusions

Polymeric microspherical beads containing the imidazole functionality were successfully prepared by suspension polymerization. Using this approach, we have gained access to a number of properties that cannot be modified when using the commercial Merrifield based resins. The bead diameter was smaller than the Merrifield resins and a larger amount of crosslinker was used resulting in a more resilient and robust support. Additionally, the surface area was approximately ten-fold greater than the Merrifield resins used in the previous chapter. The metal binding capacity of the imidazole in the p(VIM-co-EGDMA) beads allows this support to be applied not only to immobilization of oxovanadium(IV) but also many other metal based homogeneous catalysts. There was, however, a greater deal of complexity involved when using the suspension polymerization approach. Several factors including stabilizer, stirring speed and porogen used, affected the resultant polymer morphology. Another disadvantage is that one is limited to using solvents that are immiscible with water (when carrying out normal phase suspension polymerization). Thus, the solubility of the monomerized ligand should be carefully considered and even modified since several solvents are “out-of-bounds”. Nevertheless, once a successful synthetic protocol has been developed, suspension polymerization remains a useful approach for the large scale preparation of ligand-functionalized polymer microspheres.

The heterogeneous catalysts prepared by this method proved to be effective in catalyzing the hydrogen peroxide facilitated oxidation of thioanisole and also displayed excellent recyclability, with no drop in activity being observed after three successive catalytic reactions. The increased surface area and porosity of these beads over the Merrifield beads had little to no observed effect on catalytic activity. We therefore propose that the directly exposed surface area is a more important property than total surface area (which includes pores) for these reactions and thus intend to investigate the catalytic properties of ultrafine fibers.

4.6 References and notes

- (1) Arshady, R. *Colloid Polym. Sci.* **1992**, *270*, 717.
- (2) Vivaldo-Lima, E.; Wood, P. E.; Hamielec, A. E.; Penlidis, A. *Ind. Eng. Chem. Res.* **1997**, *36*, 939.
- (3) Osman, B.; Kara, A.; Uzun, L.; Besirli, N.; Denizli, A. *J. Mol. Catal. B: Enzym.* **2005**, *37*, 88.
- (4) Senel, S.; Uzun, L.; Kara, A.; Denizli, A. *J. Macromol. Sci, Part A Pure Appl. Chem.* **2008**, *45*, 635.
- (5) Kara, A.; Uzun, L.; Besirli, N.; Denizli, A. *J. Hazard. Mater.* **2004**, *106*, 93.
- (6) In a 250 mL round bottom flask, *N*-vinylimidazole (15 g, 0.16 mol) was dissolved in dried diethyl ether (200 mL). The solution was flushed with argon to remove air and cooled to -78 °C. Butyllithium (2.5 M, 0.17 mol) was then added slowly. After two hours of stirring, dry *N,N*-dimethylformamide (0.24 mol) was added. The reaction was allowed to proceed overnight after which time, water (10 mL) was added followed by 150 mL of 4N HCl. The aqueous layer was made basic by addition of potassium carbonate following which; the product was extracted into chloroform. This organic layer was concentrated and the product was distilled at 3.0×10^{-1} mbar. The clear liquid solidified and turned brown after some time. Yield: 72%. $^1\text{H NMR}$ (δ , 400 MHz, DMSO- d_6): 9.88 (s, 1H, CHO), 7.95 (m, 1H, vinyl-H), 7.54 (s, 1H, Im-H), 7.34 (s, 1H, Im-H), 5.41 (m, 1H, vinyl-H), 5.12 (m, 1H, vinyl-H). *Anal.* Calcd (Found) for $\text{C}_6\text{H}_6\text{N}_2\text{O}$ (%): C, 59.01 (59.21); H, 4.95 (4.97); N, 29.94 (29.86).
- (7) Methyl(3-allyl-2-hydroxy)salicylate was prepared as reported in literature.²¹ Ethylenediamine (5 g, 0.041 mol) was then added to the allyl functionalized salicylate (4g, 0.01 mol) and refluxed overnight. The reaction was allowed to cool and the product crystallized out and was collected by filtrated and washed with cold ethylacetate. Yield: 52%. $^1\text{H NMR}$ (δ 400 MHz, DMSO- d_6): 7.42 (d, 1H, Ar-H), 7.12 (d, 1H, Ar-H), 6.61 (t, 1H, Ar-H), 5.96 (m, 1H, allyl-H), 5.01 (m, 2H, allyl-H), 3.71 (s, 4H, Im-H), 2.51 (s, 2H, allyl- CH_2). *Anal.* Calcd (Found) for $\text{C}_{12}\text{H}_{14}\text{N}_2\text{O}$ (%): C, 71.26 (72.21); H, 6.98 (7.12); N, 13.85 (13.54).
- (8) Allylethylenediamine was prepared as reported in literature.²² Allylethylenediamine (7.45 g, 0.074 mol) was added to methylsalicylate (2.6 g, 0.017 mol) and refluxed overnight. The product was purified on a silica column using methanol/ethylacetate (4:1). After concentration *in vacuo*, a yellow solid resulted. Yield: 61%. $^1\text{H NMR}$ (δ , 400 MHz, DMSO-

- d_6): 7.36 (d, 1H, Ar-H), 7.28 (t, 1H, Ar-H), 6.98 (d, 1H, Ar-H), 6.73 (t, 1H, Ar-H), 5.89 (m, 1H, allyl-H), 5.32 (m, 2H, allyl-H), 4.01 (m, 2H, allyl-CH₂), 3.94 (t, 2H, Im-H), 3.54 (t, 2H, Im-H). *Anal.* Calcd (Found) for C₁₂H₁₄N₂O (%): C, 71.26 (72.41); H, 6.98 (7.19); N, 13.85 (13.49).
- (9) This compound was prepared as for 2-allyl-6-(2'-hydroxyphenyl)imidazoline except that *N*-ethylethylenediamine and methyl(3-allyl-2-hydroxy)salicylate were used. Purification was achieved on a silica column using a mixture of ethylacetate and methanol (4:1). Concentration yielded a yellow solid. Yield: 52%. ¹H NMR gave a mixture of rotamers in an approximately 4:5 ratio, making integration unreliable. ¹H NMR (δ , 400 MHz, DMSO- d_6): 7.71 (d, 1H, Ar-H), 7.32 (d, 1H, Ar-H), 7.25 (d, 1H, Ar-H), 7.15 (d, 1H, Ar-H), 6.79 (t, 1H, Ar-H), 6.72 (t, 1H, Ar-H), 5.97 (m, 2H, allyl-H), 5.05 (m, 4H, allyl-H), 3.83 (t, 1.5H, Im-H), 3.53 (t, 1.5H, Im-H), 3.38 (m, 7H), 2.71 (t, 2H), 2.58 (m, 2H), 1.19 (t, 2.35H), 1.02 (t, 3H). *Anal.* Calcd (Found) for C₁₄H₁₈N₂O (%): C, 73.01 (73.96); H, 7.88 (7.96); N, 12.16 (12.09).
- (10) Cui, H.; Chen, H.; Qu, R.; Wang, C.; Sun, C.; Zhou, W.; Yu, M.; Jiang, H. *J. Appl. Polym. Sci.* **2009**, *111*, 3144.
- (11) Unsal, E.; Elmas, B.; Çamlı, S. T.; Tuncel, M.; Şenel, S.; Tuncel, A. *J. Appl. Polym. Sci.* **2005**, *95*, 1430.
- (12) Fontanals, N.; Maria Marcé, R.; Galià, M.; Borrull, F. *J. Polym. Sci. Part A Polym. Chem.* **2004**, *42*, 2019.
- (13) Uğuzdoğan, E.; Denkbaz, E. B.; Öztürk, E.; Tuncel, S. A.; Kabasakal, O. S. *J. Hazard. Mater.* **2009**, *162*, 1073.
- (14) Lane, T. J.; Nakagawa, I.; Walter, J. L.; Kandathil, A. J. *Inorg. Chem.* **1962**, *1*, 267.
- (15) Overberger, C. G.; Vorchheimer, N. *J. Am. Chem. Soc.* **1963**, *85*, 951.
- (16) Wilkinson, G.; Gillard, R. D.; McCleverty, J. A. *Comprehensive Coordination Chemistry*; Pergamon Press: New York, 1987.
- (17) Groenenboom, C. J.; Sawatzky, G.; de Liefde Meijer, H. J.; Jellinek, F. *J. Organomet. Chem.* **1974**, *76*, C4.
- (18) Tshentu, Z. R.; Togo, C.; Walmsley, R. S. *J. Mol. Catal. A: Chem.* **2010**, *318*, 30.
- (19) Du, Z.; Ma, J.; Ma, H.; Wang, M.; Huang, Y.; Xu, J. *Catal. Comm.* **2010**, *11*, 732.
- (20) Campbell, N. J.; Dengel, A. C.; Griffith, W. P. *Polyhedron* **1989**, *8*, 1379.

-
- (21) Hoveyda, H. R.; Karunaratne, V.; Rettig, S. J.; Orvig, C. *Inorg. Chem.* **1992**, *31*, 5408.
- (22) Linsker, F.; Evans, R. L. *J. Am. Chem. Soc.* **1945**, *67*, 1581.

This page has been left blank intentionally

Chapter 5

Electrospun fibers as support materials for oxovanadium(IV) catalysts

5.1 Introduction

The vanadium-functionalized crosslinked polymer microspheres developed in the previous chapters (**Part 2, Chapter 3** and **4**) showed excellent promise as heterogeneous catalysts. Theoretically, as one decreases the diameter of these materials, the surface area-to-volume ratio increases (provided that porosity and roughness remain constant). This may result in improved catalytic activity due to the greater catalytic surface area.¹ Unfortunately, as one decreases the size of the beads, they become difficult to separate and often require a centrifugation step.² In some instances this has been addressed by magnetizing the smaller beads and separating them by application of an external magnetic field.³

On the other hand, small diameter fibrous materials can be prepared by alternative techniques such as drawing and electrospinning. The latter is an emerging and simple technique for obtaining very small (μm down to nm) diameter materials.⁴ While the diameter of each fiber can be made very small, the three-dimensional network structure allows these materials to be separated very simply from the reaction solution (**figure 5.1**). The fiber flexibility and porosity (inter-fiber) of the mat makes these materials ideal for continuous flow applications.

While the microspherical resins are often highly porous and hence may have comparatively larger surface areas than the fibers, it is questionable how accessible these pores are to substrates. Thus, it is likely that a large degree of catalysis takes place on the surface of the beads and since the fiber diameters are much smaller, a greater degree of catalytic surface area is directly exposed to the reaction solution.

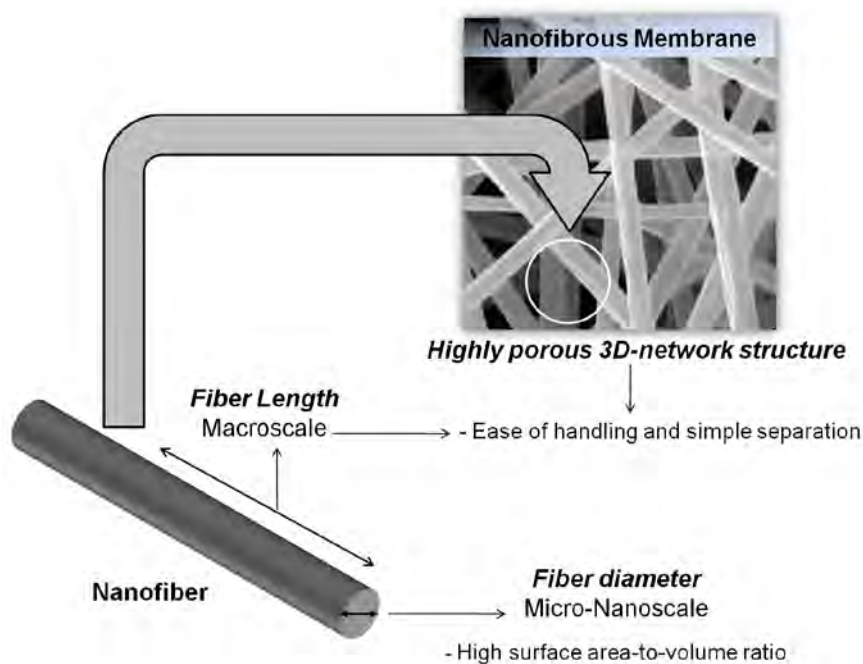


Figure 5.1 Characteristics of nanofibers and nanofibrous membranes

Fibers produced by electrospinning have been studied for a wide variety of applications including; filtration, wound dressings, tissue engineering scaffolds, artificial blood vessels, photonics, sensorics,⁵ pharmacy, energy devices,⁶ drug delivery and solid phase extraction sorbents,⁷ to name a few. The most popular use of these fibers is within the biomedical realm⁸ with several reviews available on this topic,⁹⁻¹² however there has been moderate interest in using these materials as catalyst supports. The simplest examples of electrospun fibers acting as catalyst supports are the non-metallated variety. With these, an organic molecule acts as the catalyst and may be introduced either by copolymerization or by post-electrospinning functionalization.¹³⁻¹⁵ More commonly, these fibers are used as supports for metal nanoparticles¹⁶⁻¹⁹ and to a lesser extent as metal oxide fibers produced by calcination.^{20,21} Strangely, there has been little to no work utilizing the ligand or coordination chemistry related approach for catalyst immobilization with these fibers. This may be due to the infancy of the field or due to some of the challenges associated with working with these non-crosslinked materials.

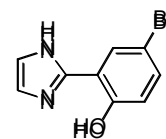
In this chapter, the preparation of oxovanadium(IV)-anchored polymer fibers is described. These materials were thoroughly characterized using various techniques including IR spectroscopy, microanalysis and SEM, to name a few. The catalytic activity of these materials was investigated

for the hydrogen peroxide based oxidation of thioanisole under continuous flow conditions and in some instances, batch conditions. Preliminary studies were conducted using non-covalently linked catalysts which had been incorporated into polystyrene fibers by mixing. Improvements to the polystyrene-based system were made, firstly by covalently anchoring the catalysts and then by incorporating a bidentate (rather than monodentate) ligand. Further improvements were then made by replacing polystyrene fibers with the thermally, chemically and mechanically stable polybenzimidazole fibers.

5.2 Preparation of ligands and oxovanadium(IV) complexes

5.2.1 2-(2'-Hydroxy-5'-bromophenyl)imidazole (pimBr)

The 2-(2'-hydroxyphenyl)imidazole derivatives were all prepared in a similar fashion to the literature procedure with minor modifications.²² 5-Bromo-2-



hydroxybenzaldehyde (5 g, 0.025 mol) and glyoxal trimer dihydrate (5.2 g, 0.025

mol) were added to glacial acetic acid (100 mL) and brought to reflux under argon until dissolved,

then ammonium acetate (18 g, 0.025 mol) was added and reflux was continued for a further 4 hrs.

The dark brown solution was allowed to cool and filtered through celite. The solution was made

basic by addition of aqueous ammonia. The resultant yellow-brown precipitate was collected by

filtration, redissolved in acetone and refluxed for an hour with activated carbon. This was filtered

through celite and concentrated to give a cream solid. Yield: 32.5%. Mp 240-242 °C. ATR-IR (cm⁻¹

¹, neat): 3370, 3230, 1588, 1551, 1492, 1488, 1391, 1287. ¹H NMR (δ, 400 MHz, DMSO-*d*₆): 8.09

(d, 1H), 7.37 (dd, 1H), 7.28 (br-s, 2H), 6.92 (d, 1H). ¹³C NMR (δ, 100 MHz, DMSO-*d*₆): 157.10,

156.01, 131.63, 126.55, 122.30, 119.43, 115.01, 110.32. *Anal.* Calcd (Found) for C₉H₇BrN₂O (%):

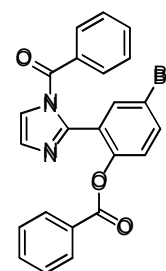
C, 45.22 (45.48); H, 2.95 (2.96); N, 11.72 (11.48).

5.2.2 N-Benzoyl-2-(2'-benzoxy-5'-bromophenyl)imidazole (dibenzoylpimBr).

A mass of 0.8 g of pimBr (0.003 mol) was dissolved in THF (20 mL). To this was added triethylamine (0.61 g, 0.006 mol) followed by benzoyl chloride (0.84 g,

0.006 mol). Stirring was continued overnight after which the solution was filtered and the filtrate concentrated to give a cream solid product. This was digested in

warm diethyl ether and washed thoroughly with the same solvent to afford a pure



product. Yield: 62.8%. Mp 131-133 °C. ATR-IR (cm⁻¹, neat): 1745, 1703, 1600, 1528, 1494, 1448,

1417, 1285. ¹H NMR (δ, 400 MHz, DMSO-*d*₆): 7.83 (m, 1H), 7.78-7.76 (m, 2H), 7.70-7.53 (m,

5H), 7.53 (s, 1H), 7.44-7.36 (m, 4H), 7.30-7.28 (d, 1H), 7.17 (s, 1H). ¹³C NMR (δ, 100 MHz,

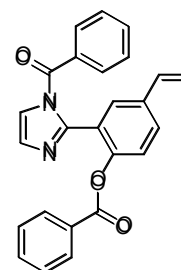
DMSO-*d*₆): 167.54, 164.48, 148.63, 135.00, 134.93, 134.30, 133.97, 131.66, 131.24, 130.08,

129.42, 128.80, 128.09, 125.94, 125.94, 122.87, 118.93. *Anal.* Calcd (Found) for C₂₃H₁₅BrN₂O₃

(%): C, 61.76 (61.91); H, 3.38 (3.83); N, 6.26 (6.17).

5.2.3 *N*-Benzoyl-2-(2'-benzoxy-5'-ethenylphenyl)imidazole (dibenzoylvpim).

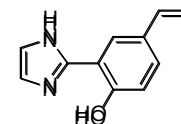
The protected ligand precursor, dibenzoylvpimBr (1 g, 2.24 mmol) was dissolved in warm toluene. To this was added tributyl(vinyl)tin (0.65 mL, 2.24 mmol) and a radical inhibitor 3,5-diterbutylcatechol (0.1 mol%). This mixture was heated to reflux under argon for 5 hours. After allowing the solution to cool, the solid was removed by filtration and the filtrate concentrated by rotary evaporation. The



resultant yellow solid was digested in a mixture of diethyl ether and hexane (2:1) overnight, filtered and the solid washed with cold diethyl ether. Yield: 74.8%. Mp 123-125 °C. ATR-IR (cm⁻¹, neat): 1736, 1707, 1598, 1504, 1448, 1288. ¹H NMR (δ, 400 MHz, DMSO-*d*₆): 7.88 (m, 2H), 7.76 (s, 1H), 7.60-7.48 (m, 5H), 7.34-7.28 (m, 5H), 7.19 (m, 2H), 6.75 (m, 1H, vinyl-H), 5.80 (d, 1H, vinyl-H), 5.32 (d, 1H, vinyl-H). ¹³C NMR (δ, 100 MHz, DMSO-*d*₆): 167.38, 164.64, 147.98, 145.78, 135.80, 133.94, 130.99, 129.56, 128.78, 128.48, 122.94, 121.27, 115.27. *Anal.* Calcd (Found) for C₂₅H₁₈N₂O₃ (%): C, 76.13 (76.23); H, 4.60 (4.66); N, 7.10 (7.25).

5.2.4 2-(2'-Hydroxy-5'-ethenylphenyl)imidazole (vpim)

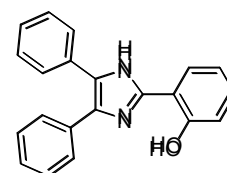
To a solution of dibenzoylvpim (1 g, 2.5 mmol) in ethanol (10 mL) was added sodium ethoxide (prepared by addition of 100 mg of sodium to 50 mL of ethanol), dropwise. Once the solution became yellow, it was concentrated and dissolved



in 0.2 M NaOH (50 mL). The pH was adjusted to 10 and the precipitate was collected by filtration and subjected to copious washing with ice-cold methanol followed by cold diethyl ether giving a pure cream solid. Yield: 54%. Mp 132-134 °C. ATR-IR (cm⁻¹, neat): 3392, 3260, 1606, 1595, 1530, 1504, 1388, 1279, 1259. ¹H NMR (δ, 400 MHz, DMSO-*d*₆): 8.03 (s, 1H), 7.33 (d, 1H), 6.91 (d, 1H), 6.65 (m, 1H, vinyl-H), 5.73 (d, 1H, vinyl-H), 5.16 (d, 1H, vinyl-H). ¹³C NMR (δ, 100 MHz, DMSO-*d*₆): 157.02, 146.57, 136.93, 129.11, 128.70, 122.89, 117.71, 114.26, 112.58, 100.37. *Anal.* Calcd (Found) for C₁₁H₁₀N₂O (%): C, 70.95 (71.01); H, 5.41 (5.43); N, 15.04 (14.99).

5.2.5 2-(4,5-Diphenyl-1*H*-imidazol-2-yl)phenol (dpimH)

All substituted 2-(4,5-diphenyl-1*H*-imidazole-2-yl)phenol derivatives were prepared according to a literature procedure.²³ Briefly, to a refluxing solution of benzil (2.0 g, 9.51 mmol) and ammonium acetate (14.7 g, 20 mol equiv)

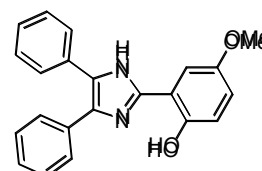


was added salicylaldehyde (1.0 mL, 9.51 mmol) and refluxing continued for a further 3 hours. The mixture was allowed to cool overnight. Occasionally a portion of the product would precipitate out. This was collected, washed with aqueous ammonia. The remaining reaction solution was poured into aqueous ammonia and the resultant solid collected and combined with the other fraction. These combined fractions were then recrystallized from ethanol to yield a yellow solid. Yield: 70%. Mp 203-204 °C. ATR-IR (cm^{-1} , neat): 3189, 3053, 1601, 1590, 1552, 1485, 1216, 1023, 766, 691. ^1H NMR (δ , 400 MHz, DMSO): 8.09 (br, d, 2H); 7.65 (m, 4H); 7.56 (m, 3H); 7.43 (m, 6H). ^{13}C NMR (δ , 100 MHz, DMSO): 159.4, 145.2, 136.0, 131.9, 130.8, 128.7, 128.4, 128.1, 127.6, 126.5, 126.4, 126.1. *Anal.* Calcd (Found) for $\text{C}_{21}\text{H}_{16}\text{N}_2\text{O}$ (%): C, 80.75 (80.17); H, 5.16 (5.22); N, 8.97 (8.87).

5.2.6 4-Methoxy-2-(4,5-diphenyl-1H-imidazol-2-yl)phenol (dpimMeO)

This was prepared as for dpimH except that 5-methoxy-2-hydroxybenzaldehyde was used instead of salicylaldehyde. Yield: 86%.

Mp 159-160 °C. ATR-IR (cm^{-1} , neat): 3194m, 3048, 1605, 1586, 1499,

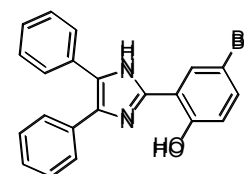


1224, 1036, 764, 696. ^1H NMR (δ , 400 MHz, DMSO- d_6): 13.02 (s, 1H); 12.47 (s, 1H); 7.67 (s, 1H); 7.40 (m, 10H); 6.89 (m, 2H); 3.77 (s, 3H). ^{13}C NMR (δ , 100 MHz, DMSO- d_6): 151.9, 150.8, 145.8, 134.2, 133.6, 128.8, 127.3, 127.1, 126.7, 117.5, 116.9, 112.5, 108.8, 55.6. *Anal.* Calcd (Found) for $\text{C}_{22}\text{H}_{18}\text{N}_2\text{O}_2$ (%): C, 77.17 (77.10); H, 5.30 (5.38); N, 8.18 (8.09).

5.2.7 4-Bromo-2-(4,5-diphenyl-1H-imidazol-2-yl)phenol (dpimBr)

This was prepared as for dpimH except that 5-bromo-2-hydroxybenzaldehyde was used instead of salicylaldehyde. Yield: 71%. Mp

186-187 °C. ATR-IR (cm^{-1} , neat): 3166, 3043, 1604, 1579, 1567, 1484,



1278, 1254, 1143, 1074, 1026, 762, 696. ^1H NMR (δ , 400 MHz, DMSO- d_6): 13.11 (br, s, 1H); 8.30 (s, 1H); 7.53-7.39 (m, 11H); 6.95 (d, 1H). ^{13}C NMR (δ , 100 MHz, DMSO- d_6): 167.3, 156.7, 154.9, 145.3, 133.2, 129.5, 128.7, 128.3, 127.9, 127.7, 119.9, 115.6. *Anal.* Calcd (Found) for $\text{C}_{21}\text{H}_{15}\text{BrN}_2\text{O}$ (%): C, 64.46 (64.26); H, 3.86 (3.90); N, 7.16 (7.25).

5.2.8 4-Nitro-2-(4,5-diphenyl-1H-imidazol-2-yl)phenol (dpimNO₂)

This was prepared as for dpimH except that 5-nitro-2-hydroxybenzaldehyde was used instead of salicylaldehyde. Yield: 62%.

Mp 219-220 °C. ATR-IR (cm⁻¹, neat): 3289, 3055, 1615, 1594, 1584,

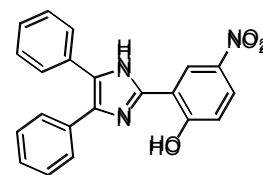
1471, 1336, 1129, 1074, 1024, 763, 739, 687. ¹H NMR (δ, 400 MHz, DMSO-*d*₆): 13.9 (br, s, 1H);

9.15 (s, 1H); 8.17 (d, 1H); 7.54 (m, 4H); 7.43 (m, 4H); 7.38 (m, 2H); 7.16 (d, 1H). ¹³C NMR (δ, 100

MHz, DMSO-*d*₆): 165.5, 157.3, 154.3, 144.4, 133.2, 130.1, 128.8, 127.9, 127.6, 127.3, 126.9,

120.3, 114.5. *Anal.* Calcd (Found) for C₂₁H₁₅N₃O₃ (%): C, 70.58 (70.29); H, 4.23 (4.18); N, 11.76

(11.46).



5.2.9 [VO(dpimH)₂]

The ligand dpimH (0.31 g, 1 mmol) was dissolved in warm methanol (10

mL). Separately, vanadyl sulfate (0.1 g, 0.45 mmol) was dissolved in 3

mL of a methanol/water (2:1 ratio) solution. This vanadyl solution was

then added dropwise to the methanolic ligand solution. The mixture was

stirred for 4 hours at room temperature. The resultant blue-green

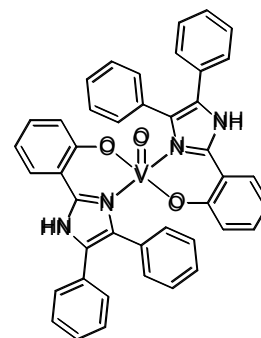
precipitate was collected by filtration and washed with water and

methanol and then dried at 100 °C. Yield: 62%. Mp > 350 °C. ATR-IR (cm⁻¹, neat): 1604, 1589,

1565, 1477, 1456, 1303, 1251, 1139, 1025, 945, 869, 750, 694. UV/Vis (DMF) λ_{max} (ε, M⁻¹cm⁻¹):

527 (53), 632 (31), 836 (43). *Anal.* Calcd (Found) for C₄₂H₃₀N₄O₃V·2H₂O (%): C, 69.51 (69.59); H,

4.72 (4.71); N, 7.72 (7.64).



5.2.10 [VO(dpimMeO)₂]

This compound was prepared as for [VO(dpimH)₂] above

except the ligand dpimMeO was used. The resultant

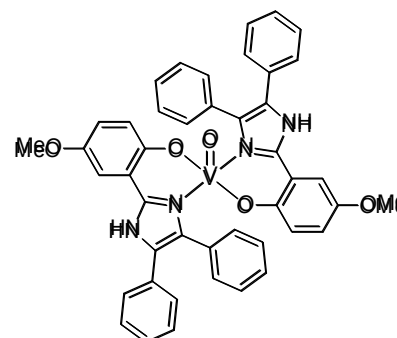
compound was a yellow-green solid. Yield: 64 %. Mp > 350

°C. ATR-IR (cm⁻¹, neat): 1587, 1489, 1225, 1034, 975, 764,

692. UV/Vis (DMF) λ_{max} (ε, M⁻¹cm⁻¹): 515 (78), 625 (48), 844

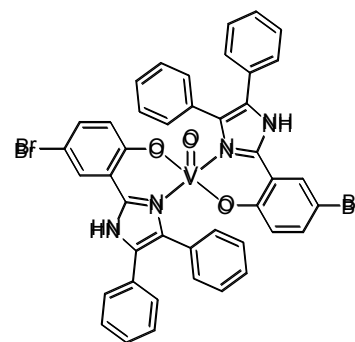
(55). *Anal.* Calcd (Found) for C₄₄H₃₄N₄O₅V·H₂O (%): C, 68.84

(68.71); H, 4.73 (4.81); N, 7.30 (7.26).



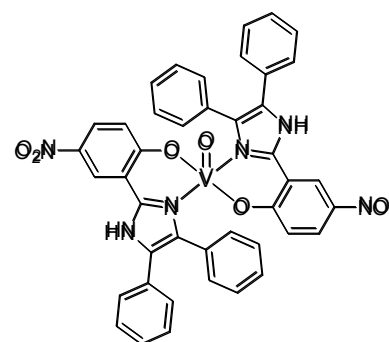
5.2.11 [VO(dpimBr)₂]

This compound was prepared as for [VO(dpimH)₂] except the ligand dpimBr was used. The resultant compound was a blue-green solid. Yield: 59 %. Mp > 350 °C. ATR-IR (cm⁻¹, neat): 1601, 1561, 1475, 1294, 1250, 1142, 1028, 958, 696. UV/Vis (DMF) λ_{max} (ε, M⁻¹cm⁻¹): 522 (54), 639 (30), 823 (42). *Anal.* Calcd (Found) for C₄₂H₂₈Br₂N₄O₃V.2H₂O (%): C, 57.20 (57.10); H, 3.59 (3.65); N, 6.30 (6.34).



5.2.12 [VO(dpimNO₂)₂]

This compound was prepared as for [VO(dpimH)₂] except the ligand dpimNO₂ was used. The resultant compound was an orange-green solid. Yield: 45 %. Mp > 350 °C. ATR-IR (cm⁻¹, neat): 1608, 1579, 1486, 1331, 1138, 1072, 964, 692. UV/Vis (DMF) λ_{max} (ε, M⁻¹cm⁻¹): 613 (49), 849 (55). *Anal.* Calcd (Found) for C₄₂H₃₂N₆O₉V.2H₂O (%): C, 61.84 (62.06); H, 3.95 (4.13); N, 10.30 (10.08).



5.3 Preparation of polymers and fabrication of fibers

Electrospinning was conducted using a top-down (or vertical) approach whereby the polymer fibers were either collected on a stationary piece of grounded aluminium foil or using a rotating drum collector. The instrument setup for each of these methods is illustrated in **figure 5.2**.

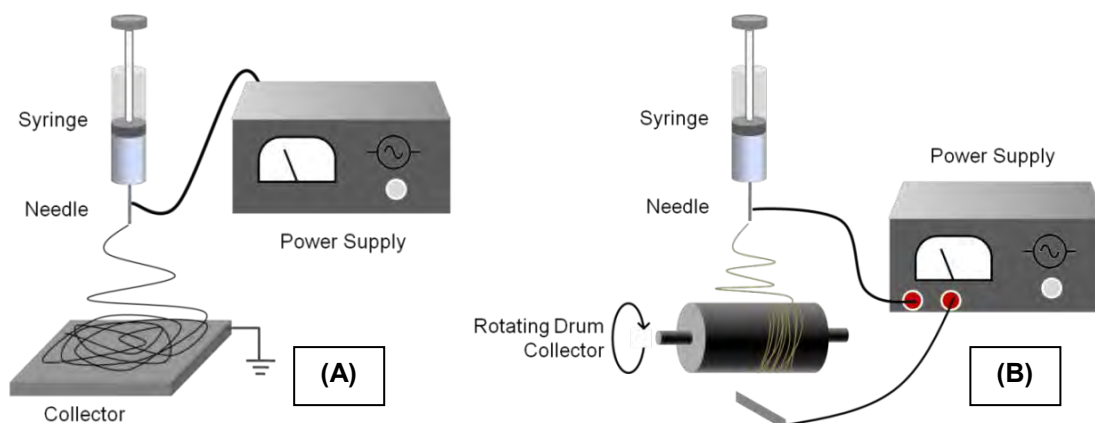


Figure 5.2 Different electrospinning configurations. Shown in (A) is the simple vertical electrospinning using a stationary grounded collector, while (B) shows the same setup except using a rotating drum collector with an oppositely charged electrode underneath to direct fiber collection

5.3.1 PS-25 fibers

A mass of 1.25 g of polystyrene (PS) was dissolved in 5 mL of a DMF:THF (4:1) solvent mixture to make a 2.5% (wt/v%) PS solution, which was subsequently stirred for 24 hours to ensure homogeneity. The solution was then transferred to a 20 mL syringe and electrospun. The voltage applied to the needle tip was 20 kV and the tip and collector distance was 15 cm. The internal diameter of the needle was 1 mm and the flow rate was 1 mL.h⁻¹. The white fibers were collected by vertical electrospinning on a piece of aluminium foil that was grounded (**figure 5.2a**). ATR-IR (cm⁻¹, neat): 1655, 1492, 1451, 749, 696. *Anal.* Found (%): C, 84.68; H, 8.08.

5.3.2 PS-25-[VO(dpimMeO)₂] fibers

Same as above for PS-25 except [VO(dpimMeO)₂] (0.25 g, 20 wt% relative to PS) was added to the mixture. The resulting fiber mat was a light green colour. ATR-IR (cm⁻¹, neat): 1491, 1451, 1281, 975, 811, 694. *Anal.* Found (%): C, 73.36; H, 7.43; N, 3.32; V, 3.00.

5.3.3 PS-15-[VO(dpimMeO)₂] fibers

Same as above for PS-25 except a mass of 1.25 g of PS was dissolved in 8.3 mL of a DMF:THF (4:1) solution to make a 15% PS solution. The internal needle diameter was 0.5 mm and the flow rate was kept constant at 0.5 mL.h⁻¹. The resulting fiber mat was a green colour. ATR-IR (cm⁻¹, neat): 1491, 1451, 1281, 975, 811, 694. *Anal.* Found (%): C, 85.85; H, 7.31; N, 1.28; V, 1.19.

5.3.4 PS-25-[VO(dpimNO₂)₂] fibers

Same as for PS-25 except [VO(dpimNO₂)₂] (0.25 g, 20 wt%) was used. The flow rate was reduced to 0.6 mL.h⁻¹. The resulting fiber mat was a yellow colour. ATR-IR (cm⁻¹, neat): 1579, 1182, 1138, 1070, 1025, 987, 966, 891, 840. *Anal.* Found (%): C, 87.22; H, 7.61; N, 1.41; V, 0.86.

5.3.5 PS-15-[VO(dpimNO₂)₂] fibers

Same as for PS-25 except that [VO(dpimNO₂)₂] was included in the mixture. The resulting fiber mat was yellow in colour. ATR-IR (cm⁻¹, neat): 1579, 1182, 1138, 1070, 1025, 987, 966, 891, 840. *Anal.* Found (%): C, 85.93; H, 7.45; N, 1.41; V, 0.84.

5.3.6 p(St-co-VIM) copolymer

In a typical reaction, VIM (1.6 g, 17.0 mmol) was mixed with styrene (6.4 g, 61.4 mmol) followed by addition of AIBN (0.2 wt%). The vial was sealed, purged with argon and the temperature increased to 60 °C. The reaction was allowed to proceed at this temperature for 48 hours. The resultant solid polymer was subsequently dissolved in warm chloroform and precipitated by addition of methanol. This precipitation process was repeated twice to ensure removal of unreacted monomers. The white polymer was dried in an oven for 48 hours at 60 °C. ATR-IR (cm⁻¹, neat): 3445, 3071, 3028, 2927, 1635, 1609, 1497, 1454, 1113, 1080, 1027, 910, 702. *Anal.* Found (%): C, 89.79; H, 8.41; N, 2.30.

5.3.7 p(ST-co-VIM) fibers

The polymer was dissolved in a DMF/THF (4:1) solvent mixture to make a 25% solution (wt/v%). The polymer solution was stirred for 24 hours to ensure complete dissolution and then loaded into a 20 mL syringe (**figure 5.2a**). Electrospinning was then conducted using the following parameters. A voltage of 21 kV was applied to the spinneret (needle tip) which had an internal

diameter of 1 mm, and the distance between the tip and collector was maintained at 20 cm whilst the flow rate was maintained at 1 mL.h⁻¹ using a syringe pump. The resultant white fibers were collected on a piece of aluminium foil. ATR-IR (cm⁻¹, neat): 3445, 3071, 3028, 2927, 1635, 1609, 1497, 1454, 1113, 1080, 1027, 910, 702. *Anal.* Found (%): C, 89.78; H, 8.41; N, 2.31.

5.3.8 p(ST-co-VIM)-VO fibers

A strip of approximately 5 cm x 12 cm of the p(ST-co-VIM) fiber mat was cut and rinsed with water to make the fibers more manageable (The dry fibers were fragile and disintegrated easily when manipulated). These were placed into a 0.1 M VOSO₄ solution (20 mL methanol/5 mL water) in a sealable beaker. The vessel was purged with argon and then stirred gently at 120 rpm on an orbital shaker for a period of 72 hrs at room temperature. The fibers were rinsed with water and soaked in methanol for 3 hrs and then filtered. This procedure was repeated until no trace of vanadium was detected in the washings. Finally, the fibers were filtered and dried at room temperature under reduced pressure for 12 hrs. ATR-IR (cm⁻¹, neat): 3439, 3039, 2932, 1635, 1603, 1491, 1460, 1155, 1118, 985, 760, 702. *Anal.* Found (%): C, 75.69; H, 7.57; N, 1.88; S, 0.88; V, 3.50.

5.3.9 p(ST-co-VPIM) copolymer

Styrene (7 g, 0.067 mol) and vpim (1.4 g, 0.0076 mol) (**5.2.4**) were mixed together along with radical initiator AIBN (0.0168 g, 0.2 wt%). To this suspension was added DMF dropwise until the solid dissolved (approximately 2 mL DMF). Oxygen was removed by bubbling with argon following which the vial was sealed and transferred to an oil bath. The temperature was maintained at 60 °C by use of a temperature regulating hotplate. After 48 hrs, the solid was dissolved in THF and precipitated by pouring this slowly into methanol. This was repeated twice to ensure complete removal of starting materials. After rinsing with methanol, the white polymer was dried in an oven at 60 °C overnight. ATR-IR (cm⁻¹, neat): 3418, 3027, 2921, 1712, 1598, 1490, 1449, 1260, 1178, 1152, 1084, 1025, 1010, 983, 966. *Anal.* Found (%): C, 84.84; H, 7.33; N, 2.16.

5.3.10 p(ST-co-VPIM) fibers

p(ST-co-VPIM) was dissolved in DMF/THF (4:1) to make various concentrations from 8 - 20% (wt/v%). The voltage applied to the needle tip was 15 kV while a negative voltage of -5 kV was

applied below the rotating drum collector (**figure 5.2b**). The distance between the needle and collector was 15 cm. The polymer solution was fed to the needle tip at a rate of 1 mL.h⁻¹ for 8-15% polymer solutions and 0.8 mL.h⁻¹ for the 20% solution. ATR-IR (cm⁻¹, neat): 3418, 3027, 2921, 1712, 1598, 1490, 1449, 1260, 1178, 1152, 1084, 1025, 1010, 983, 966. *Anal.* Found (%): C, 84.83; H, 7.36; N, 2.18.

5.3.11 p(ST-co-VPIM)-VO fibers

The p(ST-co-VPIM) fibers (0.26 g) were immersed into a methanolic VOSO₄ solution (0.1 M, 20 mL) and shaken on an orbital shaker for 72 hours. After this, unreacted vanadium was removed by rinsing the fibers copiously with methanol. Vanadium coordination was evidenced by a change in colour from cream to a deep grey-purple. Following this, the fibers were immersed in a pimBr/methanol solution (20 mM) for 72 hours. The fibers were washed with methanol and dried *in vacuo*. ATR-IR (cm⁻¹, neat): 3027, 2921, 1712, 1596, 1488, 1447, 1261, 1178, 1152, 1084, 1029, 1010, 964. *Anal.* Found (%): C, 82.13; H, 7.568; N, 2.21; V, 0.69.

5.3.12 p(benzimidazole) fibers (PBI_f)

Polybenzimidazole (PBI) (2.0 g) and lithium chloride (LiCl) (0.4 g, 4 wt/v%) were refluxed in N,N-dimethylacetamide (DMAc) (10 mL) for a period of 5 hours. The solution was allowed to cool slightly and then centrifuged to separate undissolved polymer. The viscous polymer solution was then poured into a 20 mL syringe and electrospun under the following conditions. A voltage of 15 kV was applied to the needle tip which had an internal diameter of 0.5 mm. A negative voltage of -5 kV was applied below a rotating drum collector (**figure 5.2b**) and the flow rate was kept at 0.15 mL.h⁻¹. The distance between the needle and collector was 12 cm. The nanofiber membrane was peeled off the aluminium foil, sandwiched between two pieces of filter paper and immersed in methanol overnight to remove residual solvent and lithium chloride and finally dried in an oven at 60 °C overnight. The fibers were a brownish-yellow colour. ATR-IR (cm⁻¹, neat): 3617, 3405, 3158, 1629, 1538, 1444, 1100, 801, 692. *Anal.* Found (%): C, 68.06; H, 5.11; N, 15.17.

5.3.13 p(benzimidazole)-VO fibers (PBI_f-VO)

The PBI_f fibers (0.5 g) were added to a solution containing VOSO₄ (0.54 g, 2.5 mmol) in methanol (40 mL) and heated to reflux for 24 hours under an argon atmosphere with gentle stirring. The

vanadium-functionalized fibers were rinsed with hot methanol several times to ensure complete removal of unreacted vanadium salt. The fibers were then dried in an oven for 48 hours at 60 °C. ATR-IR (cm^{-1} , neat): 3069, 1634, 1566, 1457, 1103, 1036, 978, 804. *Anal.* Found (%): C, 43.32; H, 4.91; N, 9.32; S, 7.51; V, 5.5.

5.3.14 Attempted synthesis of p(St-co-VIMCOOH)

Much like that discussed in the previous chapter (**Part 1, Chapter 4**), oxidation of the p[(styrene-co-(vinylimidazole-2-aldehyde)]²⁴ using hydrogen peroxide or oxone were unsuccessful and thus attempts at preparing this polymer were abandoned.

5.4 Catalytic activity studies

5.4.1 Homogeneous batch catalysis using $[\text{VO}(\text{dpimR})_2]$ complexes

In a typical homogeneous catalytic oxidation experiment, 20 mL of acetonitrile and the oxovanadium complex (0.25 mol%) were mixed in a 50 mL round bottom flask. The temperature of the reaction was fixed at $25(\pm 1)$ °C by use of an external temperature probe. The oxidant, H_2O_2 (20 mmol), was added followed by thioanisole (10 mmol) while the reaction was stirred at a constant rate of 300 rpm. Aliquots were withdrawn at 10 minute time intervals and analysed by GC.

5.4.2 Continuous flow using PS- $[\text{VO}(\text{dpimR})_2]$ fibers

The catalytic activity of the polymer-incorporated oxovanadium(IV) complexes was also evaluated using a continuous flow approach. The fibers (0.010 g) were packed between two filter disks (Whatmann no. 1) in a 10 mL syringe. In a separate flask; aqueous H_2O_2 (1 mmol), thioanisole (0.5 mmol) and solvent mixture ($\text{CH}_3\text{CN}/\text{H}_2\text{O}$) were mixed for 5 minutes (**figure 5.3**). The addition of water in this instance was to prevent leaching of the catalyst (it was insoluble in water) as well as prevent the fibers from dissolving. This reactant solution was poured into the syringe. The solution was passed through the fibers at a controlled rate using a syringe pump (New Era, NE-1000). Fractions of 1 mL were collected and analysed using GC.



Figure 5.3 Continuous flow set-up, when using either PS- $[\text{VO}(\text{dpimR})_2]$ or p(ST-co-VIM)-VO fibers

maintained at 25 °C using a hotplate-stirrer fitted with an external temperature probe. Thioanisole (0.124 g, 1 mmol) was added followed immediately by $\text{PBI}_7\text{-VO}$ and 30% H_2O_2 (2eq). The stirring rate was kept constant at 100 rpm throughout the reaction. Aliquots were withdrawn at regular time intervals and analyzed by GC.

5.4.6 Continuous flow using $\text{PBI}_7\text{-VO}$ fibers

The $\text{PBI}_7\text{-VO}$ fibers were packed into a filter holder (Millipore Swinnex® 13) and firmly compressed. In a separate vial, thioanisole (0.124 g, 1 mmol) and H_2O_2 (2 mmol) were mixed in acetonitrile for 5 minutes. This reactant solution was transferred to a 20 mL syringe and the filter holder containing the fibers was connected as shown in **figure 5.5**. The reactant solution was passed through the catalyst bed at a controlled rate by use of a syringe pump (New Era NE-1000). The product solution was collected in individual 0.5 mL fractions and each was analyzed by GC. The temperature of the room was maintained at 25 °C throughout the course of the reaction.



Figure 5.5 Continuous flow set-up, when using $\text{PBI}_7\text{-VO}$ fibers. The insert shows an expanded view of the catalyst bed

5.5 Results and discussion

5.5.1 General synthesis and characterization

The 4-*R*-2-(4,5-diphenyl-1*H*-imidazol-2-yl)phenol (dpim*R*) ligands chosen in this study were based on the 2-(2'-hydroxyphenyl)-1*H*-imidazole ligand used in our previous work (**Part 2, Chapter 3**) with two major exceptions. Two extra phenyl groups were added at the 4 and 5-position of the imidazole ring to provide additional stability through π - π interactions with polystyrene. The substituent at the *para*-position of the phenol ring was varied to assess the effect of electron withdrawing/donating groups on the catalytic activity.²⁵

The purity of the ligands was confirmed by NMR analysis and microanalysis. The ¹H NMR spectrum of dpimH (**figure 5.6**), a representative example, shows the presence of the aromatic signals corresponding to the benzene groups of the ligand in the region of 7.4-8.4 ppm. The ¹³C NMR (**figure 5.7**) spectrum further confirmed the successful synthesis with all expected carbon atoms being accounted for. For dpimH there were a total of twenty-one carbon atoms but in the ¹³C NMR spectrum, there were a total of fifteen peaks. This can easily be explained, since nine of these peaks corresponded to a single carbon each while the more intense remaining peaks (of which there were six) correspond to two-carbons each making up the total of twenty-one (**figure 5.7**).

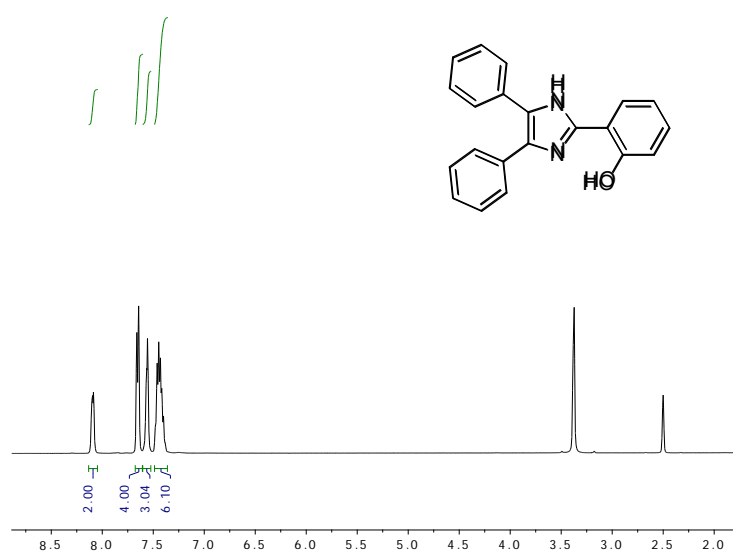


Figure 5.6 ¹H NMR spectrum of dpimH in DMSO (δ ppm). (Peaks at ~3.5 and 2.5 are due to the solvent)

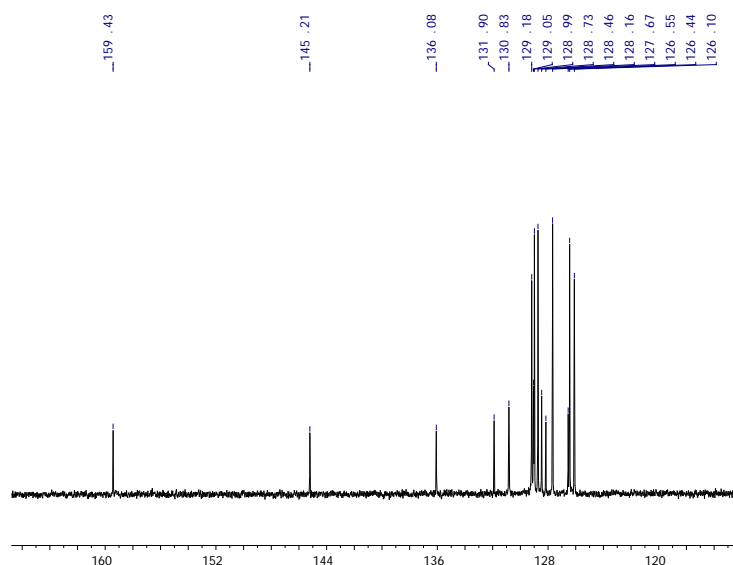
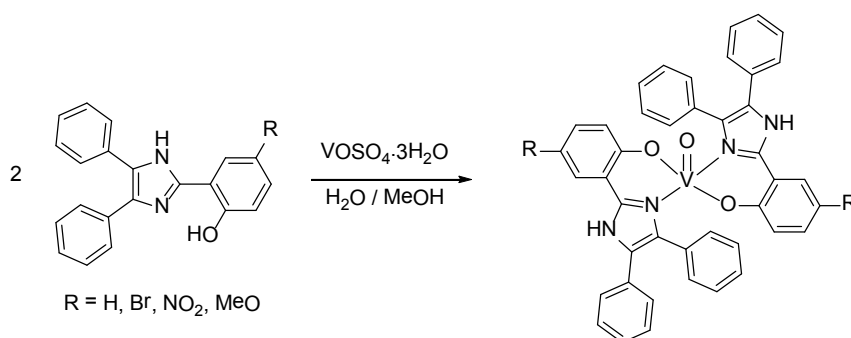


Figure 5.7 ^{13}C NMR spectrum of dpimH in DMSO (δ ppm). The solvent peak appears upfield from the range shown here at ~ 40 ppm

These ligands were reacted with VOSO_4 to afford the corresponding oxovanadium(IV) complexes (**scheme 5.1**) which precipitated out of solution and were easily collected by filtration. These complexes will be collectively termed, $[\text{VO}(\text{dpim}R)_2]$, where $R = \text{H}, \text{Br}, \text{NO}_2$ or MeO . The purity of the complexes was confirmed by microanalysis which further revealed that the complexes crystallized out with a minimum of one water molecule. Unfortunately, even after several attempts, crystals suitable for single crystal X-ray diffraction were not obtained. We speculate that the coordination is similar to that of the parent complex, $[\text{VO}(\text{pimin})_2]$ (**Part 1, Chapter 3**), with the N and O-atoms sitting trans to one another as depicted in **scheme 5.1**, especially considering the steric hindrance of the benzene rings.



Scheme 5.1 Preparation of the *bis*-coordinated oxovanadium(IV) complexes with 4- R -2-(4,5-diphenyl-1 H -imidazol-2-yl)phenol ligands ($R = \text{NO}_2, \text{Br}, \text{H}, \text{MeO}$)

Infrared spectroscopy of the ligands and complexes was performed and all complexes exhibited characteristic $\nu(\text{V}=\text{O})$ stretches between $945 - 975 \text{ cm}^{-1}$. There were also numerous coordination-induced shifts as illustrated in **figure 5.8** for $[\text{VO}(\text{dpimBr})_2]$. The azomethine stretch which appeared at $\sim 1600 \text{ cm}^{-1}$ in the ligands, shifted to lower wavenumbers in the corresponding oxovanadium(IV) complexes ($\sim 7 \text{ cm}^{-1}$ shift). This, in combination with the disappearance of the $\nu(\text{O}-\text{H})$ and the shift of the $\nu(\text{C}-\text{O})$ upon coordination, confirm the bidentate N,O-coordination mode.

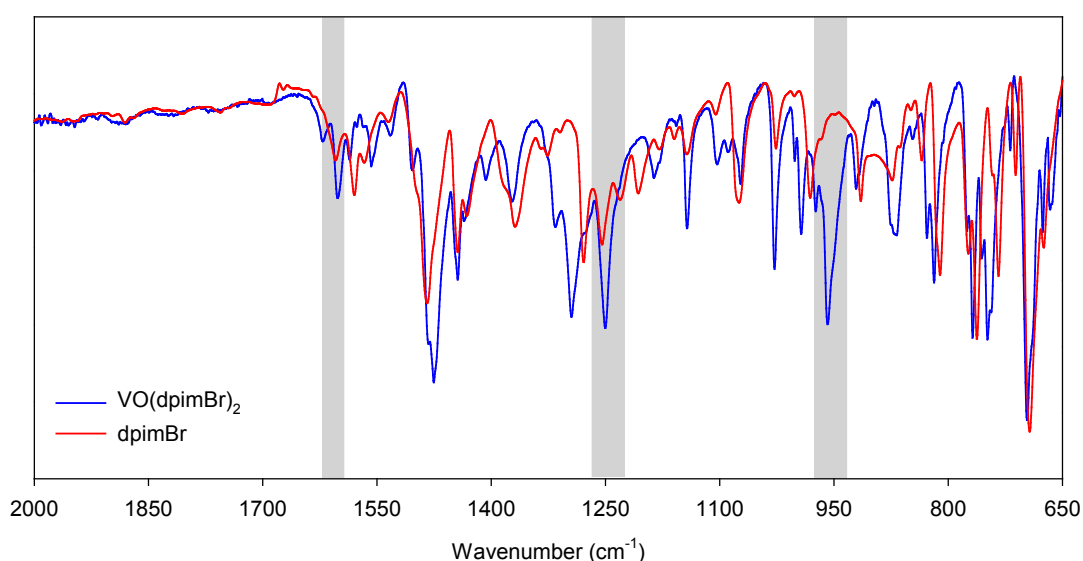


Figure 5.8 IR spectra of the ligand dpimBr and oxovanadium(IV) complex, $[\text{VO}(\text{dpimBr})_2]$. The $\nu(\text{C}=\text{N})$, $\nu(\text{C}-\text{O})$ and $\nu(\text{V}=\text{O})$ have been highlighted

The UV/Vis spectra of all of the complexes besides $[\text{VO}(\text{dpimNO}_2)_2]$ displayed three d-d transitions, which can be expected for a C_{4v} , d^1 complex. The first transition appeared between $515 - 527 \text{ nm}$ ($a_1 \leftarrow b_2$), the second between $613 - 639 \text{ nm}$ ($b_1 \leftarrow b_2$) and the third between $823 - 849 \text{ nm}$ ($e_\pi \leftarrow b_2$). The higher energy d-d transition for $[\text{VO}(\text{dpimNO}_2)_2]$ was hidden beneath the intense charge transfer band appearing in this region (**figure 5.9**). The lower symmetry (C_{2v}) of the prepared complexes has little or no effect on the observed spectra, since the splitting of the e_π^* level is generally too small to be observed experimentally.²⁶

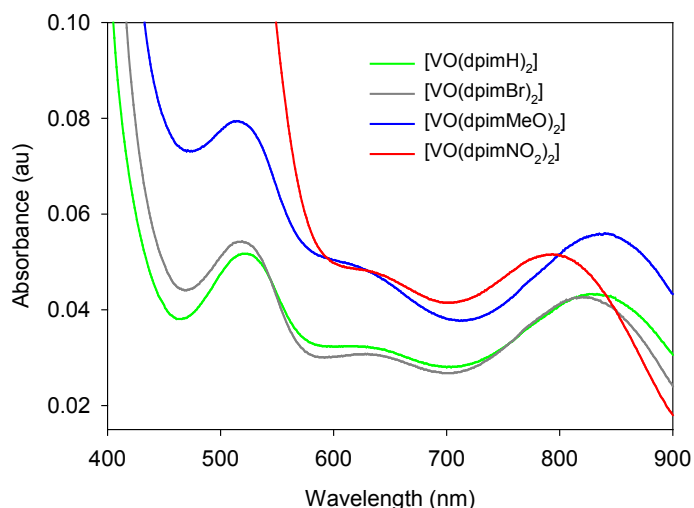
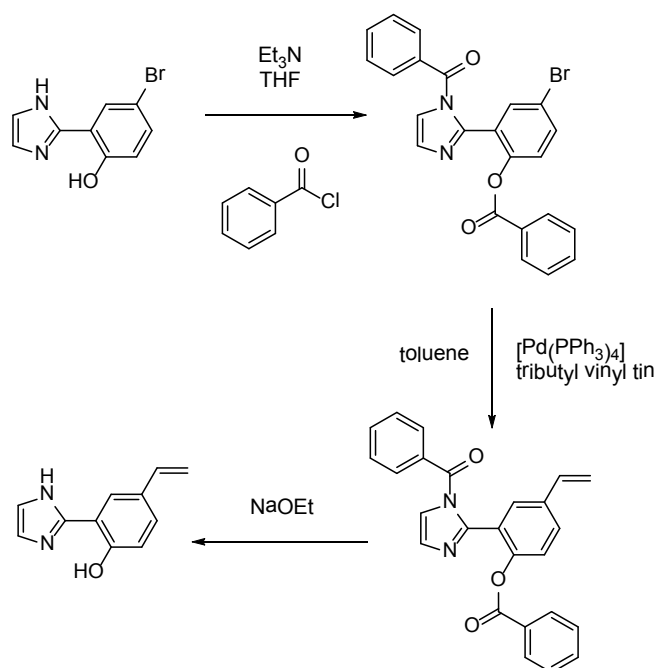


Figure 5.9 UV/Vis spectra of the $[\text{VO}(\text{dpimR})_2]$ complexes in DMSO

Synthesis of the monomerized 2-(2'-hydroxyphenyl)imidazole ligand (vpim) was achieved using a method developed by Sellergren and co-workers.²² This elaborate synthesis adequately demonstrates the difficulty associated with preparing polymerizable ligands, especially considering the relatively large quantities of monomer that are needed. The synthetic route appears in **scheme 5.2**. Firstly, the brominated 2-(2'-hydroxyphenyl)imidazole (pimBr) compound was prepared according to the procedure developed by Rogers and Bruce.²⁷ Following this, both the O-H and N-H groups from the phenol and imidazole respectively, were protected using benzoyl chloride since it is known that these basic groups can interfere with the Pd-catalyzed coupling step. After introduction of the vinyl group by this Pd-catalyzed coupling, deprotection was achieved using sodium ethoxide finally giving the vinylated monomer, 2-(2'-hydroxy-5'-ethenylphenyl)imidazole (vpim). In retrospect, NMR spectroscopy was not the most conclusive means for characterizing pimBr and vpim as the signals appeared broad due to slow rotation around the phenylimidazole bond due to conjugation and intramolecular hydrogen bonding.²⁷ The IR spectra illustrate the various changes occurring at the different synthetic steps quite well (**figure 5.10**). The N-H and O-H stretches which appear in the range $3400 - 3120 \text{ cm}^{-1}$ for pimBr disappear after protection with the benzoyl groups. The $\nu(\text{C}=\text{O})$ bands from the benzoyl groups in dibenzoylpimBr further confirm the functionalization, with two separate bands appearing at 1745 and 1705 cm^{-1} , corresponding to the O and N-substituted benzoyl groups. Similarly, deprotection

of dibenzoylpim was evident by the disappearance of the $\nu(\text{C}=\text{O})$ bands and appearance of the O-H and N-H stretches.



Scheme 5.2 Synthetic route for the preparation of the polymerizable ligand, vpim

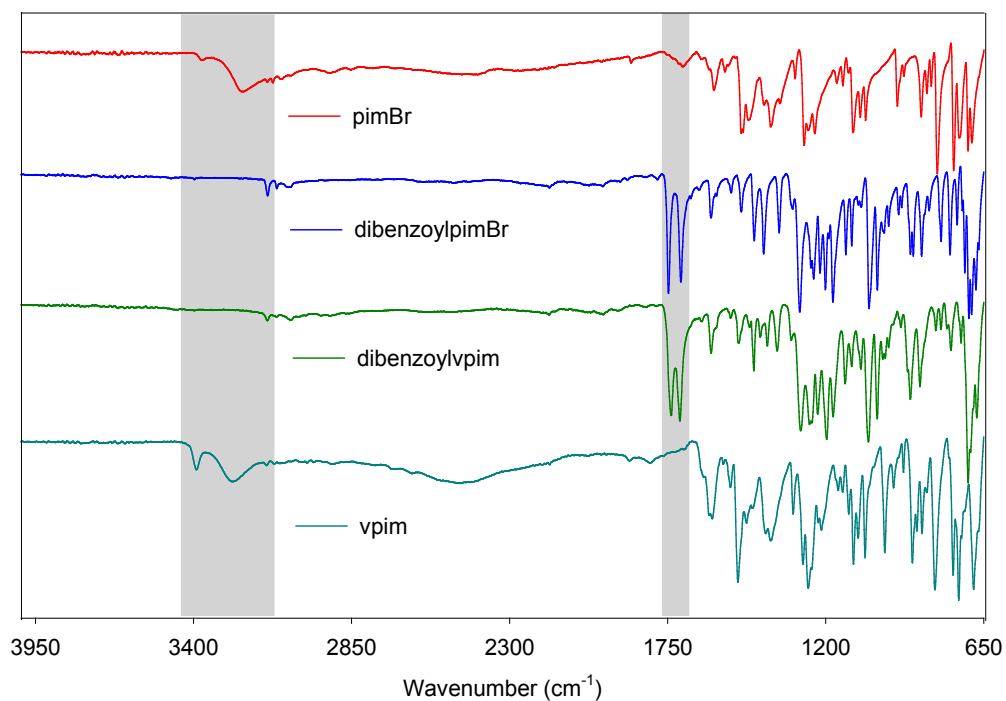


Figure 5.10 IR spectra showing the changes at various stages of synthesis of vpim

5.5.2 Synthesis of polymers, fabrication and characterization of electrospun fibers

(a) PS-15/25-[VO(dpimR)₂] fibers

The homogeneous [VO(dpimR)₂] (R = NO₂ and MeO) catalysts were incorporated into polystyrene by mixing them together in a solvent mixture of DMF/THF. This simple method of immobilization offers practical advantages in that no chemical modification of the homogeneous catalysts is required, however the van der Waals and π-π stacking forces are significantly weaker than covalent bonds²⁸ and will undoubtedly lead to some leaching of the catalyst. This approach was therefore treated as more of a proof of concept to assess how polystyrene-based fibers behaved when used as a catalytic membrane. Fibers of this composite material were then produced by using the electrospinning technique.²⁹ The major advantage of this simple method of immobilization was that the structure of the catalyst may be considered almost identical to that of the homogeneous derivative and therefore easier to characterize.

Inclusion of the complexes within the fibers was visually noticeable, since the colour of the fibers resembled that of the neat complexes (**figure 5.11**).

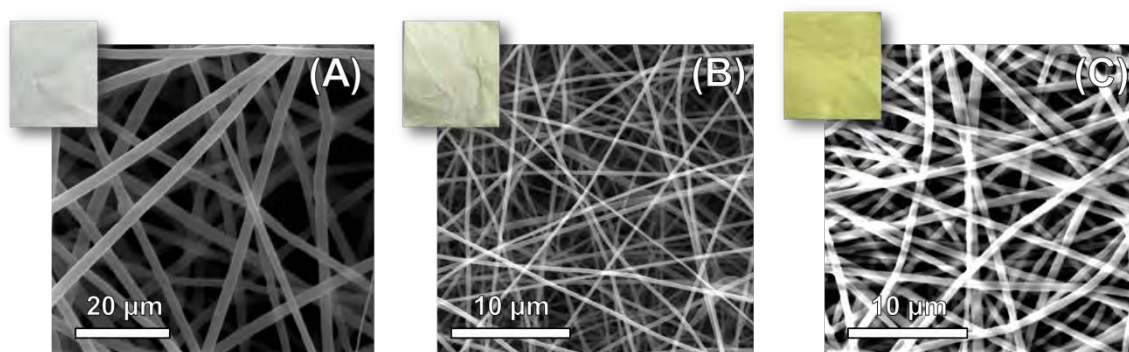


Figure 5.11 SEM images and digital pictures of the electrospun fibers, from left to right; (A) PS-25, (B) PS-15-[VO(dpimMeO)₂] and (C) PS-15-[VO(dpimNO₂)₂]

Elemental (**section 5.2**) analysis indicated the presence of nitrogen due to the embedded complexes, while infrared data (**figure 5.12**) further confirmed this. XPS also proved to be a highly useful technique, with all the expected elements (C, N, O, V) accounted for in the spectrum (**figure 5.13**). For both sets of fibers, O 1s, N 1s, C 1s and V 2p signals appeared at approximately 530, 399, 285 and 5 15 eV. An additional N 1s peak was observed for PS-15-

[VO(dpimNO₂)₂] at 405 eV due to the nitro substituent. The position of the V 2p_{3/2} signal for both sets of fibers, further confirmed that the complexes remain in the +4 oxidation state.³⁰

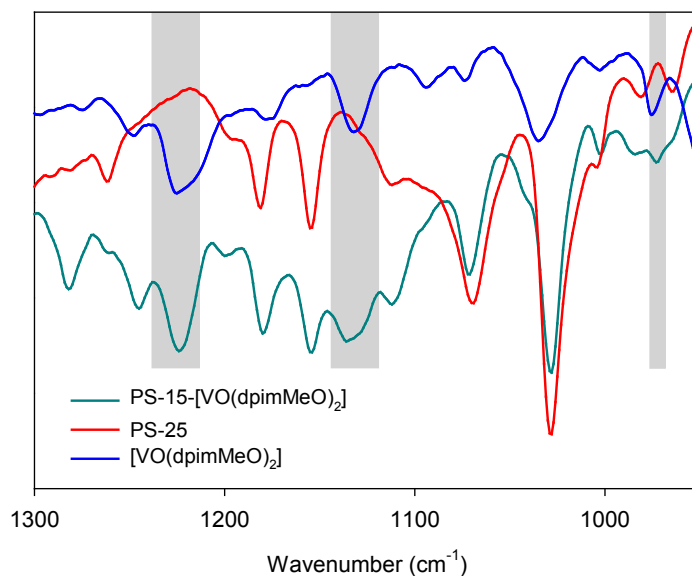


Figure 5.12 Infrared spectra of unmodified polystyrene (PS-25) fibers, the neat complex [VO(dpimMeO)₂], and the corresponding fibers, PS-15-[VO(dpimMeO)₂]. The highlighted areas show peaks found in both [VO(dpimMeO)₂] and PS-15-[VO(dpimMeO)₂] fibers

Table 5.1 Elemental binding energies of PS-15-[VO(dpimMeO)₂] and PS-15-[VO(dpimNO₂)₂] as determined by XPS

Polymer	Binding Energy (eV)				
	O 1s	N 1s	C 1s	V 2p _{3/2}	V 2p _{1/2}
PS-15-[VO(dpimMeO) ₂]	530	399	285	514	521
PS-15-[VO(dpimNO ₂) ₂]	530	399, 405	285	515	522

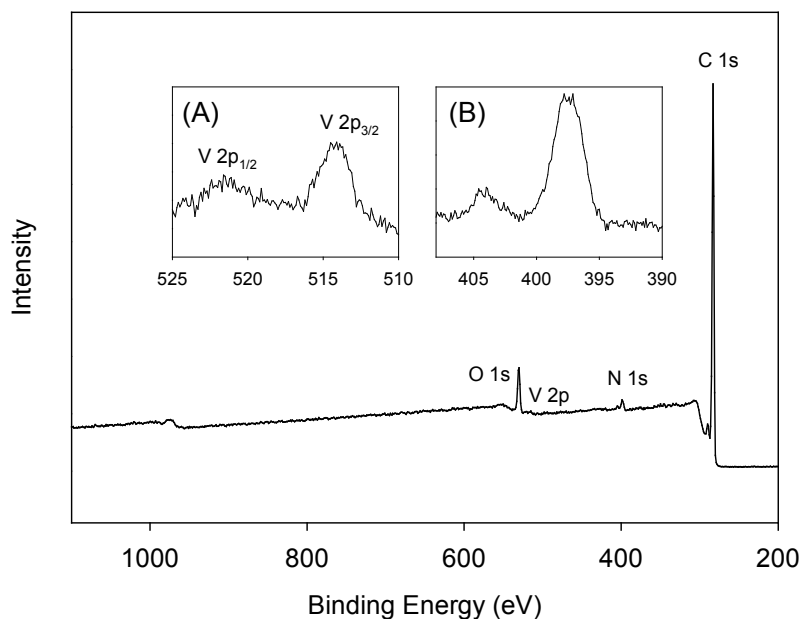


Figure 5.13 Wide scan XPS spectrum of PS-15-[VO(dpimMeO)₂]. Insert shows an expanded view of the high resolution (A) V 2p signal and (B) the N 1s signals

The amount of catalyst added to the polystyrene solution was kept constant at 20% (wt% wrt polystyrene) while the percentage of polystyrene was adjusted to tune the fiber diameters. Inclusion of the oxovanadium complexes in the polymer solution actually improved electrospinnability possibly by improving the solution conductivity. This allowed for the production of smooth fibers at both 25% (w/v%) and the lower 15% polystyrene concentrations (**figure 5.11**) while for the pure polystyrene, smooth fibers were only obtained at the higher 25% concentration, a trend commonly observed.³¹ Using lower than 15% concentrations gave undesirable bead-on-string morphologies and so these two ratio's (15% and 25%) were settled upon. The fiber diameters were measured from an average of 20 fibers; the 25% polystyrene-based fibers, PS-25-[VO(dpimMeO)₂] and PS-25-[VO(dpimNO₂)₂], had average fiber diameters of 1.37 and 1.98 μm respectively, while for the 15% polystyrene-based fibers, PS-15-[VO(dpimMeO)₂] and PS-15-[VO(dpimNO₂)₂], it was 0.33 and 0.51 μm respectively.

Thermogravimetric analysis of PS-15-[VO(dpimNO₂)₂] was carried out at a heating rate of 10 °C.min⁻¹ under a nitrogen atmosphere (**figure 5.14**). Two distinct weight loss steps were observed particularly in the derivative curve (DTG). The first weight loss ($T_{\max} = 340$ °C) was possibly due to decomposition of the oxovanadium(IV) complex while decomposition of the polymer backbone occurred at a higher temperature ($T_{\max} = 414$ °C). It should be noted that the glass transition temperature (T_g) and the melting point of polystyrene occur well below these temperatures. When the fibers were subjected to a melting point analysis they completely lost their original morphology at temperatures beyond 96 °C.

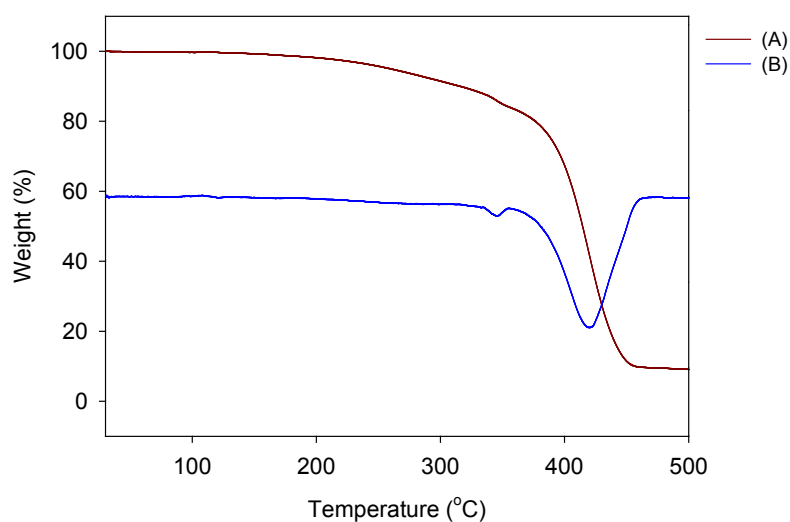
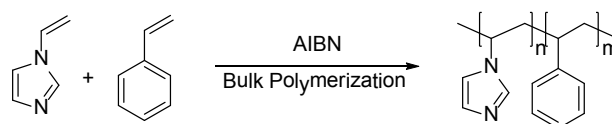


Figure 5.14 TG (A) and DTG (B) curve of PS-15-[VO(dpimNO₂)₂]

(b) Poly(styrene-co-vinylimidazole) fibers

The p(ST-co-VIM) copolymers were prepared by bulk polymerization of *N*-vinylimidazole and styrene (**scheme 5.3**). A few different ratio's of the styrene/*N*-vinylimidazole monomers were used for example; 3:1, 5:1 and 7:1 (ST/VIM). However, besides the imidazole content in the resultant copolymer there was no dramatic effect on solubility or other properties of the fibers and as such only one ratio was thoroughly studied (5:1) as this gave the best fibers.



Scheme 5.3 Synthesis of p(ST-co-VIM) copolymer

Based on the elemental composition, the styrene/imidazole content for the p(ST-co-VIM) copolymer (ST/VIM 5:1) was approximately 10:1. This ratio provided sufficient coordinating functionality as well as the required solubility parameters for electrospinning. In the first attempt to prepare the 'pre-electrospinning' functionalized oxovanadium-immobilized polymer, the copolymer was dissolved in DMF and reacted with VO_2SO_4 . This reaction produced a green solid which was insoluble in several solvents and therefore could not be electrospun. It is possible that vanadium bound to imidazole groups from neighbouring polymer chains thereby forming crosslinks and rendering the polymer insoluble. Thus, a post-electrospinning functionalization method was adopted whereby the styrene-imidazole copolymer was first dissolved in a DMF/THF solvent mixture and electrospun into fibers followed by a reaction with vanadium. Another strategy that was considered involved preparation of the oxovanadium(IV) complexes with the polymerizable ligands coordinated, followed by radical polymerization. The complexes were, however, not sufficiently soluble and thus would have resulted in comparatively lower (compared to the ligand only) incorporation into the polymer. In addition, unsymmetrically coordinated complexes would have to be prepared (one ligand containing a vinyl group and the other not) to eliminate the chance of crosslinking by the *bis*-coordinated complex.

As shown in the SEM images (**figure 5.15**), the fibers produced were smooth and non-beaded with diameters ranging from 1.3-2.1 μm . Although these diameters are quite large for electrospun fibers, they are still a couple of orders of magnitude smaller than the Merrifield beads ($\sim 600 \mu\text{m}$) (**Part 2, Chapter 3**) and the beads prepared by suspension polymerization ($\sim 300 \mu\text{m}$) (**Part 2, Chapter 4**). The imidazole-containing fibers were then immersed in a methanolic vanadyl sulfate solution and stirred for 72 hours using an orbital shaker to produce the oxovanadium(IV)-immobilized fibers. When this agitation method was used, the morphology of the fibers was unaffected as witnessed in the SEM images (**figure 5.15**). Conversely, agitation by stirrer bar broke the fibers into small pieces and as such was unsuitable. Upon functionalization with

vanadium, the average diameter of the fibers increased slightly (1.6-2.4 μm), possibly due to a thin coating of oxovanadium(IV) on the surfaces, however this cannot be concluded indisputably, since the diameter distribution of the fibers was quite large and thus this difference may not be significant.

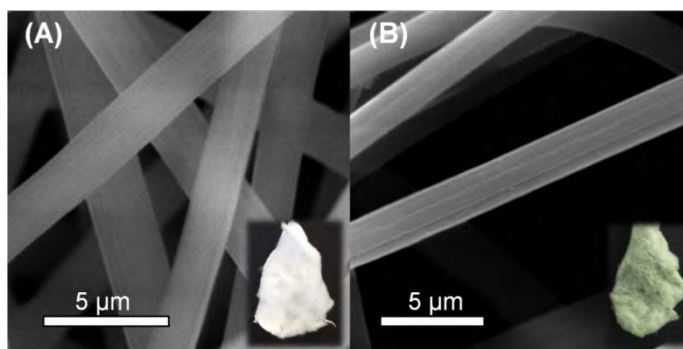


Figure 5.15 SEM images of p(ST-co-VIM) and p(ST-co-VIM)-VO with digital image showing colour changes

The surface area of the p(ST-co-VIM) fibers was determined from the N_2 absorption/desorption isotherms (**figure 5.16**) and found to be $53 \text{ m}^2 \cdot \text{g}^{-1}$, which was significantly less than the beads ($151 \text{ m}^2 \cdot \text{g}^{-1}$) prepared in the previous chapter (**Part 2, Chapter 4**) despite the smaller diameter of the fibers. This was likely due to the significantly rougher surface and internal porous structure of the beads. The pore volume and pore size of the unfunctionalized fibers was $0.49 \text{ cm}^3 \cdot \text{g}^{-1}$ and 309 Å, respectively. Functionalization of these fibers with vanadium resulted in an increase in surface area to $74 \text{ m}^2 \cdot \text{g}^{-1}$ whilst the pore volume and size were slightly higher at $0.67 \text{ cm}^3 \cdot \text{g}^{-1}$ and 344 Å, respectively. This is tentatively attributed to removal of residual electrospinning solvent after immersion in methanol (during the vanadium functionalization step), resulting in the formation of additional pores. AFM of a single fiber was attempted but proved challenging and no satisfactory images could be obtained.

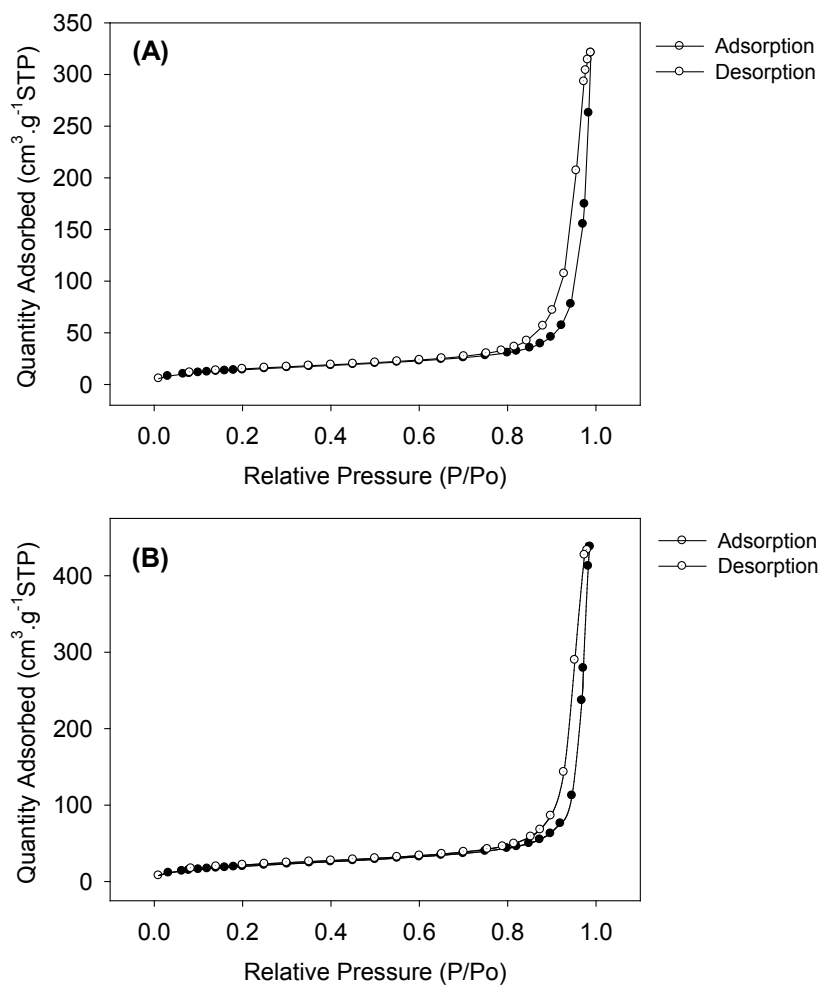


Figure 5.16 Nitrogen adsorption/desorption isotherms, for (A) p(ST-co-VIM) and (B) p(ST-co-VIM)-VO fibers

Elemental characterization data revealed an imidazole-to-vanadium ratio of close to 1:1. As shown in **figure 5.17**, the vanadium-functionalized p(ST-co-VIM)-VO fibers clearly display additional bands at 980 cm⁻¹ due to the $\nu(\text{V}=\text{O})$ and at 1154 cm⁻¹ due to a sulfate stretching vibration. As discussed previously (**Part 2, Chapter 3**), the broadness of this band, which is probably due to a series of overlapping bands, makes accurate assignment of the coordination mode of sulfate challenging. It is, however, quite likely that the sulfate coordination is monodentate as observed for vanadyl sulfate.

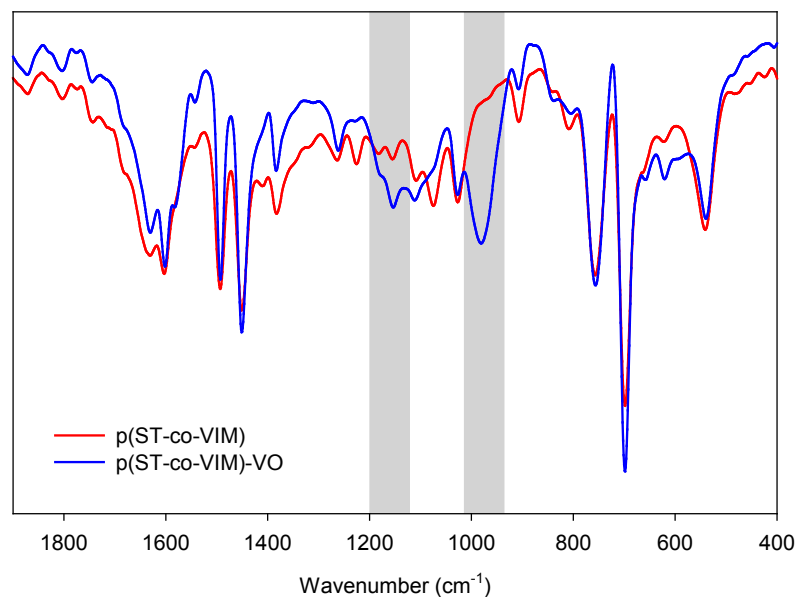


Figure 5.17 IR spectrum of p(ST-co-VIM) and p(ST-co-VIM)-VO

XPS was used to investigate the surface functionality of the material (**figure 5.18**). The V $2p_{3/2}$ binding energy appeared at 514.9 eV confirming surface functionalization as well as the +4 oxidation state of vanadium (**table 5.2**).³⁰ The N 1s peak from imidazole for both p(ST-co-VIM) and p(ST-co-VIM)-VO appeared at 399 eV (**table 5.2**). An O 1s peak observed for p(ST-co-VIM) may be attributed to inadequate drying of the sample before running the XPS, surface contaminants, or the presence of water hydrogen bonded to the imidazole residues of the polymer. The presence of sulfur as indicated by infrared and elemental analysis, was confirmed using XPS, with the S $2p_{3/2}$ peak appearing at 167 eV (**table 5.2**).

Table 5.2 Elemental binding energies of p(ST-co-VIM) and p(ST-co-VIM)-VO as determined by XPS

Polymer	Binding Energy (eV)					
	O 1s	N 1s	C 1s	V $2p_{3/2}$	V $2p_{1/2}$	S $2p_{3/2}$
p(ST-co-VIM)	530	399	285	-	-	-
p(ST-co-VIM)-VO	530	399	285	515	526	167

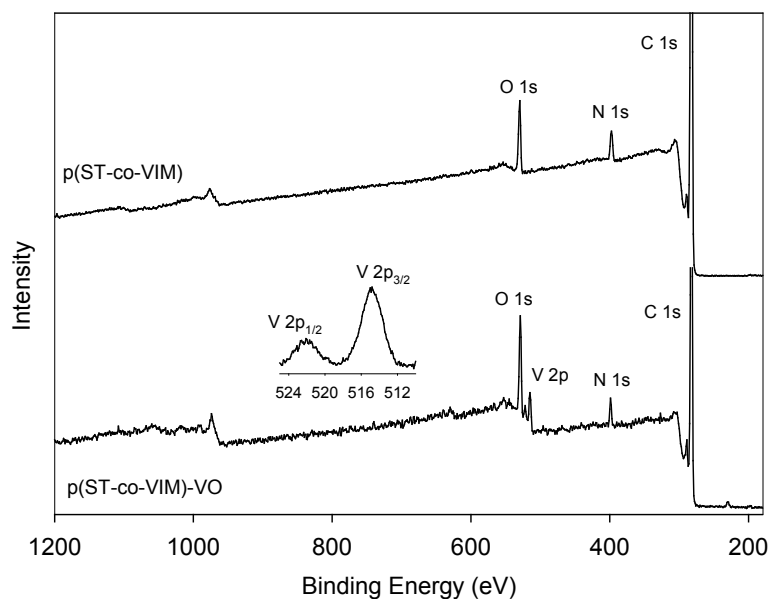


Figure 5.18 Wide scan XPS spectra of p(ST-co-VIM) and p(ST-co-VIM)-VO. Insert shows an expanded view of the V 2p signals of p(ST-co-VIM)-VO

The general thermal stability of p(ST-co-VIM) and p(ST-co-VIM)-VO was investigated briefly using TG (**figure 5.19**). For p(ST-co-VIM) no significant weight loss due to water was observed below 100 °C, however a small peak appearing at a T_{\max} of 119 °C in the DTG may be due to hydrogen bonded water, which may correspond to the O 1s signal observed in the XPS spectrum. The TG-curves for both p(ST-co-VIM) and p(ST-co-VIM)-VO were remarkably similar (**figure 5.19**) with T_{\max} values corresponding to decomposition of the polymer appearing at 401 °C and 409 °C for p(ST-co-VIM)-VO and p(ST-co-VIM), respectively. In this instance it is quite possible that decomposition of oxovanadium(IV) occurred concurrently with decomposition of the polymer and was thus not easily visible from the curve. The larger remaining mass at 500 °C of p(ST-co-VIM)-VO (~21%) compared to p(ST-co-VIM) (~4.5%), may be due to residual vanadium pentoxide.

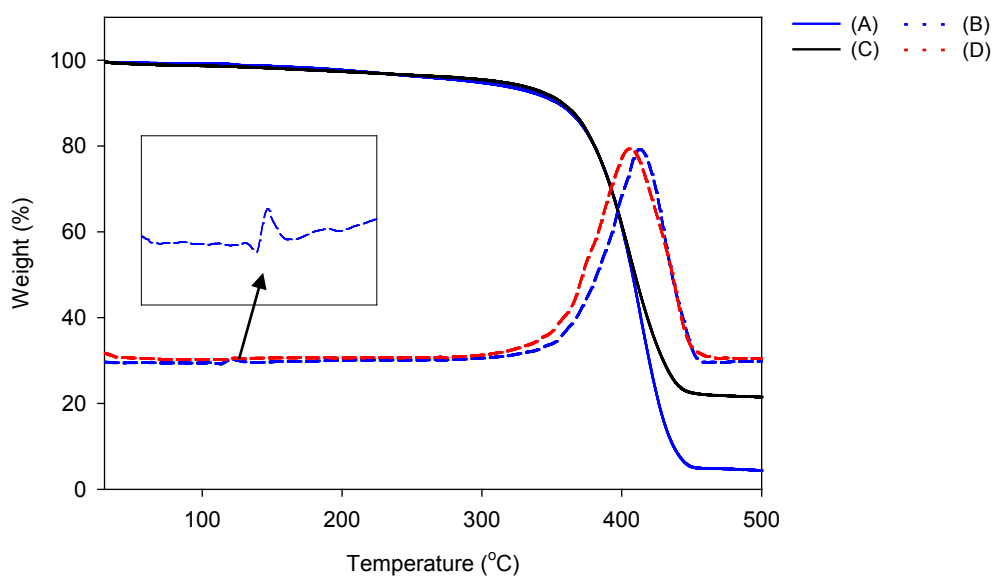
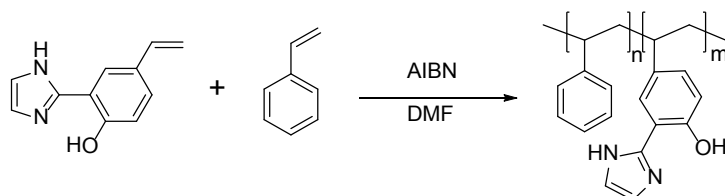


Figure 5.19 TG curves for (A) p(ST-co-VIM) and (C) p(ST-co-VIM)-VO and DTG curves for (B) p(ST-co-VIM) and (D) p(ST-co-VIM)-VO; at a heating rate of $10\text{ }^{\circ}\text{C}\cdot\text{min}^{-1}$ under N_2 . Insert shows an expanded view of the region between 30 - 200 $^{\circ}\text{C}$

(c) *Poly(styrene-co-vpim) fibers*

The p(ST-co-VPIM) copolymer was prepared by polymerization of vpim and styrene (**scheme 5.4**). Unlike the method used to prepare p(ST-co-VIM), however, a solvent (DMF) was added to the mixture of monomers since vpim was not sufficiently soluble in styrene alone. This also illustrated the advantages with this type of polymerization approach over suspension polymerization (**Part 2, Chapter 4**) which limits one to only a few solvent options (those immiscible with water).



Scheme 5.4 Synthesis of p(ST-co-VPIM) copolymer

Microanalysis indicated a ligand-to-styrene ratio of approximately 1:10. This ratio provided a balance of solubility in the electrospinning solvent as well as adequate ligand incorporation. The polymer was once again dissolved in a mixture of DMF/THF and electrospun as before. The relationship between polymer concentration (and hence viscosity) and fiber diameter is well illustrated in **figure 5.20**. At high concentrations, the fibers were quite large (average diameter of 3.8 μm) but as the concentration was reduced, fibers of much lower diameter were produced (0.6 μm using 8 wt%).

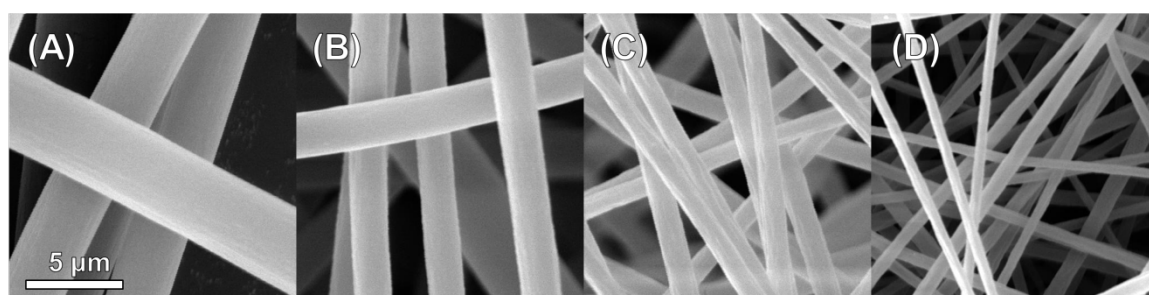


Figure 5.20 SEM images of fibers produced by electrospinning p(ST-co-VPIM) at concentrations (wt/v%) of (A) 20% ($\text{Ø} = 3.8 \mu\text{m}$), (B) 15% ($\text{Ø} = 2.3 \mu\text{m}$), (C) 10% ($\text{Ø} = 1.0 \mu\text{m}$) and (D) 8% ($\text{Ø} = 0.6 \mu\text{m}$) at the same magnification. Ø Indicates average diameter

The smaller size of the p(ST-co-VPIM) fibers electrospun from 8% solution (0.6 μm), compared to the larger p(ST-co-VIM) fibers (> 1.3 μm), had very little effect on the measured BET surface area. In fact, the surface area of the smaller fibers was less than that of the larger p(ST-co-VIM)-based fibers discussed earlier (b). For p(ST-co-VPIM) the surface area was 47.9 $\text{m}^2 \cdot \text{g}^{-1}$ while the pore volume and size were 0.49 $\text{cm}^3 \cdot \text{g}^{-1}$ and 416 Å. As was observed for the p(ST-co-VIM)-based fibers, functionalization of p(ST-co-VPIM) with vanadyl resulted in an increase in overall surface area to 60.7 $\text{m}^2 \cdot \text{g}^{-1}$ for p(ST-co-VPIM)-VO. The volume and size for p(ST-co-VPIM)-VO were 0.53 $\text{cm}^3 \cdot \text{g}^{-1}$ and 348 Å, respectively.

The smaller fibers (from 8% solution) were immersed in VO_2 as previously mentioned. These fibers were then reacted with a solution containing pimBr to create the neutral *bis*-coordinated complex. The amount of vanadium in these p(ST-co-VPIM)-VO fibers was significantly lower at 0.69%, as determined by ICP. This corresponded to a vanadium-to-ligand ratio of approximately

1:6. This coupled with the absence of sulfate (by microanalysis, XPS, and IR) suggests the formation of a *bis*-coordinated neutral complex along with some pendant ligands. Comparing the infrared spectra of polystyrene, vpim and the p(ST-co-VPIM) copolymer (**figure 5.21**), one can clearly see the presence of the 2-(2'-hydroxyphenyl)imidazole relevant stretches in the copolymer as illustrated by the highlighted regions in **figure 5.21**. The $\nu(\text{V}=\text{O})$ was not easily visible and was probably hidden beneath a more intense band. It was, however, visually detectable that vanadium was bound due to the definite colour change from light brown in the p(ST-co-VPIM) fibers, to a blue-green in the p(ST-co-VPIM)-VO fibers (**figure 5.22**). The presence of vanadium was further confirmed by ICP and XPS.

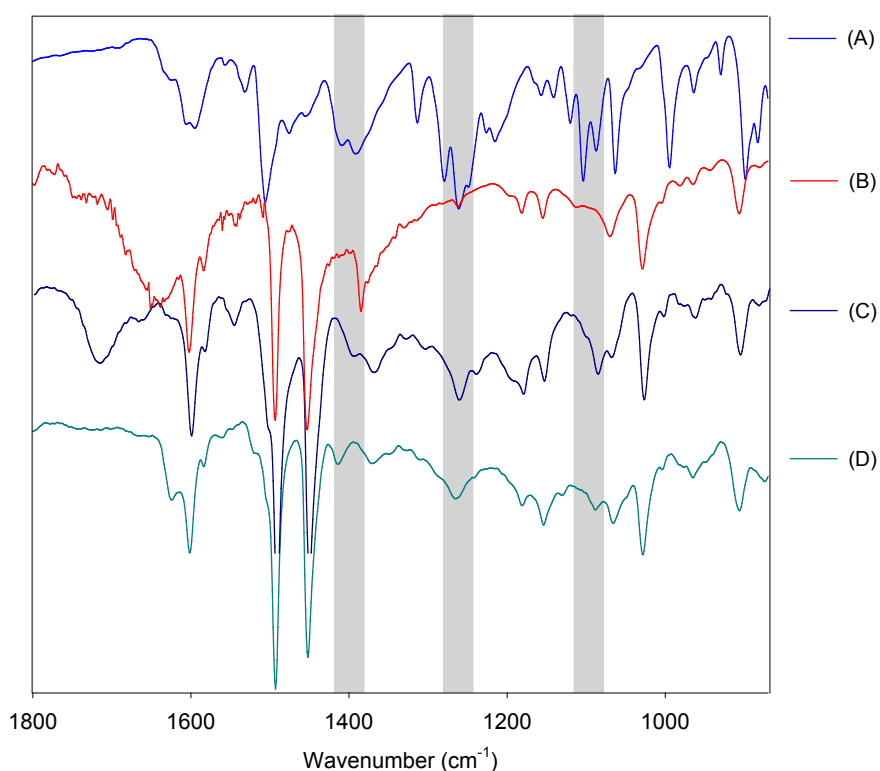


Figure 5.21 IR spectra of (A) vpim (B) polystyrene (C) p(ST-co-VPIM) (D) p(ST-co-VPIM)-VO. Highlighted regions illustrate bands common to (A), (C) and (D).



Figure 5.22 Digital images of p(ST-co-VPIM) (left) and p(ST-co-VPIM)-VO fibers (right) showing the significant colour change upon functionalization

The XPS spectra (**figure 5.23**) once again complimented the microanalysis results, showing all the expected atoms. After functionalization with vanadium, the O 1s peak intensity increased significantly, due to the V=O as well as possibly the presence of some residual solvent. The V 2p peaks although low in intensity were present at 522 (V 2p_{1/2}) and 515 eV (V 2p_{3/2}) (**table 5.3**), confirming the +4 oxidation state of vanadium. Only qualitative characterization was possible due to the low intensity of the peaks.

Table 5.3 Elemental binding energies of p(ST-co-VPIM) and p(ST-co-VPIM)-VO as determined by XPS

Polymer	Binding Energy (eV)					
	O 1s	N 1s	C 1s	V 2p _{3/2}	V 2p _{1/2}	S 2p _{3/2}
p(ST-co-VPIM)	531	404	285	-	-	-
p(ST-co-VPIM)-VO	531	404	285	515	522	-

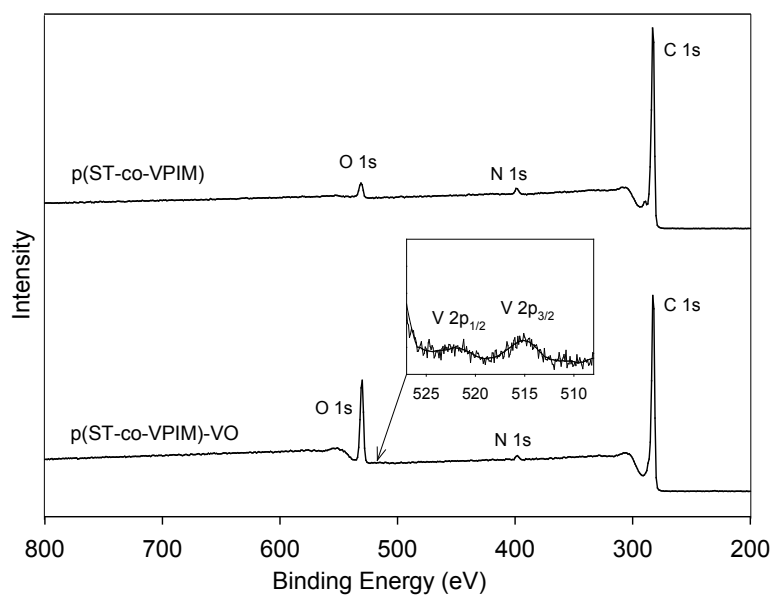


Figure 5.23 Wide scan XPS spectra of p(ST-co-VPIM) and p(ST-co-VPIM)-VO. Insert shows an expanded view of the V 2p signals of p(ST-co-VPIM)-VO

Thermogravimetric analysis of p(ST-co-VPIM) and p(ST-co-VPIM)-VO was performed and the relevant curves can be found in **figure 5.24**. The T_{\max} for p(ST-co-VPIM) was 413 °C compared to pure polystyrene which had a T_{\max} of 401 °C. The oxovanadium(IV)-functionalized, p(ST-co-VPIM)-VO fibers, displayed a significantly different decomposition profile (**figure 5.24**). Onset of decomposition of this polymer began lower ($T_{\text{onset}} = 297$ °C; $T_{\max} = 343$ °C) than that of the unmetallated derivative ($T_{\text{onset}} = 336$ °C; $T_{\max} = 413$ °C). In addition, decomposition of oxovanadium(IV) began at just below 400 °C. As was observed for p(ST-co-VIM)-VO (**figure 5.18**) the oxovanadium-functionalized fibers, p(ST-co-VPIM)-VO had a higher remaining mass (~10.6%) compared to the un-metallated p(ST-co-VPIM) fibers (~6.7%) due to residual V_2O_5 .

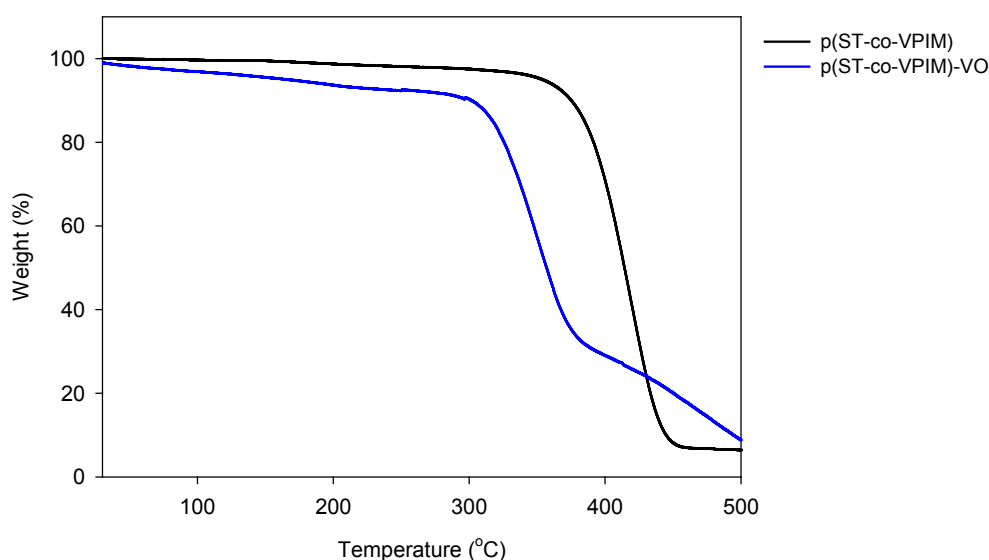


Figure 5.24 TG curves for p(ST-co-VPIM) and p(ST-co-VPIM)-VO at a heating rate of $10\text{ }^{\circ}\text{C}\cdot\text{min}^{-1}$ under N_2

(d) Polybenzimidazole fibers

First manufactured by Celanese Corporation, polybenzimidazole (PBI) (**figure 5.25**) has been recognized for its exceptional thermal and chemical resistance (see **table 5.4** and **table 5.5**).³² This in combination with its excellent textile processing characteristics has made this polymer a common choice for use in fire-protective fabrics, friction products and fire-blocking substrates in aircraft. The advantages of using this polymer over the polystyrene-based polymers are immediately apparent. The concern of organic solvents dissolving the fibers can be mostly dismissed (chemical stability), the robustness (mechanical stability) is improved and catalysis can be conducted at much higher temperatures due to the thermal stability of the polymer. Additionally, this polymer contains the metal-coordinating benzimidazole group which has been exploited in the past.^{33,34} Thus, PBI fibers possess all the desired characteristics of a catalytic support material. Until now however, only the microspherical form of polybenzimidazole has been used as a catalyst support material, albeit with great success.³³⁻³⁷

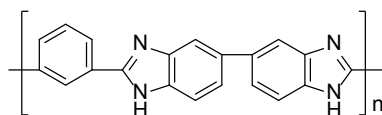


Figure 5.25 Chemical structure of polybenzimidazole

Table 5.4 Tensile strength of PBI fibers* after immersion in inorganic acids and bases³²

Compound	Concentration (%)	Temperature (°C)	Time (h)	Tensile strength retained (%)
Sulfuric acid	50	30	144	90
Sulfuric acid	50	70	24	90
Hydrochloric acid	35	30	144	95
Hydrochloric acid	10	70	24	90
Nitric acid	70	30	144	100
Nitric acid	10	70	48	90
Sodium hydroxide	10	30	144	95
Sodium hydroxide	10	93	2	65
Potassium hydroxide	10	25	24	88

* PBI fibers from Celanese Corporation

Table 5.5 Tensile strength of PBI fibers* after immersion in organic chemicals^{†32}

Compound	Strength retention (%)
Acetic acid	100
Methanol	100
Perchloroethylene	100
Dimethylacetamide	100
Dimethylformamide	100
Dimethylsulfoxide	100
Kerosene	100
Acetone	100
Gasoline	100

* PBI fibers from Celanese Corporation

† All exposures at 30 °C for 168 hours

To prepare the PBI fibers, a spinning solution was first prepared by refluxing PBI and LiCl in *N,N*-dimethylacetamide (DMAc) for 5 hours under argon. The LiCl has been shown to improve the shelf life of PBI solutions from a few days to several months and may also improve electrospinnability of polymers by enhancing the conductivity of the solution.^{38,39} After cooling to room temperature, the mixture was centrifuged. The spinning solution was then carefully decanted into a syringe, leaving the undissolved PBI pellet behind thus making the final concentration slightly less than 20 wt% (wt/v%). Several electrospinning parameters were adjusted until a stable jet was achieved. These parameters included; applied voltage, tip-to-collector distance, flow rate and the type of collector used. When a static metal plate collector was used, the fibers did not collect evenly over the surface of the plate but rather began to 'climb' towards the spinneret. This problem could not be attributed to a high flow rate since it was quite low ($0.15 \text{ mL}\cdot\text{h}^{-1}$) and may have been due to overvoltage.⁴⁰ This difficulty was circumvented when using a rotating drum collector which also allowed for partial alignment of the fiber rendering the mat much stronger in the rotation direction. At low applied voltages (<15 kV), droplets rather than fibers formed, likely due to insufficient charges present and hence an inability to overcome the surface tension of the solvent. Similarly, at high flow rates, both fibers and droplets formed. While other research groups have found distances of 6-7 cm to be effective for electrospinning PBI,^{38,40} we found 12 cm to give the most stable jet. Given that DMAc is a high boiling point solvent (bp $\sim 164 \text{ }^\circ\text{C}$), this extra distance may also improve solvent evaporation. Although not controlled in this study, the ambient humidity noticeably affected the stability of the polymer jet. The optimal conditions were obtained when using an applied voltage of 15 kV (and -5 kV underneath the rotating drum), a tip-to-collector distance of 12 cm and a flow rate of $0.15 \text{ mL}\cdot\text{h}^{-1}$.

Following electrospinning, the sheet of fibers was peeled off the aluminium foil, sandwiched between two pieces of filter paper (to keep the mat flat) and soaked in methanol overnight to remove residual solvent and LiCl. The texture of the polybenzimidazole nanofibers was markedly different from the polystyrene-based variations. The polystyrene-based fibers were fluffy, almost cotton-wool like, while the PBI-fibers were smooth and the sheet resembled thin paper.

The morphology of PBI electrospun nanofibers was investigated by scanning electron microscopy (SEM) (**figure 5.26**). The average fiber diameter was found to be 262 nm ($n = 25$), with a relatively broad range of 120 nm to 430 nm. Similar results were reported by both Weber⁴⁰ and

Reneker.³⁸ The specific surface area (BET) was significantly lower for the PBI fibers (7.5 and 7.7 $\text{m}^2\cdot\text{g}^{-1}$ for PBI_f and $\text{PBI}_f\text{-VO}$, respectively) than for the polystyrene-based fibers despite their smaller diameters. The BJH pore volume and size were 0.041 $\text{cm}^3\cdot\text{g}^{-1}$ and 232 Å for PBI_f and 0.052 $\text{cm}^3\cdot\text{g}^{-1}$ and 228 Å for $\text{PBI}_f\text{-VO}$. As we have come to see, the porosity of these materials contributed significantly to the experimentally determined surface areas. Thus perhaps the most reasonable explanation for these reduced surface areas would be due to the presence of fewer pores and smoother surface compared to the polystyrene-based polymers.

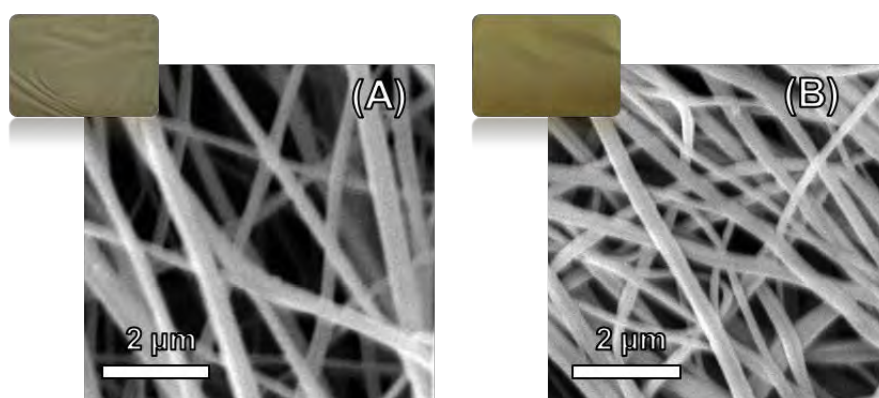


Figure 5.26 SEM images and photographs (insert) of (A) PBI_f and (B) $\text{PBI}_f\text{-VO}$ fibers

Infrared analysis (**figure 5.27**) of PBI_f clearly showed the presence of the imidazole N-H stretch at 3400 cm^{-1} as well as the expected benzimidazole ring stretching vibrations between $1635\text{-}1500\text{ cm}^{-1}$.⁴¹ An O-H stretch at 3619 cm^{-1} was due to absorbed water owing to the hygroscopic nature of PBI. After reacting PBI_f with vanadyl sulfate several new bands appeared including the $\nu(\text{V}=\text{O})$ at 978 cm^{-1} along with an intense split band at 1103 and 1036 cm^{-1} corresponding to the ν_3 sulfate stretching vibrations suggesting monodentate coordination of this ion.⁴² Microanalysis also confirmed the presence of sulfur in the polymer. The vanadium content, as determined by ICP-OES, was found to be 5.5% which corresponds to a V/N ratio of 1:6 (or 1 vanadium per 3 benzimidazole groups).

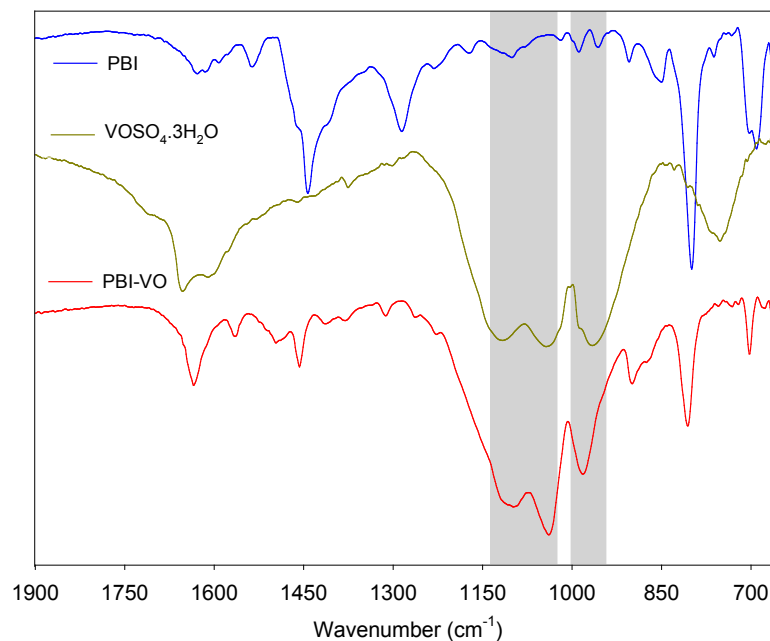


Figure 5.27 IR spectrum of PBI_f, VOSO₄ and PBI_f-VO fibers

Wide scan XPS spectra of PBI_f and PBI_f-VO shown in **figure 5.28** confirm surface modification of the fibers. For PBI_f-VO, the peaks corresponding to the S 2p, V 2p_{3/2} and V 2p_{1/2} binding energies appeared at 166, 515.2 and 522.6 eV, respectively (**table 5.6**).

Table 5.6 Elemental binding energies of PBI_f and PBI_f-VO as determined by XPS

Polymer	Binding Energy (eV)					
	O1s	N1s	C1s	V2p _{3/2}	V2p _{1/2}	S2p _{3/2}
PBI _f	531	405, 399, 396	285	-	-	-
PBI _f -VO	531	399, 396	285	515	523	166

The V 2p_{3/2} binding energy further confirmed the +4 oxidation state of vanadium (**figure 5.28**).³⁰ There were three resolvable N 1s peaks for PBI_f appearing at 405, 399 and 396 eV (**figure 5.29**). The more intense peak at 399 eV corresponds to the N-H (amine) nitrogen while the remaining two peaks at 396 and 405 eV correspond to the C=N (imine) nitrogen in the non-protonated and protonated form, respectively.⁴³ Upon coordination, however, the peak at 405 eV disappeared

completely while the peak at 396 eV was significantly diminished (**figure 5.29**), confirming coordination of vanadyl via the azomethine nitrogen. The observed O 1s peak for PBI_f is most likely due to absorbed water, the presence of which was confirmed by IR.

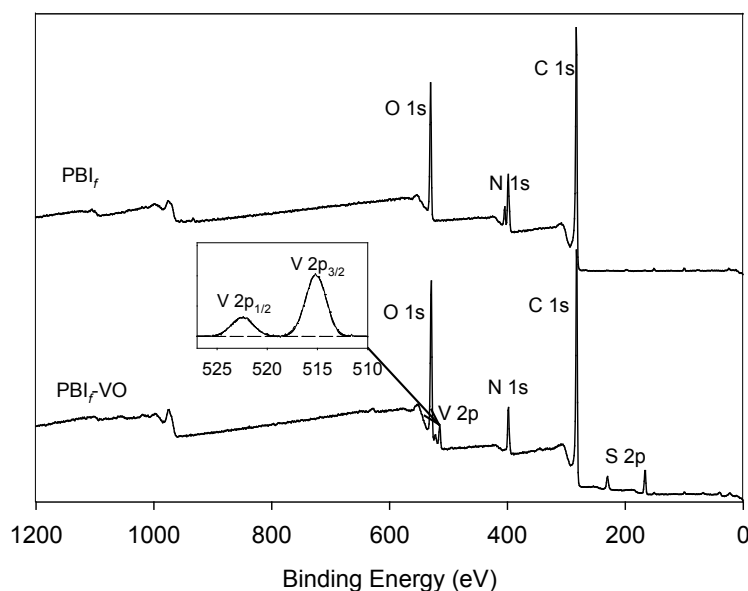


Figure 5.28 Wide scan XPS spectra of PBI_f and PBI_f-VO fibers. Insert shows an expanded view of the V 2p signals of PBI_f-VO

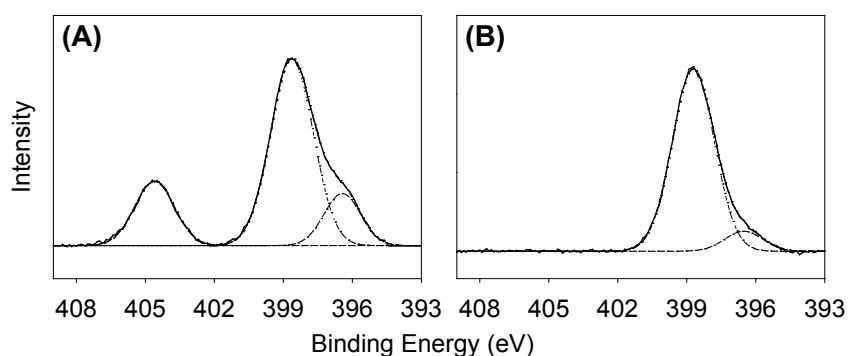


Figure 5.29 High resolution XPS spectra of (A) N1s signal for PBI_f and (B) N1s signal for PBI_f-VO

Thermogravimetric analysis of PBI_f and PBI_f-VO was conducted under a nitrogen atmosphere in a temperature range of 30 – 800 °C (**figure 5.30**). For PBI_f, three distinct weight losses were observed at below 105 °C, between 220 – 320 °C and finally between 570 – 800 °C. The first two

weight loss may be due to loss of loosely bound and coordinated water molecules or solvent, since it is well known that PBI readily absorbs moisture even after extensive drying.^{44,45} As has been reported by others,^{45,46} it was only at temperatures of over 570 °C that the polymer backbone began to degrade demonstrating the excellent thermal stability of PBI. For PBI_f-VO there were once again three distinct weight loss processes occurring (**figure 5.30**). As was the case for the un-metallated PBI_f fibers, the first weight loss occurred below 105 °C due to loss of water. The weight loss occurring between 270 – 490 °C, was however unique to the oxovanadium(IV) functionalized PBI_f-VO fibers and may be due to decomposition of the bound vanadium salt to V₂O₅.^{47,48}

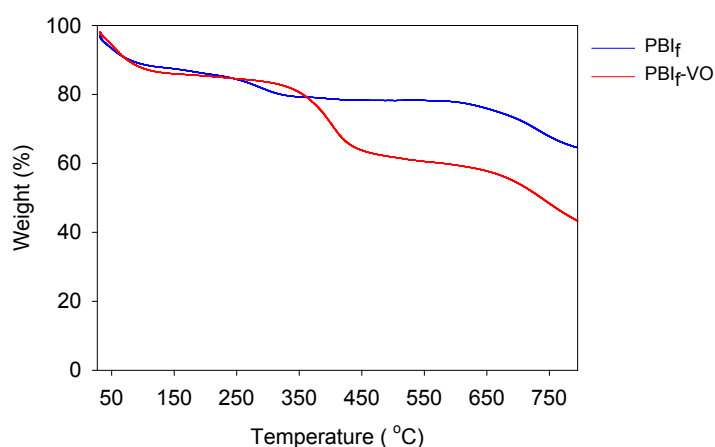


Figure 5.30 TG curves for PBI_f and PBI_f-VO at a heating rate of 10 °C.min⁻¹ under N₂

5.5.3 Catalytic activity

(a) Catalytic activity of [VO(dpimR)₂] and PS-[VO(dpimR)₂]

The activity of the homogeneous catalyst was first evaluated using a common batch reaction. The amount of catalyst and H₂O₂ was kept constant at 0.25 mol% and 2 equivalents (wrt. thioanisole) while the temperature was kept at 25 °C, since these conditions were found to be effective in earlier studies. It was observed that the electron withdrawing/donating substituents on the *para*-position of the phenol group of the ligand had a significant impact on the overall catalytic activity and selectivity. The nitro substituted homogeneous catalyst showed the best activity with a > 99% oxidation of thioanisole, being attained after just 10 minutes at 25 °C, compared to the electron donating MeO substituted catalyst, which achieved the same result in 60 minutes (**figure 5.31**).

The activity of the catalysts showed the following trend as described by their turnover frequencies (TOF); NO_2 (2400 h^{-1}) > Br (800 h^{-1}) > H (600 h^{-1}) > MeO (480 h^{-1}). Evidently, the introduction of electron withdrawing groups on the *para* position of the phenol group of the ligand seems to improve the activity perhaps by rendering the metal center electron deficient. The product selectivity was also dependent on the substituent groups. The milder MeO-substituted catalyst displayed higher selectivity towards the formation of methyl phenyl sulfoxide whereas the NO_2 -substituted derivative seemed to favour the formation of the sulfone, especially as time progressed. This was expected since the more active NO_2 -substituted derivative further oxidizes the sulfoxide to the sulfone. A table containing product selectivity and overall conversions for the catalysed reactions has been included (**table 5.7**).

When the solvent mixture was changed from pure CH_3CN to a mixture of $\text{CH}_3\text{CN}/\text{H}_2\text{O}$ the conversion dropped slightly, while the selectivity shifted slightly to favour the formation of sulfone (**table 5.7**). In the absence of catalyst low conversions were obtained (less than 25%).

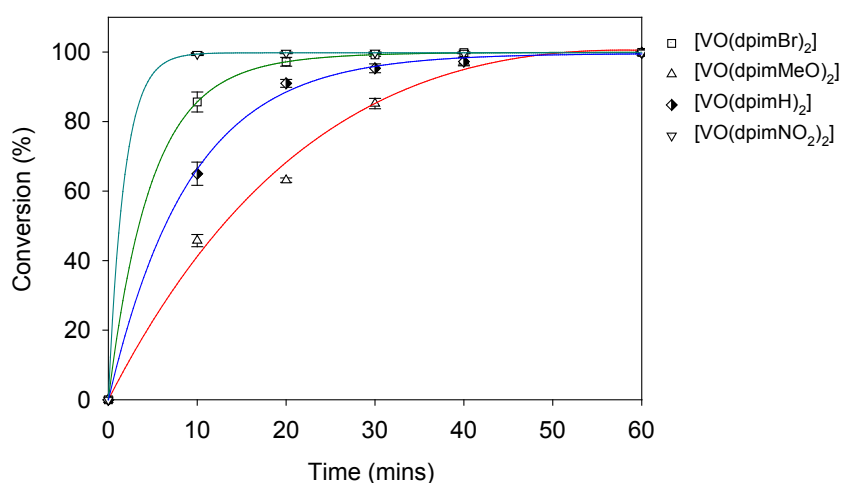


Figure 5.31 Ligand substituent effects on catalytic activity. Conditions: Catalyst (0.25 mol% wrt thioanisole), thioanisole (10 mmol), H_2O_2 (20 mmol), CH_3CN (20 mL), and at 25°C

The catalytic fibers, PS-15-[VO(dpimMeO)₂] and PS-15-[VO(dpimNO₂)₂], were then subjected to a batch-type experiment (**figure 5.32**). The trend in overall conversion observed for these heterogeneous catalysts was quite similar to that of the homogeneous counterparts, with the nitro-substituted analogue displaying greater activity than the methoxy-substituted analogue.

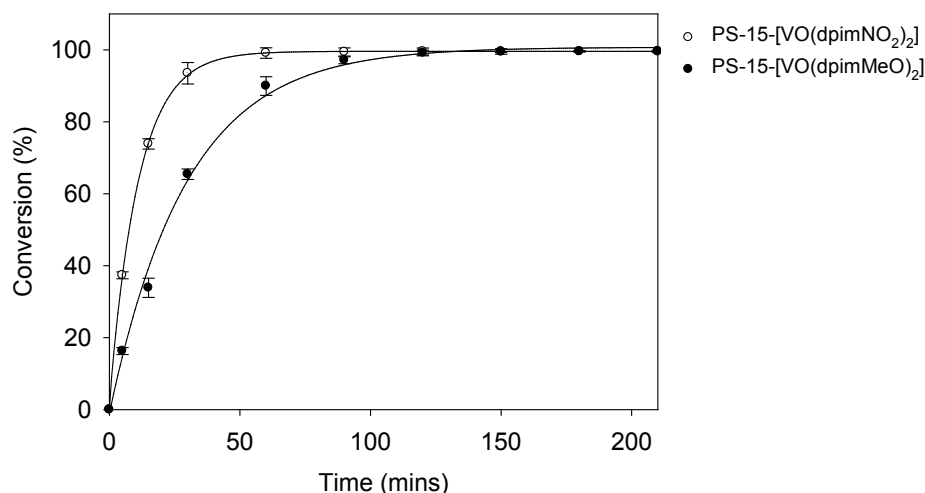


Figure 5.32 Oxidation of thioanisole under batch conditions using PS-15-[VO(dpimMeO)₂] and P S-15-[VO(dpimNO₂)₂]. Conditions: Catalyst (0.01 g), thioanisole (1 mmol), H₂O₂ (2 mmol), CH₃CN (20 mL), and at 25 °C

Unfortunately, the stirring process in the batch reaction caused the fibers to break, making separation and hence recycling difficult. This challenge was avoided when using a continuous flow process. This reactor set-up was more suited to the highly flexible and porous nature of the fiber-mats.

Since the oxovanadium complexes were highly insoluble in water and slightly soluble in CH₃CN, the solvent used in the subsequent catalyzed reactions was changed to a mixture of CH₃CN/water (1:1), rather than pure CH₃CN to limit leaching from the polymer. The effect of the flow rate, fiber diameter and catalyst type on the reaction was investigated. Only PS-15/25-[VO(dpimMeO)₂] and PS-15/25-[VO(dpimNO₂)₂] were studied, since [VO(dpimMeO)₂] and [VO(dpimNO₂)₂] were the least and the most active homogeneous catalysts respectively. Restricting the study to these two catalysts would still show if the same trend in activity would exist, without additional unnecessary experiments.

The reactant solution consisting of thioanisole, H₂O₂ and the solvent were passed through the fibrous mat at a few different flow rates. An increase in flow rate from 0.5 mL.h⁻¹ to 1 mL.h⁻¹ resulted in an improvement in overall conversions but a further increase to 1.5 mL.h⁻¹ resulted in a moderate drop in conversion and so subsequent reactions were performed at 1 mL.h⁻¹ (**table 5.7**). The different diameters of the fibers (0.33 μm and 1.37 μm for PS-15-[VO(dpimMeO)₂] and PS-

25-[VO(dpimMeO)₂] respectively, and 0.51 μm and 1.98 μm for PS-15-[VO(dpimNO₂)₂] and PS-25-[VO(dpimNO₂)₂] respectively) had no observable effect on catalytic activity and thus subsequent studies were performed using the PS-15-[VO(dpimR)₂] fibers. As shown in **figure 5.33**, PS-15-[VO(dpimNO₂)₂] showed good catalytic activity, with the conversion of thioanisole remaining above 93% over the 10 h (or 10 mL) period studied. As was the trend with the homogeneous catalysts, PS-15-[VO(dpimMeO)₂] was also slightly less active than PS-15-[VO(dpimNO₂)₂] with conversions dropping to 87.7 % in the 10th fraction. The greater activity of the NO₂-substituted catalysts similarly resulted in slightly higher formation of the sulfone compared to the MeO-substituted catalyst, for the same reason as discussed for the homogeneous catalysts. When using un-functionalized polystyrene fibers (PS-25) a maximum conversion of 22.9% was obtained on the last fraction confirming that the presence of the catalyst is crucial for these oxidation reactions. More data regarding the effect of the above mentioned conditions on selectivity and overall conversion may be found in **table 5.7**.

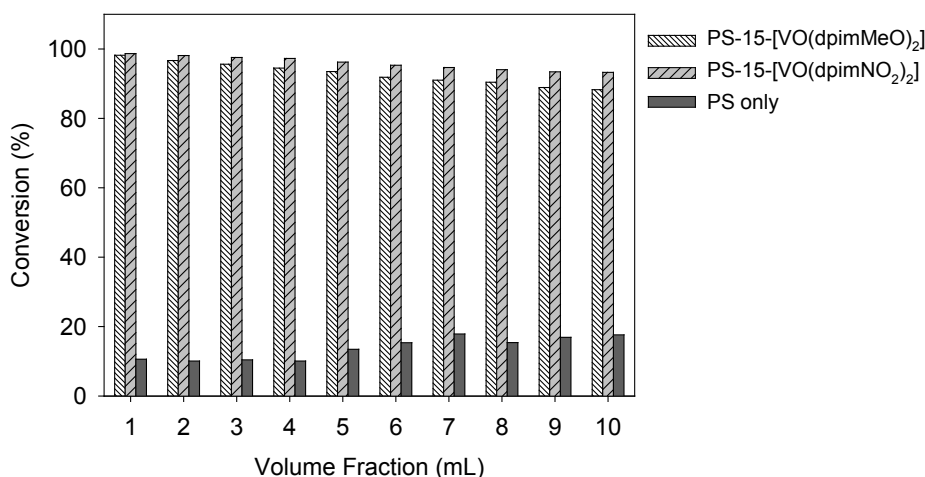


Figure 5.33 Oxidation of thioanisole under continuous flow conditions. Conditions: thioanisole (50 mM), H₂O₂ (100 mM), PS-15-[VO(dpimNO₂)₂] (0.01 g) and PS-15-[VO(dpimMeO)₂] (0.01 g) of catalyst in 1:1 CH₃CN/H₂O; flow rate (1 mL.h⁻¹) and at 25 °C

For both heterogeneous catalysts, the activity drops slightly after time and for this reason the leaching of vanadium from the polymer was quantified. Each of the 1 mL product fractions collected from the continuous flow system were evaporated to dryness. The remaining residue was digested in 0.5 mL of nitric acid (UltraPure, 69%) for 24 hours and diluted with deionised

water to a total volume of 15 mL. This solution was passed through a Millipore filter (0.45 μM) and analysed by ICP-OES. An average of 3.8(\pm 1.4)% of vanadium was lost in each fraction, thus about 38% of vanadium was leached from the polymer over the 10 h period. This also probably means that a large proportion of the observed activity can be credited to the leached, homogeneous catalyst. UV/Vis studies suggested that the leached species was a vanadium(V) species (d^0) due to the disappearance of the d-d transitions expected for a square pyramidal oxovanadium(IV) species (d^1). This study confirmed our initial suspicions that leaching would be a major problem when relying on weak forces such as π - π stacking alone. However, this provided us with a benchmark upon which we could subsequently improve on. Thus, all subsequent studies were performed using covalently-linked systems.

Table 5.7 Selected overall conversion and product selectivity data for the oxidation of thioanisole using homogeneous oxovanadium(IV) complexes (0.25 mol% wrt thioanisole) as well as the catalytic fibers PS-15-[VO(dpimNO₂)₂] and PS-15-[VO(dpimMeO)₂] (0.1 g of fibers)

<i>Homogeneous Catalysts</i>				
Catalyst	Sulfoxide (%)	Sulfone (%)	Max. Conversion (%)	TOF (h⁻¹)[*]
[VO(dpimH) ₂]	61.3	38.2	99.7	600
[VO(dpimBr) ₂]	63.9	35.9	99.9	800
[VO(dpimMeO) ₂]	68.2	31.5	99.8	480
[VO(dpimNO ₂) ₂]	54.1	45.8	99.9	2400
<i>Heterogeneous fibers - Continuous Flow</i>				
Catalyst	v (mL.h⁻¹)	Sulfoxide (%)	Sulfone (%)	Avg.Conv (%)
PS-15-[VO(dpimNO ₂) ₂]	1.0	65.9	31.92	95.8
PS-15-[VO(dpimMeO) ₂]	1.0	67.9	25.46	92.8
PS-15-[VO(dpimNO ₂) ₂]	0.5	61.9	32.33	94.3
PS-15-[VO(dpimMeO) ₂]	0.5	65.5	27.79	93.5
PS-15-[VO(dpimNO ₂) ₂]	1.5	66.3	19.36	85.7
PS-15-[VO(dpimMeO) ₂]	1.5	62.9	19.20	82.1

* Determined as moles of substrate converted/moles of vanadium/time (h)

(b) *Catalytic activity of p(ST-co-VIM)-VO fibers*

Based on the high leaching of the PS-[VO(dpimR)₂] fibers [5.5.3 (a)] and the promising results of the imidazole functionalized microspheres (Part 2, Chapter 4), covalently linked imidazole functionalized polystyrene-co-vinylimidazole copolymers were prepared as a starting point for improvement. As mentioned earlier, for a polymer to be electrospun, it must be soluble in some solvent or form a melt. This consequently means that the resultant fibers will be soluble in the same solvents unless some sort of post-electrospinning cross-linking strategy is utilized.^{49,50} For this reason methanol was selected as the solvent to be used in the fiber-catalyzed reactions since methanol did not dissolve or change the fiber morphology in any way. When placed in acetonitrile or even in an acetonitrile/water mixture however, these p(ST-co-VIM) fibers lost structural integrity as shown in the SEM image (figure 5.34). As demonstrated with the microspherical beads (Part 2, Chapter 4), methanol was not an ideal solvent for the oxidation of thioanisole, and so this solvent choice was governed by solubility constraints. Other solvents were considered but since the polymer was soluble in several organic solvents (chloroform, dichloromethane, toluene etc), methanol was the preferred choice of solvent for the oxidation reactions with the polystyrene fibers.

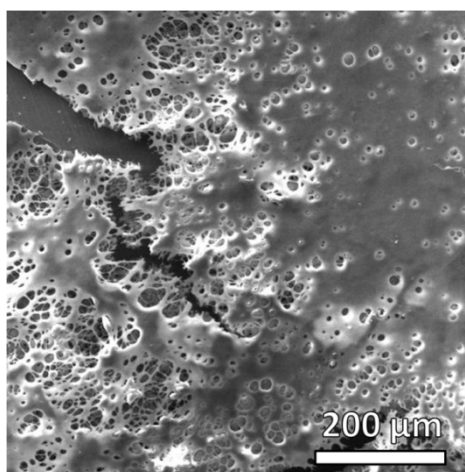


Figure 5.34 SEM image of deformed electrospun polystyrene fibers after being placed in acetonitrile

For reasons discussed earlier (in 5.3.1), the fibers were applied in a continuous flow type reactor set-up rather than a batch set-up. The effect of the amount of catalyst packed into the syringe was

first investigated (**figure 5.35**). It was only at very low catalyst amounts (0.005 g) that any drop in activity was observed over the period studied. This drop in activity may have been due to leaching of the vanadium from the fibrous support material which would have had a more pronounced effect when using lower catalyst amounts - the leaching behaviour was studied and shall be discussed later. Another possibility for the drop in activity may be due to saturation of the catalytic sites.

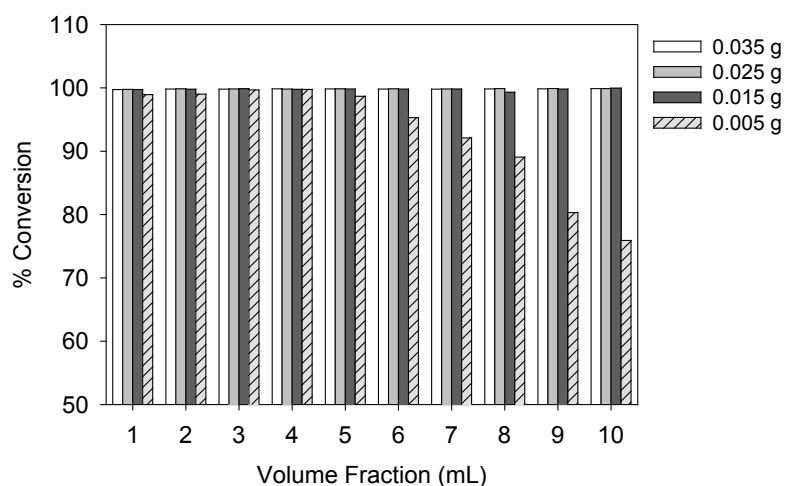


Figure 5.35 The effect of the amount of catalyst on overall conversion. Conditions: p(ST-co-VIM)-VO, H₂O₂ (2 mmol), thioanisole (1 mmol), methanol (10 mL), flow rate (1 mL.h⁻¹) and at 25 °C

Besides catalyst amount, another important parameter to be considered when conducting continuous flow reactions is the flow rate, i.e. the speed at which the reactant solution was passed through the catalyst bed. This was, in our case, carefully controlled using a syringe pump. As shown in **figure 5.36**, the flow rate was varied between 1 mL.h⁻¹ and 6 mL.h⁻¹. At the higher flow rate, less time was available for the reactant solution to interact with the catalyst bed and this resulted in a significant drop in activity at a flow rate of 6 mL.h⁻¹. Furthermore, the selectivity shifted towards the formation of the sulfoxide as the flow rate increased (**table 5.8**). By altering the catalyst amount and flow rate one can begin to shift the selectivity to either the sulfoxide (lower catalyst amounts or higher flow rates) or the sulfone (low flow rate, high catalyst amounts) depending on which product is desired. A table summarizing these results has been included (**table 5.8**).

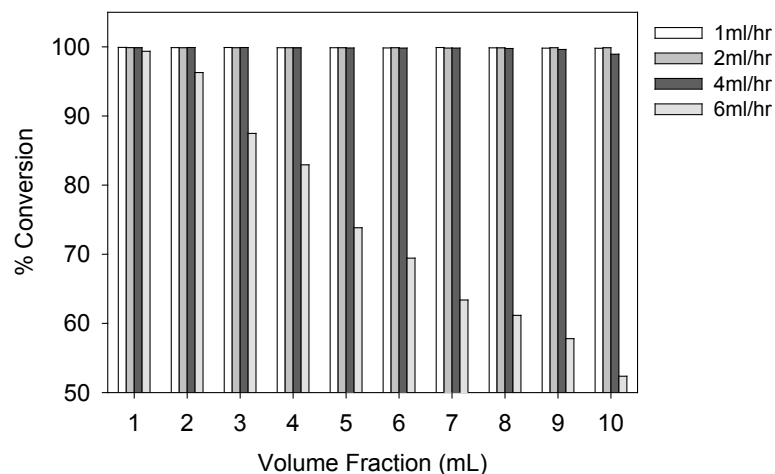


Figure 5.36 The effect of flow rate on overall conversion. Conditions: 0.025 g of p(ST-co-VIM)-VO, H₂O₂ (2 mmol), thioanisole (1 mmol), methanol (10 mL) and at 25 °C

Since the fiber-based catalysts still showed a drop in activity as time progressed (**figure 5.35**), we found it necessary to quantify the amount of vanadium leached from the fibers so that we could compare this with the non-covalently linked derivatives (PS-15-[VO(dpimR)₂]). Each 1 mL fraction of product solution that was collected was concentrated to remove any organic solvent. After digesting the remaining residue in nitric acid and diluting appropriately, the vanadium content was determined by ICP-OES. In the first fraction about 1.2 (±0.05)% of vanadium was detected. This decreased and then stabilized at around about 0.41 (±0.02)% (**figure 5.37**) making up a total amount of 7.18% (after combining the 10 mL fractions). Although still relatively high, this represents a huge improvement over the non-covalently linked counterpart.

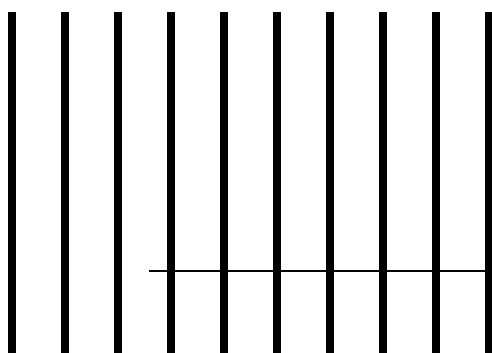


Table 5.8 Summary of reaction conversions and selectivities for p(ST-co-VIM)-VO catalyzed reactions under continuous flow set-up

Mass (g)	v (ml.h ⁻¹)	% Sulfoxide	% Sulfone	Average conversion*
Blank ^a	2	5.98	4.12	10.1
0.005	2	63.8	29.0	92.9
0.015	2	55.6	44.1	99.7
0.025	2	55.3	44.4	99.9
0.035	2	42.7	57.1	99.9
0.025	1	39.7	60.1	99.9
0.025	2	49.0	50.8	99.9
0.025	4	56.1	43.6	99.7
0.025	6	55.7	18.6	74.4

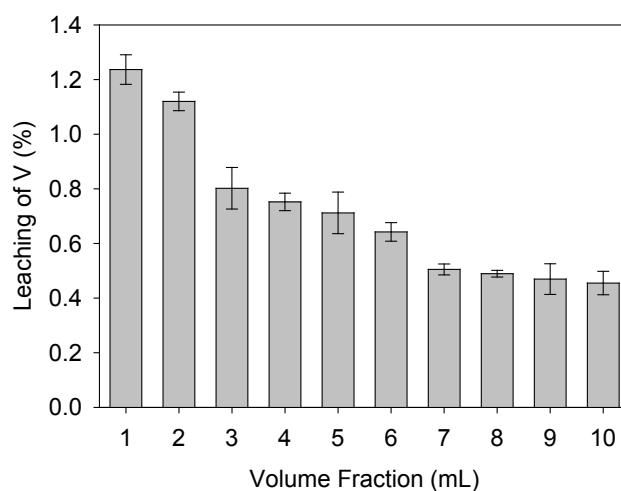


Figure 5.37 Vanadium leaching behaviour of p(ST-co-VIM)-VO. Conditions: p(ST-co-VIM)-VO (0.025g), thioanisole (1 mmol), H₂O₂ (2 mmol), methanol (10 mL), flow rate (2 ml.h⁻¹) (n = 3)

(c) Catalytic activity of p(ST-co-VPIM)-VO fibers

In an attempt to further reduce leaching, we decided to use a bidentate rather than a monodentate ligand in the hope that the additional chelate stability would improve leaching behaviour. The major issue was that the low solubility of the monomerized ligand resulted in a low incorporation in

the copolymer and thus low vanadium content. Initial trials using the continuous flow method developed for the before-mentioned systems proved unsuccessful. The larger amount of polymer fibers did not sit comfortably within the syringe, but swelled substantially and eventually came adrift. A new and improved device was designed which involved packing the fibers into a small column rather than placing them loosely at the end of the syringe – the device has been illustrated in **figure 5.38**. Furthermore, this device made more sense from a reproducibility and commercial standpoint.⁵⁰ Using this method under the optimized conditions gave excellent conversion throughout the 10 h period studied (**figure 5.39**). Reducing the mass of fibers from 0.1 g to 0.06 g resulted in lower, albeit fairly constant, conversions (**figure 5.40**). The fact that at this mass (0.06 g) there was no successive drop in overall conversion suggests that the decreased conversion was due to the lack of catalyst rather than catalyst leaching. Nevertheless, the leaching behaviour was studied and a total of 3.52% over the combined 10 h period was determined. There was, therefore, some improvement over the monodentate p(ST-co-VIM)-VO system in which a total leaching of 7.18% was determined. A summary of the product selectivity and overall activity of p(ST-co-VPIM)-VO has been included in **table 5.9**.



Figure 5.38 The modified column used in the continuous flow reactions, containing the p(ST-co-VPIM)-VO fibers (0.1 g)

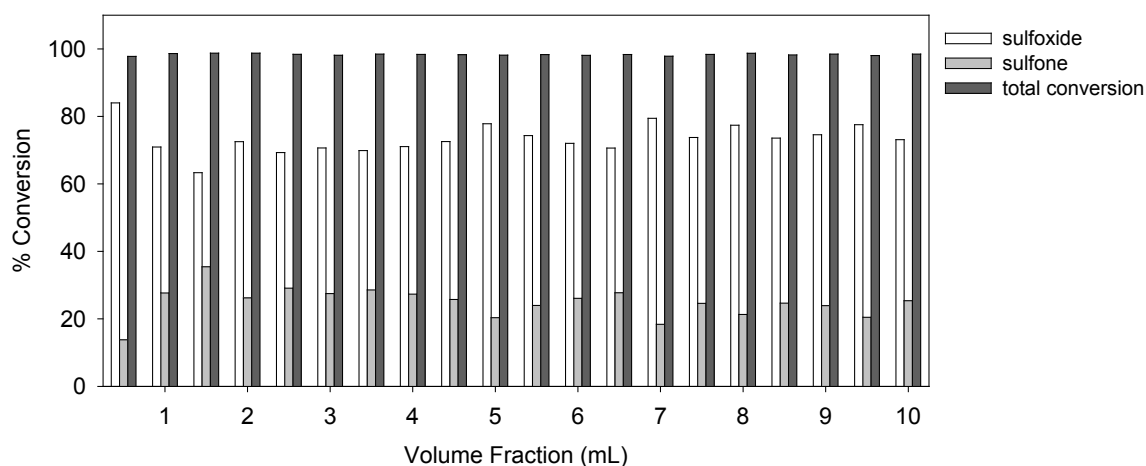


Figure 5.39 Continuous flow oxidation of thioanisole using p(ST-co-VPIM)-VO. Conditions: p(ST-co-VPIM)-VO (0.1 g), thioanisole (1 mmol), H₂O₂ (2 mmol), methanol (10 mL), flow rate (1 ml.h⁻¹) and at 25 °C

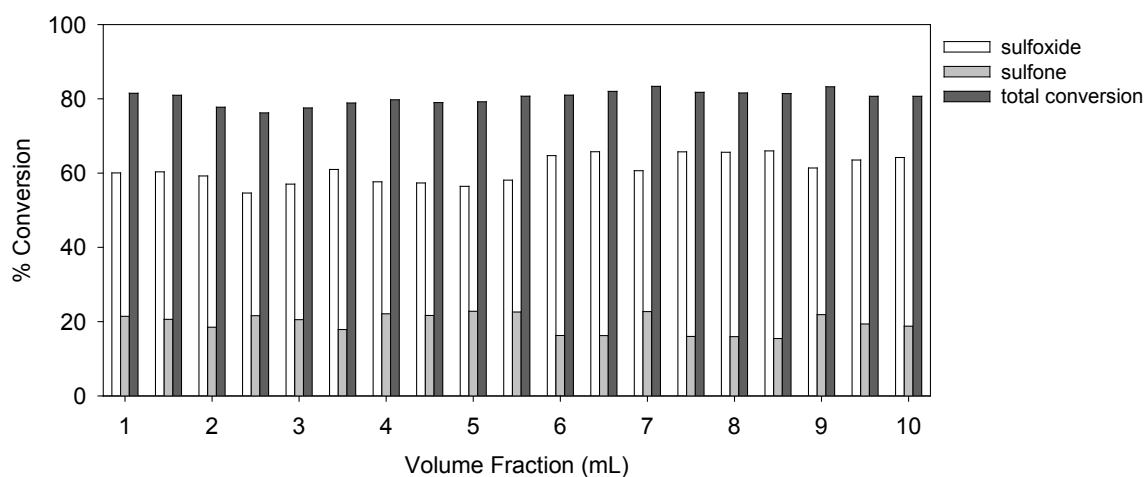


Figure 5.40 Continuous flow oxidation of thioanisole using p(ST-co-VPIM)-VO. Conditions: p(ST-co-VPIM)-VO (0.06 g), thioanisole (1 mmol), H₂O₂ (2 mmol), methanol (10 mL), flow rate (1 ml.h⁻¹) and at 25 °C

Table 5.9 Summary of reaction conversions and selectivities for p(ST-co-VPIM)-VO catalyzed reactions under continuous flow conditions

<i>Continuous Flow</i>				
Amount (mg)	v (ml.h⁻¹)	Sulfoxide (%)	Sulfone (%)	Avg.Conv (%)
60	1	60.92	18.96	79.6
100	1	73.41	24.91	98.3

(d) Catalytic activity of PBI_f-VO fibers

The significantly improved mechanical and chemical properties of the PBI_f fibers allowed us to carry out stirred-batch reactions without too much concern about fiber disintegration. The batch method was studied first to allow for quick optimization of reaction conditions.

The mass of the catalytically active fibers was varied from 0.010 g to 0.050 g. This equates to approximately 1.0 to 5.3 mol% of vanadium relative to thioanisole, respectively. At all catalyst masses, near quantitative conversions were obtained with TOF's of 88.39, 36.70 and 36.71 h⁻¹ for 0.010 g, 0.025 g and 0.050 g respectively. At the higher mass (0.050 g) however, the reaction was nearly complete in just 30 mins compared to 1 hour at the lower masses (0.010 and 0.025 g) (**figure 5.41**). When the oxovanadium-functionalized nanofibers were substituted with the unfunctionalized PBI nanofibers (PBI_f), a maximum conversion of 9.12% was observed after 90 mins, illustrating the catalytic effect of vanadium. The recyclability of the fibers was also investigated as shown in **figure 5.42**. An initial drop in activity was observed after the first cycle following which the conversion remained fairly constant. The leaching data corresponds quite well to this trend, with an initial leaching of 7.29% vanadium after the first reaction, followed by leaching of between 0.52 - 0.69% in the subsequent cycles, a similar trend to that observed by others.⁵²

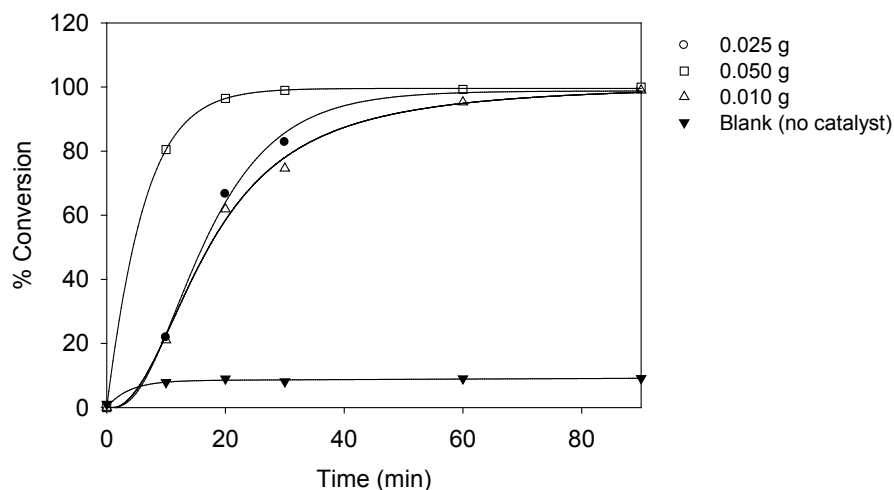


Figure 5.41 Effect of catalyst amount for the batch oxidation of thioanisole using PBI-VO. Conditions: PBI-VO, thioanisole (1 mmol), H₂O₂ (2 mmol), acetonitrile (20 mL), and at 25 °C

Despite the improved mechanical stability of the PBI fibers compared to the polystyrene-based fibers, after a few successive runs there was some catalyst break-up. The fine paper-like texture of the nanofiber mat was undeniably more suited to a continuous flow system rather than being subjected to mechanical agitation.

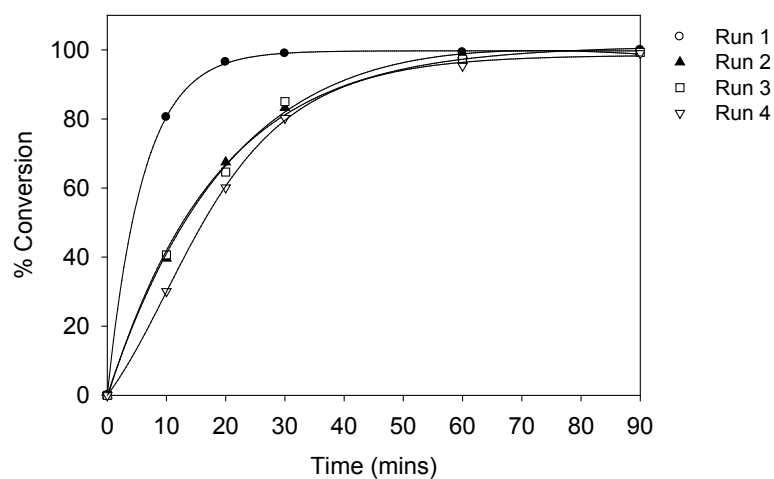


Figure 5.42 Recyclability for the batch oxidation of thioanisole using PBI-VO. Conditions: PBI-VO (0.05 g), thioanisole (1 mmol), H₂O₂ (2 mmol), acetonitrile (20 mL), and at 25 °C

Once again the method in which these fibers were applied was different to the other fiber-based catalysts. The more paper-like (rather than cottonwool-like for the polystyrene-based systems) texture of the PBI_r-VO fiber mat forced us to modify the continuous flow device. A Millipore filter holder proved to be an excellent holder for these fibers, and allowed them to be tightly compacted which was necessary since these fibers did not swell as much as the polystyrene-based fibers.

Since the larger mass of fibers (0.050 g) gave faster initial conversion under batch conditions (**figure 5.41**), this mass was used for the continuous flow reactions. As shown in **figure 5.43**, excellent conversion of thioanisole was obtained over the tested period. At flow rates of between 0.5 – 2 mL.h⁻¹, > 98% conversion was achieved. Furthermore, the product selectivity could be tuned by changing the flow rate. At a flow rate of 0.5 mL.h⁻¹, for example, the ratio of sulfoxide/sulfone was 0.41, while at a higher flow rate of 4 mL.h⁻¹ this shifted to 2.13, along with a slight drop in overall conversion (**table 5.10**). For comparative purposes, aliquots were withdrawn from the syringe before the reactant solution had passed through the catalyst bed, representing the un-catalyzed reaction. In the 5th, 10th and 20th fraction, a conversion of 9.0%, 9.3% and 9.4% respectively, was observed. This clearly demonstrated the success of the catalyst.

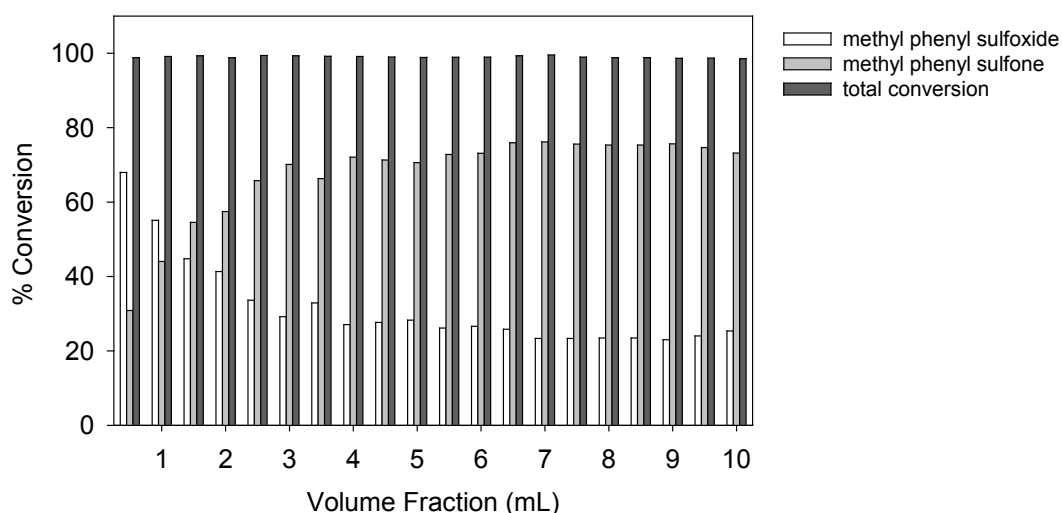


Figure 5.43 Continuous flow oxidation of thioanisole using PBI_r-VO. Conditions: PBI_r-VO (0.05 g), thioanisole (50 mM), H₂O₂ (100 mM) in acetonitrile, flow rate (1 mL.h⁻¹) and 25 °C

Leaching under continuous flow conditions was also monitored. Here, each of the individual fractions was combined, concentrated and diluted appropriately. Between 0.376% - 0.808%

vanadium leaching (combined over 10 mL) was recorded depending on the reaction conditions. This was by far the lowest leaching of all the fiber-based catalysts.

Table 5.10 Summary of reaction conversions and selectivities for PBI-VO catalyzed reactions under batch and continuous flow conditions

<i>Batch Reaction</i>				
Amount (mg)	Sulfoxide (%)	Sulfone (%)	Max. Conversion (%)	TOF (h⁻¹)*
50	67.23%	32.72%	99.95%	36.7
50 ^a	68.03%	31.44%	99.47%	18.3
50 ^b	70.36%	28.90%	99.27%	18.1
50 ^c	70.39%	28.51%	98.90%	17.7
25	68.23%	30.95%	99.18%	36.7
10	50.99%	47.99%	98.99%	88.4
<i>Continuous Flow</i>				
Amount (mg)	v (mL.h⁻¹)	Sulfoxide (%)	Sulfone (%)	Avg.Conv (%)
50	0.5	28.88	69.79	98.68
50	1.0	31.62	67.54	99.00
50	2.0	40.65	58.64	99.20
50	4.0	63.29	29.78	92.83

^aAfter one catalytic run; ^bAfter a second run; ^cAfter a third run; * Determined as moles of substrate converted / moles of vanadium / time (h)

5.6 Conclusions

The initial hypothesis when beginning this work was that reducing the diameter of the support material would result in higher surface areas and hence improved catalytic performance (i.e. when going from microspheres to fibers). However, the more delicate nature of the fibers (specifically the polystyrene-based fibers) meant that the simple batch reaction set-up that was used for the beads could not be applied to the fibers which disintegrated upon stirring. It was immediately apparent that direct comparison of the two different materials could not be performed due to the different reactor set-ups. The effect of fiber diameter did not seem to play a major role and thus was not thoroughly studied. Nevertheless, the ultrafine, flexible and porous structure of the fiber mats was highly suited to a continuous flow set-up and under optimized conditions, excellent conversion of thioanisole was attained throughout the period tested. Leaching of vanadium from the support was reduced by covalently linking the ligand to the support rather than relying on the comparatively weaker vd Waals forces and pi-stacking. Further improvements to leaching were observed when incorporating a bidentate ligand, although the lowest leaching was observed using polybenzimidazole fibers as support material. These gold coloured fibers were the “gold standard” in terms of mechanical, chemical and thermal stability. These properties in cahoots with the metal-coordinating nature of the benzimidazole group make this material an ideal support, not only for vanadium, but for a range of metals or metal nanoparticles.

5.7 References and notes

- (1) Ebert, K.; Bengtson, G.; Just, R.; Oehring, M.; Fritsch, D. *Appl. Catal. A* **2008**, *346*, 72.
- (2) Wang, Y.; Chen, J.; Xiang, J.; Li, H.; Shen, Y.; Gao, X.; Liang, Y. *React. Funct. Polym.* **2009**, *69*, 393.
- (3) Fu, B.; Zhao, P.; Yu, H.-C.; Huang, J.-W.; Liu, J.; Ji, L.-N. *Catal. Lett.* **2009**, *127*, 411.
- (4) Huang, Z. M.; Zhang, Y. Z.; Kotaki, M.; Ramakrishna, S. *Compos. Sci. Technol.* **2003**, *63*, 2223.
- (5) Ding, B.; Wang, M.; Wang, X.; Yu, J.; Sun, G. *Mater. Today* **2010**, *13*, 16.
- (6) Dong, Z.; Kennedy, S. J.; Wu, Y. *J. Power Sources* **2011**, *196*, 4886.
- (7) Chigome, S.; Darko, G.; Torto, N. *Analyst* **2011**, *136*, 2879.
- (8) Andradý, A. L. *Science and Technology of Polymer Nanofibers*. John Wiley and Sons, Inc: New Jersey, 2008.
- (9) Piskin, E.; Bölgen, N.; Egri, S.; Isoglu, I. A. *Nanomedicine* **2007**, *2*, 441.
- (10) Agarwal, S.; Wendorff, J. H.; Greiner, A. *Polymer* **2008**, *49*, 5603.
- (11) Ashammakhi, N.; Ndreu, A.; Piras, A.; Nikkola, L.; Sindelar, T.; Ylikauppila, H.; Harlin, A.; Chiellini, E.; Hasirci, V.; Redl, H. *Journal of Nanosci. Nanotech.* **2006**, *6*, 2693.
- (12) Venugopal, J.; Ramakrishna, S. *Applied Biochem. Biotechnol.* **2005**, *125*, 147.
- (13) Degni, S.; Wilén, C.-E.; Leino, R. *Org. Lett.* **2001**, *3*, 2551.
- (14) Xuefei, C.; Yang, H.; Zhen-Liang, X. *Mater. Lett.* **2011**, *65*, 1719.
- (15) Stasiak, M.; Röben, C.; Rosenberger, N.; Schleth, F.; Studer, A.; Greiner, A.; Wendorff, J. H. *Polymer* **2007**, *48*, 5208.
- (16) Dong, H.; Wang, D.; Sun, G.; Hinestroza, J. P. *Chem. Mater.* **2008**, *20*, 6627.
- (17) Sidorov, S. N.; Bronstein, L. M.; Kabachii, Y. A.; Valetsky, P. M.; Soo, P. L.; Maysinger, D.; Eisenberg, A. *Langmuir* **2004**, *20*, 3543.
- (18) Obuya, E. A.; Harrigan, W.; Andala, D. M.; Lippens, J.; Keane, T. C.; Jones Jr, W. E. *J Mol. Catal. A: Chem.* **2011**, *340*, 89.
- (19) Chen, L.; Hong, S.; Zhou, X.; Zhou, Z.; Hou, H. *Catal. Comm.* **2008**, *9*, 2221.
- (20) Sambasivudu, K.; Reddy, Y. B.; Yadav, J. S.; Sabitha, G.; Shailaja, D. *Int. J. Polym. Mater.* **2008**, *57*, 891

-
- (21) Chuangchote, S.; Jitputti, J.; Sagawa, T.; Yoshikawa, S. *ACS Appl. Mater. Interfaces* **2009**, *1*, 1140.
- (22) Sellergren, B.; Karmalkar, R. N.; Shea, K. J. *J. Org. Chem.* **2000**, *65*, 4009.
- (23) Eseola, A. O.; Li, W.; Gao, R.; Zhang, M.; Hao, X.; Liang, T.; Obl-Egbedi, N. O.; Sun, W. H. *Inorg. Chem.* **2009**, *48*, 9133.
- (24) N-vinylimidazole-2-carboxylaldehyde (1.6 g, 0.013 mol) was mixed with styrene (6.4 g, 0.061 mol) and initiator AIBN was added (0.016 g, 0.2 wt%). The solution was purged with argon, sealed and then heated to 60 °C. Polymerization was allowed to proceed for a period of 24 hours. Following this, the polymer was dissolved in chloroform and precipitated by addition of methanol. This process was carried out thrice to ensure complete removal of unreacted monomer. Finally, the polymer was washed with methanol and diethyl ether and dried in an oven at 60 °C. ATR-IR (cm⁻¹, neat): 3028, 2928, 1692, 1453, 762, 696. *Anal. Found (%)*: C, 86.47, H, 7.68, N, 3.16.
- (25) Huang, J.; Huang, K.; Liu, S.; Luo, Q.; Shi, S. *J. Colloid Interface Sci.* **2008**, *317*, 434.
- (26) Selbin, J. *Chem. Rev.* **1965**, *65*, 153.
- (27) Rogers, G. A.; Bruce, T. C. *J. Am. Chem. Soc.* **1974**, *96*, 2463.
- (28) Caselli, A.; Buonomenna, M. G.; de Baldironi, F.; Laera, L.; Fantauzzi, S.; Ragaini, F.; Gallo, E.; Golemme, G.; Cenini, S.; Drioli, E. *J. Mol. Catal. A: Chem.* **2011**, *317*, 72.
- (29) Greiner, A.; Wendorff, J. H. *Angew. Chem. Int. Ed.* **2007**, *46*, 5670.
- (30) Groenenboom, C. J.; Sawatzky, G.; de Liefde Meijer, H. J.; Jellinek, F. *J. Organomet. Chem.* **1974**, *76*, C4.
- (31) Eda, G.; Shivkumar, S. *J. Appl. Polym. Sci.* **2007**, *106*, 475.
- (32) Hearle, J. W. S., *High-performance fibers*; Woodhead Publishing Ltd: Cambridge, 2001.
- (33) Miller, M. M.; Sherrington, D. C. *J. Chem. Soc., Chem. Comm.* **1994**, 55.
- (34) Miller, M. M.; Sherrington, D. C. *J. Catal.* **1995**, *152*, 368.
- (35) Li, N. H.; Fréchet, J. M. J. *J. Chem. Soc., Chem. Comm.* **1985**, 1100.
- (36) Tang, H.-G.; Sherrington, D. C. *Polymer* **1993**, *34*, 2821.
- (37) Leinonen, S.; Sherrington, D. C.; Sneddon, A.; McLoughlin, D.; Corker, J.; Canevali, C.; Morazzoni, F.; Reedijk, J.; Spratt, S. B. D. *J. Catal.* **1999**, *183*, 251.
- (38) Kim, J.-S.; Reneker, D. H. *Polym. Eng. Sci.* **1999**, *39*, 849.
-

-
- (39) Qin, X-H.; Yang, E-L.; Li, N.; Wang, S-Y. *J. Appl. Polym. Sci.* **2006**, *103*, 3865.
- (40) von Graberg, T.; Thomas, A.; Greiner, A.; Antonietti, M.; Weber, J. *Macromol. Mater. Eng.* **2008**, *293*, 815.
- (41) Sannigrahi, A.; Ghosh, S.; Maity, S.; Jana, T. *Polymer* **2010**, *51*, 5929.
- (42) Nakamoto, Z. *Infrared and raman spectra of inorganic and coordination compounds*; John Wiley and Sons: New York, 1978.
- (43) Zeng, X-R.; Ko, T-M. *Polymer* **1998**, *39*, 1187.
- (44) Jouanneau, J.; Mercier, R.; Gonon, L.; Gebel, G. *Macromolecules* **2007**, *40*, 983.
- (45) Sannigrahi, A.; Arunbabu, D.; Sankar, R. M.; Jana, T. *J. Phys. Chem., B* **2007**, *111*, 12124.
- (46) Lobato, J.; Canizares, P.; Rodrigo, M.; Linares, J.; Aguilar, J. *J. Membr. Sci.* **2007**, *306*, 47.
- (47) Udupa, M. R. *Thermochim. Acta* **1981**, *51*, 169.
- (48) Srivastava, S.; Pandey, O. P.; Sengupta, S. K. *Trans. Met. Chem.* **1996**, *21*, 262.
- (49) Tang, C.; Saquing, C. D.; Harding, J. R.; Khan, S. A. *Macromolecules* **2009**, *43*, 630.
- (50) Xu, X.; Zhang, J.-F.; Fan, Y. *Biomacromolecules* **2010**, *11*, 2283.
- (51) If one considers this from an organic chemistry perspective - it would be extremely useful to be able to buy a column through which a set of reagents could be passed and the product collected on the other end (this rather than having to filter the catalyst off). This would greatly simplify the synthesis process and satisfy the organic chemists' desire for running columns. While beyond the scope of this thesis, one can consider combining these catalytic fibers with fibers functionalized with other various groups which retain by-products of a reaction. Thus, after passing reagents through the column, the pure product would be collected only! Of course, the ability to reuse such an "all-in-one" column would be highly advantageous.
- (52) Miller, M. M.; Sherrington, D. C. *J. Catal.* **1995**, *152*, 377.

This page has been left blank intentionally

Chapter 6

Conclusions and future work

6.1 Conclusions

In this study, a range of new catalytically active VHPO-inspired oxovanadium(IV) functionalized materials were prepared and characterized. The Merrifield-based catalysts (**Part 2, Chapter 3**) demonstrated promising catalytic activity for the hydrogen peroxide facilitated oxidation of thioanisole, styrene and ethylbenzene. The harsh conditions required for achieving high conversions of the latter two substrates, resulted in degradation of the support material. For thioanisole, however, excellent conversions were obtained under milder conditions and the catalysts also demonstrated a high degree of recyclability.

Suspension polymerization was then used to create a new metal-coordinating resin (**Part 2, Chapter 4**). These imidazole-bound, rough-surfaced microspherical beads had significantly higher surface areas than the Merrifield-based beads. Despite this, however, there was very little difference in catalytic activity between the two types of beads. Nevertheless, these beads also showed good catalytic activity for the oxidation of thioanisole with excellent recyclability and mechanical stability.

Fibers were then fabricated by electrospinning (**Part 2, Chapter 5**). These fibers had small diameters and thus a large exposed catalytic surface area, but are comparatively long and form a web-like mat. This makes these materials very easy to separate from the reaction solution. The polystyrene-based fibers, however, proved to have limited mechanical stability under the agitation of a mechanical stirrer but were very successfully applied under continuous flow conditions. Near quantitative conversions were obtained over a reasonable time period. Leaching of vanadium from the support was reduced by incorporating a bidentate ligand instead of the monodentate imidazole ligand. The limited mechanical and chemical stability of the polystyrene-based fibers was then overcome by using polybenzimidazole fibers. This material proved to be ideal, not only was this polymer thermally, mechanically and chemically more robust, but it contained a large

number of coordinating benzimidazole groups allowing for a high metal loading compared to the other copolymers. This work represents one of the first instances of using oxovanadium(IV) functionalized electrospun fibers as heterogeneous catalysts.

Generally, the crosslinked beads displayed better mechanical robustness than the electrospun fibers. For this reason the fibers were less suited to the stirred-batch reactions. On the other hand, the flexibility and porous three dimensional mat structure of the fibers was more suited to continuous flow processes. The differences in surface area between the materials did not seem have a significant effect on overall catalytic activity.

6.2 Future work

Electrospun fibers have excellent properties for use as a catalyst support material, as they have extremely small diameters but are easily separable from solution. As shown in this study, these fibers are especially well suited for use under continuous flow conditions. However, since linear polymers are required to prepare the electrospinning solution, solubility and mechanical robustness of fibers proved to be a challenge. In the future, this could be addressed by electrospinning a more chemically and mechanically stable polymer (such as nylon) followed by grafting the necessary coordinating functionality to the fibers. In this way, high levels of coordinating moieties could be introduced without compromising the mechanical and chemical stability of the material. Another approach involves post-electrospinning crosslinking. This would dramatically improve the chemical stability properties of the material but could make it more brittle. Nevertheless, there certainly remains some room for improvement in terms of stability of the material.

Based on the work in this study, it is believed that a tetradentate rather than mono or bidentate ligands, could improve the leaching characteristics of the metal. In addition, using a tetradentate ligand would result in a coordination environment more similar to the homogeneous derivative and allow for easier comparison between the two.

The imidazole-functionalized electrospun fibers prepared in this study were used to immobilize oxovanadium(IV), however, several other transition metals could be immobilized in the same way. Thus, several other metal-catalyzed reactions could be carried out using the same materials prepared herein, with only slight modifications in the final synthetic step. In addition, the use of imidazole-containing beads for removal of heavy metals is widespread. These imidazole-functionalized fibers, with their unique properties, could similarly be used for such applications.